Hydrogen absorption property of nanocrystalline-magnesium films

Dissertation

zur Erlangung des mathematisch-naturwissenschaftlichen Doktorgrades

"Doctor rerum naturalium"

der Georg-August-Universität Göttingen

-

im Promotionsprogramm ProPhys

der Georg-August University School of Science (GAUSS)

vorgelegt von

Helmut Takahiro Uchida
aus Stuttgart

Göttingen 2015

Betreuungsausschuss

....
(Name, Abteilung/Arbeitsgruppe, Institution)

....
(Name, Abteilung/Arbeitsgruppe, Institution)

....
(Name, Abteilung/Arbeitsgruppe, Institution)

Mitglieder der Prüfungskommission

Referent/in: Prof. Dr. Astrid Pundt, Institut für Materialphysik, Universität Göttingen.
(Name, Abteilung/Arbeitsgruppe, Institution)

Korreferent/in: Prof. Dr. Konrad Samwer, I. Physikalisches Institut, Universität Göttingen.
(Name, Abteilung/Arbeitsgruppe, Institution)

ggf. 2. Korreferent/in: ....
(Name, Abteilung/Arbeitsgruppe, Institution)

Weitere Mitglieder der Prüfungskommission:

Prof. Dr. Reiner Kirchheim, Institut für Materialphysik, Universität Göttingen.
(Name, Abteilung/Arbeitsgruppe, Institution)

Prof. Dr. Hans-Ulrich Krebs, Institut für Materialphysik, Universität Göttingen.
(Name, Abteilung/Arbeitsgruppe, Institution)

Prof. Dr. Michael Seibt, IV. Physikalisches Institut, Universität Göttingen.
(Name, Abteilung/Arbeitsgruppe, Institution)

Prof. Dr. Wolfram Kollatschny, Institut für Astrophysik, Universität Göttingen.
(Name, Abteilung/Arbeitsgruppe, Institution)
Tag der mündlichen Prüfung: 27. Nov. 2015

Table of Contents

1. Introduction

The global demand for energy is increasing, and predicted to increase additionally by 37 % by 2040 [EIA14]. Since the global energy crisis in the 1970's, the utilization of alternative and renewable energy sources has been proceeded. Recently, renewable energy provided an estimated 19.1% of global final energy consumption by 2013 [REN15], and also accounts for 43.6% of newly installed generating capacity in 2013 [UNEP14]. As a matter of policy to a sustainable future, further installation of environment-friendly energy systems is required. Furthermore, the creation of energy dispersive society is essential in the viewpoint of energy security, lowering risks of disasters and crisis. In those social backgrounds, efficient techniques for energy storage and energy transportation are becoming more and more important. Hydrogen has potential to play a major role as one key material.

Developing hydrogen storage techniques is therefore of greatest importance, as we approach the hydrogen society in the near future. Metals are known to store hydrogen compactly and safely, the understanding of hydrogen behavior in metal is in all cases required as its cornerstone and background.

Hydrogen is the smallest and most abundant element in the universe, mostly and practically existing as water, which is one of the major components in the environment on the surface of the earth [Wint09]. The phenomenon that hydrogen can solute into several metals is well known since a long time. A pioneering work in this field was conducted by Sieverts [Siev29,Siev35]. It is known that hydrogen can be reversibly stored through metal/metal hydride (MH) phase transition, even up to several wt.% in some alloys or intermetallic compounds, just by tuning gas pressure or temperature [Vught70]. Not only due to their ease to handle, but also from the economical and industrial point of view, intermetallic compounds of $LaNi_5$- or TiFe-based alloys are typically chosen for hydrogen storage. Currently, further research and development is on the way, focusing on improving gravimetric hydrogen density and the reaction kinetics [Dorn07,Orimo07,Hirs10]. Hydrogen storage has also been utilized for other technical applications. For example, fuel cell systems [Iwasa03] and their co-generation systems such as Ene-Farm [Pana13,Cart13], MH-batteries [Nott00,Kane08], MH-chemical compressor systems [Mal78,Nomu83,Loto14], MH-heat pump systems [Gure78,Orga87] as MH refrigerators [Uchi04] or air conditioners [Ron84], are good examples of developed applications in this field. Metal hydrides can store hydrogen with high volume density and high stability, in comparison with other storage methods like liquid hydrogen or high-pressure H_2 gas tanks [Zütt03,Zütt04]. For example, the volume density of hydrogen increases ca. 950 times upon absorption by Pd, compared to its gaseous state [Koss11]. Or, as another example, fully hydrogenated magnesium hydride contains hydrogen with a volume density 1.5 times higher than the density of liquid H_2 [Petr09].

Nano-structuring has attracted much attention apart from those developments in a viewpoint of controlling the total performance of the M-H reaction, including thermodynamics of the system

and interaction of hydrogen with defects. Actually, many studies reported that the metal nano-clusters and metallic thin films have rather different, as well very interesting hydriding reaction properties from that of massive metals [Pundt04,Pundt06,Yama08], also with incidental optical property changes [Huib96] for some materials.

In case of bulk material, hydrogen absorption in interstitial sites yields lattice expansion in three dimensions, forming defects such as cracks at the surface through creating dislocations in the material. Metallic thin films are allowed to expand only in the out-of-plane direction, as long as the film is not detached from the substrate. This out-of-plane expansion contains a linear contribution from the applied in-plane stress, according to the linear elastic theory [Laud99^{+},Slau02]. The in-plane compressive stress of the film can reach the GPa range during the hydrogen absorption, while it is zero for out-of-plane direction.

From an engineering point of view, a high hydrogen capacity in weight ratio is required for storage materials for mobile and automotive applications [Hirs10]. Actually, Mg-H is known to be the most interesting system in this regard. Its hydride has a high theoretical hydrogen content of 7.6 wt.%, which is the largest content in the hydrides of industrially low-cost metals [Dorn07]. Furthermore, Mg is abundantly supplied, as is shown in **Fig. A3.1** [Vesb12] in **Appendix A3**. This high weight content material has an advantage in usage for a practical mobile storage.

However, the slow sorption rate hinders its practical use [Akib82,Nott09]. The slow hydrogen sorption kinetics is caused by the MgH_2 itself, which blocks hydrogen diffusion ("Blocking effect" [Zhda93,Fried97]). Various attempts overcoming this effect have been reported. Furthermore, decomposition of the too stable magnesium hydride is also difficult for a practical mobile storage: a hydride decomposition enthalpy between -30 kJ/(mol H_2) and -48 kJ/(mol H_2) is required [Schl01,Baldi09^{++}]. The decomposition enthalpy of the bulk MgH_2 is much higher (-74.4 kJ/(mol H_2) [Stamp60]), which denotes the hydride phase is thermodynamically too stable from a practical application perspective. Thermodynamically stable bulk β-MgH_2 needs temperature higher than 553 K in p_{H2} = 0.1 MPa [Stamp60] to decompose. As this thermodynamical property limits its practical use, destabilisation of the β-MgH_2 phase is one of the interests from the viewpoint of hydrogen storage technique.

In order to improve the thermodynamic properties of MgH_2, alloying with Ni and Cu has been investigated [Reil67,Reil68]. But, still a reaction temperature of more than 513K is needed in p_{H2} = 0.1 MPa, in case of alloying with Ni [Dorn09]. Investigations in Mg-based intermetallic phases [Kohn00,Rönn03,Kyoi04,Goto05,Taka07,Kama08,Zhan11], in alloys [Kame05,Zhou13, Zhon14,Zhou14], and in composite systems with other hydrides or mixed compounds [Ichi10,Nori11,Shep11,Godu12,Wan13,Pist14], are proceeding.

For a better reaction rate, researchers used nano-crystallization upon mechanical alloying (ball-milling) [Chen95,Huot01] or by the equal channel angular pressing (ECAP) treatments [Skri04], proposed by suitable catalysts [Mintz78,Oele01,Bark03,Hana05,Andr06,Fried06, Hana06,Koji06,Du08,Lillo08,Luo08,Yu09,Sabi10,Sing10,Dana12,Zhou13^{+},Must14,Ren14].   Up

to now, the pure impact of grain boundaries on the hydrogen sorption kinetics in Mg is still unclear.

Also, it is known that the mechanical stress in metal films on hard substrates could reach up to the GPa orders. Under such conditions, the stress can significantly change the films thermodynamics with hydrogen, on the basis of previous studies for Nb-, Gd-, Y-, Pd-, and Ti-films [Pundt06,Wagn08,Tal-G10,Kirch14,Wagn15]. Because of the high stability of Mg hydrides, an investigation for the possibility of the adsorption temperature reduction in film Mg-H system is of a large interest not only from a scientific viewpoint, but also for applications.

This thesis focusses on the kinetic aspects of hydrogen absorption in Mg thin films which is strongly affected by the hydride formation and the blocking effect. Especially the formation of the blocking layer turned out to be a central and still unsolved issue. The determination of diffusion constants in different concentration regimes and study of an impact of grain boundaries are further points of consideration in this thesis.

To address these points, hydride formation and growth as well as the evolution of inner stress will be analyzed in details. The influence of hydrogen loading conditions and the driving force on the hydrogen absorption behavior of pure Mg is studied. Also, the impact of the stress on thermodynamics of Mg-H system will be evaluated. Furthermore, the influence of the grain boundaries on the hydrogen permeability will be addressed. Finally, a hydrogen absorption model on Mg films will be formulated, which includes all the experimental results.

To investigate these points systematically, Mg films were prepared with different thicknesses, mainly at room temperature. Some films were also annealed. On these films their crystal structure and development of in-plane stress were characterized by *in-situ* and *ex-situ* X-ray diffraction (XRD) setups. Step-by-step (gas- and electrochemical) hydrogen loading, and constant pressure gas loading were used in this work. Permeation measurements have been performed for Mg-films on palladium substrates, to see the hydrogen diffusivity at different hydrogen concentrations. The influence of stress on thermodynamic properties of the Mg-H system was evaluated, from *in-situ* gas loading measurements at different temperatures. To explain the results, a hydrogen absorption model with two stages was developed; applying calculations via Finite Element Method (FEM) were also performed.

This thesis consists of 7 chapters. After the background and motivation of this study described in Chapter 1, Chapter 2 treats the theoretical background of the Mg-H system, and related hydrogen- and temperature- induced volume expansion, and stress-increase based on linear elastic theory are presented. In Chapter 3, the experimental techniques and the calculation methods used in this study are summarized. Chapter 4 shows the as-prepared states of samples. Chapter 5 introduces experimental results during hydrogen loadings. It is separated into individual sections, and the individual results are shortly discussed. In Chapter 6, all of these results are globally discussed in a combined way, especially focusing on the degrees of different hydrogen concentration stages. Chapter 7 summarizes this thesis.

2. Hydrogen in thin films

This chapter introduces on thermodynamical and kinetical aspects of hydrogen absorbed in metals, focusing on Mg, Pd and their intermetallic compounds. Afterwards, it explains the hydrogen induced volume expansion and stress arising in a Mg film clamped to a substrate. At the end of this chapter, temperature induced thermal stress in Mg films, with its unavoidable effects on film measurements at different temperatures, is explained.

2.1 Hydrogen in metals

Hydrogen atoms solute in metals, after an adsorption- and dissociation process on metal surfaces [Chris88]. Hydrogen atoms occupy typically 2 different interstitial sites that are denoted as tetragonal site (T-site) and octahedral site (O-site), respectively. **Fig. 2.1** shows typical examples of the interstitial sites for hydrogen atoms occupation in metals, which depend on the crystal structures. For example, the BCC lattice contains 3 possible O-sites and 6 T-sites per metal atom, resulting in a maximum theoretical solubility of 3 H/Me and 6 H/Me, respectively. It is known that the occupation of hydrogen atoms in metal usually follows the "Westlake's criterion"; a geometric model that uses only a minimum hole radius (0.40 Å) and a minimum H-H distance (2.10 Å) in the development of a rationale for the observed stoichiometries in hydrides of intermetallic compounds. All the hydrogen atoms keep distances to each other, at least the length of 2.1 Å [Westl83,Westl83b]. Often, the site occupation of H in BCC lattices changes from T-site to O-site as the hydrogen concentration increases. Mg has the HCP structure and keeps it until the solid solution limit (see details in **Chap. 2.1.5.1**).
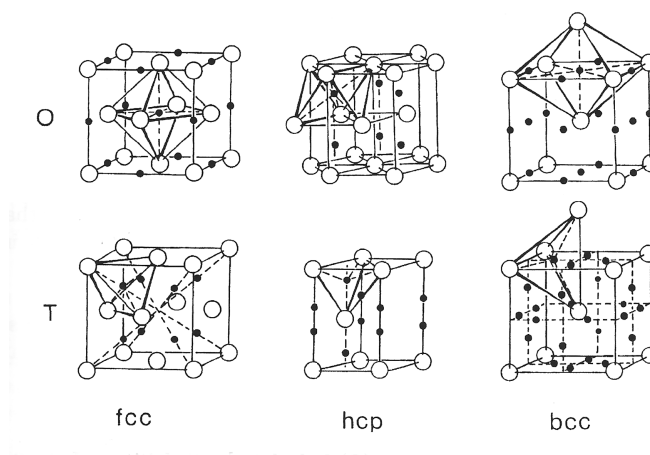
Fig. 2.1 Interstitial sites for hydrogen atoms in the FCC, HCP and BCC metal host lattices. (T = "tetrahedral site", O = "octahedral site") [Fukai05]. Full circle marks are possible hydrogen atoms positions. Open circles depict metal atom positions.

2.1.1 Hydrogen induced lattice expansion

The introduction of one hydrogen atom into a metal crystal lattice with lattice constant a induces a volume expansion, $\Delta\upsilon$. The relative volume change $\Delta V/V$ in the hydrogen concentration range of the solid solute state is defined as

$$\frac{\Delta V}{V} \approx 3 \cdot \frac{\Delta a}{a} = c_{\mathrm{H}} \cdot \frac{\Delta\upsilon}{\Omega} \tag{2.1}$$

where V is the whole metal volume, Δa is the change of the lattice constant, and Ω is a mean atomic volume [HinMeI]. The metal lattice expands and increases its volume by the hydrogen uptake. This volume expansion is approximately 2-3 Å^3 per hydrogen atom [Fukai89,Bara71].

Thus, hydrogen uptake yields a linear relationship with the hydrogen concentration c_{H} (H/M) in the ideal case. The linear increase of the lattice parameter is experimentally verified for most metals with cubic structures [HinMeI]. The relative sample volume change $\Delta V/V$ can be experimentally determined by XRD-lattice parameter measurements or by dilatometric measurements at several c_{H}, applying Eq.(2.1).

For bulk Pd, which has a solid solution limit in the order of $c_{\mathrm{H}} \sim 10^{-2}$ H/Pd [Fries73] (see also **Fig. 2.13** in **Chap. 2.1.6.1**), the expansion coefficient is reported as $\Delta\upsilon/\Omega = 0.19$ [HinMeI]. In contrast, the total expansion in the solid solution is small for the Mg-H bulk system, compared to that due to the phase transformation ($\Delta V/V = 0.3$), because of the small solubility limit of hydrogen in α-Mg phase. The solid solution limit is in the order of $c_{\mathrm{H}} = 10^{-7}$ H/Mg - 10^{-6} H/Mg at $T = 300$ K [Koen59,Sanma87]. For bulk Mg-MgH$_2$ system, $\Delta\upsilon/\Omega = 0.0787$ is determined by Schober *et al.* [Schob81], applying their TEM observation results for a lattice formation model.

2.1.2 Hydrogen solution in metals

Hydrogen solution from gas phase into metals can be expressed by the following reaction [HinMeI].

$$\frac{1}{2}\mathrm{H}_2(\mathrm{gas}) \rightarrow \mathrm{MH}(\mathrm{solid}) \tag{2.2}$$

The condition of thermal equilibrium is given by the equality of the chemical potential of hydrogen in the two phases,

$$\frac{1}{2}\mu_{\mathrm{H}_2}^{\mathrm{gas}} = \mu_{\mathrm{H}}^{\alpha} \tag{2.3}$$

where $\mu_{\mathrm{H}_2}^{\mathrm{gas}}$ is the chemical potential of gaseous hydrogen per molecule, and $\mu_{\mathrm{H}}^{\alpha}$ is that of hydrogen in the solid solution per atom.

The change of μ_H^α and regarding Gibbs's free energy are then expressed as,

$$\Delta\mu_H^\alpha = \Delta\overline{H}_s - T\Delta\overline{S}_s \tag{2.4}$$

$$\Delta G = \Delta H_s - T\Delta S_s \tag{2.5}$$

where $\Delta\overline{H}_s$ and $\Delta\overline{S}_s$ are called partial molar enthalpy and partial molar entropy, respectively. At a given temperature, the relationship

$$\Delta G = -RT \ln K_p \tag{2.6}$$

is known, where K_p is an equilibrium constant.

Under the equilibrium, the condition $\Delta G = 0$ is established. Hence,

$$
\begin{aligned}
\Delta G &= \mu_H^\alpha - \frac{1}{2}\mu_{H_2}^{gas} \\
&= \left(\mu_H^{\alpha,0} + RT\ln a_{H_2}\right) - \left(\frac{1}{2}\mu_{H_2}^{gas,0} + \frac{1}{2}RT\ln f_{H_2}\right) \\
&= \mu_H^{\alpha,0} - \frac{1}{2}\mu_{H_2}^{gas,0} + RT\ln a_H - \frac{1}{2}RT\ln f_{H_2} \\
&= \Delta G_0 + RT\ln\frac{a_{H_2}}{(f_{H_2})^{1/2}} = 0
\end{aligned}
\tag{2.7}
$$

where ΔG_0 is the standard free energy change of hydrogen solution reaction per mol H atoms, a_H is the activity of solved H atom, and f_{H_2} is the fugacity of H_2 gas. If $c_H \sim 0$, and the pressure of hydrogen p_{H_2} is below several MPa, one can approximate the activity coefficient γ_H and the fugacity coefficient β_{H_2} as ~1 and thus $a_H \sim c_H$ (defined as $c/(1-c) = H/Me$) and $f_{H_2} \sim p_{H_2}$.

By this, the logarithmic term in Eq.(2.7) becomes

$$\frac{a_H}{(f_{H_2})^{1/2}} = \frac{c_H \cdot \gamma_H}{(p_{H_2} \cdot \beta_{H_2})^{1/2}} \cong \frac{c_H}{(p_{H_2})^{1/2}} \tag{2.8}$$

Combining Eqs. (2.7) and (2.8) results in

$$\Delta G^0 = -RT\ln\frac{c_H}{(p_{H_2})^{1/2}} \tag{2.9}$$

Eq.(2.6) and Eq.(2.9) gives a relationship between $(p_{H_2})^{1/2}$ and c_H as follows.

$$
\begin{aligned}
K_p &= \frac{c_H}{(p_{H_2})^{1/2}} \\
c_H &= K_p \cdot (p_{H_2})^{1/2}
\end{aligned}
\tag{2.10}
$$

This indicates that the hydrogen concentration c_H is proportional to the square root of the hydrogen pressure, $(p_{H_2})^{1/2}$. This relationship was firstly found by Sieverts [Siev29] and is called Sieverts' law and the equilibrium constant K_p is called as Sieverts' constant often noted as K_s or S.

From Eq.(2.5) and Eq.(2.9), c_H can be calculated at given p_{H_2} and T as follows, if ΔH^0 and ΔS^0 or ΔG^0 are known.

$$c_H = \frac{-\Delta G^0}{RT} \cdot (p_{H_2})^{1/2} = \exp\left(\frac{\Delta H_s^0 - T\Delta S_s^0}{RT}\right) \cdot (p_{H_2})^{1/2} \tag{2.11}$$

Hydrogen solution enthalpy ΔH_s^0 depends on the conditions of p_{H_2} and T. **Table 2.1** summarizes the reported hydrogen solution enthalpy in Mg with various conditions.

Table 2.1 Hydrogen solution enthalpy ΔH_s in bulk-Mg, reported by [Wata75,Shap81,Popov75].

$-\Delta H_s^0$ [kJ (mol H)$^{-1}$]	Conditions	Ref.
21.06	469-867 K, gasloading with $p_{H2} = 10^5$ Pa	[Wata75]
20.0 ± 0.4	675-918 K, gasloading with $p_{H2} = 10^5$ Pa	[Shap81]
24.4 ± 1.2	676-876 K, gasloading with $p_{H2} = 10^5$ Pa	[Popov75]

It is noted that Eq.(2.10) and Eq.(2.11) are strictly valid in ideal case that the interaction of hydrogen atoms is negligible. In the actual case, the enthalpy term in Eq.(2.11) is known to change at elevated temperature (for example, [Flan91]), or at high c_H, because of the effect of interactions between solute hydrogen atoms [Fukai05], and therefore the enthalpy term could change. Stress effect on hydrogen potential is also known [Li66,Kirch86]. These effects cause a deviation from Sieverts' law.

As an example for hydrogen solution in a bulk Pd, the temperature dependence and the concentration dependence of the hydrogen solution enthalpy in Pd are shown in **Fig. 2.2**. Mg is excluded in this figure, because of its small hydrogen solubility. Those values are for the bulk material, and could be changed under a stressed condition such as clamped thin films. Details about ΔH_s^0 and ΔS_s^0 for Pd is will be shown in **Chap. 2.1.6.1**.
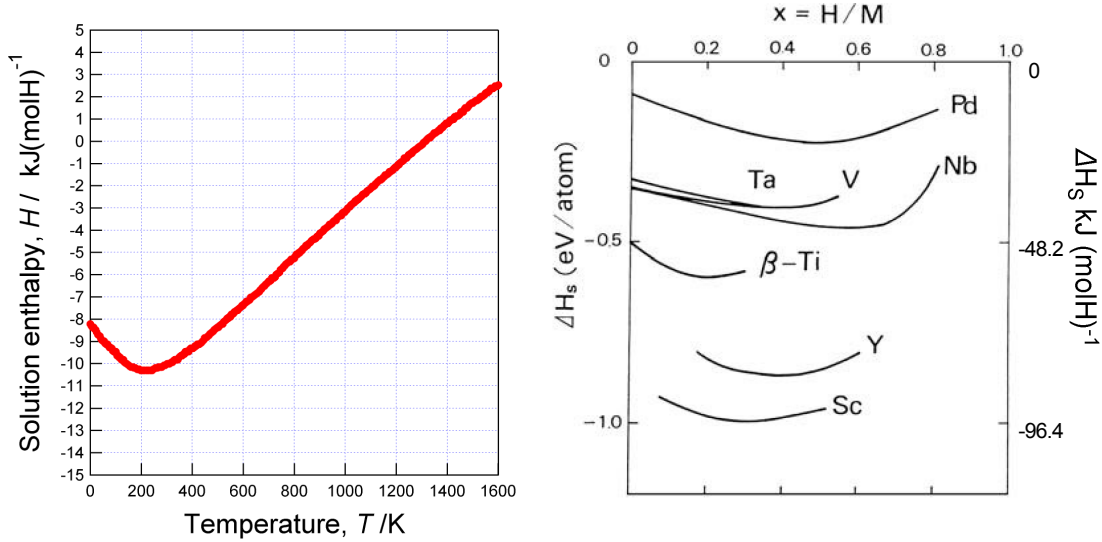
Fig. 2.2 Hydrogen solution enthalpy ΔH_s in bulk-Pd, temperature dependency (left, taken from [Flan91]) and concentration dependency of ΔH_s in different bulk materials (right, axis added to [Fukai05]).

2.1.3 Formation of hydride phase

At high hydrogen concentrations ($c_H > 0.1$ H/M), interactions among hydrogen atoms become important because of the lattice expansion, and the phase transition into hydride phase (β-phase) takes place. Hydride formations from gaseous hydrogen can be described by the pressure-composition isotherms (p-c-T diagram, *e.g.* **Fig. 2.10** for Mg-H system, or **Fig. 2.13** for Pd-H system). In the hydrogen concentration range where α-phase and β-phase coexist, there is a plateau in the isotherm curve. This plateau has a width, giving the miscibility gap in phase diagrams. At the higher c_H range in the pure β-phase region, hydrogen pressure rises steeply with the concentration. Hydride formation is suppressed at high temperatures, because of entropy. For a system which has no structure change in the matrix phase such as Pd-H, the miscibility gap ends in a critical point (T_C), above which the change from the α- to the high-concentration phase is continuous. Thus, there is no transition any more. The equilibrium pressure p_{eq} is related to the enthalpy change ΔH and the entropy change ΔS, respectively. Hence, p_{eq} can be expressed as a function of temperature by the van't Hoff equation [Zütt04]:

$$\ln\left(\frac{p_{eq}}{p_{eq}^0}\right) = \frac{\Delta H}{R} \cdot \frac{1}{T} - \frac{\Delta S}{R} \qquad (2.12)$$

where p_{eq}^0 is the standard pressure, R is the gas constant, and T is the temperature of the system. Entropy change term ΔS corresponds mostly to the loss of the entropy of molecular hydrogen gas. The standard entropy of hydrogen is approximately $\Delta S_0 = 130$ J·K⁻¹mol⁻¹ [Fukai05], therefore the entropy change in Eq.(2.12) can be treated as $\Delta S \approx -130$ J·K⁻¹(mol H₂)⁻¹ for all metal-hydrogen systems.

The enthalpy term ΔH concerns the bonding energy between hydrogen and the metal. The

enthalpy is expressed as the slope in the van't Hoff plot, which describes the equilibrium hydrogen pressure logarithmically. This term strongly characterizes the stability of the metal hydride.

Fig. 2.3 shows van't Hoff plots corresponding to transitions of bulk Pd-PdH$_{0.6}$ [Fries73] and bulk Mg-MgH$_2$ [Stamp60]. Hydrogen uptake gives a β-MgH$_2$ phase with a plateau pressure of about $p_{H2} \approx 3 \cdot 10^{-6}$ bar at room temperature, which is 4 orders of magnitude lower than that of bulk β-Pd formation. Detailed plot for Mg-MgH$_2$ transition is shown in **Fig. 2.12** in **Chap. 2.1.5.3**, and p-c-T plot for this Pd-PdH$_{0.6}$ transition will be shown in **Fig. 2.13**.

For materials combinations, hydrogen will preferentially solve in Mg and form the hydride at lower pressures.
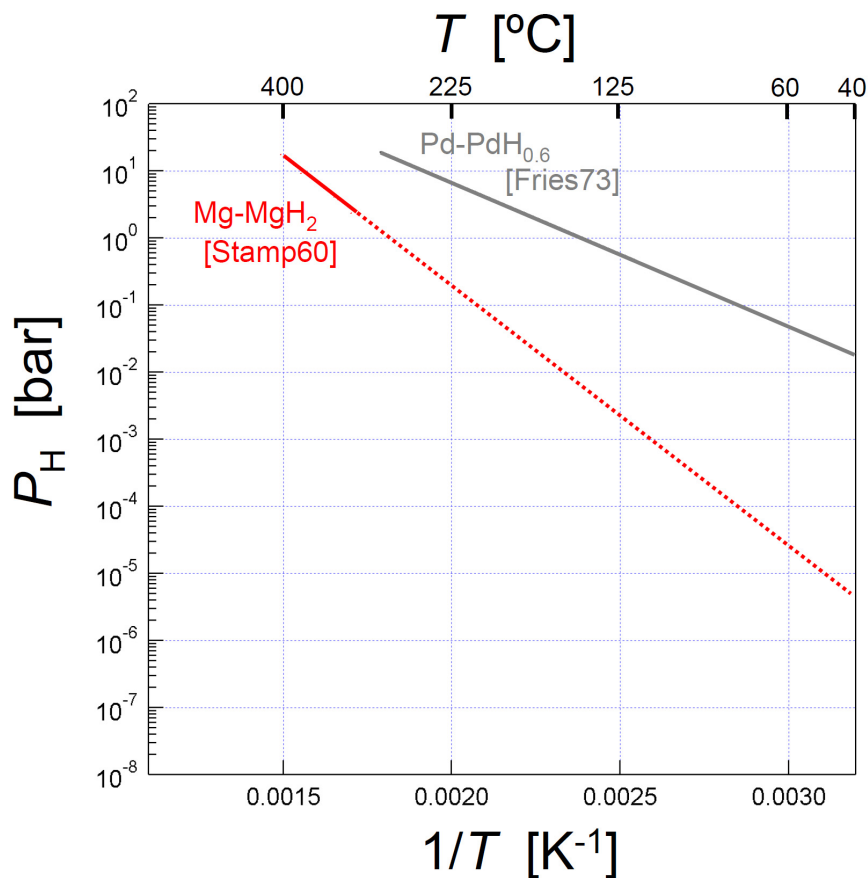
Fig. 2.3 Van't Hoff plot for Mg-MgH$_2$ transition [Stamp60] and Pd-PdH$_{0.6}$ transition [Fries73]. Extrapolation line to lower temperature is inserted in the figure, for data by Stampfer *et al*.

2.1.4 Hydrogen diffusion in metal

Hydrogen atoms in metal have a large mobility, and diffuse [HinMeI]. In case of the Mg-H system, Mg is known to have a strong affinity to hydrogen and the crystal properties change from metallic into almost ionic, associated with structural change from hexagonal α-Mg into tetragonal β-MgH$_2$ (see details in **Chap. 2.1.5.1**). Therefore, hydrogen atoms in Mg-lattices behave different regarding their motion, depending on the hydrogen concentration. To understand the diffusion behavior of hydrogen in the Mg-H system, diffusion theory for interstitial diffusion and self-diffusion are explained in this section. In this study, thin Pd film of the thickness 20 nm is deposited as capping layer to avoid oxidation of underlying Mg layer. Also, a Pd-substrate is used for permeation measurement. Therefore, hydrogen diffusion in Pd is also subsequently treated in this section.

2.1.4.1 Diffusion in the α-phase [Abba08]

In the low hydrogen concentration regime, hydrogen exits interstitially in the metal lattice. In the expression of the interstitial diffusion is therefore related to the numbers of nearest interstitial sites p , and the diffusion coefficient of interstitial atoms is expressed by

$$D = \alpha a^2 p \upsilon \exp\left(-\frac{\Delta F_{diff}}{RT}\right) \tag{2.13}$$

where D m^{2}s^{-1} is the diffusion coefficient, α is a geometrical factor that depends on the crystal, a is the lattice Parameter of the crystal, υ is the vibration frequency of a solute atom in a substitutional site, ΔF_{diff} kJ mol^{-1} is the free energy for diffusion, R (= 8.314 J mol^{-1}K^{-1}) is the gas constant, and T K is temperature.

In case of interstitial diffusion, the free energy term equals the free energy per mole required for solute atoms to jump over their energy barriers into next cites, ΔF_m . Therefore,

$$\Delta F_{diff} = \Delta F_m \tag{2.14}$$

is valid for interstitial diffusion.

Because a free-energy change is capable of being expressed in the form,
$$\Delta F = Q - T\Delta S \tag{2.15}$$
the expression for the interstitial diffusivity can be written by

$$D = \alpha a^2 p \upsilon \exp\left(\frac{\Delta S_m}{R}\right) \cdot \exp\left(-\frac{\Delta Q_m}{RT}\right) \tag{2.16}$$

where ΔS_m and ΔQ_m are the entropy change of the lattice (per mole solute atoms) and the work (per mole of solute atoms) associated with bringing solute atoms to the saddle point during a jump between interstitial positions.

2.1.4.2 Diffusion in the hydride phase

In the hydride phase, because of the large difference of electronegativities, the strong affinity of H to Mg affects the diffusion mechanism. The bonding is almost ionic and strong in the hydride phase. Hydrogen atoms in this state need additional energy to cut the bonds with neighbouring Mg atoms, and jumps into the next position. This bonding energy is an additional energy term, which has to be considered [Ande54]. This concept resembles that of the concept treating substitutional diffusion. Therefore, this substitutional diffusion process is introduced in this section.

The self-diffusion coefficient of atoms in a dilute solid solution in metal is expressed by rewriting Eq.(2.13) as

$$D = \alpha a^2 Z \upsilon \exp\left(-\frac{\Delta F_{diff}}{RT}\right) \tag{2.17}$$

where D m^{2}s^{-1} is the diffusion coefficient of the substitutional atom, α is a geometrical factor that depends on the crystal, a is the lattice Parameter of the crystal, Z is the coordination number, and υ is the vibration frequency of a solute atom in a substitutional site. Z is known to be 12 for FCC lattice, and 8 for BCC lattice. In case of substitutional diffusion, diffusing atom needs a vacancy next to it. Due to this additional process, an additional free-energy change term associated with the formation of vacancies, ΔF_f, is introduced in the energy term. Therefore in case of substitutional diffusion, the ΔF_{diff} part is expressed as

$$\Delta F_{diff} = \Delta F_f + \Delta F_m \tag{2.18}$$

where ΔF_f and ΔF_m are the free-energy change per mole associated with the formation of vacancies and the free energy per mole required for solute atoms to jump over their energy barriers into vacancies, respectively. Comparing Eq.(2.14) and Eq.(2.18), ΔF_{diff} for the substitutional diffusion is larger than that of interstitial diffusion. This change of free energy changes the diffusion coefficients drastically, as will be shown in the next section.

2.1.4.3 General expression of diffusion coefficient

Eq.(2.13) and Eq.(2.17) are the theoretical expressions for interstitial and substitutional diffusion. However, using experimental results, D is usually expressed in the form

$$D = D_0 \exp\left(-\frac{\Delta Q}{RT}\right) \tag{2.19}$$

where D_0 is a constant that is known as the frequency factor, and Q is the experimental activation energy for diffusion. Eq.(2.18) is an expression of D as a function of temperature. Transforming Eq.(2.6) yields

$$\ln D = D_0 - \frac{\Delta Q}{R}\left(\frac{1}{T}\right) \qquad \text{or} \qquad \log_{10} D = D_0 - \frac{\Delta Q}{2.3R}\left(\frac{1}{T}\right) \tag{2.20}$$

Thus, D is often plotted as Arrhenius plot. **Fig. 2.4** shows an Arrhenius plot, which compares the diffusion coefficients of interstitial diffusion and substitutional diffusion, as example diffusion coefficients of Pd in Pd, Mg in Mg, H in Mg and H in Pd. The diffusion coefficients of H in α-Mg are larger than that of Mg in Mg, comparing at same temperature. Likewise, the diffusion coefficients of H in Pd are larger than that of Pd in Pd. Slopes in this figure correspond to the $\Delta Q / 2.3R$ term in Eq.(2.20), and the intercept is equivalent to D_0. Because D is expressed in logarithmic scale, it is obvious that the activation energy Q drastically affects the diffusion coefficient. This difference of slopes are clearly visible in **Fig. 2.4** between substitutional diffusion coefficients and interstitial coefficients, which is the difference of energy of diffusion, as is described in former section. Details of hydrogen diffusion in Mg and Pd will be subscribed later in
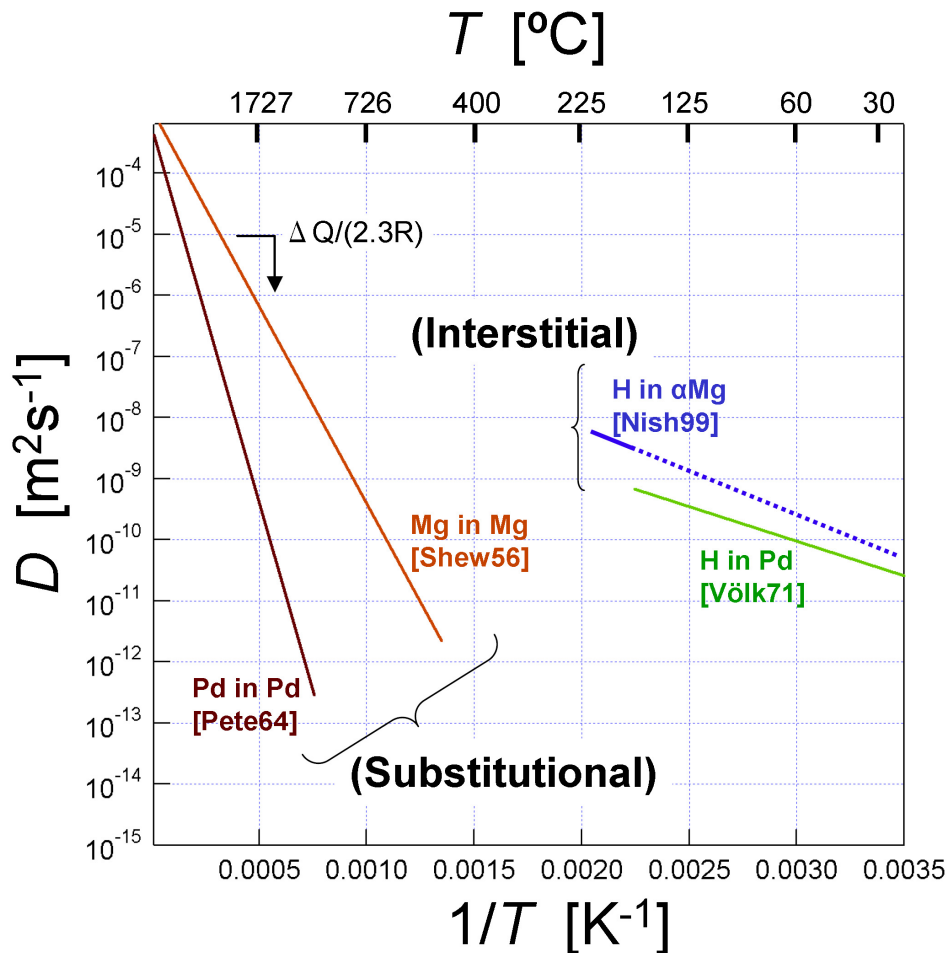
Fig. 2.4 Diffusion coefficient of Pd in Pd [Pete64] and Mg in Mg [Shew56] as substitutional diffusion, and diffusion coefficients of hydrogen in αMg [Nish99] and in Pd [Völk71], as interstitial diffusion. Dashed line is an extrapolation to room temperature. Details of hydrogen diffusion in Mg and Pd will be subscribed later in section 2.1.4.4 and section 2.1.4.5, respectively.

Chap. 2.1.4.4 and **Chap. 2.1.4.5**, respectively. In **Fig. 2.4**, The diffusion coefficient of H in α-Mg is smaller than that of H in Pd. The hydrogen solution enthalpy (ΔH_s) of H in α-Mg is larger than that of H in Pd (see **Table 2.1** and **Fig. 2.2**). The difference in the diffusion coefficients is explained by these contribution differences on the related Q.

Comparing Eq.(2.16) with the theoretical expression of Eq.(2.19), following relationships are available with both parameters:

$$Q = Q_m \qquad \text{and} \qquad D_0 = \alpha a^2 p \upsilon \exp\left(\frac{\Delta S_m}{R}\right) \tag{2.21}$$

A point to keep in mind here is that the relationships of Eq.(2.6) is valid in a state of dilute interstitial solid solutions. Increasing concentration of the solute in the solid solution phase makes large numbers of interstitial sites being occupied, causing solute atoms interact, or interfere with each others jumps. Moreover, logarithmic change of the concentration yields changes of the chemical potential of solute atoms. Hydrogen diffusion in metal lattice is no exception, and therefore, the diffusion coefficient depends on c_H.

Another point to keep in mind is, Eq.(2.14) is valid only in ideal diffusion in material. In realistic experimental condition, depending on methods, the energy for diffusion includes the effects from environment such as surface, inner stress, or defects. Non-homogeneous stress, which could happen such as in a bended metal foil, is also known to cause long-range diffusion [Cant69]. For nanocrystalline materials, trapping effect [Oria70,Kello80,Yang91,Fukai05] is known to happen at low hydrogen concentration [Kirch88,Kirch88+,Aran93]. Details about individual experimental techniques are available, for example in ref. [Bocq96].

A preferential experimental method in this work is the permeation method. It could contain surface effects, including dissociations of hydrogen at the surface or penetration of hydrogen through surface barriers [From76,From96]. Details about permeation measurements applied in this work will be described in **Chap. 3.8**.

2.1.4.4 Diffusivity of H in Mg and MgH$_2$

Fig. 2.5 shows a series of hydrogen diffusion coefficients reported in literature mainly for bulk Mg-H systems. Diffusion coefficients of individual sources show the expected linear relationship to the reciprocal temperature. But the data deviate over more than 25 orders at room temperature, when different sources are compared. Corresponding works discussed here are listed in **Table A3.1** in **Appendix A3**.
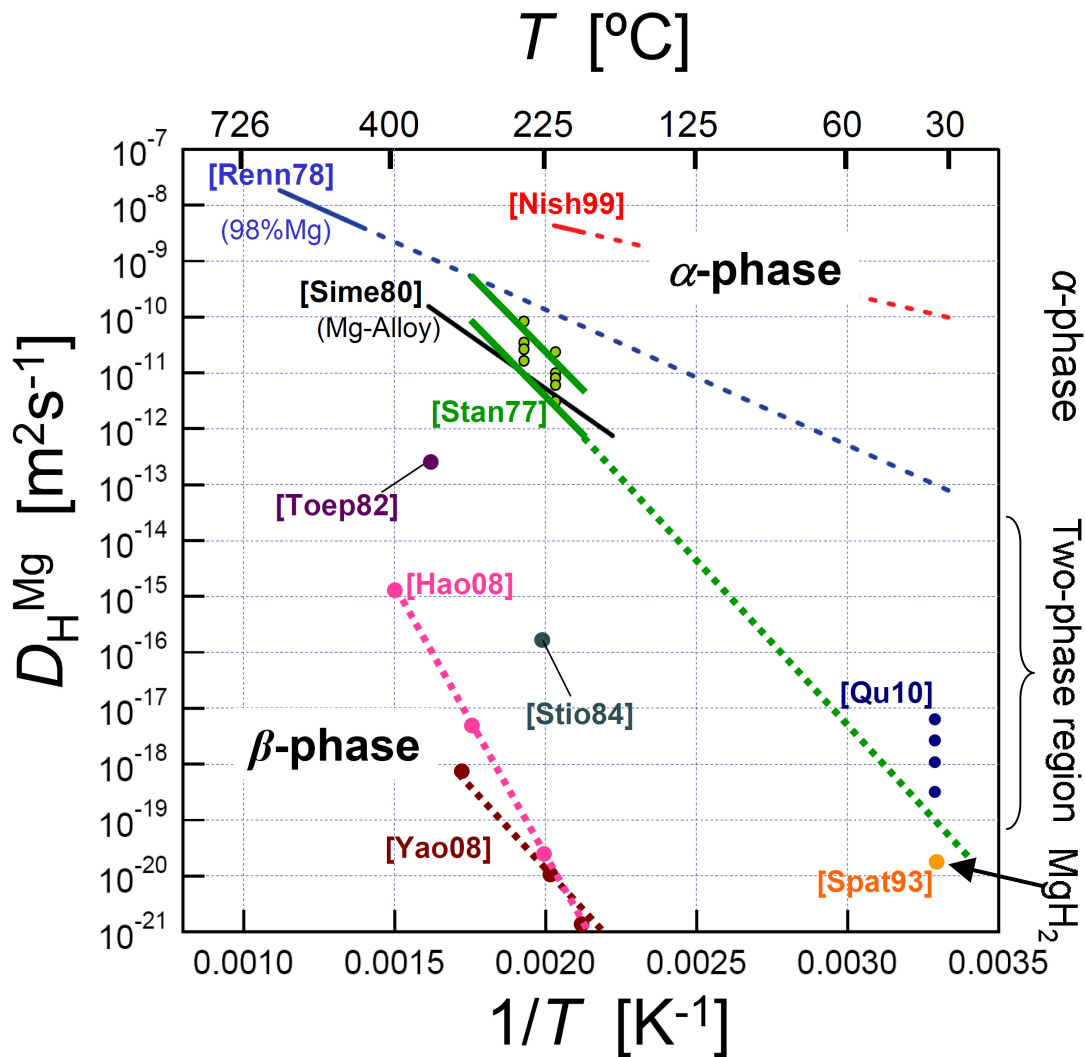
Fig. 2.5 Series of reported hydrogen diffusion coefficients in Mg-H system, reported by Stander [Stan77], Renner and Grabke [Renn78], Simensen *et al.* [Sime80], Yao *et al* [Yao08], Nishimura *et al.* [Nish99], Töpler [Toep82], Stioui *et al.*[Stio84] as measured at elevated temperatures and those of Spatz *et al.* [Spatz93] and Qu *et al*. [Qu10] at room temperature, with theoretical calculation results by Hao and Scholl [Hao08]. Here, experimentally obtained diffusion constants for pure Mg were reported by Nishimura *et al.* in α-region, and by Spatz *et al.* and Qu *et al.* in two-phase region, and by Stioui *et al.* in β region. Extrapolations to room temperature are appended to values by Stander, Renner and Nishimura *et al.*. Details are described in **Table A3.1**.

Hydrogen diffusion coefficients reported in literature can be sorted by different regimes of hydrogen concentration: in I) the α-phase, where hydrogen diffuses via the interstitial diffusion process, II) the two-phase region, where the hydrogen coefficients are often obtained as over-all diffusion coefficients, for example by measuring the growth of the hydride layer thickness, or III) in the hydride phase.

In α-phase, Nishimura *et al.* [Nish99] investigated hydrogen permeation measurements for a palladium capped magnesium membranes using a gas permeation technique, and reported an equation of $D_H^{\alpha Mg} = 1.54 \times 10^{-6} \exp\left[-(24100)/RT\right]$ m^{2}s^{-1}, where R is the gas constant in J mol^{-1}K^{-1}. It was measured in the temperature range 473-493 K and in the hydrogen pressure range p_{H_2} of 0.1-10 kPa. In this study, the grain size is unknown. In Simensen's study, an equation of $D_H = 9.5 \times 10^{-6} \exp(-46400/RT)$ m^{2}s^{-1} is obtained for interstitial diffusion of hydrogen in magnesium, in the temperature range of 723K-873K.

In the two-phase region, a diffusion coefficient of hydrogen was reported by Renner and Grabke [Renn78] to be $D_H^{Mg} = (3.8 \pm 1) \times 10^{-6} \exp\left[-(40000 \pm 5000)/RT\right]$, where D_H^{Mg} is in m^{2}s^{-1}. They measured the thickness of the hydride layer, grown at different temperatures ranging from $T = 698$ K to $T = 798$ K. However it is noted that this value was obtained for a sample with only 98% purity of Mg including 2 wt.% of cerium.

For pure Mg, it is known that the hydrogen diffusion constant decreases logarithmically as the hydrogen concentration increases [Stan77]. At high temperature, Stander *et al.* reported the hydride fraction dependency of the hydrogen diffusion coefficient at $T = 523$ K and $T = 490$ K with hydrogen loading pressure of $p_{H_2} = 3$ MPa [Stan77], shown in **Fig. 2.6**. Increasing hydride fraction x, the apparent hydrogen diffusion coefficient keeps almost constant up to $x = 0.5$, and drastically decreases at further reacted state. At room temperature, Spatz *et al.* measured $D_H^{MgH_2}$ to be in the order of $D_H^{MgH_2} = 1.1 \times 10^{-20}$ m^{2}s^{-1} at $T = 305$ K [Spatz93]. They studied the kinetics of hydrogen absorption in thin Mg-thin films with the thickness of 20 Å-800 Å that were
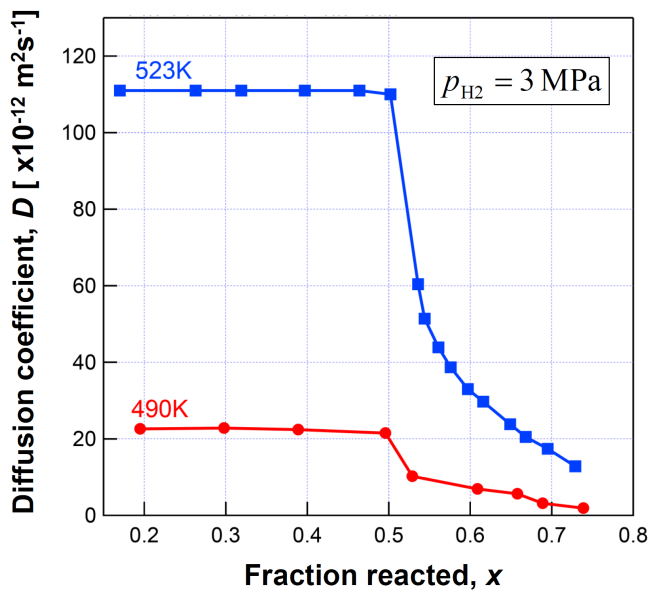

Fig. 2.6 Variation of diffusion coefficient (D) with fraction reacted, under p_{H2} = 3 MPa at T = 523 K (blue) and T = 490 K (red), reported by Stander [Stan77].

UHV evaporated onto a previously hydrided Pd-foil, with help of XPS technique, developing a simple diffusion model that the hydride is preferentially formed on the PdH_x/Mg-interface and forms a diffusion barrier for subsequent diffusion of hydrogen. The measured diffusion coefficient by Spatz *et al.* [Spatz93] is an mean diffusion coefficient of H in Mg-film.

In β-phase regime, the crystal is known to be almost ionic [Chen04]. In ionic crystals, the diffusing atom is sometimes the cation, and sometimes the anion. With respect to the β-MgH_2 structure, Luz [Luz80,Luz80$^+$] showed that the H$^-$ anion diffuse through the growing β-phase layer, from their direct observation with Kirkendall marker movements by photomicrographic technique, rather than the Mg$^+$ cation [Mintz78]). This growth mechanism of the β-phase was confirmed by Vigeholm *et al.* [Vige84] after rough calculations using the data of Töpler *et al.* [Toep82].

The measured hydrogen diffusion coefficient $D_H^{MgH_2}$ is very small. For example, Töpler *et al.* [Toep82] measured $D_H^{MgH_2} \approx 2.5 \times 10^{-13}$ m^{2}s^{-1}, by means of a quasielastic neutron scattering, at T = 623 K. This diffusion coefficient is 3 orders smaller than the value reported by Renner and Grabke [Renn78]. Also, Stioui *et al.* [Stio84] found a small value as $D_H^{MgH_2} = 1.5 \times 10^{-16}$ m^{2}s^{-1} at $T \approx 503$ K, using nuclear magnetic resonance. Hao and Sholl [Hao08] calculated $D_H^{MgH_2}$ for H$^-$ via density functional theory to be smaller than 10^{-36} m^{2}s^{-1} at room temperature, concluding that H diffusion is dominated by mobility of negatively charged interstitial H. Yao *et al.* calculated $D_H^{MgH_2}$ applying a hydrogen diffusion model for a spherical geometry for comparison with their results of gasloading at different temperatures, and obtained $D_H^{MgH_2}$ to be in the order of 10^{-18} m^{2}s^{-1} to 10^{-24} m^{2}s^{-1} at $T = 573$ K and $T = 373$ K, respectively [Yao08]. Applying linear fitting for obtained $D_H^{MgH_2}$ in Arrhenius plot, they calculated a value as activation energy of hydrogen diffusion in MgH$_2$, $\Delta F_H^{MgH_2}$, to be $\Delta F_H^{MgH_2} = 107.9$ kJ/(mol H) (See Eq.(2.13)). This value is the largest reported value. The purity of Mg is unknown for this work.

The vacancy formation energy of MgH$_2$ (corresponding to ΔF_f in Eq.(2.18)) is larger compared to other metallic bonding materials, since the chemical bond of Mg-H is between metallic and covalent or ionic [Chen04], and thus, more strong. Because of this large activation energy, hydrogen diffusivity in the MgH$_2$ grains is quite small.

Qu *et al.* [Qu10] measured Mg-thickness-dependent D_H^{Mg} on films. They found decreasing $D_H^{Mg} = 7.8 \cdot 10^{-18}$ m^{2}s^{-1} to $3.7 \cdot 10^{-19}$ m^{2}s^{-1}, increasing Mg film thickness from 20 nm to 100 nm, applying Hagi's model [Hagi90] for electrochemical discharging results, in the two-phase region. Yang *et al.* [Yang11,Yang11$^+$] applied a diffusion model for describing the hydrogen absorption kinetics in a V-coated nano-wire, and obtained $D_H^{MgH_2}$, increasing from $4.36 \cdot 10^{-19}$ m^{2}s^{-1} to $6.31 \cdot 10^{-18}$ m^{2}s^{-1}, by increasing T from 500 to 570 K.

Apart from those works, Corey *et al.* [Core08] and Conradi *et al.* [Conr07] measured the activation energy of hydrogen in coarse grained MgH$_2$ by NMR in the temperature range $T > 533$ K. Their value which corresponds to a diffusion coefficient of $D_H^{MgH_2} \approx 4 \cdot 10^{-35}$ m^{2}s^{-1} and $D_H^{MgH_2} \approx 7 \cdot 10^{-33}$ m^{2}s^{-1} when extrapolated to room temperature. These values are the smallest value in literatures reported at the moment.

In this manner, the diffusion coefficient of hydrogen in Mg at room temperature varies exponentially to the mean hydrogen concentration. It is in the order of 10^{-10} m^{2}s^{-1} in the α-Mg region and in the order of 10^{-20}-10^{-35} m^{2}s^{-1} in the β-MgH$_2$ region, progressing through the two-phase region. Thereby the diffusion coefficient varies over 25 orders of magnitude. However, hydrogen diffusivities in α-Mg are not determined below 30 °C, up to now.

2.1.4.5 H diffusion in Pd

Hydrogen diffusion coefficients in bulk-α-Pd ($D_H^{\alpha\text{Pd}}$) and that in bulk-β-Pd ($D_H^{\beta\text{Pd}}$), by selected methods, are listed in **Table A3.3** in **Appendix A3**. $D_H^{\alpha\text{Pd}}$ and $D_H^{\beta\text{Pd}}$ are separated in the table. Comparing both values at $T = 300$ K, $D_H^{\alpha\text{Pd}}$ varies between $1.3{\cdot}10^{-11}$ m^{2}s^{-1} ~ $6.6{\cdot}10^{-11}$ m^{2}s^{-1} and $D_H^{\beta\text{Pd}}$ varies between $1.45{\cdot}10^{-10}$ m^{2}s^{-1} ~ $6.6{\cdot}10^{-10}$ m^{2}s^{-1} at $T = 300$ K. This difference of diffusion coefficients supports the suggestion by Jewett and Makrides [Jewe65] and Sakamoto *et al.* [Saka82] that $D_H^{\beta\text{Pd}}$ tends to be 10 times larger than $D_H^{\alpha\text{Pd}}$.

As an example, $D_H^{\alpha\text{Pd}}$ values for bulk-sample, involving room temperature in temperature condition ranges, are plotted in **Fig. 2.7**, collected from literatures of [Boes76,Wick64$^+$,Riba73, Seki75, Kirch80, Sams73, Holl67, Völk71, Simo65, Birn72, Hase77, Züch70, Katl78, Koff68]. Corresponding short explanations are shown in **Table A3.2** in **Appendix A3**. A referential value of $D_H^{\beta\text{Pd}}$ by Wicke and Bohmholdt [Wick64$^+$] is selected and plotted in **Fig. 2.7**, to clarify the difference with $D_H^{\alpha\text{Pd}}$ visually. An average value obtained from collected literature at room temperature, $D_H^{\text{Pd}} = 3.5(\pm2.0)\cdot10^{-11}$ m^{2}s^{-1}, is treated as referential value of $D_H^{\alpha\text{Pd}}$. This value is 9 orders of magnitude larger than $D_H^{\beta\text{MgH2}}$ (see **Fig. 2.5**). Thus, hydrogen can permeate through 20 nm of Pd-capping layer within 10^{-3} seconds, and the time delay induced by the hydrogen permeation through the Pd capping layer is negligible.

However, the effect of the difference between $D_H^{\alpha\text{Pd}}$ and $D_H^{\beta\text{Pd}}$ on the total effective diffusion coefficient (D_H^{eff}), obtained from permeation measurement results for Pd/Mg/Pd films, is not negligible, because of the existence of α/β moving boundary in the Pd-lattice. This topic is described later in **Chap. 5.5**.

The slopes of temperature dependency correspond to the activation energy for the diffusion. Hydrogen diffusion coefficients determined from permeation measurements generally contains the effect of the surface dissociation and penetration process of hydrogen. This is considered in this work.

The mean hydrogen concentration in the equilibrium state for Pd is fundamentally measured in the α-phase range in this work. Therefore, the β-phase could exist during hydrogen loading process. Both of $D_H^{\alpha\text{Pd}}$ and $D_H^{\beta\text{Pd}}$ are interstitial diffusion, and more than two orders of magnitude larger than $D_H^{\alpha\text{Mg}}$ at room temperature, reflected by the difference of the hydrogen solution enthalpies (see **Table 2.1** and **Fig. 2.2**).

The kinetics of hydrogen permeation process through α-Pd via electrochemical hydrogen permeation measurement, consisting of i) discharging of electron on the surface of metal, ii)

hydrogen adsorption process, iii) solution and storage process, vi) diffusion process in the material and v) desorption process at the output side, is generally known to be controlled by the diffusion process [Deva62]. However at higher hydrogen concentrations for Pd, it is not clear what is the rate limiting process for hydrogen permeation, especially for the case that the β-phase nucleates at the sample surface, and the α/β boundary moves into sample interior [Stac64,Jewe65,Bohm67,Saka82]. For example on one hand, Jewett and Makrides [Jewe65] reported the diffusion coefficient of hydrogen in β-Pd ($D_{\mathrm{H}}^{\beta\mathrm{Pd}}$) at 293 K to be $D_{\mathrm{H}}^{\beta\mathrm{Pd}} = 1.5 \cdot 10^{-10}$ $\mathrm{m}^2\mathrm{s}^{-1}$ which is 10 times larger than that in α-Pd ($D_{\mathrm{H}}^{\alpha\mathrm{Pd}}$), $D_{\mathrm{H}}^{\alpha\mathrm{Pd}} = 1.6 \cdot 10^{-11}$ $\mathrm{m}^2\mathrm{s}^{-1}$ [Jewe65]. On the other hand, the value of Boes and Züchner [Boes76] at the same temperature at $c_{\mathrm{H}} \approx 37\%$ is measured to be $D_{\mathrm{H}}^{\beta\mathrm{Pd}} = 4 \cdot 10^{-11}$ $\mathrm{m}^2\mathrm{s}^{-1}$. Moreover, also for Mg layer, the diffusion coefficient decreases logarithmically with increasing of c_{H} (see **Chap. 2.1.4.4**).
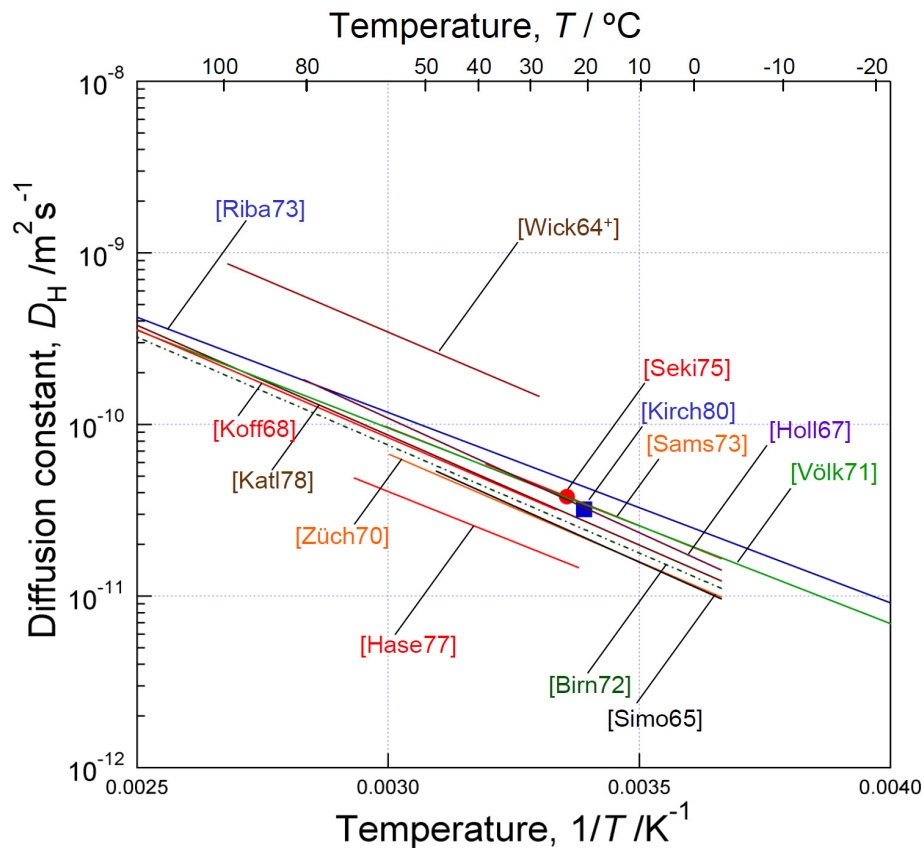
Fig. 2.7 A collection of bulk- $D_{\mathrm{H}}^{\alpha\mathrm{Pd}}$, as functions of reciprocal temperature $1/T$, compared with $D_{\mathrm{H}}^{\beta\mathrm{Pd}}$ by Wicke and Bohmholdt [Wick64+]. See **Table A3.2** in **Appendix A3** for more information.

2.1.4.6 Hydrogen diffusion in grain boundaries and nanocrystalline Pd

Hydrogen can diffuse through a grain boundary different than through the lattice. For example, Harris and Latanision [Harr91] reported a value as grain boundary diffusion coefficient of hydrogen in nickel at least $D_{\mathrm{H}}^{\mathrm{Ni\text{-}GB}} = 3\cdot 10^{-12}$ m^2/s, from their electrochemical permeation measurements performed on fine-grained foils produced by electrodeposition. This grain boundary diffusion coefficient was a factor of 40 greater than the lattice diffusion coefficient. Moreover, the activation energy for grain boundary diffusion in this system is reported to be approximately three-fourths of the activation energy for hydrogen diffusion in single-crystal nickel [Harr91].

In contrast to this, Mütschele and Kirchheim [Muet87] show a reduction of the hydrogen diffusion coefficient for nanocrystalline Pd ($D_{\mathrm{H}}^{\mathrm{n\text{-}Pd}}$) compared to that of single crystal ($D_{\mathrm{H}}^{\mathrm{s\text{-}Pd}}$) at hydrogen concentration $c_{\mathrm{H}} < 3.15\cdot10^{-4}$ H/Pd, by electrochemical permeation measurement for sample with average grain size of 10 nm. Increasing the concentration gives rise to an increase of the $D_{\mathrm{H}}^{\mathrm{n\text{-}Pd}}$ for $c_{\mathrm{H}} > 3.0\cdot10^{-2}$ H/Pd is also measured for nanocrystalline sample, reaching up to $D_{\mathrm{H}}^{\mathrm{n\text{-}Pd}} = 1.58\cdot10^{-10}$ m^{2}s^{-1}, which is about 3 times larger compared to $D_{\mathrm{H}}^{\mathrm{s\text{-}Pd}}$. This hydrogen diffusion depends on concentration. Arantes *et al.* [Aran93] conducted electrochemical hydrogen permeation measurements and reported an increase of hydrogen permeability in nanocrystalline Ni (grain size ~100 nm) compared to microcrystalline Ni (grain size ~2 μm), and concluded this result due to an increase of both hydrogen solubility and hydrogen diffusivity. The diffusivity of hydrogen increases by two orders of magnitude when the hydrogen activity is enlarged. However, measurements of the time lag during transient permeation show that at very low hydrogen activities the diffusion coefficient can be smaller when compared to a microcrystalline sample. This effect at lower hydrogen concentration was explained by the trapping effect [Muet87].

Taking the simple assumption that the hydrogen diffusion takes place in cubic-shaped grains with low diffusivity and through their grain boundaries with high diffusivity, Demouchy *et al.* applied following equation to estimate the grain boundary diffusion of hydrogen through their olivine samples [Dorn02,Pundt06,Demo10]

$$D_{\mathrm{H}}^{\mathrm{eff}} = D_{\mathrm{H}}^{\mathrm{bulk}} + \frac{3\delta}{d} D^{\mathrm{GB}} \tag{2.22}$$

where $D_{\mathrm{H}}^{\mathrm{eff}}$ is the effective hydrogen diffusion coefficient, $D_{\mathrm{H}}^{\mathrm{bulk}}$ is the hydrogen diffusion coefficient in the bulk grains, D^{GB} is the hydrogen diffusion coefficient in the grain boundaries, d is the grain size, and δ is the width of the grain boundaries. The value of δ is often approximated to be about 2-3 monolayers [Muet87,Herz03].

Further theoretical models about grain boundary diffusion are suggested and shown with their historical development in the book [Kaur95] written by Kaur, Mishin and Gust. Some of them are discussed in this work to estimate contribution of grain boundary diffusion, in **Chap. 6.3**.

Grain boundary pathway can be estimated by the excess of the estimated hydrogen flux

compared to grain-through diffusion process, as described in the **Appendix A1**.

2.1.5 Mg-H systems

Several hydrogenation properties and thermodynamical aspects of the bulk- and film-Mg-H system and its hydrides will be presented in this section.

2.1.5.1 H in bulk-Mg
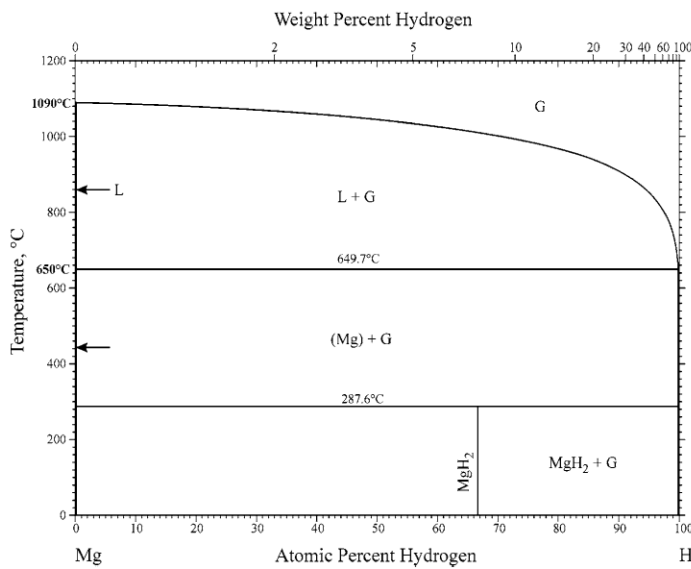
Fig. 2.8 A phase diagram of the bulk Mg-H system [Okam01].

Fig. 2.8 shows the binary phase diagram of the bulk Mg-H system, at a hydrogen pressure $p_{H2} = 25$ MPa. Mg forms a solid solution (α-Mg phase) upon sorption of small hydrogen content. At this pressure condition, The hydride phase decomposes at $T = 287.6\,^{\circ}$C ($= 560$ K), and the melting point of Mg is at $T = 650\,^{\circ}$C ($= 923$ K).

The solubility limit of hydrogen in the bulk α-Mg under a normal pressure is reported as functions of temperature T (unit in K) by Koeneman and Metcalfe [Koen59], and San-Martin and Manchester [Sanma87], as follows;

$$X_{\alpha/(\alpha+\beta)} = 7.8 \cdot 10^{-3} \exp(-2320/T) \quad \text{[Koen59]} \tag{2.23a}$$

$$X_{\alpha/(\alpha+\beta)} = 107 \exp(-6225/T) \quad \text{[Sanma87]} \tag{2.23b}$$

Hence, the solubility at $T = 300$ K is calculated to be $c_{H} = 3 \times 10^{-6}$ H/Mg and $c_{H} = 1 \times 10^{-7}$ H/Mg, respectively. This low solubility limit is represented by the vertical line matching the T-axis, in **Fig. 2.8**.

Further hydrogenation yields forming of the hydride phase. It is known that thermodynamically stable hydride phase is β-MgH$_2$, under moderate conditions. This is

represented by the horizontal line ranging up to 287.6 °C in **Fig. 2.8**. However, further structures are also reported as metastable phases, under moderate condition, such as γ-, δ- and ε-phase. The crystal structures of Mg and its hydrides are listed in **Table 2.2**. They vary from orthorhombic (*orth.*), tetragonal (*tetr.*), and tetragonal (*tetr.*) to cubic (*cubic*).

Upon hydrogenation at ambient hydrogen pressure and low temperature, magnesium with hexagonal structure changes into the β-MgH$_2$ phase (TiO$_2$-rutile type structure) [Pred96]. This structure change was observed by Ellinger *et al.* by XRD measurements [Ellin55]. The structure of the β-MgH$_2$ phase was determined by Zachariasen *et al.*, applying neutron diffraction measurements for its deuteride [Zach63].

Table 2.2 Crystal structures of magnesium and its hydrides [Kele07,Ellin55,Mori06,Vaje06,Semenk78,Bort99, Lity85,Ravi04]. Hexagonal Mg and thermodynamically stable β-MgH$_2$ structure, which are mostly treated in this work is marked in the list. Further information about symmetry is available in the ref. [Ecke71].

Phase	Structure	Type (sym.)	a [nm]	b [nm]	c [nm]	Ref.
Mg	*hex.*	$(P6_3/mnm)$	0.321	0.321	0.521	[Kele07]
β-MgH$_2$	*tetr.*	TiO$_2$ (rutile) $(P4_2mnm)$	0.45618 ($\pm$0.0005) 0.4515 0.45176	0.30205 ($\pm$0.0005) 0.3019 0.30206	(= a) (= a) (= a)	[Ellin55] [Mori06] [Vaje06]
γ-MgH$_2$	*orth.*	α-PbO$_2$ $(Pbcn)$	0.4526 0.45213(3)	0.5448 0.54382(3)	0.4936 0.49327(3)	[Semenk78] [Bort99]
δ-MgH$_2$	*tetr.*	Distorted CaF$_2$ $(Pa\bar{3})$	0.4470 0.46655	0.4470 0.46655	0.4735 0.46655	[Lity85] [Vaje06]
ε-MgH$_2$	*cubic*	AlAu$_2$ $(Pnma)$	0.52804	0.30928	0.59903	[Ravi04]

Recently, another β-MgH$_{1<x<2}$ phase was observed by Schimmel *et al* [Schim05], which doesn't occur in bulk hydride phase but appears characteristic for small particles. It has the same structure but smaller lattice constant. A similar phase with slightly smaller lattice constants was also detected by Borgschulte *et al* [Borg07] as β-MgH$_{2-\delta}$ phase, using XRD technique. In this study, the amount of this phase was reported to depend on the degree of nanostructuring and the used additive [Borg07].

The thermodynamically stable tetragonal β-MgH$_2$ can be partially transformed into a metastable γ-MgH$_2$ phase with orthorhombic structure, under a compressive stress state [Bast80], or at higher temperature. This γ-MgH$_2$ phase, which structure was determined by Bortz *et al.* [Bort99], is known to occur often as a by-product in the high-pressure synthesis of Mg-based ternary metal hydrides in GPa order (*e.g.* [Bort98,Nagen99]) by multianvil device, or observed in ball milled samples at high temperature, i.e., in nanostructured MgH$_2$ [Hana05,Huot01], after long milling times [Vari06,Chit13]. This phase transition from β-MgH$_2$ into the γ-MgH$_2$ also takes place by heating at $T = 629$ K [Semenk78]. Recently, Ham *et al.* [Ham14] reported that the stress-induced orthorhombic γ-MgH$_2$ is thermodynamically destabilized at $T = 373$ K or lower, suggesting drastic destabilization arisen by large tensile stress in single layer γ-MgH$_2$ bonded to

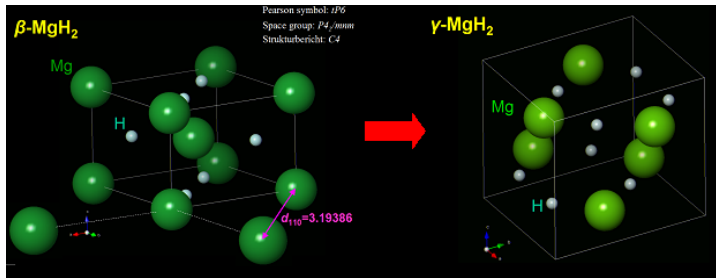rigid substrate, or compressive stress due to large volume change incompatibility in Mg/Nb multilayers.

Fig. 2.9 shows a schematic drawing of the structure transition from β- to γ- phase. Concerning the β-γ transition pressure, Vajeeston *et al.* studied the stability of MgH$_2$ structures in the pressure range up to 20 GPa using density-functional total-energy calculations, and predicted that the β-MgH$_2$ transforms into γ-MgH$_2$ at 0.39 GPa [Vaje02]. The calculations via the Full-Potential Linear Muffin-Tin Orbital (FP-LMTO) Method and the Vienna *Ab-initio* simulation package (VASP) performed by Ravindran *et al.* also suggest the β-γ transition pressure to be 0.385 GPa and 0.387 GPa respectively [Ravi04]. However, Moriwaki *et al.* reported the transition pressure to be 9 GPa from their *in-situ* high-pressure XRD measurements up to 57 GPa, carried out at room temperature [Mori06]. In their high-pressure investigation, they also pointed out that a complete conversion from β-phase to the γ-phase didn't take place, and two more high-pressure phases exists under a high pressure in the GPa range [Mori06].

Apart from the above reactions, a transition from the tetragonal β-MgH$_2$ phase to the δ-MgH$_2$ phase (distorted CaF$_2$-type lattice) at a pressure of 8 GPa was reported by Lityagina *et al.* [Lity85]. Based on these results, it is assumed that γ-, δ-, and ε-MgH$_2$ phases are not stable under the conditions that are used in this work. Therefore, hexagonal Mg and tetragonal β-MgH$_2$ phase are mainly treated in subsequent parts of this work.

Table 2.3 shows a list of reported enthalpy changes for the Mg-βMgH$_2$ system with corresponding entropy change ΔS^0 and temperature ranges, collected from series of different studies [Stamp60,Kenn60,Ellin55,Vige83,Shao04,Peder83,Fried88,Pask10,Tanguy76,Reil68, Bogd95,Abba08,Klos95,Kroz90,Stan78], mainly for the bulk system. Enthalpy values are sorted from the viewpoint of reaction directions, expressed by the hydride formation enthalpy $\Delta_f H^0$ in absorption direction, and the hydride decomposition enthalpy $\Delta_d H^0$ in desorption direction. Energy change of the reaction (ΔG^0) can be calculated for both directions at each temperature by relationship of $\Delta G^0 = \Delta H^0 - T\Delta S^0$.

Krozer *et al.* [Kroz90] reported that $\Delta_f H$ is more exothermic than $\Delta_d H$ by about $\Delta_f H - \Delta_d H \approx 11$ kJ/molH$_2$ for Mg films, obtained from a piezoelectric quartz crystal microbalance measurements (gravimetric method) at $T = 290$-370 K with $p_H = 1.33$-80 Pa. This was done for a thin film sample, being affected by elastic energy change due to induced volume expansion. Similar tendency with $\Delta_f H$ and $\Delta_d H$ was reported by Pivak [Pivak12^{+}] for thin film, from hydrogenography measurements at $T = 333$-545 K. In contrast, for bulk materials,

difference of only 1.2 kJ/molH$_2$ between $\Delta_f H$ and $\Delta_d H$ was reported by Shao *et al.* [Shao04] from *p-c-T* measurements at $T = 623$-673 K.

Rudman [Rudm80] pointed out that apparent enthalpy of hydrogen loading of Mg could contain not only the enthalpy of hydride formation (which is negative) but also enthalpy of hydrogen solution into Mg (which is positive). Also, regarding to the transformation of Mg-MgH$_2$, it is noted that the energy of hydride formation or decomposition are affected by the nucleation process, therefore the state before each loading/unloading cycle could make a difference in the apparent thermodynamics (*e.g.* [Evar10]).

Table 2.3   A list of reported enthalpy changes for the Mg- βMgH$_2$ system in absorption direction (-$\Delta_f H^0$) and in desorption direction (-$\Delta_d H^0$), with corresponding entropy change (-ΔS^0), measured at different temperature ranges, collected from series of literatures [Stamp60,Kenn60,Ellin55,Vige83,Shao04,Peder83,Fried88,Pask10,Tanguy76, Reil68,Bogd95, Bohm99,Klos95,Kroz90,Stan78,Borg07,Pivak12P+]. See also **Fig. 2.12** in **Chap. 2.1.5.3** and **Fig. 5.39** in **Chap. 5.6.2**.

T [K]	-$\Delta_f H^0$ [kJ (mol H$_2$)$^{-1}$]	-$\Delta_d H^0$ [kJ (mol H$_2$)$^{-1}$]	-ΔS^0 [J K^{-1}(mol H$_2$)$^{-1}$]	Direction	Ref.
587-849		74.4 ± 0.3	135.1 ± 1.9	Des.	[Stamp60]
713-833		74.06 ± 2.9	135.8	Des.	[Kenn60]
723		66.94		Des.	[Ellin51]
533-698	70.0		126	Abs.	[Vige83]
623-673	74.87	76.05	135.6 ± 5.1	Abs. & Des.	[Shao04]
553-633		85	135	Des.	[Peder83]
553-643		74.3 ± 0.5	136 ± 1	Des.	[Fried88]
573-633		74.06 ± 0.42	133.4 ± 0.7	Des.	[Pask10]
573-623		77.4	138.3	Des.	[Tanguy76]
507-623		74.4 ± 4	138.3 ± 2.9	Des.	[Reil68]
573-723		80.9	144.8	Des.	[Bogd95][Bohm99]
543-618		81.86 ± 0.5	146.2 ± 0.3	Des.	[Klose95]
333-545	[b] 61.6	[b] 78.3	(Abs.)110.9, (Des.)136.1	Abs. & Des.	[Pivak12+]
290-370	[b] 60.7 ± 6.3	[b] 71 ± 4.2		Abs. & Des.	[Kroz90]
298		83.4		Des.	[Stan78]
298		74.9	135.1	Des.	[Stamp60]
573-633		[a] 71.22 ± 0.49	[a] 129.6 ± 0.8	Des.	[Pask10]
447-540	[a] 67	[a] 64		Abs. & Des.	[Borg07]

a); Nano particles, b); Thin film, No annotations; Bulk or powder samples

Apart from the above, metastable β-MgH$_{2-\delta}$ phase is reported by Borgschulte *et al.* [Borg07] in their differential scanning calorimetry (DSC) measurements under hydrogen atmosphere at $T = 447$-540 K, for Mg-nanoparticles with diameter of 80-130 nm. In their study, the β-MgH$_{2-\delta}$ phase is reported to have the tetragonal β-MgH$_2$ structure, but containing more vacancies, and increases

reaction kinetics. A correspondence to the new $MgH_{1.2}$ phase, determined by recent neutron diffraction measurements [Schim05], is suggested [Borg07]. However, almost no difference between $\Delta_f H$ and $\Delta_d H$ was measured for Mg-nanoparticle sample.

The value experimentally determined by Stampfer *et al.* from most wide temperature range [Stamp60], ΔH^0 = -74.4 kJ/(mol H_2), is used in this work as the reference value of hydriding reaction for bulk Mg.

Fig. 2.10 shows a *p-c-T* diagram of the bulk Mg-H system [Osum99]. At 300 $^\circ$C, β-MgH_2 phase exhibits a decomposition pressure of $p_{eq} \approx 5$ bar. Oelerich *et al.* [Oele00] and and Zhou *et al.* [Zhou13] experimentally obtained equilibrium pressures in the same order at 300 $^\circ$C. But at room temperature, a quite low equilibrium pressure of $p_{eq} \approx 5 \cdot 10^{-6}$ bar is expected, from extrapolation of the measurement of Stampfer *et al.* [Stamp60] (See **Fig. 2.3**).

With respect to the results in **Chap. 2.1.4.4**, which suggests slow reaction kinetics for Mg-H, special care is required for finding proper equilibrium states, especially when blocking effects are possible.
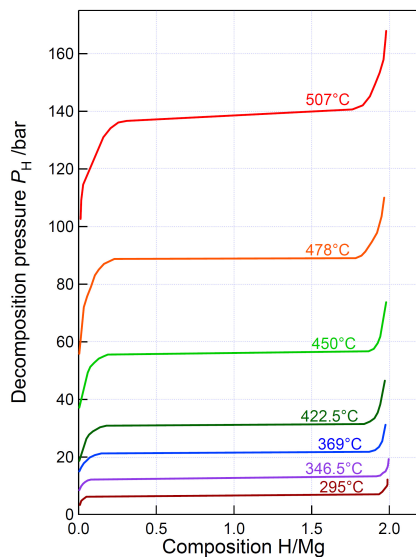
Fig. 2.10 A *p-c-T* diagram of the bulk Mg-H system, original data from the study by Osumi [Osum99]. See also Van't Hoff plot for Mg-MgH_2 in **Fig. 2.12**.

While α-Mg is a metal, the chemical bond for MgH_2 turns to ionic [Luz80^{+},Vaje02,Chen04], and MgH_2 is insulating [Wester08]. The large band gap of β-MgH_2, E_B^{Mg}, is experimentally determined to be E_B^{Mg} = 5.16 eV by Krasko [Kras82], E_B^{Mg} = 5.8 eV by He and Pong [He90], and E_B^{Mg} = 4.3-4.5 eV by Paik *et al.* [Paik12] for bulk Mg.

2.1.5.2 Hydride formation in Mg-films

Limited hydride layer growth is reported by different studies. On thin films, Westerwaal *et al.* reported on a maximum MgH_2 layer thickness of 100 nm [Wester08]. Giebels *et al.* could hydrogenate 120 nm Mg films completely [Gieb04], but only at elevated temperatures of 373 K. Vermeulen *et al.* achieved 4.5 wt% H/Mg (60% of the 200 nm Mg-film) that gives a 120 nm MgH_2 layer. Lohstroh *et al.* achieved a hydride layer thickness of 220 nm Mg_2NiH_4 in Mg_2Ni

films [Lohs04], however, this was an alloyed system. For Mg-alloyed thin films, Lohstroh *et al.* [Lohs04,Lohs05] and Borsa *et al.* [Bors07] reported the hydride nucleation from substrate side, whereas it is reported from the surface for pure Mg thin films (*e.g.* [Ryde89]). To summarize, about 120 nm thick MgH$_2$ layer forms on the surface of pure Mg films before blocking happens.

All hydrides were β-MgH$_2$ phase. In contrast, random nucleation of metastable γ-MgH$_2$ phase is reported by Gautam *et al.* [Gaut11, Gaut12] from their XRD measurement study conducted for magnetron sputtered Mg film prepared on glass substrate after hydrogen loading with $p_{H2} = 0.2$ MPa at $T = 523$ K. Also, Le-Quoc *et al.* [LeQu14] recently showed the possibility to grow the metastable γ-MgH$_2$ film on Si substrate by Reactive Plasma Assisted sputtering at low hydrogen pressure (0.4 Pa) and close to room temperature.

As described in last section, Krozer and Kasemo [Kroz90] reported the reaction enthalpy difference of $\Delta_f H - \Delta_d H \approx 11$ kJ/molH$_2$ at $T = 290\text{-}370$ K for Mg films, from a gravimetric method. Pivak [Pivak12$^+$] reported $\Delta_f H - \Delta_d H \approx 17$ kJ/molH$_2$ for thin film, from hydrogenography measurements at $T = 333\text{-}545$ K. Those values are larger compared to the value by Shao *et al.* [Shao04], and the different tendencies of them are clearly contrasting, as shown in **Table 2.5**. This is a larger hydride growth model.

Crystallographic relationships between magnesium matrix and the nucleated thermodynamically stable β-MgH$_2$ phase are reported by different studies, as listed in **Table 2.4**. They are specified in absorption direction (*Abs.*) and desorption direction (*Des.*). Observations on bulk samples have been done by Schober [Schob81], with transmission electron microscopy (TEM). The crystallographic relationship of β-MgH$_2$(100)[001] // α-Mg(0001)[11-20] was shown for $T = 543$ K with $p_{H2} = 5$ MPa. Alternatively, β-MgH$_2$(110)[001]//α-Mg(0001)[10-10]

Table 2.4 Crystallographic relationships between the Mg matrices and its hydrides (β- and γ-phase) for thin films. Whisker-, nanofiber-, and powder samples are also listed for a comparison purpose. Determination methods (XRD, TEM and EELS) and the reaction directions with hydrogen (Abs./Des.) are remarked for each work.

Relationships	Shape	T [K]	P_{H2}[MPa]	Reaction	Methods	Ref.
β-MgH$_2$ [001]// αMg [10-10] β-MgH$_2$ (110)// αMg [10-10]	Epitaxial Mg (0002) thin film on Al$_2$O$_3$(0001) substrate	373	0.6	Abs.	XRD	[Kele07]
β-MgH$_2$ [001]// αMg [-1101] β-MgH$_2$ (200)// αMg(11-20)	Epitaxial Mg (0002) thin film on LiGaO$_2$(320) substrate	373	0.6	Abs.	XRD	[Kele07]
β-MgH$_2$ (110)// αMg(0002)	Mg film on glass substrate	363	1	Abs.	XRD	[Özgi10]
	Mg film on glass or quartz-glass	300-773	0.1	Abs. & Des.	XRD	[Yama02]
	Mg-Ni multilayer-film on Si(100) substrate	533	---	Abs.	XRD	[Ye06]
γ-MgH$_2$ (random nucleation)	Mg film on glass	523	0.2	Abs.	XRD	[Gaut11]
β-MgH$_2$ (110)// αMg(0002)	MgH$_2$ whisker				TEM	[Bokh87]
	Nanofiber			Abs.	TEM	[Zhu11]
β-MgH$_2$ (110)// αMg (-110-1) β-MgH$_2$ [-111] // αMg[01-11]	TiF$_3$-catalyzed MgH$_2$ powder	673	6	Abs.	TEM	[Dana12]
β-MgH$_2$ (110)// αMg(0002) β-MgH$_2$ [001]// αMg [-2110]	MgH$_2$ powder (commercial, purity 95%)	---	---	Abs.	TEM, EELS	[Paik10]
β-MgH$_2$ [001]// αMg [-1-120] β-MgH$_2$ (100)// αMg(0002)	MgH$_2$ disc	543	5	Abs.	TEM	[Schob81]

relationship for films on $Al_2O_3(001)$ substrates and β-$MgH_2(200)[001]//$ α-$Mg(11\text{-}20)[11\text{-}21]$ relationship for films on $LiGaO_2(320)$ substrates were reported by Kelekar *et al.*, in their observations on 400 nm epitaxial film upon the hydrogenation reaction at $T = 373$ K with $p_{H2} = 0.6$ MPa [Kele07]. An (0001)-orientation of Mg was observed in films deposited on glass substrates by Özgit *et al.* [Özgi10], with orientation relationship of β-$MgH_2(110)$ //α-$Mg(0001)$. This relationship were also observed by Yamamoto *et al.* [Yama02] in films deposited on glass substrate and by Ye *et al.* [Ye06] in films deposited on Si substrate. Apart from film samples, an orientation relationship of β-$MgH_2(110)$ //α-$Mg(0001)$ is discussed by Zhu *et al.* [Zhu11], which same orientation relationship observed by Bokhonov *et al.* [Bokh87] by single crystals of MgH_2 whiskers.

Other relationships of β-$MgH_2(110)$ //α-$Mg(\text{-}110\text{-}1)$ and β-MgH_2 [-111] //α-Mg [01-11] are also reported by Danaie and Mitlin [Dana12] from their TEM measurements for MgH_2 powder samples, at $T = 673$ K. Those works are also listed in **Table 2.4**.

With respect to the orientation relationships, a preferential growth in <110>-direction of the β-MgH_2 was measured by Saita *et al.* [Saita06] from their XRD study for MgH_2 -nanowire investigated via CVD in hydrogen gas. Theoretically calculation has been also conducted by Vajeeston *et al.* [Vaje08], and proved that the energetically most stable plane is β-$MgH_2(110)$, as well as the (0002) plane of the α-Mg. Therefore, the texture of α-Mg (0002) and preferential growth of β-$MgH_2(110)$ is generally expected in this work. These planes are shown as the pink planes in **Fig. 2.11**.

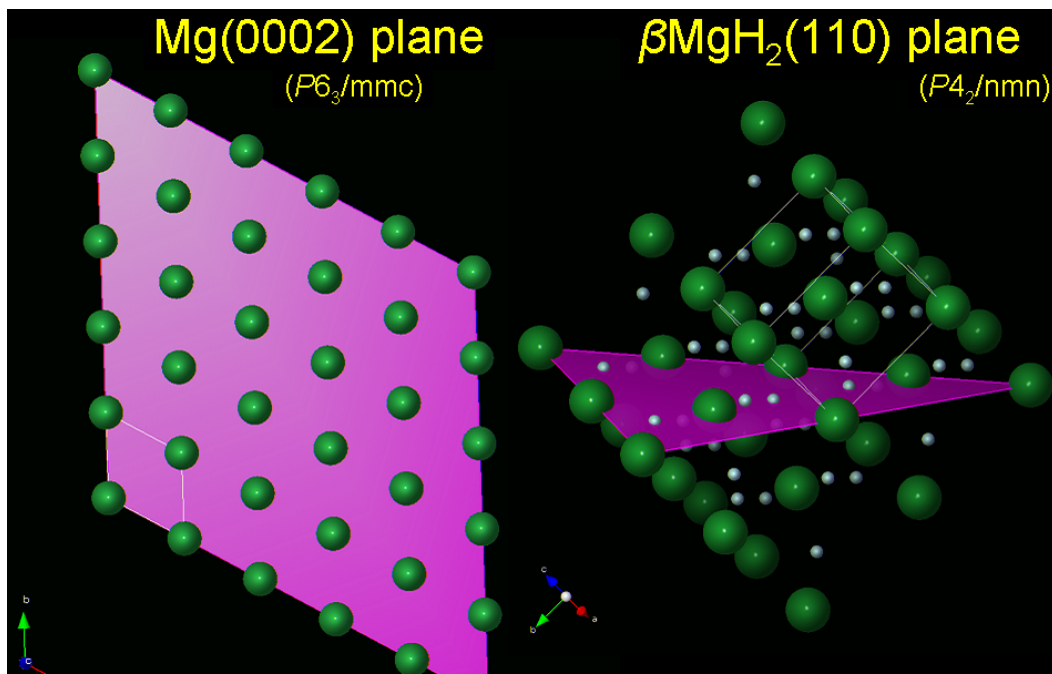**Fig. 2.11** A schematic figure of the α-Mg(0002) plane (left) and the β-$MgH_2(110)$ plane (right), drawn by VENUS [Izumi05]. Both planes are shown with pink layer in the matrices, consisting of Mg atoms (green) and hydrogen atoms (blue). Edge of unit cell is drawn with white line, and axes for both crystals are shown respectively.

Apart from hydride formation, interdiffusion of Mg and capping material, such as Pd or Pt is known to cause property degradations for Mg-based film type hydrogen sensors. Details about this phenomenon will be described in **Chap. 2.1.7**.

With respect to the β-MgH$_2$ phase in Mg-film samples, insulating properties are reported [Wester08], and a large band gap of E_B^{Mg} = 5.7 eV is experimentally determined by Isidorsson *et al.* [Isido03]. Also, many works are conducted by means of hydrogenography (*e.g.* [Dam07,Baldi09,Baldi10,Pivak12]). The drastic change of the optical properties is known upon the phase transition between α-Mg and β-MgH$_2$ phase, as is also known for the Y-H system [Huib96]. This optical property change is also seen in thick films treated in this work. (Shown later in **Fig. 5.13** in **Chap. 5.2.1.3**)

Electrical resistivity works are also frequently conducted for Mg films. The electrical resistivity ρ_{Mg}, is reported by Isidorsson *et al.* [Isido03] to be ρ_{Mg} = 6 $\mu\Omega$cm for 188 nm Mg films with 10 nm Pd on top, and ρ_{Mg} = 6.5 $\mu\Omega$cm for 150 nm Mg films with 12 nm Pd on top, respectively. These values contains the influence of the surface Pd.

The resistivity of β-MgH$_2$ ρ_{MgH_2} is measured by *ex situ* measurements to be ρ_{MgH_2} = 630 $\mu\Omega$cm by Isidorsson *et al.* [Isido03] for Mg film with Pd-capping layer, and by Giebels *et al.* corrected this value to be ρ_{MgH_2} =10 mΩcm, removing the effect of the surface Pd layer [Gieb04]. Westerwaal *et al.* [Wester08] reported a value of ρ_{MgH_2} > 1 MΩcm by *in-situ* measurements for Mg films with better purity. Details of resistivity measurement will be described in **Chap. 3.7**. **Table 2.5** summarize the values of band gap energes of the β-MgH$_2$, resistivities and the difference of hydride formation/decomposition enthalpies for bulk-Mg and Mg thin film, which were described in this section.

Table 2.5 Band gap energy (E_B^{Mg}) for β-MgH$_2$ and electric resistivities of α-Mg (ρ_{Mg}) and β-MgH$_2$ phase (ρ_{MgH_2}) for bulk and thin film samples, and difference of ΔH from literatures. [Kras82,He90,Paik12,Isido03,Lide04, Aved99,Gieb04,Kroz90,Pivak12+,Shao04].

		Bulk	(Ref.)	Thin film	(Ref.)
E_B^{Mg}		5.16 eV 5.8 eV 4.3-4.5 eV	[Kras82] [He90] [Paik12]	5.7 eV	[Isido03]
ρ	ρ_{Mg}	4.51 $\mu\Omega$cm 4.53 $\mu\Omega$cm (*a*-axis) 3.78 $\mu\Omega$cm (*c*-axis)	[Lide04] [Aved99]	6.5 $\mu\Omega$cm	[Isido03]
	ρ_{MgH2}	---		630 $\mu\Omega$cm 10^4 $\mu\Omega$cm >10^{12} $\mu\Omega$cm	[Isido03] [Gieb04] [Wester08]
$\Delta_f H$ -$\Delta_d H$		11 kJ/(molH$_2$) 17 kJ/(molH$_2$)	[Kroz90] [Pivak12+]	1.2 kJ/(molH$_2$)	[Shao04]

2.1.5.3 Tuning reaction properties of the Mg-MgH₂ system kinetics

Most of studies in past concerning Mg-H system were done at elevated temperatures. First reason of that is the blocking effect of the hydride phase at the reaction interface [Uchi11], and the small hydrogen diffusivity in the Mg-MgH$_2$ system (see **Chap. 2.1.4.4**). Another reason is the thermodynamical stability of the hydride phase.

Fig. 2.12 shows the reported equilibrium plateau pressures for Mg-MgH$_2$, as well as the expected equilibrium plateau pressure for Mg-MgH$_2$ at 300 K. The van't Hoff plots summarizes the literature data reported by Wiberg and Baner [Wibe52], Ellinger *et al.* [Ellin55], Cummings and Powers [Cumm74], Stampfer *et al.* [Stamp60] for bulk samples, and for thin films by Pivak [Pivak12+], Borgschulte *et al.* [Borg07], and Baldi *et al.* [Baldi09++]. Extrapolation gives the range of $p_{H2} = 2 \times 10^{-5}$ bar and $p_{H2} = 8 \times 10^{-5}$ bar at $T = 60$ °C. Chemical potential of galvanostatic measurements by Vermeulen *et al.* [Verm06], or thermodynamic modelling by Zeng *et al.* [Zeng99] or by Vermeulen *et al.* [Verm07] also result in a similar range.
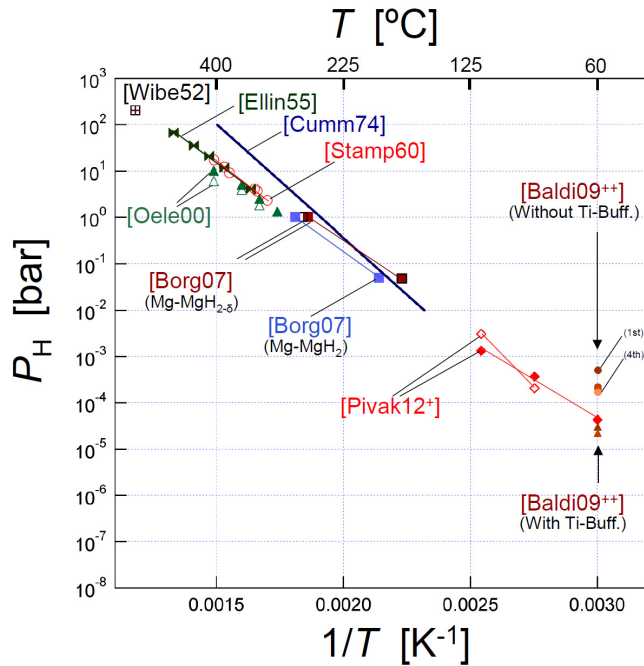
Fig. 2.12 A series of Van't Hoff plots for Mg-MgH₂ transition, reported by Wiberg and Baner [Wibe52], Ellinger *et al.* [Ellin55], Stampfer *et al.* [Stamp60], Cummings and Powers [Cumm74], Oelerich *et al.* [Oele00], Baldi *et al.* [Baldi09P++], Borgschulte *et al.* [Borg07], Pivak [Pivak12P+]. Hollow- and filled symbols are plots, which corresponds to hydride decomposition reaction and formation reaction, respectively.

Addition and alloying with Ni, Cu has been investigated by Reilly and Wiswall [Reil67,Reil68]. Increase of the plateau pressures are reported in their work, nevertheless, a reaction temperature of over 573K is needed.

For powder samples, decreasing of the hydride decomposition enthalpy by decreasing particle size below 20 nm is reported by Aguey-Zinsou and Ares-Fernández in their review [Aguey10]. Significant drop in particle stability of magnesium hydride with particle sizes below 2 nm ranges is reported by Cheung *et al.* [Cheu05], Wagemans *et al.* [Wage05], and Vajeeston *et al.* [Vaje12], by theoretical calculations. Most significantly, the desorption energy of the β-MgH$_2$ phase, which is 74 kJ/(mol H$_2$) for the bulk form, drastically decreased to 65.3 kJ/(mol H$_2$) for nanowires with diameters of 30-50 nm [Saita06]. Aguey-Zinsou and Ares-Fernández [Aguey08] also

demonstrated the size dependency of hydride properties experimentally, for surfactant-stabilized magnesium nanoparticles with a diameter of 5 nm. An explanation for such size effect of Mg nano-cluster on the thermodynamic properties is discussed by Aguey-Zinsou and Ares-Fernández [Aguey10] to be the contribution of the surface free energy to the total energy of the system.

For thin films, Baldi *et al.* [Baldi09] reported that the thermodynamics of hydrogen absorption in Mg can be tuned by elastic clamping. The loading isotherms measured by hydrogenography show that Mg films covered with Mg-alloy-forming elements, such as Pd and Ni, have hydrogen plateau pressures more than 2 orders of magnitude higher than bulk Mg at the same temperature. A Mg thickness dependence of the hydrogen plateau pressure is also reported [Wagn08,Baldi09]. For thin Mg films (< 14 nm) sandwiched by Fe nanolayers, Mooij *et al* [Mooij14] recently reported the presence of multiple plateau pressures, whose nature are related to be tuned by the film thickness, whereas the hydrogen desorption occurs via a single plateau which does not depend on the Mg layer thickness. Furthermore, Tang *et al* [Tang12] recently reported that the biaxial strain, which is introduced in clamped films, also affects the structural stabilities of magnesium hydrides on the Mg(0001) surface, using density-functional theory calculations.

Apart from the above, from viewpoint of increasing reaction rate, application of suitable catalysts is actually considered [Mintz78,Oele01,Bark03,Hana05,Andr06,Fried06,Hana06,Koji06, Du08,Lillo08,Luo08,Yu09,Sabi10,Sing10,Dana12,Zhou13^{+},Must14,Ren14].   However,   most studies are done at elevated temperature. The understanding of the reaction process on the Mg-MgH$_2$ system is still not enough to avoid surface-blocking layers at room temperature, up to now.

2.1.6 Pd-H systems

In this study, thin Pd capping layer is deposited on the sample surface, to avoid oxidation of underlying Mg layer. Also, Pd-substrate is used for permeation measurement. Therefore, thermodynamic properties of Pd-H binary system with bulk and film samples are introduced in this section.

2.1.6.1 H in bulk-Pd

In the bulk Pd-H system, the α-Pd phase solves hydrogen up to $c_H = 0.01$ H/Pd at 298 K, for a bulk system [Fries73], shown in **Fig. 2.13**. Fitting function for the temperature dependency of the partial molar enthalpy of solution ΔH_s^{bulk} (unit in J/(molH)) and partial molar enthalpy entropy ΔS_s^{bulk} (in J/(molH$\cdot$K)) for hydrogen at infinite dilution in the bulk-Pd is supposed as

$$\Delta H_s^{bulk} = -9.20 - 1.29 \times 10^{-2} T + 3.97 \times 10^{-5} T^2 - 2.02 \times 10^{-8} T^3 \qquad (2.24a)$$

$$\Delta S_s^{bulk} = -71.78 + 7.02 \times 10^{-2} T - 6.88 \times 10^{-5} T^2 + 2.89 \times 10^{-8} T^3 \qquad (2.24b)$$
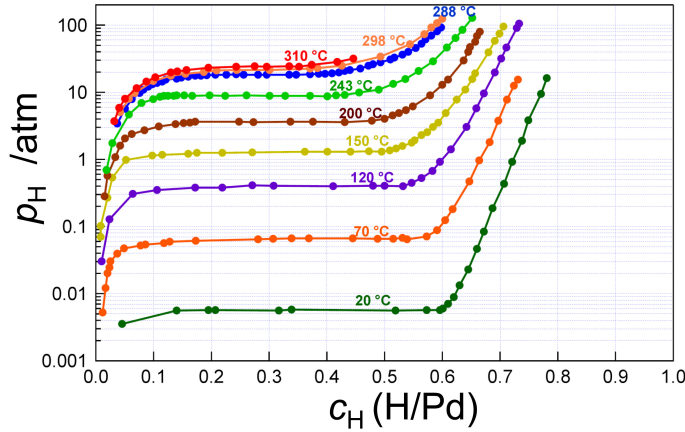
Fig. 2.13 PCT diagram of the bulk Pd-H system, at different temperatures between T = 298K and 510K. Original data from the study by Frieske and Wicke [Fries73].

where T is the temperature (unit in K) and should be in the range of 200 K < T < 1000 K [Manc94]. Applying Eq.(2.24a) and Eq.(2.24b), $\Delta H_s^{bulk} \approx$ -10 kJ/(molH) and $\Delta S_s^{bulk} \approx$ -56.2 J/(molH) is available at T = 298 K.

Further hydrogen uptake gives a α'-Pd phase with a plateau pressure of about $p_{H2} \approx 10^3$ Pa at room temperature, which is 4 orders of magnitude higher than that of bulk β-MgH$_2$ formation (See **Fig. 2.3**).

It is known that Sieverts' law [Siev29] is obeyed in bulk Pd at low-hydrogen concentrations [Manc94]. At 10^{-3} Pa and at 298 K, the c_H is similarly calculated as shown in Eq.(2.11) and yield c_H = 1.3· 10^{-5} H/Pd.

The hydride formation enthalpy of Pd hydride is reported by Flanagan *et al.* [Flan91$^+$] to be ΔH_f^{bulk} = -19.09±0.10 kJ/(molH) from calorimetric measurement at a temperature range of 333 K < T < 433 K. This value is in good agreement with other reported values, by Lässer and Klatt (ΔH_f^{bulk} = -18.7±0.15 kJ/(molH) [Läss83]) or by Zhang *et al.* (ΔH_f^{bulk} = -19.1 kJ/(molH) [Zhan99]). Furthermore, Flanagan *et al.* found the same enthalpy value for dehydrogenation, (ΔH_d^{bulk}) with accuracy within ±0.10 kJ/(molH). Therefore, the enthalpy change of Pd-PdH$_x$ for both transition directions is treated to be constant, and ΔH_f^{bulk} = -19.09 kJ/(molH) is used in this work.

2.1.6.2 H in Pd-films and nano-Pd

It is known that the thermodynamic properties of metal-hydrogen systems are affected by the stress dependency of the chemical potential.

Under the presence of compressive biaxial stress, for clamped films on the substrate, the solubility limit of hydrogen is extended and hydride phases are destabilized [Feen83,Laud98,Pundt06,Wagn08,Pivak09,Wagn11]. For strongly adhering epitaxial Pd-films, Wagner *et al.* reported that the hydride formation plateau pressure shifts up to p_{H2}^{film} = 400 mbars in contrast to p_{H2}^{bulk} = 18 mbars for bulk, and the formation enthalpy increases from ΔH_f^{bulk} = -19.1 kJ/(molH) to ΔH_f^{film} = -17.5 kJ/(molH) [Wagn08].

Also, the grain size affects the solubility limits. For nanocrystalline films, Mütschele and

Kirchheim [Muet87,Muet87^{+}] determined an increase of the hydrogen solubility limit for nanocrystalline Pd with grain size of 8-12 nm, prepared by gas-phase synthesis. Solubility limits for the α-phase $c_H^{nano} = 0.03$ H/Pd, and for the (α'-)hydride phase $c_H'^{nano} = 0.44$ H/Pd are obtained by them, which are reported by Wicke *et al.* for polycrystalline Pd as $c_H^{bulk} = 0.008$ H/Pd and $c_H'^{bulk} = 0.607$ H/Pd, respectively [HinMeII]. Therefore the miscibility gap of Pd-H system for nanocrystalline samples is narrowed, compared to bulk. This effect is also found for nanocluster samples [Pundt99,Zütt00,Sach01,Yama08,Yama09,Sule09], and the different types of nanocrystalline Pd-H system, for example by Natter *et al.* [Natt97] for films by pulsed electrodeposition, or by Kürschner *et al.* [Kuer14] for films by Ar-sputtering. Kürschner *et al.* [Kuer14] recently reported $c_H^{film} = 0.12$ H/Pd for the α-phase limit, and $c_H'^{film} = 0.5$-0.55 H/Pd for the β-phase limit. Similar hydrogen solubility limit is expected for Pd-capping layer prepared in this work. However in this work, the solution limit of hydrogen in the Pd-capping layer is treated as a constant value of $c_H'^{film} = 0.6$ H/Pd, to estimate hydrogen concentration in Mg.

2.1.7 Mg-Pd system and Mg-Pd-H system

At the interface of Pd/Mg, formation of intermetallic compounds or intermixing is possible, during measurements at elevated temperatures. Therefore Mg-Pd and Mg-Pd-H system are regarded in this section. **Fig. 2.14** shows the binary phase diagram of the bulk Mg-Pd system [Naye85].
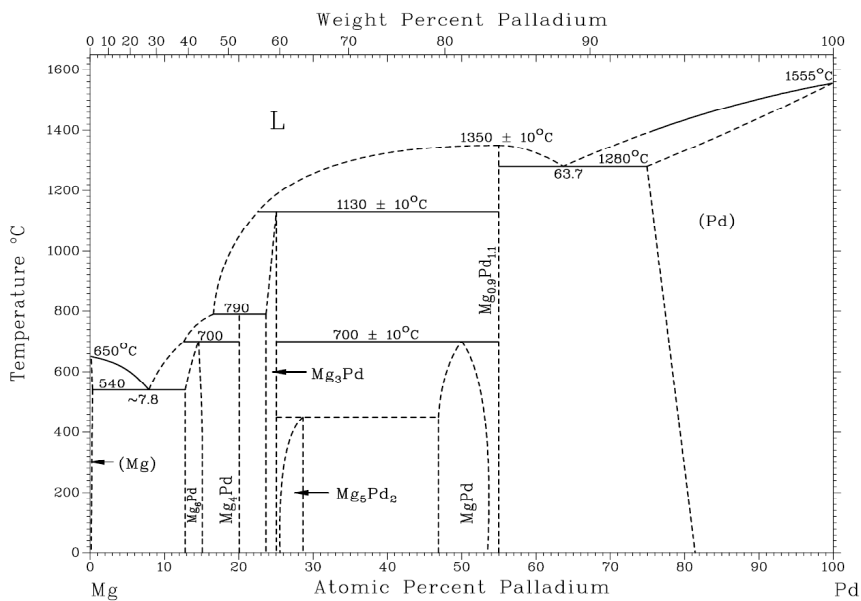

Fig. 2.14 Binary phase diagram of the bulk Mg-Pd system [Naye85].

A large thermodynamical solubility limit of Mg in the bulk Pd at room temperature (about 19 at.% of Mg) can be seen at the right side of the diagram. Thus, solutions of Mg atoms into the Pd

layer, which could happen at the interfaces of both materials through interdiffusion, is reported as a factor of property degradations of the Pd-capped Mg-based hydrogen sensors, or causes thermodynamical change of the hydrogen- film-Mg systems.

Furthermore, several complex intermediate phases, as visible in **Fig. 2.14**, are known to be formed in the Mg-Pd system [Mako06]. Formation of the fragile intermetallic phases at the interlayer, such as Mg_6Pd, $Mg_{57}Pd_{13}$, $Mg_{56.4}Pd_{13.5}$, Mg_4Pd, $Mg_{306}Pd_{77}$, $Mg_{78.5}Pd_{21.5}$, $Mg_{64}Pd_{17}$, Mg_3Pd, Mg_5Pd_2, Mg_2Pd, $MgPd$, $Mg_{0.9}Pd_{1.1}$, $MgPd_2$, $MgPd_3$ or $MgPd_6$ ([Ferr59,Naye85,Wann01,Yama02,Mako06,Dufo07, Deng08,Kunk11,Wu14]), makes it difficult to apply Pd-capped Mg-based thin films at higher temperatures. Introducing hydrogen in the system, hydrides such as α-$MgPd_3H_{\approx1}$ (tetragonal, $ZrAl_3$-type), β-$MgPd_3H_{0.67}$ (cubic, anti-perovskite) [Kohl05], and Mg_2PdH_x (cubic, Mg_2PdC_x-like FCC) [Goto05] form, as recognized from high-pressure investigations in GPa range. Those metastable hydrides could affect the thermodynamics of the total Mg-film system, including equilibrium pressures. These intermetallic compounds are known to react with hydrogen and cause disproportionation reactions, as reported for example by Callini *et al.* [Call10].

In this work, annealing treatments are done for some samples. Special care is taken in sample annealing, to avoid influences of artifacts. Therefore, annealing of Mg-films is done only without the surface-capping layer of Pd. Furthermore, hydrogen sorption measurements have been done at room temperature.

Also, *in-situ* measurements are done at elevated temperatures. To prevent the interdiffusion in thin films, a maximum temperature of $T_{max} = 363$ K was chosen for Mg film in this work.

An alternative way to prevent the film from formation of intermetallic compounds, for example, using Ti-buffer layer between Pd- and Mg-layer, is proposed by Baldi *et al.* [Baldi09, Baldi09^{+}]. To prevent formation of the intermetallic compounds, Mg-film samples for measurements at elevated temperatures in this study, are directly deposited on Si-substrate. About the reactions at Mg/Si interface will be described in the next section.

2.1.8 Mg-Si system

Mg-films directly deposited on Si-substrate are prepared in this study, containing an interface of Mg/Si. The solubility of Si in Mg is quite low (maximum solubility is $c_{Si} = 0.005$ Si/Mg at $T = 910$ K) [Okam07]. Therefore, the solution of Si in Mg is was neglected in this study, even at elevated temperature. Only a partial formation of pure Mg silicide will be discussed in this work. Details regarding this topic will be described in **Chap. 5.6.4**.

2.2 Hydrogen induced volume expansion and stress in thin Mg films

Hydrogen uptake into a metal matrix yields an elastic lattice expansion and incidental mechanical stress, which can be calculated by the linear elastic theory [Laud99+,Slau02,Pundt06,Kirch14]. Generally, the in-plane compressive stress arises during hydrogen absorption in a thin film, since the volume usually expands upon the hydrogen absorption (**Fig. 2.15**), while the backside of the film is clamped to the rigid substrate. This film behavior upon hydrogen loading can be explained by using linear elastic theory, as long as no stress release happens, such as film buckling or plastic deformation [Niki08,Wagn10,Pivak11,Cize13]. Since the film is clamped to the substrate, a change of the substrate curvature is often observed. It can be used to measure the mechanical stress in the film.
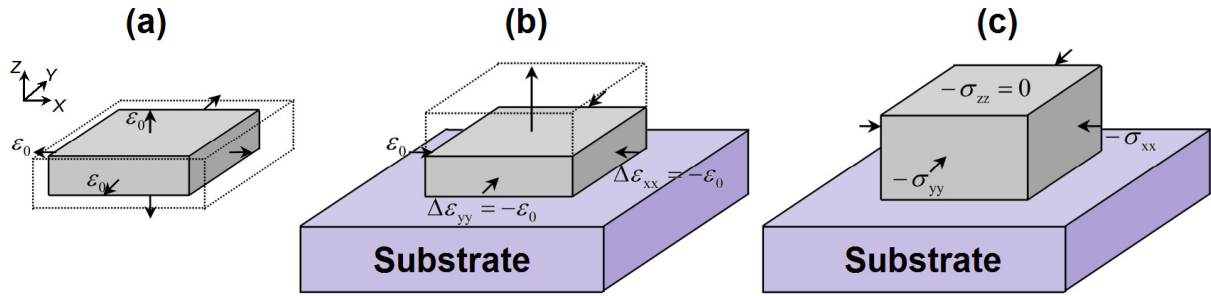
Fig. 2.15 Schematic view of stress and strain development during film expansion: (a) 3-dimensional hydrogen induced volume expansion of stress-free film. (b) 1-dimensional expansion of a fixed film. (c) Biaxial-stressed working on the film and resulting expansion to vertical direction.

In case of many bulk-M-H systems, the hydrogen absorption induced volume expansion ε_0 takes place in 3 directions (x and y in the in-plane direction, and z in the out-of-plane direction). The modality of this expansion depends on crystal structure of film material. **Fig. 2.15 a)** describes the case of cubic structure, which the expansion ε_0 is known to be homogeneous. In contrast, in case of the thin film sample deposited on elastically hard substrates like Si or Al_2O_3, the expansion of the sample in the in-plane directions is restricted due to the clamping by the substrates (a). As a result, the in-plane stress increases during the hydrogen absorption. Because of the Poisson effect, additional expansion in the out-of-plane direction occurs (b), (c). As already said, this compressive stress can be as huge as several GPa [Laud99,Nört06,Pundt06].

The compressive biaxial stress in-plane (x-y plane) $\sigma^{in-plane}$, which is induced by the hydrogen absorption, can be simply calculated [Gemm11] from the Young's modulus E and the Poisson's ratio ν, according to Hooke's law.

$$\sigma^{in-plane} = \frac{E}{1-\upsilon} \cdot (\Delta\varepsilon_0) \qquad (2.25)$$

where $\sigma < 0$ relates to compressive stress.

This explanation of the elastic behavior is valid as far as following two assumptions are fulfilled:

- the film material is elastically isotropic

- the in-plane configuration of the grain is homogeneous

To understand strain of the film in z- direction during hydrogen absorption, theory of linear elasticity is explained in the next section.

2.2.1 Theory of linear elasticity for hexagonal (α-Mg) and tetragonal (β-Mg) films

α-Mg has hexagonal and β-MgH$_2$ has tetragonal structure. Therefore the strain during hydrogen absorption in matrix is known to be anisotropic. Understanding of the anisotropic nature of the Mg-matrix is essential to discuss the inner stress development in Mg films [Nye85]. This section deduces the anisotropy of stress in α-Mg and β-MgH$_2$.

The states of stress and strain in a deformed crystal being idealized as a continuum are characterized by symmetric second-rank tensors σ_{ij} and ε_{kl}, respectively. Each being symmetric and comprising six independent components. Hooke's law of linear elasticity for the most general anisotropic solid expresses each component of the stress tensor linearly in terms of all components of the strain tensor in the form [Nye85]:

$$\sigma_{ij} = C_{ijkl} \cdot \varepsilon_{kl} \qquad\qquad (2.26)$$

where C_{ijkl} is the array of elastic stiffness constants. Alternately, the inverse form of Hooke's law is written to express each component of the strain tensor linearly in terms of all components of the stress tensor as

$$\varepsilon_{ij} = S_{ijkl} \cdot \sigma_{kl} \qquad\qquad (2.27)$$

where S_{ijkl} is the array of elastic compliance constants. In Eq.(2.26) or Eq.(2.27), each of the six equations for a stress or strain component involves nine material parameters. Each of the fourth-order tensors C_{ijkl} and S_{ijkl} comprise 81 components. The symmetry of the stress and strain tensors, that is, $\sigma_{ij} = \sigma_{ji}$ and $\varepsilon_{ij} = \varepsilon_{ji}$, further imply that the components of the stiffness tensor must satisfy $C_{ijkl} = C_{ijlk} = C_{jikl}$; likewise, $S_{ijkl} = S_{ijlk} = S_{jikl}$. As a consequence, the number of independent elastic constants is reduced from 81 to 36 in either case. Actual values of the S and C for various metals are summarized, for example by Gray or Hearmon, in literature of [Gray72] and [Hear79], respectively.

The tensor form of the constitutive equation in Eq.(2.26) provides a concise and effective statement of Hooke's law for use in theoretical developments. However, it is often more convenient to adopt a matrix form of the constitutive equation from viewpoints of measurement and calculation. Such a form is suggested naturally by the fact that there are six independent components of stress, six independent components of strain, and 36 material parameters

representing the relationship between stress and strain. For this purpose, a contracted notation is commonly introduced, whereby a six-component array σ_i is constructed by means of the replacements $\sigma_{11} \rightarrow \sigma_1$, $\sigma_{22} \rightarrow \sigma_2$, $\sigma_{33} \rightarrow \sigma_3$, $\sigma_{23} = \sigma_{32} \rightarrow \sigma_4$, $\sigma_{13} = \sigma_{31} \rightarrow \sigma_5$ $\sigma_{12} = \sigma_{21} \rightarrow \sigma_6$ [Kelly12]. Then,

$$\sigma_i = C_{ik} \cdot \varepsilon_k \tag{2.28}$$

The elastic energy density is given by [Ashc76]:

$$f_{el} = \frac{1}{2} \cdot C_{ik} \cdot \varepsilon_i \cdot \varepsilon_k \tag{2.29}$$

The right-hand side is summed over all subscripts (Einstein convention).

For further symmetry reasons this tensor simplifies. Its components can be found for the different lattice systems. For triclinic system, 21 components are independent, for cubic systems the number of independent components reduces to 3 and for isotropic systems it reduces to 2.

2.2.1.1 Hexagonal system (α-Mg)

For hexagonal systems the stiffness tensor is given by [Nye85].

$$C^{hex}{}_{\alpha\beta} = \begin{pmatrix} C_{11} & C_{12} & C_{13} & 0 & 0 & 0 \\ C_{21} & C_{22} & C_{23} & 0 & 0 & 0 \\ C_{31} & C_{32} & C_{33} & 0 & 0 & 0 \\ 0 & 0 & 0 & C_{44} & 0 & 0 \\ 0 & 0 & 0 & 0 & C_{55} & 0 \\ 0 & 0 & 0 & 0 & 0 & C_{66} \end{pmatrix} = \begin{pmatrix} C_{11} & C_{12} & C_{13} & 0 & 0 & 0 \\ C_{12} & C_{11} & C_{13} & 0 & 0 & 0 \\ C_{13} & C_{13} & C_{33} & 0 & 0 & 0 \\ 0 & 0 & 0 & C_{44} & 0 & 0 \\ 0 & 0 & 0 & 0 & C_{44} & 0 \\ 0 & 0 & 0 & 0 & 0 & \frac{1}{2}(C_{11} - C_{12}) \end{pmatrix}$$

(2.30)

Information for other systems can be found, for example in ref. [Kelly12,Nye85]. The coordinates of the stiffness tensor C_{ij} are given with respect to the internal crystal coordinate system.

In case of 0001-oriented hexagonal film, the free energy density can be expressed by

$$f_{el} = \frac{1}{2} \cdot C_{11}(\varepsilon_1^2 + \varepsilon_2^2) + \frac{1}{2} \cdot C_{33}\varepsilon_3^2 + C_{12}\varepsilon_1\varepsilon_2 + C_{13}(\varepsilon_1\varepsilon_3 + \varepsilon_2\varepsilon_3) \tag{2.31}$$

Using the relationships of

$$\frac{\partial f}{\partial \varepsilon_3} = \sigma_3 = C_{33}\varepsilon_3 + C_{13}(\varepsilon_1 + \varepsilon_2) = 0 \tag{2.32}$$

gives

$$\varepsilon_3 = -\frac{C_{13}}{C_{33}}(\varepsilon_1 + \varepsilon_2) \tag{2.33}$$

The total film expansion ε_3^{tot} is obtained as

$$\varepsilon_3^{tot} = \left(1 + 2\frac{C_{13}}{C_{33}}\right)\varepsilon_0 \tag{2.34}$$

Using Eq.(2.33), the Eq.(2.31) is simplified as

$$f_{el} = \frac{1}{2}C_{11}(\varepsilon_1^2 + \varepsilon_2^2) + C_{12}\varepsilon_1\varepsilon_2 - \frac{C_{13}^2}{2C_{33}}(\varepsilon_1 + \varepsilon_2)^2 \tag{2.35}$$

the in-plane stresses can be obtained from the derivatives of elastic energy density, by

$$\frac{\partial f_{el}}{\partial \varepsilon_1} = \sigma_1 = C_{11}\varepsilon_1 + C_{12}\varepsilon_2 - \frac{C_{13}^2}{C_{33}}(\varepsilon_1 + \varepsilon_2) = -\left(C_{11} + C_{12} - 2\frac{C_{13}^2}{C_{33}}\right)\varepsilon_0 \tag{2.36a}$$

$$\frac{\partial f_{el}}{\partial \varepsilon_2} = \sigma_2 = C_{11}\varepsilon_1 + C_{12}\varepsilon_2 - \frac{C_{13}^2}{C_{33}}(\varepsilon_1 + \varepsilon_2) = -\left(C_{11} + C_{12} - 2\frac{C_{13}^2}{C_{33}}\right)\varepsilon_0 \tag{2.36b}$$

In case of 0001-oriented hexagonal Mg-film, applying elastic constants of ref. [Hunt58] (shown in **Table 2.6**) for Eq.(2.36a) and Eq.(2.36b) yields

$$\sigma_1 = \sigma_2 = -\left(C_{11} + C_{12} - 2\frac{C_{13}^2}{C_{33}}\right)\varepsilon_0 = -\left(59.7 + 26.2 - 2\frac{21.7^2}{61.7}\right)\varepsilon_0 = -70.63\varepsilon_0$$

$$\tag{2.37}$$

with units in GPa. Here, σ_1 and σ_2 is the corresponding stress of the the x_1- and x_2- axes, respectively, which can be chosen randomly in the basal plane.

Table 2.6 Elastic constants of c_{ij} (units in GPa) and s_{ij} (units in GPa^{-1}) at room temperature for hexagonal Mg (x_3- axis parallel to [0001], x_2- and x_1- axes anywhere in the basal plane) [Hunt58,Hear79]. Parameters for tetragonal β-MgH$_2$ [Yu88,Bara94,Hect07,Zars13] are also associated as reference.

Material	C_{11}	C_{12}	C_{44}	C_{33}	C_{13}	C_{66}	s_{11}	s_{33}	s_{44}	s_{12}	s_{13}	Ref.
Mg	59.7	26.2	16.4	61.7	21.7	---	0.022	0.0197	0.061	-0.00785	-0.0050	[Hunt58]
	59.3	25.7	16.4	61.5	21.4	---	0.022	0.0197	0.06098	-0.00775	-0.00496	[Hear79]
β-MgH$_2$	72.01	38.19	41.1	140.47	31.99	54.44	---	---	---	---	---	[Zars13]
	77.3	39.2	40.2	138.9	32.6	56.3	---	---	---	---	---	[Hect07]
	73.1	33.9	38.5	131.9	20.4	52.3	---	---	---	---	---	
	(C_{11}+ C_{12}= 110)	---	100	30	---	---	---	---	---	---	---	[Yu88]
	(C_{11}+ C_{12}= 107)	171	139	22	22	---	---	---	---	---	---	[Bara94]

2.2.1.2 Volume expansion upon phase transition from α-Mg into β-MgH$_2$

Using Eq.(2.36a) and Eq.(2.36b), the stress dependency on the hydrogen concentration can be calculated when the relationship between ε_0 and c_H is available. For materials with high hydrogen solubility (such as Pd or Nb), the hydrogen induced volume expansion can be transformed into uniaxial change (see Eq.(2.1)). However Mg has a low solubility limit of hydrogen at room temperature, and nucleates as hydride already at low c_H (see **Chap. 2.1.5.1** for details), therefore this estimation is not suitable. Alternatively, the microscopic volume expansion upon phase transition from α-Mg into β-MgH$_2$ is applied.

The volume expansion per unit cell is calculated as

$$\Delta\upsilon = \frac{\upsilon^{\beta MgH_2} - \upsilon^{Mg}}{\upsilon^{Mg}} = \frac{\upsilon^{MgH_2}}{\upsilon^{Mg}} - 1 = \frac{0.32093^2 \cdot \sin(60°) \cdot 0.52107}{0.45168^2 \cdot 0.30205} - 1 \approx 0.32585$$

(2.38)

where $\upsilon^{\beta MgH_2}$ and υ^{Mg} is the unit cell volume of β-MgH$_2$ and Mg, respectively. Here, the unit cell of Mg consists of two Mg atoms, and four H atoms are stored per unit cell upon this transition-induced volume expansion. Therefore,

$$(\Delta\upsilon/\Omega) \approx [0.32585/4] = 0.081$$

(2.39)

is obtained for the volume expansion upon phase transition from Mg into β-MgH$_2$.

Strictly speaking, this volume expansion is microscopically not isotropic. This approach approximates the expansion with an isotropic expansion factor. Therefore,

$$\varepsilon_0 = 0.081 \cdot c_H$$

(2.40)

is obtained. This simplified approach is also compatible with the value determined by Schober *et al.* [Schob81] (see **Chap. 2.1.1**). Applying Eq.(2.40) into Eq.(2.37),

$$\sigma_1 = \sigma_2 = -70.63\varepsilon_0 = -5.72[GPa] \cdot c_H$$

(2.41)

are calculated as the biaxial in-plane stress working in the film.

With respect to the total expansion in z direction, applying Eq.(2.40) and Eq.(2.34), a relationship between ε_3^{tot} and c_H is obtained as follows:

$$\varepsilon_3^{tot} = \left(1 + 2\frac{C_{13}}{C_{33}}\right) \cdot \varepsilon_0 = \left(1 + 2 \cdot \frac{21.7}{61.7}\right) \cdot 0.081 c_H = 0.137 \cdot c_H$$

(2.42)

In case of Mg-H system treated in this work, c_H varies from $c_H = 0$ H/Mg to $c_H = 2$ H/Mg according to the phase transition from α-phase into β-MgH$_2$ phase. Using simplified model,

$$\sigma_{max} = -11.44[GPa]$$

(2.43a)

and

$$\varepsilon_{zz,\max} = 0.274 = 27.4\% \tag{2.43b}$$

are derived for thin Mg film on hard substrate.

2.2.1.3 Tetragonal system (β-MgH₂)

Likewise, linear elasticity theory can be applied for the tetragonal β-MgH$_2$ structure. Eq.(2.30) can be rewritten in two different expressions.

First expression is

$$C^{tet-\mathrm{I}}{}_{\alpha\beta} = \begin{pmatrix} C_{11} & C_{12} & C_{13} & 0 & 0 & 0 \\ C_{21} & C_{22} & C_{23} & 0 & 0 & 0 \\ C_{31} & C_{32} & C_{33} & 0 & 0 & 0 \\ 0 & 0 & 0 & C_{44} & 0 & 0 \\ 0 & 0 & 0 & 0 & C_{55} & 0 \\ 0 & 0 & 0 & 0 & 0 & C_{66} \end{pmatrix} = \begin{pmatrix} C_{11} & C_{12} & C_{13} & 0 & 0 & 0 \\ C_{12} & C_{11} & C_{13} & 0 & 0 & 0 \\ C_{13} & C_{13} & C_{33} & 0 & 0 & 0 \\ 0 & 0 & 0 & C_{44} & 0 & 0 \\ 0 & 0 & 0 & 0 & C_{44} & 0 \\ 0 & 0 & 0 & 0 & 0 & C_{66} \end{pmatrix} \tag{2.44}$$

for $4_2/mmm$, 422, $\overline{4}2m$ or $4mm$ symmetry systems [Ladd03], due to the relationships of $C_{55} = C_{44}, C_{22} = C_{11}$ and $C_{13} = C_{23}, C_{31} = C_{32}$ [Nye85]. (6 independent coefficients.)

Another expression is

$$C^{tet-\mathrm{II}}{}_{\alpha\beta} = \begin{pmatrix} C_{11} & C_{12} & C_{13} & 0 & 0 & C_{16} \\ C_{21} & C_{22} & C_{23} & 0 & 0 & C_{62} \\ C_{31} & C_{32} & C_{33} & 0 & 0 & 0 \\ 0 & 0 & 0 & C_{44} & 0 & 0 \\ 0 & 0 & 0 & 0 & C_{55} & 0 \\ C_{61} & C_{62} & 0 & 0 & 0 & C_{66} \end{pmatrix} = \begin{pmatrix} C_{11} & C_{12} & C_{13} & 0 & 0 & C_{16} \\ C_{12} & C_{11} & C_{13} & 0 & 0 & -C_{16} \\ C_{13} & C_{13} & C_{33} & 0 & 0 & 0 \\ 0 & 0 & 0 & C_{44} & 0 & 0 \\ 0 & 0 & 0 & 0 & C_{44} & 0 \\ C_{16} & -C_{16} & 0 & 0 & 0 & C_{66} \end{pmatrix} \tag{2.45}$$

for $4/m$, 4 or $\overline{4}$ symmetry systems [Ladd03], due to the relationships of $C_{55} = C_{44}$, $C_{33} = C_{11}$. $C_{13} = C_{12} = C_{21} = C_{23} = C_{32}$, $C_{16} = C_{61} \neq 0$ and $C_{26} = C_{62} = -C_{16}$ [Nye85]. (7 independent coefficients.)

Elastic constants of β-MgH$_2$ listed in **Table 2.6** corresponds to the axis system of $a = b \neq c$, and β-MgH$_2$ structure has symmetry of $4_2/mnm$ which belongs to the Patterson symmetry of $4/mmm$ [Hahn96]. Therefore, Eq.(2.44) is applied [Nye85].

In case of 001-oriented tetragonal film with $4_2/mnm$ symmetry, the free energy density can be expressed by

$$f_{el} = \frac{1}{2} \cdot C_{11}(\varepsilon_1^2 + \varepsilon_2^2) + \frac{1}{2} \cdot C_{33}\varepsilon_3^2 + \frac{1}{2} \cdot C_{44}(\varepsilon_4^2 + \varepsilon_5^2) + \frac{1}{2} \cdot C_{66}\varepsilon_6^2 + C_{13}(\varepsilon_1\varepsilon_2 + \varepsilon_2\varepsilon_3 + \varepsilon_3\varepsilon_1)$$

(2.46)

and relationships of Eq.(2.32) and Eq.(2.33) are valid in this case. Therefore, the in-plane stresses can be obtained from the derivatives of elastic energy density, Eq.(2.45) give

$$\frac{\partial f_{el}}{\partial \varepsilon_1} = \sigma_1 = C_{11}\varepsilon_1 - \frac{C_{13}^2}{C_{33}}(\varepsilon_1 + \varepsilon_2) + C_{13}\varepsilon_2 = -\left(C_{11} - 2\frac{C_{13}^2}{C_{33}} + C_{13}\right)\varepsilon_0 \qquad (2.47a)$$

$$\frac{\partial f_{el}}{\partial \varepsilon_2} = \sigma_2 = C_{11}\varepsilon_1 - \frac{C_{13}^2}{C_{33}}(\varepsilon_1 + \varepsilon_2) + C_{13}\varepsilon_1 = -\left(C_{11} - 2\frac{C_{13}^2}{C_{33}} + C_{13}\right)\varepsilon_0 \qquad (2.47b)$$

and as a result, $\sigma_1 = \sigma_2$. Using elastic constants shown in **Table 2.6**, stresses are calculated. In this work, average values of elastic constants by Zarshenas *et al.* [Zars13], Hector *et al.* [Hect07], and Baraille *et al.* [Bara94] are used for β-MgH$_2$.

$$\sigma_1 = \sigma_2 = -\left(C_{11} + C_{12} - 2\frac{C_{13}^2}{C_{33}}\right)\varepsilon_0 = -\left(74.65 + 38.64 - 2\frac{28.66^2}{139.45}\right)\varepsilon_0 = -101.5 \cdot \varepsilon_0$$

(2.48)

is obtained.

However, in most of cases, the most dense 110-oriented tetragonal system is found. In this case, the internal crystal coordinates should be expressed by the external coordinate system. Applying the transformation matrix a_{ij}, the transformation of the strain matrix from ε'_{mn} to ε_{ij} is possible by using the following relationships:

$$\left(\varepsilon_{ij}\right) = {}^T\left(a_{im}\right) \cdot \left(\varepsilon'_{mn}\right) \cdot \left(a_{jn}\right) \qquad (2.49)$$

Coordinate transformation from the xyz-system (internal crystal coordinate system) to the x'y'z'-system (external coordinate system) is brought to realization by -90 degrees of rotation around x-axis and additional -135 degrees of rotation around the reoriented z-axis (**Fig. 2.16**). Therefore, corresponding rotation axis is obtained [Dorn02] as

$$\left(a_{ij}\right) = \begin{pmatrix} -\dfrac{1}{\sqrt{2}} & \dfrac{1}{\sqrt{2}} & 0 \\ 0 & 0 & 1 \\ \dfrac{1}{\sqrt{2}} & \dfrac{1}{\sqrt{2}} & 0 \end{pmatrix} \quad \text{with} \quad {}^T\left(a_{ij}\right) = \begin{pmatrix} -\dfrac{1}{\sqrt{2}} & 0 & \dfrac{1}{\sqrt{2}} \\ \dfrac{1}{\sqrt{2}} & 0 & \dfrac{1}{\sqrt{2}} \\ 0 & 1 & 0 \end{pmatrix} \qquad (2.50)$$

Therefore,

$$\left(\varepsilon_{ij}\right) = \begin{pmatrix} \dfrac{1}{2}(\varepsilon'_{11}+\varepsilon'_{33}) & \dfrac{1}{2}(-\varepsilon'_{11}+\varepsilon'_{33}) & 0 \\ \dfrac{1}{2}(-\varepsilon'_{11}+\varepsilon'_{33}) & \dfrac{1}{2}(\varepsilon'_{11}+\varepsilon'_{33}) & 0 \\ 0 & 0 & \varepsilon'_{22} \end{pmatrix} \qquad (2.51)$$

In the external coordinates $\varepsilon'_{12} = \varepsilon'_{13} = \varepsilon'_{23} = 0$ is taken into account, in Eq.(2.51). In Voigt

notation, $\varepsilon_1 = \dfrac{1}{2}(\varepsilon'_1 + \varepsilon'_3)$, $\varepsilon_2 = \dfrac{1}{2}(\varepsilon'_1 + \varepsilon'_3)$, $\varepsilon_3 = \varepsilon'_2$, $\varepsilon_4 = \dfrac{1}{2}(-\varepsilon'_{11} + \varepsilon'_{33})$, $\varepsilon_5 = 0$

and $\varepsilon_6 = 0$ is derived from Eq.(2.51). Applying those values for Eq.(2.46), the elastic energy

density of the tetragonal system is expressed with external coordinates for (110)-direction as

$$f'_{el} = \frac{1}{4} \cdot C_{11}(\varepsilon_1'^2 + \varepsilon_3'^2 + 2\varepsilon'_1 \varepsilon'_3) + \frac{1}{2} \cdot C_{33}\varepsilon_2'^2 + \frac{1}{8} \cdot C_{44}(\varepsilon_1'^2 + \varepsilon_3'^2 - 2\varepsilon'_1 \varepsilon'_3)$$
$$+ \frac{1}{4} \cdot C_{13}(\varepsilon_1'^2 + \varepsilon_3'^2 + 2\varepsilon'_1 \varepsilon'_3 + 4\varepsilon'_1 \varepsilon'_2 + 4\varepsilon'_2 \varepsilon'_3)$$

$$(2.52)$$

Using the condition of thin films $\sigma'_3 = \dfrac{\partial f'_{el}}{\partial \varepsilon'_3} = 0$ and assuming similar expansion in the
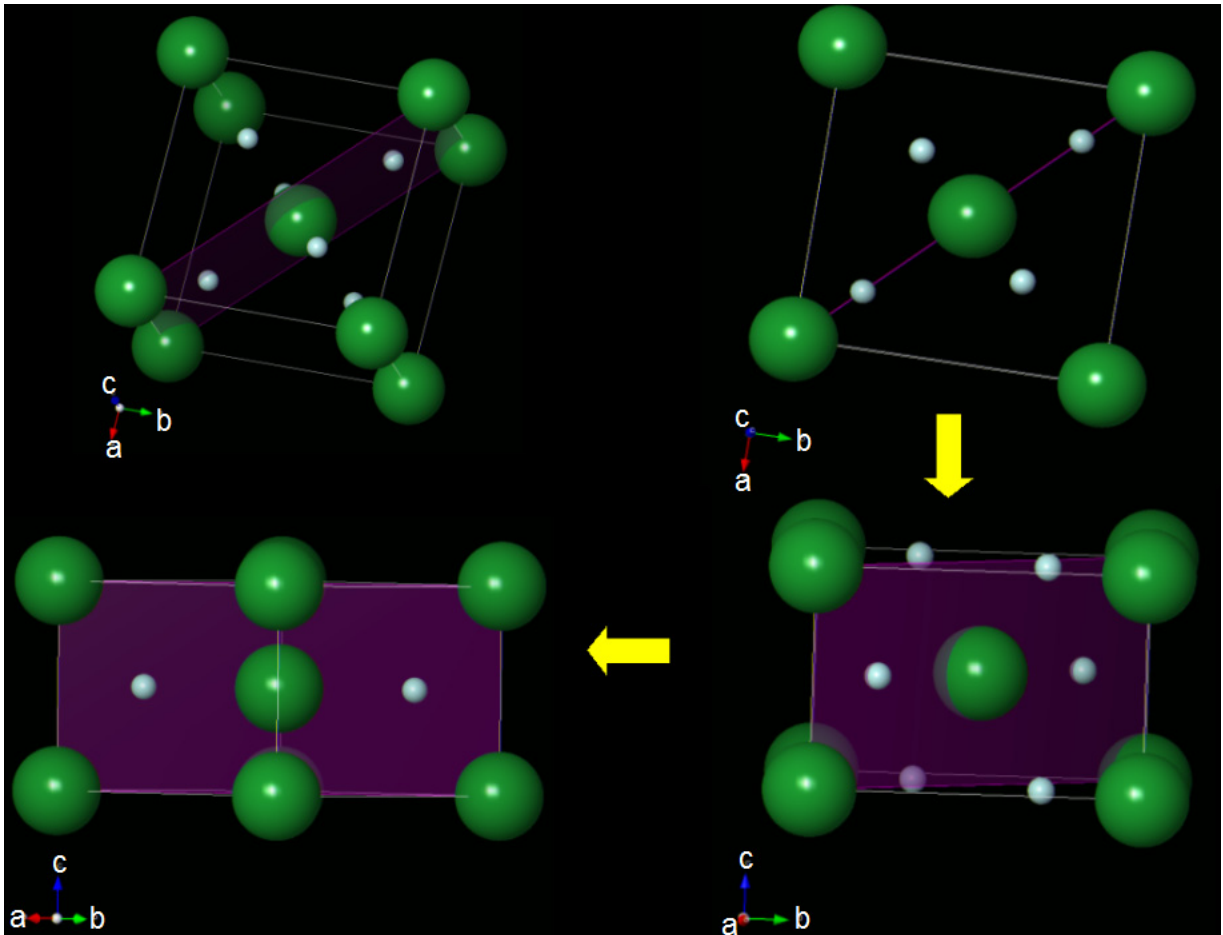
Fig. 2.16 Schematic picture about the rotation of the tetragonal βMgH$_2$ crystal structure: a view from (001)-direction (right side in upper), another view from (100)-direction after -90 degree rotation around the *b*-axis (right side in bottom), and further view from (110)-direction after additional rotation of -135 degrees around the *c*-axis (bottom, left side in bottom). Mg-atoms are drawn with green ball, the (110)-plane in the unit cell is marked with pink, and the edge of the unit cell is brawn with white solid lines. The *x*-, *y*-, and *z*-axis in the sample orientation corresponds to the *a*-, *b*-, and *c*-axis respectively, and especially for current case, the (110)-plane is parallel to the substrate surface after hydrogen loading, as will be shown later in **Chap. 4**.

in-plane directions $\varepsilon'_1 = \varepsilon'_2 = -\varepsilon_0$, the total strain in out-of-plane direction for (110) oriented tetragonal film, ε'^{tot}_3 is expressed as

$$\varepsilon'^{tot}_3 = \varepsilon_0 + \varepsilon'_3 = \left(1 + \frac{2C_{11} + C_{66} + 3C_{13}}{2C_{11} + C_{66} + C_{13}}\right)\varepsilon_0 \qquad (2.53)$$

and

$$\sigma'_1 = \frac{\partial f'_{el}}{\partial \varepsilon'_1} = -\frac{1}{4}\left[2C_{11} + C_{44} + 6C_{13} - (2C_{11} - C_{44} + 2C_{13})\left(\frac{2C_{11} - C_{44} + 6C_{13}}{2C_{11} + C_{44} + 2C_{13}}\right)\right]\varepsilon_0$$

$$(2.54)$$

For the (110)-oriented β-MgH$_2$, this gives

$$\sigma'_1 = -76.35\varepsilon_0 \qquad (2.55)$$

when average constants are used (see **Table 2.6**).

It is noted that $\varepsilon'_1 = \varepsilon'_2 = -\varepsilon_0$ is strictly not realized for the tetragonal (110)-plane. With Eq.(2.55), it is possible to calculate σ' from experimentally obtained ε_0^{tot}, for example in this work by measuring the XRD peak position change. This relationship explains the fact that a change of inner stress of about 0.76 GPa yields 1 % of strain for (110)-oriented β-MgH$_2$ film. This value has error of about 30 %, because of strong dependency on the c_{44} values, which makes the largest differences in Eq.(2.55), compared with other referential elastic coefficients for β-MgH$_2$, listed in **Table 2.6**.

2.2.2 Angular anisotropy of hexagonal Mg

Tromans [Trom11] discussed the angular anisotropy of the Young's Modulus E and the Rigidity (Shear) Modulus G of hexagonal materials, and obtained

$$E_\theta = \left[s_{11}(\sin^4\theta) + s_{33}(\cos^4\theta) + (2s_{13} + s_{44})(\cos^2\theta)(\sin^2\theta)\right]^{-1} \qquad (2.56a)$$

$$G_\theta = \left[s_{44} + (s_{11} - s_{12} - 0.5s_{44})(\sin^2\theta) + 2(s_{11} + s_{33} - 2s_{13} - s_{44})(\cos^2\theta)(\sin^2\theta)\right]^{-1}$$

$$(2.56b)$$

where θ is the angle between the N directions to the xyz planes of the normal x$_3$-axes and transformed x'$_3$-axes (**Fig. 2.17**).

Tromans applied Eq.(2.56a) and Eq.(2.56b), for a series of hexagonal materials. For Mg, the stiffness parameters of Hearmon [Hear79] (shown in **Table 2.6**) are applied, and they obtained a result that E varies from 42.85 GPa (at $\theta = 42.85°$) to 50.76 GPa (at $\theta = 0°$) as shown in **Fig. 2.18**, left side. This demonstrates the anisotropy of the E-modulus for hexagonal Mg. In this study,

the anisotropy is neglected and E_θ= 45 GPa is used, which contains an error of up to 11%. In a similar way, G_θ is available by solving Eq.(2.56b), results shown in **Fig. 2.18 right**. It can be seen in **Fig. 2.18** that the angular anisotropy of Mg is much smaller, than that of Cd and Zn.
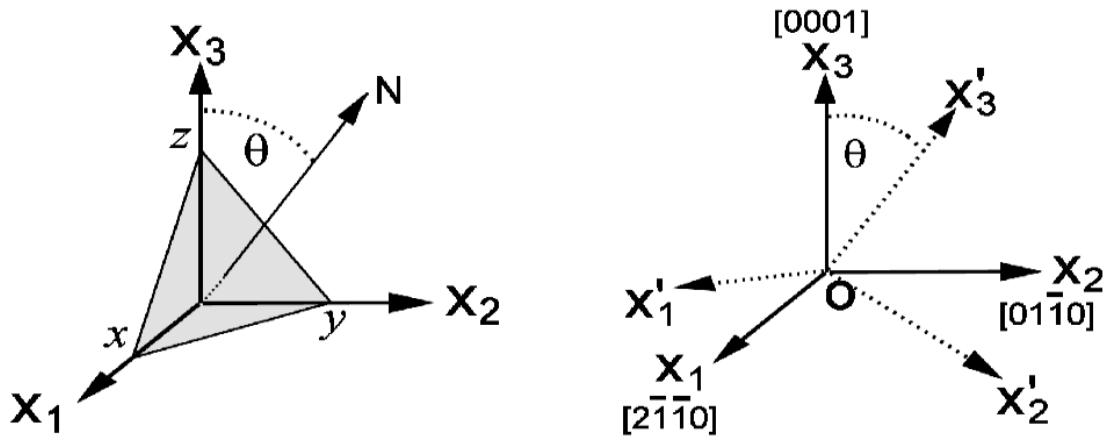

Fig. 2.17 (a) Direction (θ degrees) of the normal N to the plane xyz with respect to X3 (b) Transformed orthogonal axes X'1 ,X'2 and X'3 such that 3 X*i* is rotated by θ to coincide with N direction. Drawing quoted from literature [Trom11].
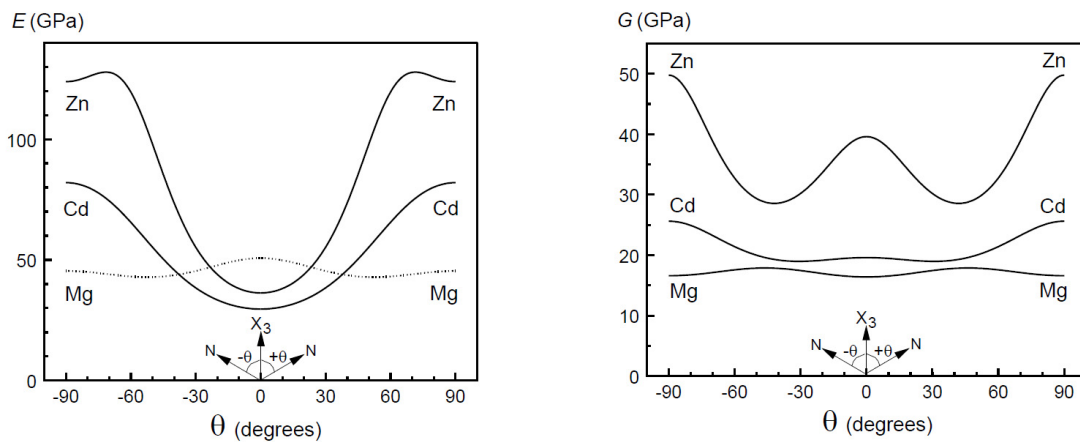
Fig. 2.18 Angular variation of Young modulus E (left) and Shear modulus G (right) for hexagonal Mg, calculated by Tromans [Trom11] from Eq.(2.56a) and Eq.(2.56b) with stiffness parameters reported by Hearmon [Hear79] (**Table 2.6**), compared with results for hexagonal Cd and Zn.

2.3 Thermal stress in thin films

In this work, elevated temperature measurements will be conducted for the Mg films, sputtered on Si substrates. Stress in Mg films is not only affected by absorbed hydrogen, but also by difference of thermal expansion between the film and the substrate. This is introduced in this chapter.

The linear thermal expansion coefficient α is defined for a solid as

$$\alpha = \frac{1}{L}\frac{dL}{dT} \tag{2.57}$$

where L is the length of the solid, and T again is given temperature of the solid with unit in [$^{\circ}$C]. α is often assumed to be constant, and in this case, L_T is expressed as

$$L_T = L_0(1 + T \cdot \alpha) \tag{2.58}$$

where L_0 is the length of standard state, T with unit [$^{\circ}$C], and α is thermal expansion constant and has dimension of K^{-1}. In Eq.(2.58), L_T is proportional to the temperature T, and standard temperature $T = 0$ [$^{\circ}$C] yields $L_T = L_0$. For example, $\alpha = 2.3$ $\mu m \cdot m^{-1} \cdot K^{-1}$ for Si at $T = 301$ K- 473 K [Burk69], or $\alpha = 12$ $\mu m \cdot m^{-1} \cdot K^{-1}$ for Pd at $T = 300$ K- 663 K [Rabi93] are reported as linear thermal expansion coefficients.

However in fact, α is experimentally obtained as temperature dependent coefficient. In this case, the length of the solid at each temperature Eq.(2.57) is expressed as

$$L_T = L_0[1 + T \cdot \alpha(T)] \tag{2.59}$$

where L_0 is the length of standard state, and $\alpha(T)$ is thermal expansion coefficient expressed as a function of temperature.

This expansion is allowed in case of freestanding materials. For thin film samples sputtered on rigid substrates, expansion of in-plane direction is prohibited, as is shown in **Fig. 2.15** in **Chap. 2.2**. This fact explains why thermal stress occurs at different temperature conditions.

Specifically, for films prepared at elevated temperatures (T_2) and then cooled down to room temperature (stress measurement temperature, T_1) will be thermally stressed because of the difference in the thermal expansion coefficients between the thin film and the substrate.

Assuming no plastic deformation of the substrate, the magnitude of the thermal stress in the coating is: [Sue94]

$$\sigma_{therm.} = \frac{E_F}{1 - \upsilon_F} \cdot (\alpha_F - \alpha_S)(T_1 - T_2) \tag{2.60}$$

where E_F and υ_F are Young's modulus and Poisson's ratio of the film (F), respectively, and α_F and α_S are thermal expansion coefficients of film (F) and substrate (S), respectively. For a Mg film on a Si substrate, $\alpha_F > \alpha_C$. Therefore in this case, deposited film exhibits tensile stress ($\sigma_{therm.} > 0$) at low temperature. Likewise, Mg films prepared at room temperature reveals compressive biaxial stress ($\sigma_{therm.} < 0$) at elevated temperature.

In Eq.(2.59), the thermal expansion of the substrate is not implemented. Strict expressions are following equations [Ohring91]:

$$\varepsilon_F = \alpha_F \Delta T + \frac{1-\upsilon_F}{E_F d_F w} \cdot \sigma_{\text{Therm}} \qquad (2.61a)$$

$$\varepsilon_S = \alpha_S \Delta T - \frac{1-\upsilon_S}{E_S d_S w} \cdot \sigma_{\text{Therm}} \qquad (2.61b)$$

where w is the width of sample, E_S is Young's modulus of substrate, d_F and d_S are the thickness of film and substrate, respectively, and ε_F and ε_S are thermal expansion of the film and substrate, respectively. In realistic situations, strain compatibility requires $\varepsilon_F = \varepsilon_S$, therefore from Eq.(2.61a) and Eq.(2.61b), a relationship of

$$\sigma_{\text{Therm}} = \frac{w(\alpha_S - \alpha_F)\Delta T}{\{(1-\upsilon_F)/E_F d_F\} + \{(1-\upsilon_S)/E_S d_S\}} \qquad (2.62)$$

is derived. Applying an approximation of $(1-\upsilon_S)/E_S d_S \gg (1-\upsilon_F)/E_F d_F$ for Eq.(2.62) yields the Eq.(2.60), as is the case for Mg film on Si substrate.

Hidnert and Sweeney [Hidn28] reported $\alpha(T)$ for Mg at temperature range of $T = 273$ K-773 K as follows:

$$\alpha(T) = (24.80 + 0.00961T) \cdot 10^{-6} \qquad (2.63)$$

Fig. 2.19 compares this temperature dependent $\alpha(T)$ with other thermal expansion constants reported by Davis [Davi98], Avedesian and Baker [Aved99], Hodgmann [Hodg20], and Grüneisen [Grün10] for each temperatures and temperature ranges. The temperature dependent value by Hidnert and Sweeney [Hidn28] at highest temperature treated in this work ($T = 180\,^{\circ}\text{C}$) yields $\alpha = 26.3\ \mu\text{m} \cdot \text{m}^{-1} \cdot \text{K}^{-1}$. This value (shown in **Fig. 2.19** with black line) is 5-10 % larger than most values of the working temperatures used in this work, and chosen with assumption of constant value, to compare thermally induced stress with H-induced stress. It, therefore, overestimates the maximal thermal stress in the Mg layer. This value is almost 10 times higher than the value for Si, reported by Burkhardt and Marvel [Burk69].

Using $E_F = 45$ GPa (See **Chap. 2.2**), $\upsilon_F = 0.35$ and $\alpha_F = 26.3\ \mu\text{m} \cdot \text{m}^{-1} \cdot \text{K}^{-1}$ (Mg-film), and $\alpha = 2.3\ \mu\text{m} \cdot \text{m}^{-1} \cdot \text{K}^{-1}$ (Si-substrate) to Eq.(2.60), the contribution of the thermal stress in a Mg film is calculated as

$$\sigma_{\text{therm.}} = \frac{45 \cdot 10^9 [\text{Pa}]}{1 - 0.35} \cdot (26.3 - 2.3) \cdot 10^{-6}(T_1 - T_2) = 1.661 \cdot \Delta T [\text{MPa}] \qquad (2.64)$$

This shows that temperature increase of 100 K for Mg-film on Si-substrate sample results biaxial stress increase of 166 MPa in Mg film. Therefore, Mg-films prepared at elevated temperatures yield 166 MPa biaxial tensile stress upon cooling by $\Delta T = 100$ K. The calculated thermal stress involves 5-10 % of overestimation. However, it is much smaller than the H-induced

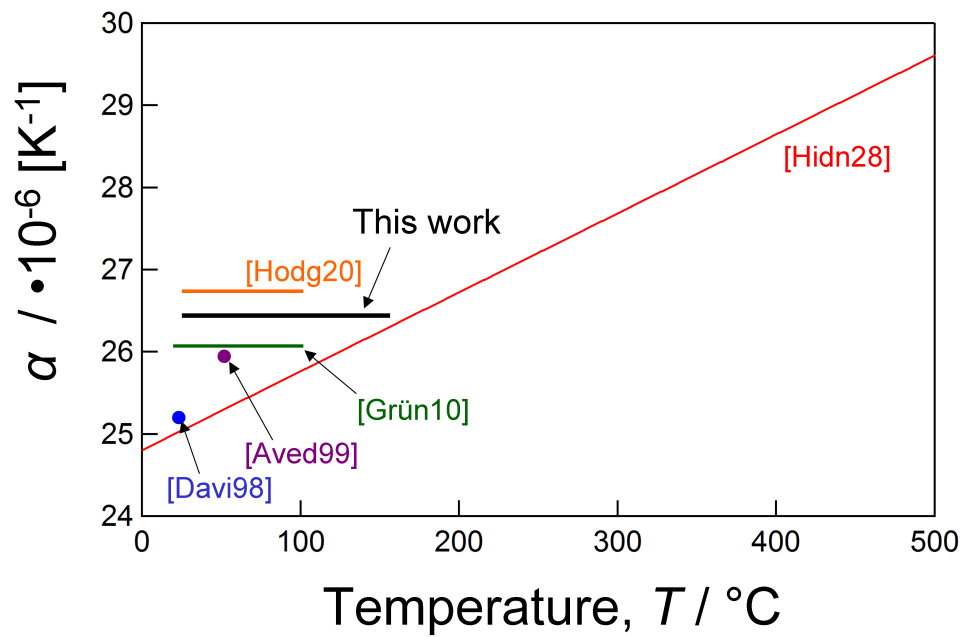stress, which could reach up to GPa order (see **Chap. 2.2.1**).

Fig. 2.19 Thermal expansion coefficient α of pure Mg as a function of temperature t (red line) [Hidn28], compared with thermal expansion constants reported by Davis [Davi98], Avedesian and Baker [Aved99], Hodgmann [Hodg20], and Grüneisen [Grün10]. Chosen value for this work is shown with black line in figure.

3. Experimental

In this chapter, the experimental techniques rquired for this study are presented. First, the available Ar beam sputtering technique is introduced for sample preparation. Next, gas- and electrochemical hydrogen loading techniques are explained. Then, the X-ray technique to evaluate the characteristics of the samples, such as phase transition and crystallography is introduced with *in-situ* hydrogen loading setups. Furthermore, the intrinsic stress evaluation is explained by using X-ray techniques and by using profilometer. A setup for EMF measurement is described, and in the end the electrochemical hydrogen permeation measurements is presented.

3.1 Sample preparation

The investigated film samples were prepared by using an Ar beam sputter deposition in a UHV chamber. A procedure of 0.5-4 hours pre-sputtering is conducted before every sample preparation, to obtain a clean target surface and better background atmosphere. Therefore, the base pressures in the main vacuum chamber are lower than $2 \cdot 10^{-10}$ mbar at room temperature, at the state before sample preparation. Substrate heating up to 453 K was applied to prepare coarse-grained samples, which is half the melting point of bulk-Mg (melting point: 923 K [Aved99]). Substrate heating in the UHV system induces an increase of the base pressure up to 10^{-9} mbar, due to degassing from the inner walls of the chamber. Further deposition, such as Pd capping of the surface, was carried out only after sample cooling at room temperature, to prevent the formation of intermetallic phases or the solution of magnesium atoms into the palladium layer, which could affect hydrogenation properties of the samples.

The target holder in the system is rotational and can mount 4 targets at maximum. This system is designed for thin film preparation. A low ion current density can be applied and therefore the sputtering rate is approximately 10 times smaller (less than 1 nm min^{-1}.) than that of other systems operated with a hot cathode. The outlook of the UHV system is illustrated in **Fig. 3.1**.

The substrate, the thickness of film, and annealing conditions were varied on purposes of the experiments. Typical sputtering parameters are summarized in **Table 3.1a.**

Si(100) substrates with thickness of 0.5 mm and 12.5 μm, supplied by Crystec GmbH, were used. Specified conditions, depending on the purpose of the experiments will be shown, correspondingly. For most samples, a 20 nm thick Pd buffer layer at $T_{dep.} = 300$ K was added to prevent Mg oxidation from the SiO$_x$ existing on the surface of the Si substrate.
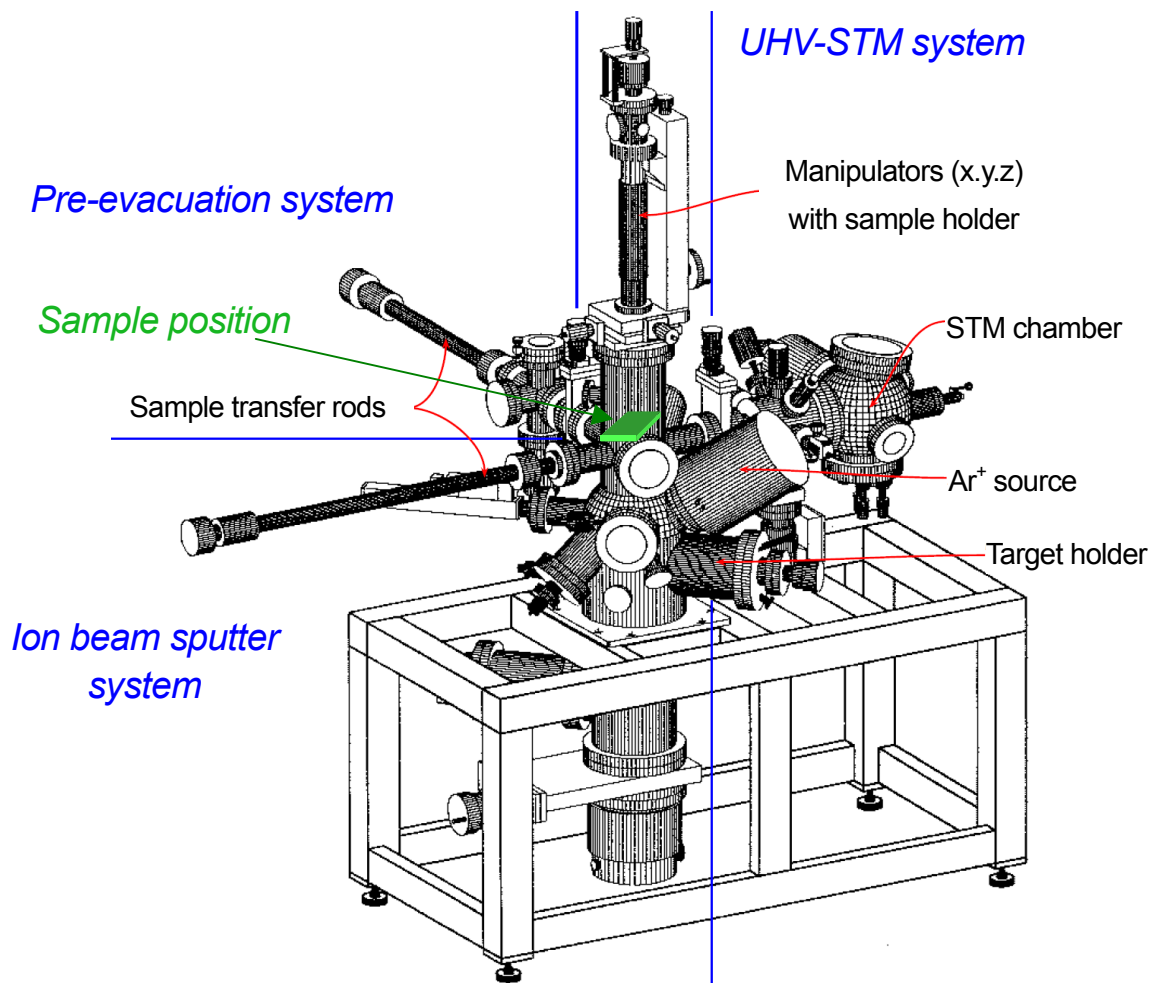
Fig. 3.1 Schematic view of the Ar-ion beam sputtering system used in this study (The picture is taken from the ref. [Nört06].). The system can be mainly divided into 3 parts; pre-evacuation chamber, sputter chamber and STM-AFM chamber as is divided by the blue lines. The manipulator is capable of motion in the directions of x, y and z. The target holder is a cube-shaped Cu block, with a cooling system by the continuous water flow in it. Mg and Pd targets were mounted on this cube side-by-side for the successful preparations.

Those Mg film samples exposed to higher temperature upon annealing or upon measurements, were directly deposited on the Si substrate without this Pd buffer layer. In case of the annealed samples, this allows the solution of Mg atoms into the Pd-layer, or formation of intermetallic compounds of the Mg-Pd system. Also in case of thick Mg films of $d > 1$ μm, the Pd buffer layer is excluded to prevent detachment of the films during hydrogen loading. Furthermore, in all preparation for samples exposed to higher temperature upon annealing or upon measurements, a 10 minutes Ar-ion beam sputtering treatment has been done on the Si substrates, in order to remove the surface oxide and prevent oxidation of Mg. Detailed annealing conditions will be

described later in this chapter.

Table 3.1a Applied conditions for sputter deposition.

Sputtering gas	Ar (purity: 99.9999%)	
Sputtering gas pressure [mbar]	2.0×10^{-5} - 2.4×10^{-4}	
Substrate-target distance [cm]	5 - 15	
Target purity (Mg, Pd) [%]	>99.9	
Energy of Ar^+ [eV]	880	
RF power [W]	76	
	Si (100) 10 mm x 10 mm x 0.5 mm 10 mm x 10 mm x 80 µm	
	Pd-foil (annealed) For permeation measurements 10 mm x 10 mm x 250µm 10 mm x 10 mm x 12.5 µm For in-situ XRD measurements 10 mm x 10 mm x 12.5 µm	
	Pd-plate (annealed) For in-situ XRD measurements 10 mm x 10 mm x 12.5 µm	
Deposition rate [nm/min.]	Pd	0.91 ~ 1.02
	Mg	2.25 ~ 1.35
Substrate temperature [K]	300 - 453	

In this work, Mg film samples with thickness range from 20 nm up to 2800 nm were prepared, and all the film samples were prepared at $T_{dep.}$ = 300 K. Samples were prepared on Si (100) substrates and on Pd-substrates. The Pd-substrates were previously annealed at T = 1073 K for 12 hours, and cooled down in vacuum condition. Deposition rates of Mg and Pd are shown in **Table 3.1a**.

After Mg deposition, an annealing treatment by joule heaters from behind of the substrates has been also performed for samples with Si-substrate, in the UHV system. All the annealed Mg films were deposited on the Si (100) substrate with a thickness of 0.5 mm, at room temperature. Annealing temperatures of T_{sample} = 453 K and 503 K have been chosen. The heating rate of the target was 20 K·min^{-1}. The start of the annealing treatment is defined in this work, when the sample temperature reached the targeted temperature, and then the annealing time t_{anneal} is started to count up. The down rate of the targeting temperature condition was -20 K·min^{-1} in the sample temperature range of T_{Sample} > 353 K. Sample was naturally cooled down without controlling

temperatures. After cooling down of the sample to $T_{Sample} = 300$ K, the 20 nm thick Pd capping layer was deposited on the annealed Mg film.

During the sample annealing, the maximum total pressures in the chamber were measured to be $p_{total} = 3 \cdot 10^{-9}$ mbar for $T_{sample} = 453$ K and $p_{total} = 7 \cdot 10^{-9}$ mbar for $T_{sample} = 503$ K, respectively. This increase of the chamber pressure is attributed to the degassing from the chamber wall inside. The maximum partial pressures of oxygen and water were also monitored by QMS to be $P_{O2} < 10^{-13}$ mbar and $P_{H2O} < 4 \cdot 10^{-10}$ mbar.

Pd plates and foils were also used to investigate hydrogen diffusivity through Mg layers, since Pd is chemically stable against electrolytes and is able to permeate hydrogen. It allows hydrogen loading from the backside, which is not possible in the case of Si substrates. Furthermore, Pd is also one of the most studied materials as a hydrogen permeation membrane, and suitable as substrate for this purpose.

Pd plate- and foil substrates with thickness of 12.5 μm and 250 μm were applied for the permeation measurements. Pd foils of the purity 99.99 at.% were supplied by Goodfellow GmbH, and the thicknesses of some plates were derived by means of cold rolling. All Pd substrates were annealed at 1173 K for 8 h in a reduced Ar atmosphere, and cleaned in the chamber by Ar-beam for 3 minutes, before deposition of Mg at $T = 293$ K.
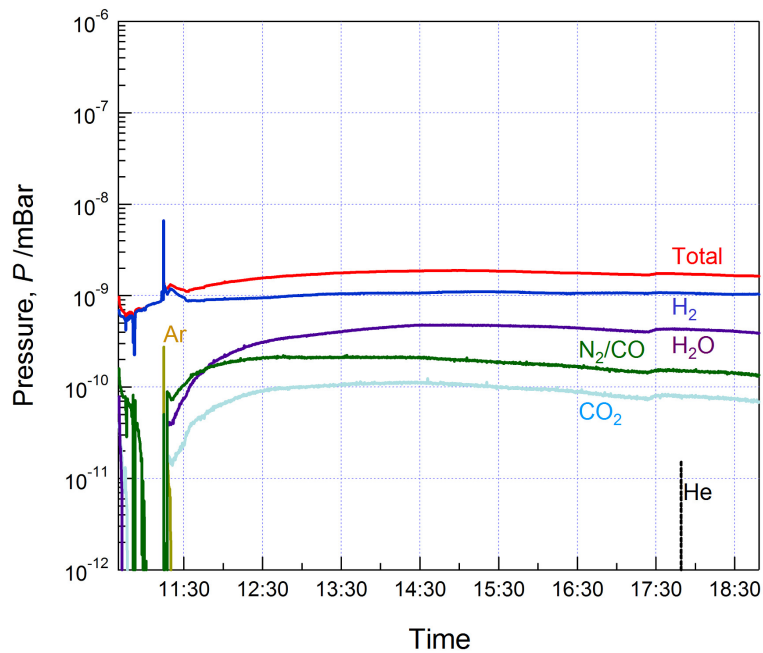
Fig. 3.2 Time change of the total pressure (red) and partial pressures of Ar, CO_2, H_2, H_2O, C_xH_y, N_2/CO, O_2 and He in the chamber, during sample annealing at $T = 503$ K, measured by QMS directly before sample heating. Pressure increase in the beginning is attributed to the degassing in the chamber.

Fig. 3.2 shows an example of pressure development for $T_{sample} = 503$ K in a wide time range. Monitoring of the pressure by QMS is conducted for all annealed samples. The atmosphere in the evacuated sputter chamber before sample deposition showed $P_{O2} < 10^{-14}$ mbar and $P_{H2O} < 10^{-14}$

mbar at room temperature, which are below the minimum detection limit.

Samples were measured promptly after preparation. Edges of the samples for the electrochemical loading measurements were covered by a polymer material, as soon the samples were prepared. A detailed description about preparation for electrochemical loading measurements is found in **Chap. 3.2.1**. All of the samples prepared were followed by capping of Pd over-layer in order to prevent oxidation and to facilitate subsequent hydrogen absorption [Jain88].

Thicknesses of Mg samples prepared in this work are listed in **Table 3.1b** for gas loading measurements, and in **Table 3.1c** for electrochemical loading measurements. All Mg films were deposited on 0.5 mm thick Si(100) substrates, or annealed Pd substrates with 12.5 μm or 250 μm thickness. Details of the loading procedures and the measurement methods will be described later in this section.

Table 3.1b Mg layer thicknesses of samples prepared for hydrogen gas loading measurements in this work (unit in [nm]), sorted by hydrogen loading procedures. Si(100) substrates with thickness of 0.5 mm were used.

	Mg thickness	Annotations
Stepwise loading	60, 200, 2800	In-situ XRD measurement
	180 (annealed at 503 K for 30 min.)	In-situ XRD measurement
	1450 (annealed at 453 K for 30 min.)	Measurements at elevated temperatures
const. pressure	500, 2800	In-situ XRD measurement
	2800 (annealed at 453 K for 30 min.)	In-situ XRD measurement

Table 3.1c Mg layer thicknesses of samples prepared for electrochemical hydrogen loading measurements in this work (unit in [nm]). Si(100) substrates with thickness of 0.5 mm and the annealed Pd substrates with 12.5 μm or 250 μm thicknesses were used.

		Mg thickness	Annotations
Si-Substrate		80,165, 200, 250, 270, 500	Effect of loading current
		20, 200, 500, 750, 2000.	Ex-situ XRD measurement
		60,188,1400	In-situ XRD measurement
		1000	Intrinsic stress evaluation
Pd-Substrate	**12.5 μm**	250	In-situ XRD measurement
		2100	Permeation measurements
	250 μm	80, 200, 2088	Permeation measurements

3.2 Electrochemical- and gas- hydrogen loading

Hydrogen loading has been conducted by electrochemical loading and, alternatively, with H_2 gas phase loading. This section introduces in hydrogen loading techniques and the setups which are used in this work. At first, electromotorical force is introduced, with the process to optimize successful electrochemical loading conditions for Mg-films. Second part of this section explains the procedure for hydrogen gas loading used in this work.

3.2.1 Electrochemical hydrogen loading

The hydrogen loading treatment for the films deposited on Si (100) and annealed Pd-foil substrates were carried out electrochemically, by using a homemade current pulse source in the Institut für Materialphysik, Göttingen University. The simplest loading setup consists of this pulse-current source, an impedance converter, a time circuit, a reference electrode (Ag/AgCl$_{sat.}$), a counter electrode (Pt or Pd) and the electrolyte. **Fig. 3.3** shows schematic view of step-by-step electrochemical hydrogen loading setups applied in this work.
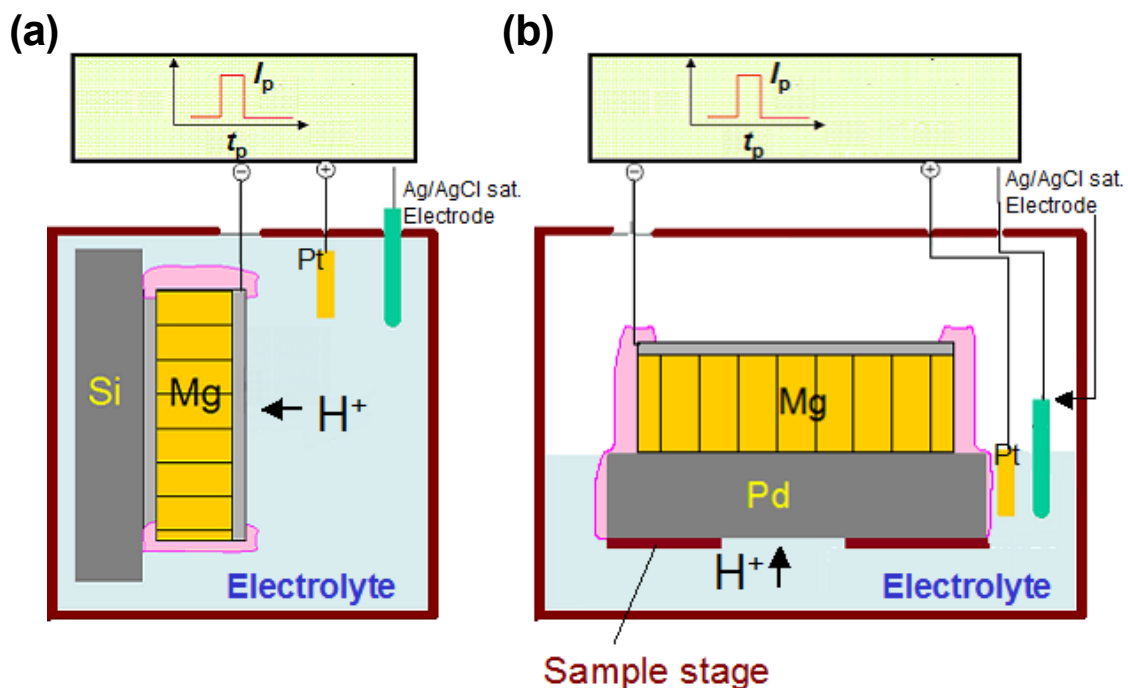
Fig. 3.3 Schematic pictures of step-by-step electrochemical hydrogen loading setups, for Mg-film sputtered on (a) Si- substrate, and (b) Pd substrate. Hydrogen was loaded from the surface for Si-substrate samples, and from back side for Pd-substrate samples. Pd substrate was fastened on a polymer sample stage, and has partially contact with electrolyte, in the center of area.

It is widely known that magnesium reacts with water (including salt solutions) and forms oxyhydrides or oxides [ASM87,Czer11,Song11]. Magnesium is known to be rapidly attacked by all mineral acids except hydrofluoric acid (HF) and H_2CrO_4 [ASM87], and also forms soluble complexes, such as tartrate and metaphosphate, or insoluble salts, such as oxalate, carbonate, phosphate, and fluoride [Ghal10]. In this viewpoint, most of acid solution electrolytes including H_3PO_4 are not suitable, or an additional suitable coating material is needed. Indeed, this corrosion reaction starting from the edge of the samples was observed by a light microscope, when the sample is set in the H_3PO_4 -based electrolyte, despite of the surface capping with the Pd-layer. As a result, the sample will be damaged and solved almost completely into the electrolyte in this case, as shown later in this section. Furthermore, those corrosion reactions change the EMF potentials, which depend on each reaction [Ghal10]. To prevent this corrosion process, several coating materials for the sample edge or additional parts coating were tried in advance, to find out good combination of electrolyte and polymer material which is stable against the electrolyte.

Some aqueous electrolytes of different chemical materials with different conditions of concentration or the mixing ratio were prepared for electrochemical hydrogen loading measurement for Mg-films, applying different loading current conditions. Some of results are shown in **Table 3.2**.

KOH aqueous solution (KOH aq.) is one of the common electrolytes for electrochemical hydrogen loading of Mg-based material, for example used in refs [Rous10,Verm06^{+},Qu10]. In strong alkali conditions (pH > 11.5), a passive magnesium surface hydroxide layer is predicted to build up at the surface, which dominates the electrochemical behavior of Mg [Pour73,Hawk99]. However in this work, application of KOH aq. solution with concentration of y M ($y = 1, 2, 3$ and 6) for Mg-film loading with various loading current densities i A/cm^2 ($10^{-7} < i < 10^{-2}$) was not successful, mainly due to damage of the cable connection and the chemical instability of the polymer materials.

Another candidate of electrolyte shown in **Table 3.2** is, a 1: 2 (vol.) mixture of H_3PO_4 (85%) and Glycerin (85%) [Kirch14]. Applying this electrolyte for measurements without polymer coating mostly resulted in erosion from the edge, and in its final state, to dissolution of the sample. This erosion procedure from sample edge is visually confirmable after 1-2 hour being in touch with the electrolyte. Also, pitting corrosion-like damage can be visible, in case of an imperfect Pd surface capping layer.

Fig. 3.4 exemplarily shows the development of the EMF potential during a step-by-step electrochemical hydrogen loading measurement on a Mg-film sputtered on a Si (100) substrate, without polymer coating. A loading current condition of $i = 10^{-4}$ A/cm^2 was applied for this sample. The obtained EMF potential was not stable in the early stage, and stayed almost constant near 0.17 V after 2 hours. Corrosion-like damages were observed by means of the optical microscope, for the film sample after the loading measurement. **Fig. 3.5** shows examples of a damaged film in comparision to a buckled film. Such damage was typically detected for when the Pd-capping layer

thickness was smaller than 17 nm. For samples in contact with acidic electrolyte (H_3PO_4 + Glycerin) and without polymer coating, such damage was also detected near the edge of the samples even with thicker (35 nm) Pd-coated samples. Results of different measurement setups are also shown in **Chap.3.2.1**.
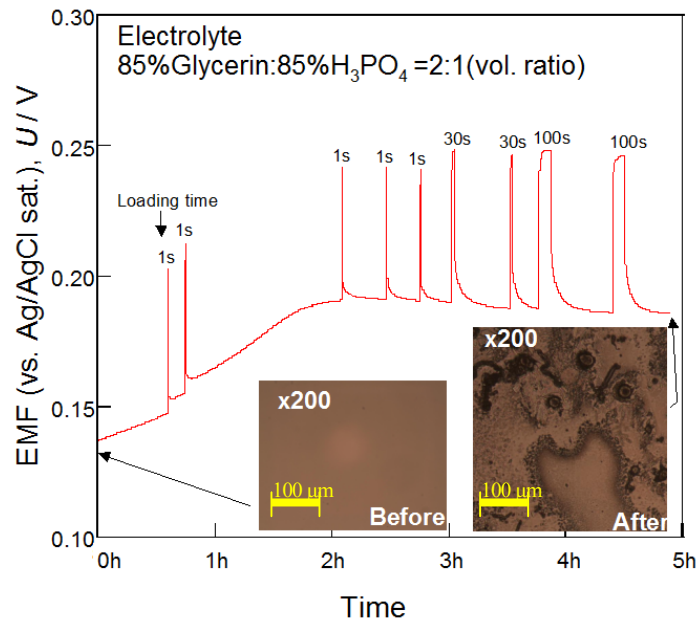

Fig. 3.4 Time change of the EMF potential for 20nm Pd capped 160nm Mg film on Si (100) substrate, during step-by-step electrochemical hydrogen loading with current density of $i = 10^{-4}$ A/cm^2 at room temperature, using volume mixture 2:1 of 85% Glycerin and 85% H_3PO_4 solution as electrolyte, without polymer coating. Inserted pictures are optical microscope observation for the sample surface before and after loading.
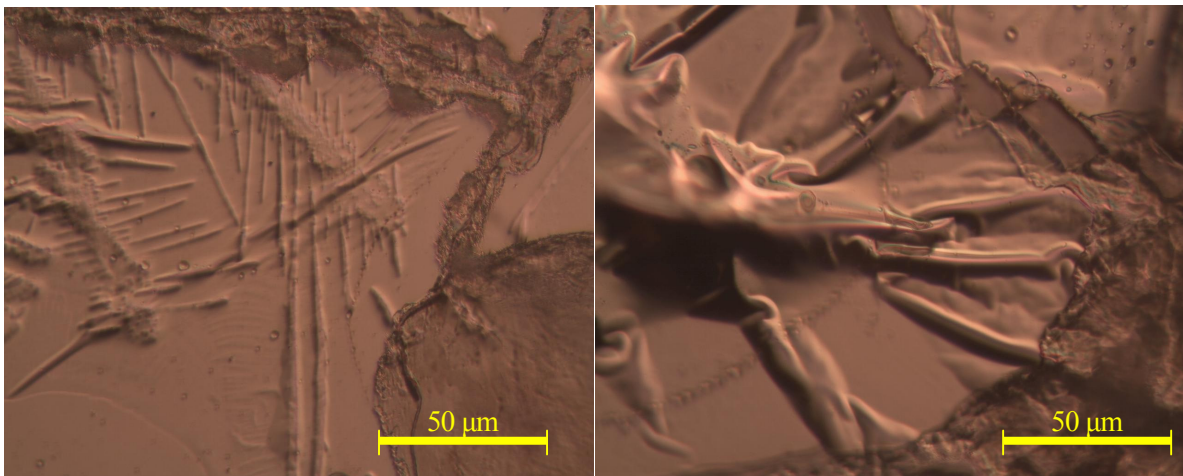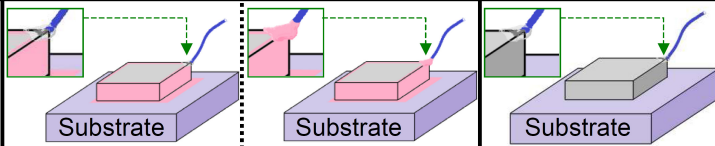
Fig. 3.5 Damaged film (left), and buckled film (right, 1400 nm Mg film) after electrochemical hydrogen loading.

Table 3.2 Results of different measurement setups of Mg-films for electrochemical hydrogen loading measurements sorted by electrolyte and coating ways, presented with schematic drawings of different sample preparations. Loading measurements with each condition are tried at least 6 times, and the results are sorted by the probability of successful loading, expressed by three expressions; ○ (better than 80%), △ (20%-80%), and × (lower than 20%).

		Polymer coating								
		Yes						No		
		Only Edge			Edge+Connection					
Electrolyte	KOH	A	B	C	A	B	C	A	B	C
		×	○	×	×	○	△	×	△	×
	H_3PO_4+Glycerin	A	B	C	A	B	C	A	B	C
		○	×	△	○	△	△	○	×	△

Annotations:
A: Stability of Polymer material against electrolyte
B: Sample stability (No corrosion or solution into electrolyte / Stable equilibrium EMF)
C: Durability of sample and connections for long measurement
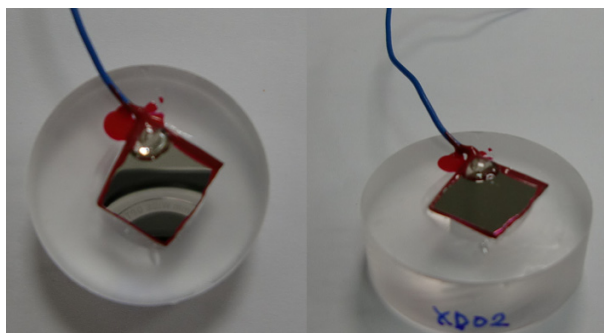
Fig. 3.6 Pictures of a polymer-coated sample at the edges and cable connection, prepared on a stage for an *in-situ* electrochemical loading, views from top (left) and from side (right), respectively.

A stable EMF potential value was available, when all the edges and cable connection were properly covered with polymer coating material.

With respect to the polymer material, different coating materials diluted with Acetone were tried, however mixing with acetone yielded waker polymer coatings. Only the original state of the material was applied for all electrochemical measurement in this work.

Additionally, any treatment with alcohol was prevented, because Mg can react with alcohol, such as forming of ethoxides with ethanol, under catalysed conditions [Turo02]

$$2CH_3CH_2OH + Mg \rightarrow (CH_3CH_2O)_2Mg + H_2 \qquad (3.1)$$
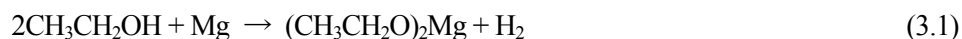
Main components of the coating polymer material are Acrylate polymers (Poly-(ethyl methacrylate), and Polyarylate−PAR) and nitrocellulose. One of the reasons why the

electrochemical loading with alkaline electrolyte was unsuccessful can be explained by the instability of the containing polymers against alkaline KOH solution [Harp00], such as Polyarylate−PAR. Actually, the solution of the polymer coating material was observed within 3 hours in the contact with 3M KOH electrolyte. Furthermore, hydrolysis reaction of nitrocellulose under alkaline condition is known [Chris01].

As a result, a combination of electrolyte (H$_3$PO$_4$ + Glycerin) with polymer coating of sample edges and cable connection was best choice at this stage. However, this was not enough durable for a long loading measurement.

Another way to overcome this problem, the thickness of the surface Pd-layer avoiding damage in long-time measurements was optimized to be 20 nm. This value is larger than what is conventionally used in the group. It was found that samples are unstable in case of Pd-capping thickness of less than 17 nm.

The polymer coating has been done directly after the sample was carried out from UHV-chamber. With this improvement, successful electrochemical hydrogen loading was done with a proper electrolyte, a stable coating material, and suitable Pd-capping layer thickness. The polymer material was checked to be stable against H$_3$PO$_4$ electrolyte at least for 5 days at room temperature.

In this work, all further results of electrochemical loading measurements are conducted in 20 nm Pd-capped samples with 1: 2 (vol.) mixture of H$_3$PO$_4$ (85%) and Glycerin (85%) [Kirch14], capped with polymer at the edges and at the cable connections, covered in a in a fresh state. An example of polymer-covered sample on the sample stage is shown in **Fig. 3.6**.

The hydrogen content in the samples during the step-by-step loading can be calculated by Faraday's law [Kirch88]. At each loading step, hydrogen atom produced at the sample surface diffuses in and the process is observed as a change of electromotorical force (EMF) until it equilibrates. The EMF value at equilibrium as a measure of the chemical potential of hydrogen is directly translated into hydrogen partial pressure p_{H_2} by the Nernst equation [Atkins82,ASM87].

$$p_{\mathrm{H}_2} = p_0 \cdot \exp\left(\frac{(U - U_0)nF}{RT}\right) \tag{3.2a}$$

Here, p_0 is the standard pressure of hydrogen, U is the measured EMF value, U_0 is the standard potential of reference electrode ($U_0 \approx 0.195$ V for the Ag/AgCl$_{sat}$ saturated electrode with 3M KCl solution at 298 K [Rieg93,Ghal10], calibrated to be 0.197 V for this work), n is the number of electrons related to the reaction ($n = 2$ for hydrogen), $F = 96500\,[\mathrm{C/mol}]$ is the Faraday constant, R is the gas constant and T is absolute temperature. Another expression of Eq.(3.2a) yields

$$\Delta G = RT \ln\left(\frac{p_{\mathrm{H}_2}}{p_0}\right) = (U - U_0)nF \tag{3.2b}$$

where the ΔG is the free energy change of hydrogen compared to the standard state. Eq.(3.2b)

provides a direct relationship between p_{H_2} and U in the dimension of energy, which is important to understand driving force of hydrogen loading process, discussed later in **Chap. 6.2**. Detailed process of electrochemical hydrogen absorption is found *e.g.* in [Dorn07].

A pressure-composition isotherm (*p-c-T*) can be drawn from one measurement. **Fig. 3.7** shows a schematic picture of hydrogen loading pulses and isotherm potential curve.

In a dilute hydrogen concentration range, Sieverts' equation is expected. Using Eq.(2.7) and Eq.(2.8) with Eq.(3.2b), a relationship of

$$\frac{\partial (U - U_0)}{\partial \ln c_H} = \frac{RT}{nF} (= const.)$$ (3.2c)

Eq.(3.2c) explains the fact that the EMF change is proportional to the logarithmic change of c_H in an ideal metal. In actual situation, typically external stress or existence of defects in lattice could cause a deviation from the potential.

With respect to the total amount of hydrogen loaded into the specimen $c_{H/(Pd+Mg)}$, calculation by Faraday's law [Kirch88] was done.

$$c = c_0 + \sum \Delta c = c_0 + \frac{\sum \Delta n_H^+}{n_M} = c_0 + \left(\frac{1}{n_M} \right) \cdot \frac{\sum (I \cdot \Delta t)}{F}$$ (3.3)

where c_0 is the initial hydrogen concentration in atomic ratio, n_M is the total molar amount of metal, Δn_H^+ is the molar amount of loaded hydrogen, I is the loading current, Δt is the loading time, and Δc is the calculated change of the hydrogen concentration in atomic ratio per loading step. The related hydrogen gas pressure is calculated, for comparison to gas-phase measurements by Eq.(3.2a).

On purposes of *in-situ* measurement in this study, the basic H loading set up was combined with an induction gauge for film stress measurements, and with XRD at HASYLAB, respectively. Some special hydrogen loading cells used for these measurements are shown in the next section.
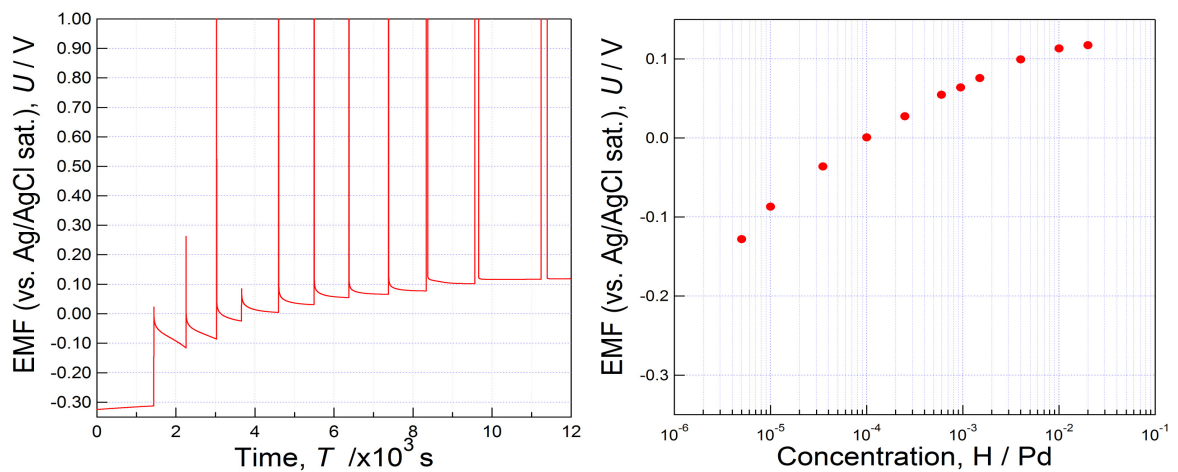

Fig. 3.7 A schematic picture showing H loading pulses (left) and an *isotherm potential* curve derived from a series of the equilibrium values of EMF (right) via Eq.(3.2a).

3.2.2 Hydrogen gas phase loading setup for *in-situ* XRD measurement

The *in-situ* hydrogen gas loading XRD measurements for the films deposited on Si (100) substrates were performed by using a homemade UHV setup, at beamlines HASYLAB B2 and PETRA P08 in DESY for room temperature measurements, and at ESRF BM20 for high temperature measurements.

Fig. 3.8 shows a schematic diagram of a hydrogen gas loading system applied in this work, for the measurements at room temperature and at elevated temperature. The simplest loading setup consists of a turbomolecular pump, a pre pump, the hydrogen gas source (purity > 99.99%), a pre-loading chamber and the sample cell. Hydrogen gas in each chamber was remotely controlled by valves. The samples were measured in a vacuum cell equipped with a kapton- or Al-window that is transparent for synchrotron X-ray but can shield inner gas from outside. The base pressure in this system was 10^{-2} Pa. Hydrogen gas pressure of the sample cell was measured by capacitance manometer (BARATRON, range of 10^{1}-10^{5} Pa). Details of each measurement condition will be described in **Chap. 3.2.3.2**.
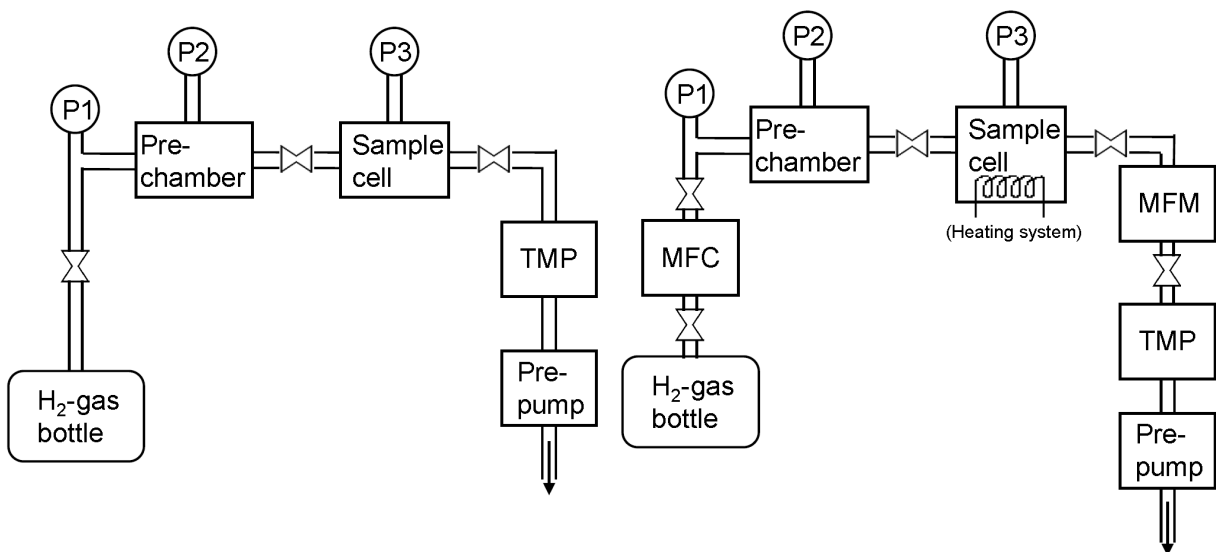
Fig. 3.8 A schematic diagram of a hydrogen gas loading system applied in this work, for the measurements at room temperature (left) and for the measurements at elevated temperature (right). Sample was installed in the sample cell for the in-situ XRD measurements, and hydrogen was loaded from the gas bottle through pre-chamber. Pressures at each state were monitored by pressure gauges at position P1, and by capacitance manometers (BARATRON) at positions P2 and P3. Turbomolecular pump (TMP) was used to evacuate the whole system, before the hydrogen introduction. Continuous flowing hydrogen gas was used for measurements at elevated temperature, controlled and measured by the mass flow controller (MFC) and mass flow meter (MFM) respectively. Sample heating and each valve were remotely controlled to stabilize temperature and pressure conditions.

3.2.3 *In-situ* XRD measurement

In-situ XRD measurement, during electrochemical- and gaseous hydrogen loading, is one of the key techniques of this study. *In-situ* XRD measurements were performed at the B2 beam line of HASYLAB (DESY in Hamburg), the P08 beam line of Petra (DESY in Hamburg), and the BM20 beam line (ROBL, ESRF in Grenoble). These *in-situ* XRD measurements have been conducted using a specially designed electrochemical loading cell and the gasloading setups developed by "Hydrogen in Metals group" in University Göttingen (described in **Chap. 3.2**), except for the setups for the high-temperature gas loading measurement at BM20 in ESRF.

3.2.3.1 *In-situ* electrochemical hydrogen loading measurement

Fig. 3.9 shows the electrochemical loading cell for the *in-situ* synchrotron XRD measurements at HASYLAB, Petra and ESRF. The initial cell was designed by N.M. Jisrawi from the University of Western Ontario and further optimization has been done by M. Dornheim [Dorn02]. The portion of the electrolyte in the loading cell is controllable by manipulating the injector. During the XRD scan, the electrolyte is removed by this injector and for the next loading step it again covers the sample surface.

The cell was purged by the inert gas (N_2 or Ar), which is important to prevent H-loss of the sample. During the XRD scan, the sample surface is exposed to the N_2- or Ar atmosphere, however no reaction with oxygen at the surface is expected.
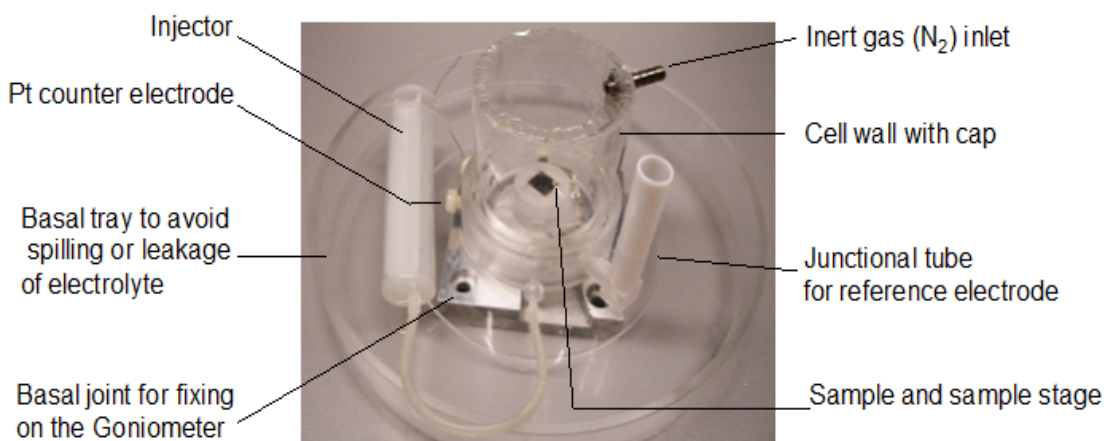

Fig. 3.9 The electrochemical hydrogen loading cell applied for the *in-situ* XRD measurements at DESY and ESRF. Original design was made by N.M. Jisrawi.

In-situ electrochemical XRD measurements with Si-substrate samples have been done at the beamline ESRF BM20 and HASYLAB B2, and for Pd-substrate samples at beamline PETRA P08. Conditions of wavelength are listed in **Table 3.4** in **Chap. 3.3**.

Fig. 3.10 shows an example of a setup at HASYLAB B2 at DESY. The sample in this cell is

mounted on an Euler cradle so that the rotation and tilt of the sample can be adjusted. In the *in-situ* electrochemical loading measurement, a known amount of hydrogen is loaded in the sample in each step-by-step loading cycle, and at each step the diffractogram is recorded. The electrochemical loading cell shown in **Fig. 3.10** is the same loading cell shown in **Fig. 3.9**.

For *in-situ* XRD measurements during electrochemical hydrogen loading for Pd substrate samples, two different sample stages (Type A and Type B) installed in the loading cell were applied. The applied sample stages were cut and polished, as shown in **Fig. 3.11**. The shape of
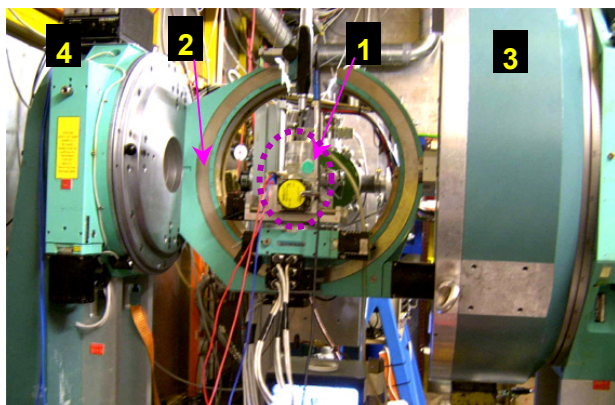
Fig. 3.10 The experimental station at

HASYLAB B2.

1: Electrochemical loading cell,

2: Euler cradle,

3: Goniometer for detector,

4: Goniometer for sample

(a) **(b)** **(c)**
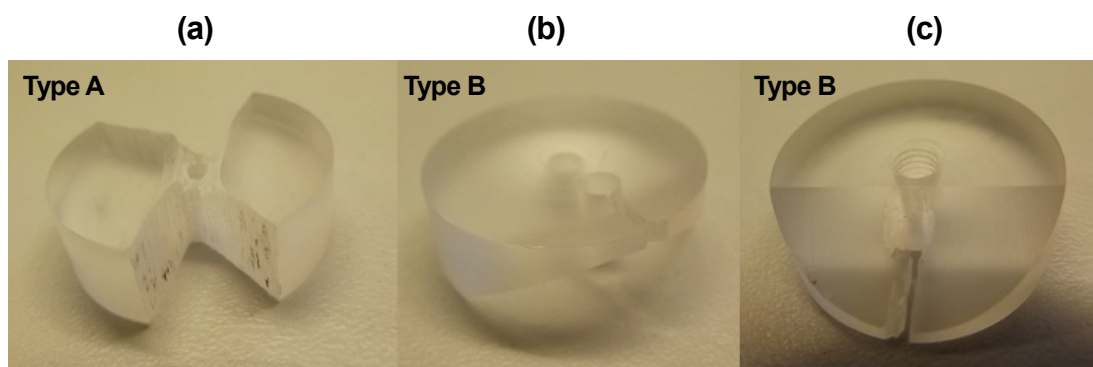
Fig. 3.11 Different types of applied sample stage for in-situ electrochemical hydrogen loading measurements; (a) Stage Type A, a view from top, (b) and (c) Type B, views from top and bottom, respectively.
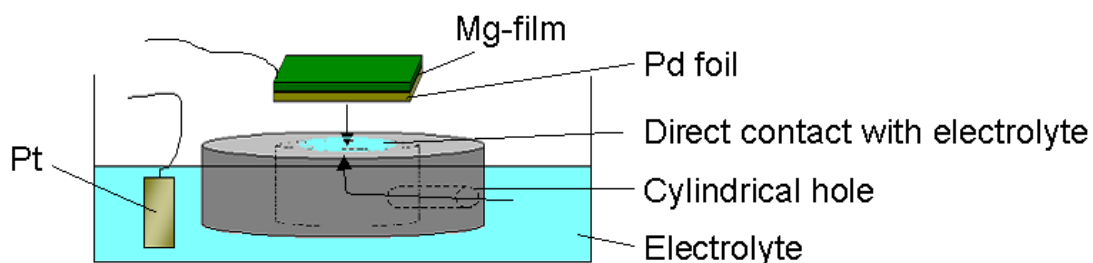

Fig. 3.12 Explanation of sample stage to realize direct contact of sample backside with the electrolyte. (Type B), for the *in-situ* electrochemical loading measurements at DESY and ESRF. Whole setup is schematically shown in **Fig. 3.3**.

each stage was chosen in advance, so that bubbles are not hanging and contacting sample during hydrogen loading. This avoids artefacts during the EMF measurement.

Hydrogen was loaded from backside (**Fig. 3.12**). Measurement with sample stage Type A yielded bending of sample due to hydrogen absorption (**Fig. 3.13 (d),(e)**). This bending yields disappearance of Mg Bragg peak during hydrogen loading. Therefore, Type B is applied for the measurement.
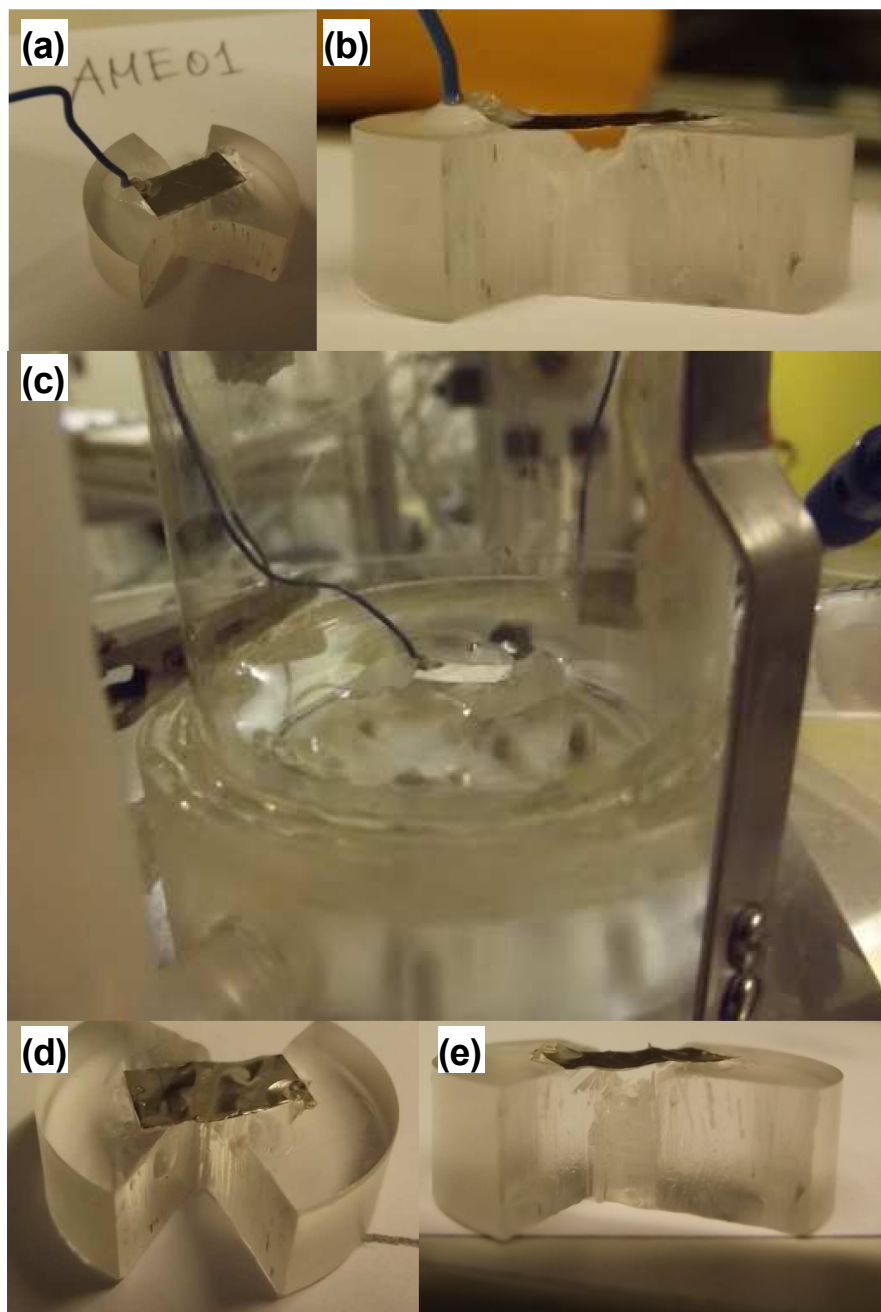

Fig. 3.13 Pictures of sample stage Type A (shown in **Fig. 3.11 (a)**) for electrochemical measurement of Pd-foil sample: Views of the prepared sample on the stage **(a)** from top and **(b)** from side, after polymer coating at side edges; (c) Sample fastened in the electrochemical loading cell setup, during electrochemical hydrogen loading at Beamline P08 PETRA; Views of the bended sample **(d)** from top and **(e)** from side, after loading up to $c_H = 2$ H/Mg. The same sample is shown in these pictures.

Electrochemical loading conditions for Si-substrate samples are the same as described in **Chap. 3.2.1**. Same loading conditions and coating treatments are applied for Pd-substrate samples, but the loading has been done from the backside, avoiding the uncontrollable decrease of the XRD peak intensity due to the remaining electrolyte on the surface after the loading process.

3.2.3.2 *In-situ* gas loading measurement

Fig. 3.14 shows a picture of the sample fastened on a holder, which is specially aligned for *in-situ* gasloading XRD measurements at HASYLAB B2, PETRA P08 and ESRF BM20 (shown in **Chap. 3.3.2**). The edges of the sample are connected to cables for resistivity measurements with Silver (Ag) conductive paste. This sample holder is directly connected in an UHV-supported vacuum chamber by inserting into a metal tube with X-ray windows. An example of a setup for gas loading at Petra P08 is also shown in **Fig. 3.14 right**. These setup shown in **Fig. 3.14** are for the measurements at room temperature.
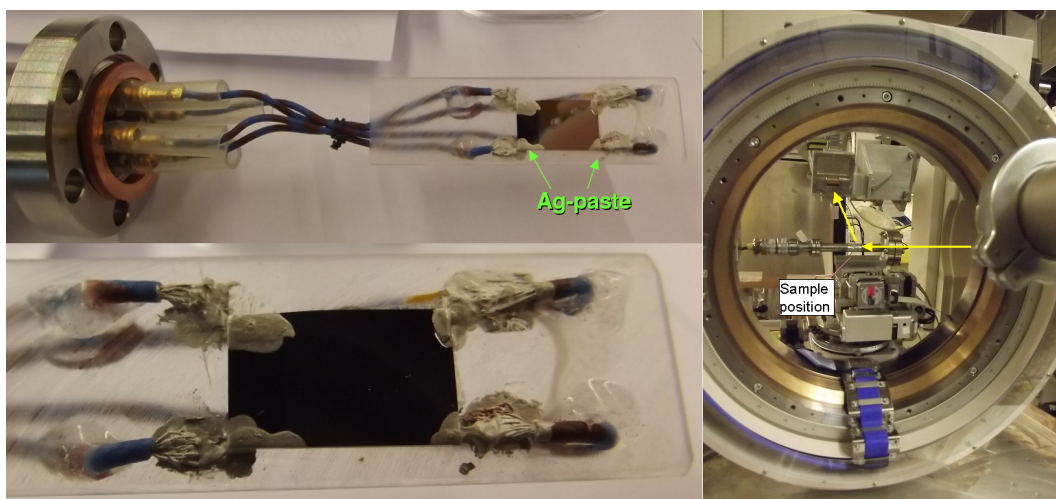

Fig. 3.14 A view of sample on the sample stage for *in-situ* hydrogen gas loading measurements at room temperature, constructed by original work of S.Wagner (left), and an example of a gas loading setup at Petra P08 in DESY (right). Contacts with Ag-pastes are for the contacts for electric resistivity measurements, as shown in picture with green arrows. Yellow arrows indicate the synchrotron beam direction.

In-situ high-temperature XRD measurements have been done at beam line BM20 at ESRF, Grenoble. **Fig. 3.15** and **Fig. 3.16** show some pictures of the setup. This setup was established by the group of C.Baehtz *et al.*, at BM20 at ESRF [ROS1]. With this setup, the measurable hydrogen pressure range is $1 \cdot 10^{-6}$ mbar $< p_H < 800$ mbar, and the sample temperature T_S ranges up to 1074 K. Conditions applied in this work were $p_H < 200$ mbar and $T_S < 363$ K were for high temperature *in-situ* gasloading XRD measurements.

Kapton is used as windows material, installed on the main chamber by epoxy glue for XRD measurements. An exhaust pumping tube is directly connected to the main chamber, which is

connected to a diaphragm and TMP pumps. A pressure of $p_H = 1 \cdot 10^{-6}$ mbar was the typical vacuum condition for this work. Constant fresh hydrogen gas flow with gas purity of 99.99 % was coming into the chamber, and going out to the pumping direction. During the measurement continuously controlled by mass flow meters at the inlet- and the outlet side.

Fig. 3.16 shows pictures of the sample setup, installed inside of the main chamber. Four-point measurement contacts are installed to the sample stage. The T_S and substrate temperature were directly measured by K-type sheath thermoelements, and recorded. Both of the thermoelement connections are established by mechanical contacts. Time change of T_S was continuously monitored, recorded and controlled by Joule-heating. All the XRD scans measured in this work have been done at a constant condition of p_H and T_S.

In this work, the decomposition pressure were measured by decreasing the hydrogen pressure at different constant temperature conditions. Detailed prcedure will be shown in **Chap. 5.6.2**.
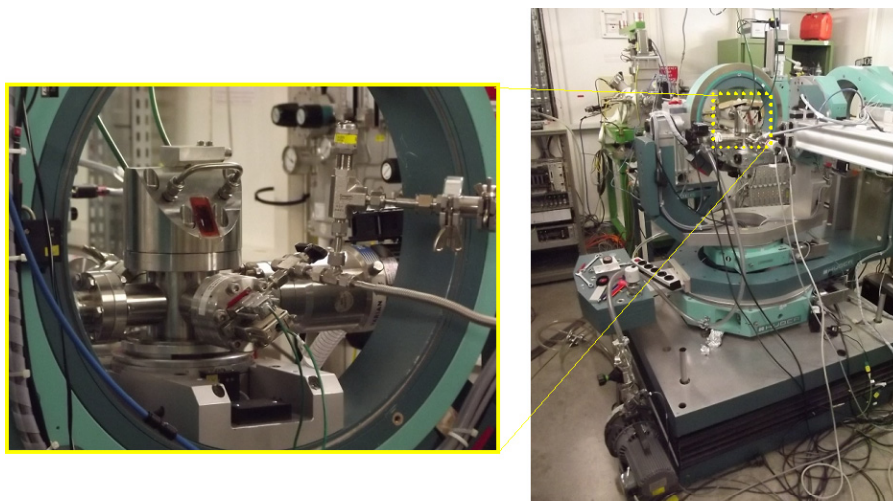
Fig. 3.15 Outlook of the apparatus for the *in-situ* XRD measurements for continuous hydrogen loading measurements at beam line P08 in ESRF (right) and a close-up view around the sample stage (left). Inside of the sample stage is described in **Fig. 3.16**.
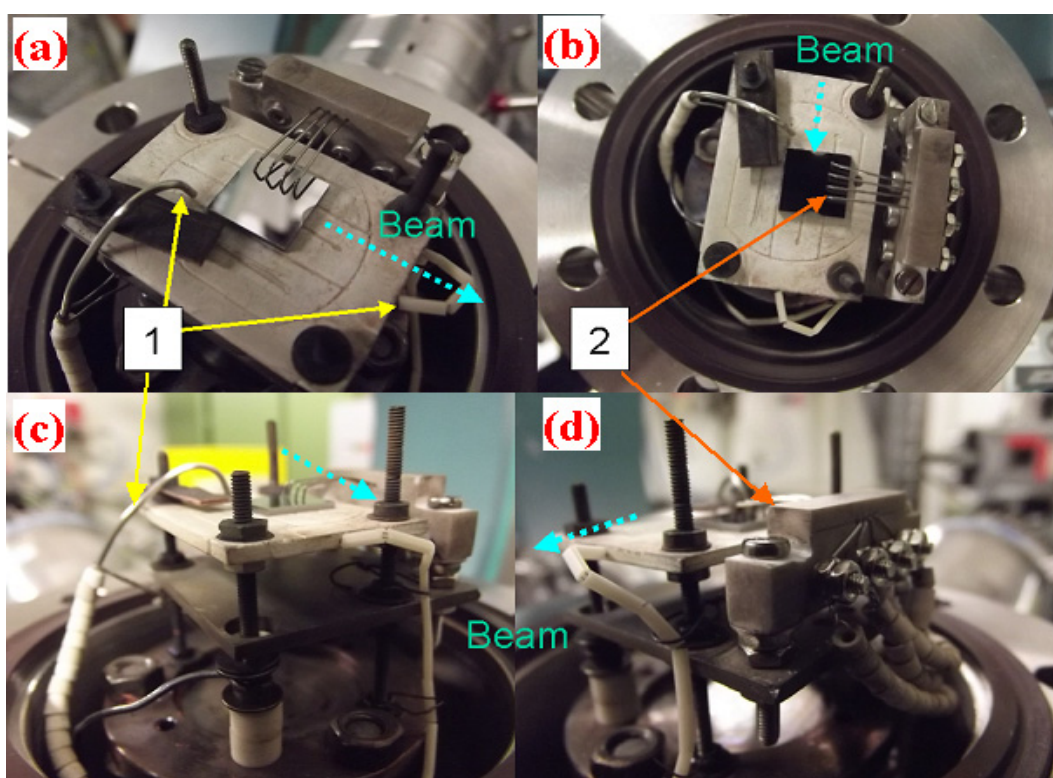

Fig. 3.16 Sample stage for *in-situ* XRD measurements at elevated temperatures, conducted at beam line P08 in ESRF, view from the top (a and b) and from side (c and d). The beam direction is indicated with a blue arrow in the pictures.

1. Thermocouple for sample and substrate (K-Type, sheath); 2. Terminal of the four-point measurement

3.3 X-ray diffraction (XRD)

X-ray diffraction (XRD) [Culli78] has been carried out to estimate microstructures, texture, lattice expansion and inner strain changes during hydrogen absorption. Texture measurements were carried out with X'pert MRD (Philips), using wavelength of Co-Kα (λ = 1.790263 Å). Additionally to normal 2θ-ω scans, rocking curves for some films were recorded. According to Bragg's law [Bragg13], the interplanar atomic distance d was obtained from the peak position in 2θ. The interplanar atomic distance d depends on a set of numbers (h, k, l), called Miller indices. Assuming a, b and c as the length of the unit cell respectively,

$$\frac{1}{d_{hkl}^2} = \frac{1}{(1+2\cos\alpha\cos\beta\cos\gamma - \cos^2\alpha - \cos^2\beta - \cos^2\gamma)}$$
$$\times \left\{ \frac{h^2\sin^2\alpha}{a^2} + \frac{k^2\sin^2\beta}{b^2} + \frac{l^2\sin^2\gamma}{c^2} + \frac{2hk}{ab}(\cos\alpha\cos\beta - \cos\gamma) + \frac{2kl}{bc}(\cos\beta\cos\gamma - \cos\alpha) + \frac{2lh}{ca}(\cos\gamma\cos\alpha - \cos\beta) \right\} \quad (3.4)$$

where, α, β, and γ are the inter-edge angles between the vectors consisting the unit cell, in the counter planes of a, b and c, respectively.

Relationships between d_{hkl} and the lattice parameters are listed in **Table 3.3**. Pd has cubic structure, and α-Mg has hexagonal structure, thermodynamically stable β-MgH$_2$ has tetragonal structure, and the metastable γ-MgH$_2$ phase has orthorhombic structure, as described in **Chap. 2.1.5**. δ-MgH$_2$ and ε-MgH$_2$ are not considered here, because they are rarely found. The d-values of α-Mg(0002), β-MgH$_2$(110) and Pd(111) calculated from the crystal information of bulk materials are presented in **Table 3.3**. Atomic plane distances in crystal structures in bulk material are gven for stress free samples.

XRD patterns of β-MgH$_2$ and γ-MgH$_2$ are simulated for the wavelength of Co-Kα in **Fig. 3.18**. Typical peaks of nucleated hydrides are reported in lower angles such as β-MgH$_2$(110), γ-MgH$_2$(110) or γ-MgH$_2$(111) peak. Therefore, searches for nucleated hydride peak were mainly done in this 2θ region (2θ = 28°-60°).

Additionally, the full width at half maximum (FWHM) of the peak gives information about the domain size or about the lattice coherency in the out-of-plane direction of the film [Culli78]. For the determination of this XRD domain size, Scherrer's formula [Sche18] was applied;

$$t = \frac{\omega\lambda}{B\cos\theta_B} \quad (3.5)$$

where, ω is a constant, t is the domain size in the out-of-plane direction, λ is the applied wavelength, B is the FWHM of the diffraction peak, and θ_B is the peak position of the object, in degree. Strictly speaking, the ω is a scale factor and depends on the theoretically assumed peak shape, the distribution of the material (the shape of the grain), and the corresponding mirror numbers (h, k, l) of the peak. (Details are available in refs. [Stok48,Lang78]). For convenience, a

constant value of $\omega = 0.9$ is used in this study.

Applied wavelength for all *in-situ* and *ex-situ* measurements in this work are listed in **Table 3.4**.

Table 3.3 Relationships between d_{hkl} and the lattice parameters $a,b,c,\alpha,\beta,\gamma$ for some crystal structures; Each structure shown here is associated with phases being treated in this study (marked with blue area).

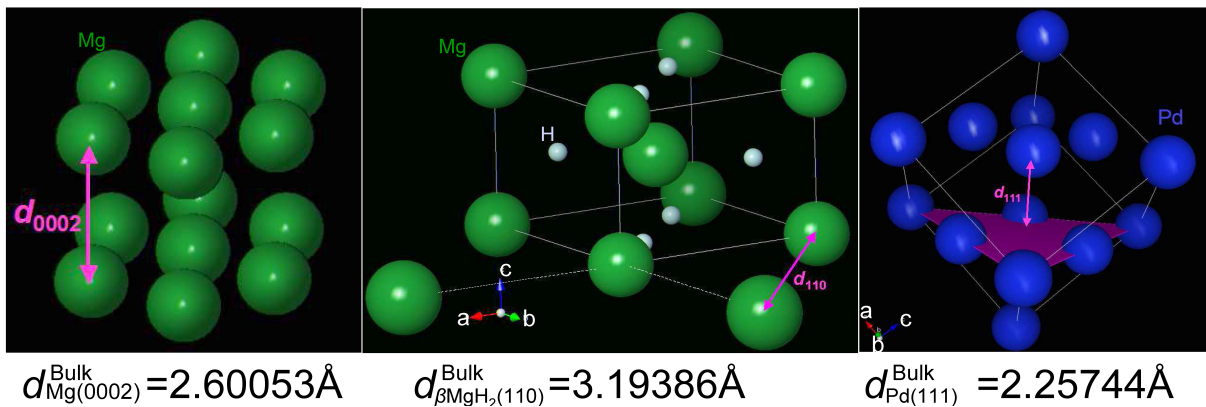| Structure		Conditions	Relationsihps between d_{hkl} and a,b,c.
Cubic	Pd	$a = b = c$ $\alpha = \beta = \gamma = 90$	$d = a \cdot \left(h^2 + k^2 + l^2 \right)^{-1/2}$
Hexagonal	Mg	$a = b \neq c$ $\alpha = \beta = 90, \gamma = 120$	$d = \left\{ \dfrac{4}{3} \left(\dfrac{h^2 + hk + k^2}{a^2} \right) + \dfrac{l^2}{c^2} \right\}^{-1/2}$
Tetragonal	βMgH_2	$a = b \neq c$ $\alpha = \beta = \gamma = 90$	$d = \left\{ \dfrac{h^2 + k^2}{a^2} + \dfrac{l^2}{c^2} \right\}^{-1/2}$
Orthorhombic	γMgH_2	$(a-b)(b-c)(c-a) \neq 0$ $\alpha = \beta = \gamma = 90$	$d = \left\{ \dfrac{h^2}{a^2} + \dfrac{k^2}{b^2} + \dfrac{l^2}{c^2} \right\}^{-1/2}$

$$d^{Bulk}_{Mg(0002)} = 2.60053\text{Å} \qquad d^{Bulk}_{\beta MgH_2(110)} = 3.19386\text{Å} \qquad d^{Bulk}_{Pd(111)} = 2.25744\text{Å}$$

Fig. 3.17 Schematic draw of d values for hexagonal αMg (0002), tetragonal βMgH$_2$ (110) and cubic Pd (111), in the stress-free state.
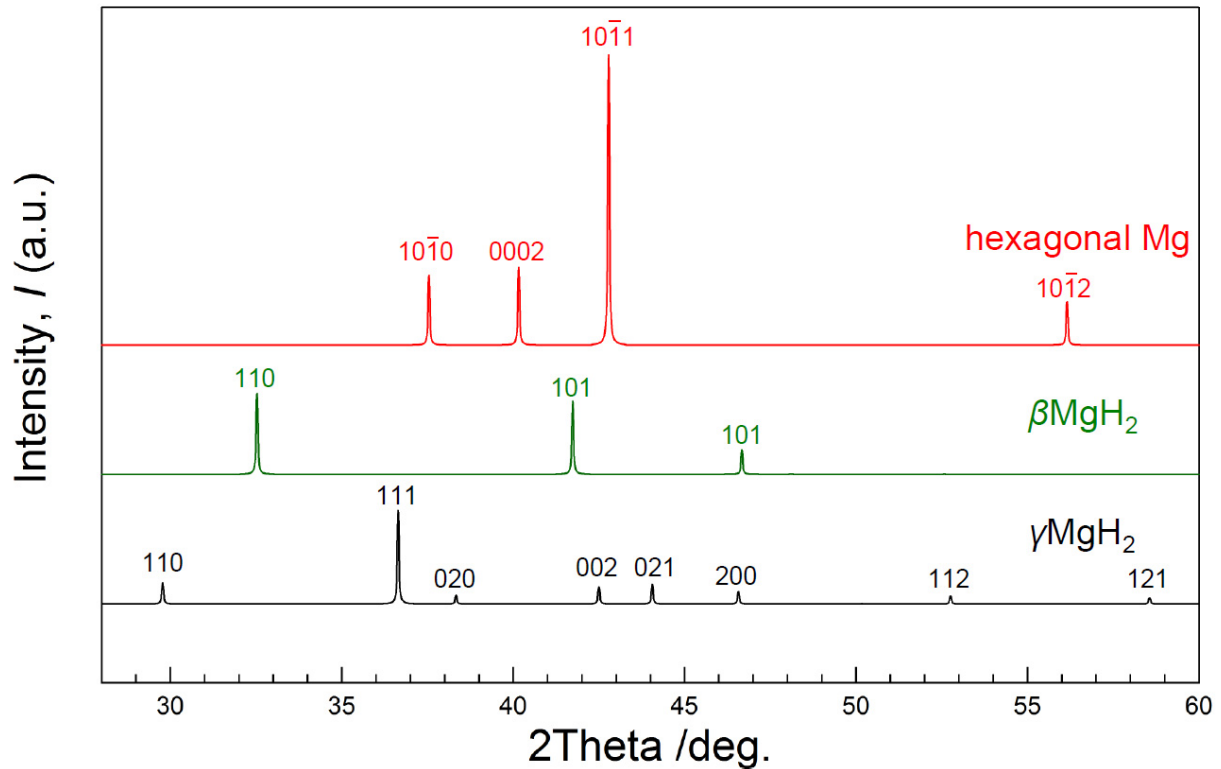
Fig. 3.18 Simulated XRD patterns of hexagonal Mg, β-MgH$_2$ and γ-MgH$_2$ with the wavelength of Co-Kα (λ = 1.790263 Å), under assumption of stress-free (bulk) powder state. Each peak is indexed with mirror numbers. Information of crystal structures quoted from [Zach63,Bort99,Vill98]. Powder Cell [Krau96] was applied for these simulations.

Table 3.4 Wavelength applied in this work for *in-situ* XRD measurements conducted at ESRF and DESY, and for *ex-situ* XRD measurements in the institute für Materialphysik (Phillips X'pert).

Beamlines/Equipments	Wavelength, λ [Å]
ESRF Grenoble BM20	1.07812
DESY Hasylab B2	0.999119, 0.999615
DESY Petra P08	1.000034
X´pert (IMP, Univ.Göttingen)	1.790263 (Co-Kα)

3.4 Evaluations of hydride formation kinetics by XRD

X-ray based evaluation techniques used in this work are explained in this section. By finding the maximum intensity position, the (0002) reflection peak of α-Mg phase, is used to evaluate mechanical stress in the film.

The increase of the hydride volume content x_{hydride}, upon hydrogenation time t is determined by the peak area change $A^{\text{Mg(0002)}}\big/A_0$ of the α-Mg (0002) reflection upon time, by using the following equation

$$x_{\text{hydride}} = x_0 - x_{\text{Mg}} = x_0 \cdot \left(1 - \frac{A^{\text{Mg(0002)}}}{A_0} \cdot \frac{v^{\text{mol}}_{\text{hydride}}}{v^{\text{mol}}_{\text{Mg}}} \right) \tag{3.6}$$

where x_0 is the initial α-Mg volume content, x_{Mg} is the content of the α-Mg volume content upon hydrogenation, $v^{\text{mol}}_{\text{Mg}} = 14.0$ cm^3/mol is the molar volume of the α-Mg [Aved99], $v^{\text{mol}}_{\text{hydride}} = 18.54$ cm^3/mol is the molar volume of the β-MgH$_2$ [Vill98].

The $A^{\text{Mg(0002)}}/A_0$ term corresponds to the molar ratio of α-Mg in the perpendicular direction, during the reaction. Multiplying the terms of Eq.(3.6) by the sample area, which remains constant during hydrogenation, yields the relationship of the volume changes of each phase.

A diffusion constant D^{Mg}_{H} is finally obtained by using a one-dimensional diffusion law for the growing hydride phase as simple approximation

$$\sqrt{D^{Mg}_H t} = \frac{\Delta x_{hydride}}{w} \qquad \text{and} \qquad D^{Mg}_H = \frac{1}{t}\left(\frac{\Delta x_{hydride}}{w}\right)^2 \tag{3.7}$$

where w is the surface area of the sample.

Further details about the time dependent growth of the hydride phase are described in the **Appendix A1**.

Turning back to the evaluation method of hydride fraction in the Mg-film, Eq. (3.6) is used in this work. However, in case of the disappearance of the α-Mg (0002) reflection, which is not due to hydrogen loading, Eq.(3.6) is not applicable. Such situation happens in case of the *in-situ* electrochemical loading by a coverage of electrolyte on the surface. In this case, another alternative evaluation is applied [Kael68]:

$$x_{\text{hydride}} = x_0 \cdot \left(\frac{A^{\beta\text{Mg(110)}}}{A^{\text{Mg(0002)}}_0 + A^{\beta\text{Mg(110)}}} \right) \cdot \frac{v^{\text{mol}}_{\text{hydride}}}{v^{\text{mol}}_{\text{Mg}}} \tag{3.6'}$$

where $A^{\text{Mg(0002)}}_0$ and $A^{\beta\text{Mg(110)}}$ are the peak area of the initial α-Mg (0002) reflection and the β-MgH$_2$(110) reflection, respectively. It is remarked that the evaluation using Eq.(3.6') has valibity only when the initial Mg-film has a α-Mg (0002) texture (see **Chap. 4.1**) and with assumption of crystallographic relationship of α-Mg (0002)//β-MgH$_2$(110) (see **Table 2.4** in **Chap. 2.1.5.2** and in **Chap. 5.1.2**). In this study, Eq.(3.6') was used only in **Chap. 5.3.2**.

3.5 Stress and strain evaluations

In-plane stress in the films is evaluated with three different methods in this study. This chapter explains the theoretical background of in-plane stress evaluation by means of XRD-based peak-shift method and $\sin^2\psi$ method, and by profilometer-based curvature measurement. Profilometer-based strain evaluation will be also shown together in the end. In this work, negative

direction of all the stresses are defined as compressive stress.

3.5.1 Stress evaluations from XRD peak shift: σ^p

In-plane mechanical stress σ^p arising during hydrogen absorption in the n-Mg films is evaluated from the α-Mg (0002) lattice spacings by the formula of Freund and Suresh [Freund03]

$$\sigma^p = -\frac{E_{\mathrm{Mg}}}{2\nu_{\mathrm{Mg}}}\left(\frac{d_\sigma^m - d_0}{d_0}\right) \tag{3.8}$$

where E_{Mg} is Young's modulus of magnesium, ν_{Mg} is the Poisson ratio of magnesium, d_σ^α and d_0^α are lattice spacings of the α-Mg (0002) planes with and without stress σ, respectively. In this work the bulk values of polycrystalline Mg were used with $E_{\mathrm{Mg}} = 45\,\mathrm{GPa}$, $\nu_{\mathrm{Mg}} = 0.35$, and $d_0^\alpha = 2.60053\,\text{Å}$ were used. This simple prediction could include an error of up to 17 %, due to the anisotropic elastic behavior of the hexagonal structure. Details about this point are described in **Appendix A2**.

3.5.2 Stress evaluation with "sin²ψ method": σ^t

Alternatively, the in-plane stress σ^t was evaluated by the position change of the α-Mg (0002)-reflection upon ψ-tilt of the sample using

$$\sigma^t = \left(\frac{E_{\mathrm{Mg}}}{1 + \nu_{\mathrm{Mg}}}\right) \cdot \frac{1}{d_0}\left(\frac{\partial d_\psi^m}{\partial \sin^2 \psi}\right) \tag{3.9}$$

where d_ψ^m is the value of d^m at the ψ sample-tilting angle [Freund03]. This method is called "sin²ψ method"[Janss07], as is also called in the further sections in this work.

3.5.3 Stress evaluation by curvature method: σ^{St}

Evaluations of the film curvature changes using a profilometer (Dektak 150 from Veeco Instruments Inc.) before and after hydrogenation, has been conducted in the Institut für Materialphysik, University Göttingen.

In-plane stresses of Mg-films were evaluated from the measured curvatures by using Stoney's equation [Ston09]

$$\sigma^{St} = -\frac{1}{6h_{\mathrm{f}}} \cdot \frac{E_{\mathrm{s}}}{1 - \upsilon_s} \cdot h_s^2 \kappa \tag{3.10}$$

where σ^{St} is the in-plane stress in the film, h_{f} is the thickness of thin film, E_{s} is the Young modulus of substrate, υ_s is the Poisson's ratio of substrate, h_{s} are the thickness of substrate, and κ is the curvature of the substrate. Here, $\sigma^{St} < 0$ is defined as compressive stress, and κ is defined as the inverse of the curvature radius. $E_{\mathrm{s}}/(1 - \upsilon_s) = $ 180 GPa for Si (100)

[Hopc10,Proo02,Nye85] is used in this work. The value of κ is measured at each state, and the average of 20 measurements from different places is adopted.

The curvature κ_x at a given position ($x = x_0$) is calculated by [Klin98], measuring sample surface geometry $f(x)$,

$$\kappa_x = \frac{f''(x_0)}{\left\{1 + \left(f'(x_0)\right)^2\right\}^{3/2}} \tag{3.11}$$

where $f'(x)$ and $f''(x)$ are the derived functions of the first and second derivative, respectively.

The thickness of each sample was determined by averaging of obtained thickness from 20 different measurements conducted at more than 2 positions at the sample edge. To calculate σ^{St} by Eq.(3.10), the curvature κ of each sample was determined by averaging over κ_x-values obtained by Eq.(3.11) from 1500 μm-scans at more than 10 different positions on sample surface, where at each position κ_x is averaged value of 3 calculations for 1 scan.

The evaluation methods applied in this work are classified in **Table 3.5**. Comparing these three methods, the $\Delta\sigma^t$ by sin²ψ-method can be applied only for equilibrium states since more than one scan at different ψ-positions is required. The $\Delta\sigma^{St}$ obtained by profilometer measurements contains larger errors and needs longer measurement times, furthermore doing many scans damages the sample surface layer. Obtaining the $\Delta\sigma^p$ by peak shift method allows continuous measurements and can be applied with ease. Therefore, $\Delta\sigma^p$ by peak shift method is applied for *in-situ* stress measurements.

Table 3.5 Classification of stress evaluation applied in this work.

Methods	Expression	Equations
peak shift	σ^p	$\sigma^p = -\dfrac{E_{\text{Mg}}}{2\nu_{\text{Mg}}}\left(\dfrac{d^{\text{Mg(0002)}} - d_0^{\text{Mg(0002)}}}{d_0^{\text{Mg(0002)}}}\right)$
sin²φ method	σ^t	$\sigma^t = \left(\dfrac{E_{\text{Mg}}}{1+\nu_{\text{Mg}}}\right)\cdot\dfrac{1}{d_0^{\text{Mg(0002)}}}\left(\dfrac{\partial d_\psi^{\text{Mg(0002)}}}{\partial \sin^2 \psi}\right)$
curvature method	σ^{St}	$\sigma^{St} = -\dfrac{1}{6h_f}\cdot\dfrac{E_s}{1-\upsilon_s}\cdot h_s^2 \kappa$

3.6 Film expansion upon hydrogen loading measurement

The film expansion of the sample before and after hydrogen loading was calculated. Since there is volume changes of about 33 % upon the transformation from α-Mg to β-MgH$_2$ (see Eq.(2.38)), a large change of the thickness is expected. In terms of films, the expansion of the

out-of-plane direction is considered, because of the film clamping to the substrate. Actually, the thickness change is also reported by means of directly measurement by SEM [Gaut13].

In this work, evaluation of the film thickness changes have been conducted in the Institut für Materialphysik, University Göttingen, using a profilometer (Dektak150) before and after hydrogenation. From the measured thickness of the film (d'), the fraction of hydride phase f_{MgH_2} is estimated by applying the following relationship

$$d' = f_{Mg} d_0 + f_{MgH_2} d_0 (1 + \varepsilon_{MgH_2}^{tot}) \qquad (3.12a)$$

where d_0 is the as-prepared thickness of the Mg film (without surface Pd capping layer), $\varepsilon_{MgH_2}^{tot}$ is 0.27 for the hydrided state (see **Chap. 2.2.1**), f_{Mg} and f_{MgH_2} are the fraction of Mg phase and hydride phase in the film respectively, with $f_{Mg} + f_{MgH_2} = 1$.

In case of Mg, the expansion regarding the solid solution limit of hydrogen is negligible (see **Chap. 2.1.5.1**). Therefore Eq.(3.12a) can be rewritten by

$$d' = \left(1 + \frac{\varepsilon_{MgH_2}^{tot}}{2} \cdot c_H\right) d_0 \qquad (3.12b)$$

where c_H is the hydrogen concentration in the Mg layer with units of H/Mg. The increase of film thickness (Δd) has therefore a relationship of $\Delta d = d' - d_0 = \left(\varepsilon_{MgH_2}^{tot} / 2\right) \cdot c_H d_0$.

This assumption is based on a parallel layer model (described in **Fig. 3.19**), and d' was determined by the average of 20 scans for different positions of sample edges.

Thickness measurement for as-prepared film were conducted for samples prepared together with samples for loading, to prevent Mg from oxidation due to damaging Pd-capping by thickness measurement.

Thickness measurements for hydrogen-loaded film were conducted as soon as possible, after hydrogen gas loading. Stability of hydride phase was also visible by optical changes, as will be shown later in **Fig. 5.13**.

It is noted that this estimation is valid only for samples sputtered on Si-substrate, because of hydrogen induced volume expansion of Pd foil.

A schematic presentation of the parallel layer model is shown in **Fig. 3.19**. Nucleation of hydride phase is here assumed homogeneously at the sample surface, and the hydride layer starts to grow into the film, consuming the Mg layer, keeping the interface plane with Mg-layer macrospically parallel to the substrate surface. On evaluation for results of electrochemical loading measurements, the hydrogen content in the surface Pd capping layer is treated to be PdH$_{0.6}$, to calculate hydrogen concentration in Mg-layer (H/Mg) during the hydrogen loading process.
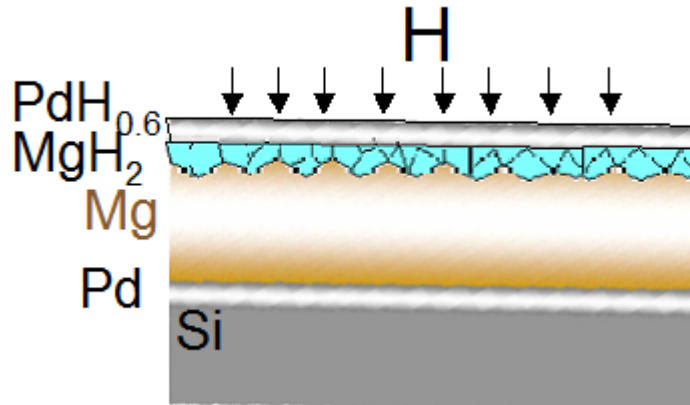
Fig. 3.19 Schematic draw of the parallel layer model: 1-dimensional growth of MgH_2 layer (light blue) from sample surface consuming Mg layer (brown) during hydrogen loading, keeping the interface with Mg macroscopically parallel to the substrate surface.

3.7 *In-situ* electroresistivity measurement

Four-point electroresistivity measurements were carried out for Mg-films. The four-point measurement sample stage was shown in **Fig. 3.14** and **Fig. 3.16**.

The effective resistivity of Mg-MgH_2 system ρ' is evaluated by two different equations. The first one is the Bruggeman equation [Qu10]:

$$f_{Mg} \frac{\rho_{Mg} - \rho'}{L \cdot \rho' + (1-L)\rho_{Mg}} + f_{MgH_2} \frac{\rho_{MgH_2} - \rho'}{L \cdot \rho' + (1-L)\rho_{MgH_2}} = 0 \qquad (3.13a)$$

where ρ_{Mg} and ρ_{MgH_2} are the resistivity of Mg and MgH_2, respectively, L is the geometrical factor and equals to 1/3 for spherical hydride nucleation and growth, f_{Mg} and f_{MgH_2} are the volume fraction of Mg and MgH_2 in the film respectively, having relationship of $f_{Mg} + f_{MgH_2} = 1$. ρ_{Mg} = 6.5 µΩcm and ρ_{MgH_2} = 10 mΩcm, which are reported by Giebels *et al.* [Gieb04] are applied in this work. Details about those resistivity values are described in **Chap. 2.1.5.2**.

By solving Eq.(3.13a), volume fraction of the hydride phase, f_{MgH_2}, is estimated. It is noted that this calculation is based on an assumption that hydride has spherical geometry and is nucleating randomly in the film, and not as a parallel layer (see **Fig. 3.19**).

Another calculation applied in this work is an equation that is based on the parallel layer model,

$$\frac{d_{Mg} + d_{MgH_2} + d_{Pd}}{\rho'} = \frac{d_{Mg}}{\rho_{Mg}} + \frac{d_{MgH_2}}{\rho_{MgH_2}} + \frac{d_{Pd}}{\rho_{Pd}} \qquad (3.13b)$$

where d_{Pd} and ρ_{Pd} ($\approx 1.5 \cdot 10^{-5}$ Ωcm) [Wagn10] are the thickness and resistivity of surface Pd layer, respectively.

Electroresistivity during hydrogen loading is measured by four-point measurement, and the relative change of resistance R/R_0 is evaluated, which eliminates other artefacts coming from sample shape difference.

3.8 Electrochemical hydrogen permeation measurements

Monitoring the permeation of hydrogen is one of the powerful tools to evaluate the diffusivity of hydrogen in metals, especially when the sample shape is a foil, a film or a plate like with precisely known thickness. The electrochemical loading technique allows the exact control of loaded hydrogen amount, applying Faraday's equation (Eq.(3.3)). Since this is an advantage for the thin films, the electrochemical loading technique is used in this work.

3.8.1 Pulse loading condition

In this work, the time-lag method [Kirch80,Cran75,Züch70] with pulse hydrogen loading current is adopted in the electrochemical double cell [Kest00] under pulse-conditions [Cran75], at 298 K. A schematic figure for the setup is shown in **Fig. 3.20**. The total hydrogen diffusion coefficient D_H^{tot} through a plate of single Pd layer with thickness s was determined by measuring the breakthrough time t_b by using the following equation:

$$D_H^{tot} = \frac{s^2}{19.98 \cdot t_b} \tag{3.14}$$

However, since the diffusion constant of hydrogen in Mg is of interest, here, the hydrogen permeation model for film stackings has to be applied, as published by Schmitz *et al.* [Schm98]. For a bilayer of Mg and Pd, equation 23 in ref. [Schm98] yields,

$$t_b = \frac{1}{2}\frac{\left(a^{Pd}\right)^2}{D_{Pd}} + \frac{1}{2}\frac{\left(a^{Mg}\right)^2}{D_{Mg}} + \frac{a^{Pd} \cdot a^{Mg}}{kD_{Mg}} \tag{3.15}$$

which is strictly correct only in the solid solution phase. Here, a^{Mg} is the thickness of the Mg film and a^{Pd} is that of the Pd substrate. D_H^{Pd} was measured separately for the Pd substrates. Up to a concentration of $c_H = 1 \cdot 10^{-2}$ H/Pd it is $D_H^{Pd} = 3.1 \pm 0.1 \cdot 10^{-11}$ m²s⁻¹. Furthermore, k is the difference of hydrogen solubility, which is calculated as [Kest00,Fukai05,Gemm11]

$$k = \frac{c_{Mg}}{c_{Pd}} = \exp\left(\frac{\Delta G_{HinPd}^{Sol.} - \Delta G_{HinMg}^{Sol.}}{RT}\right) = 10^{-3} \tag{3.16}$$

where the changes of the free energy of solution $\Delta G_{\text{HinMg}}^{\text{Sol.}} = 22.5$ kJ/(mol-H), for bulk Mg [Bohm99], and $\Delta G_{\text{HinPd}}^{\text{Sol.}} = 5.3$ kJ/(mol-H) for bulk Pd [From76], at 300 K were used, respectively. Finally, this calculation yields the hydrogen diffusion constant in Mg, D_{H}^{Mg} as obtained from the time-lag method. The 20 nm Pd-coverage layer is neglected in this study. Therefore, the calculated hydrogen diffusion constant is expected to be slightly underestimated.
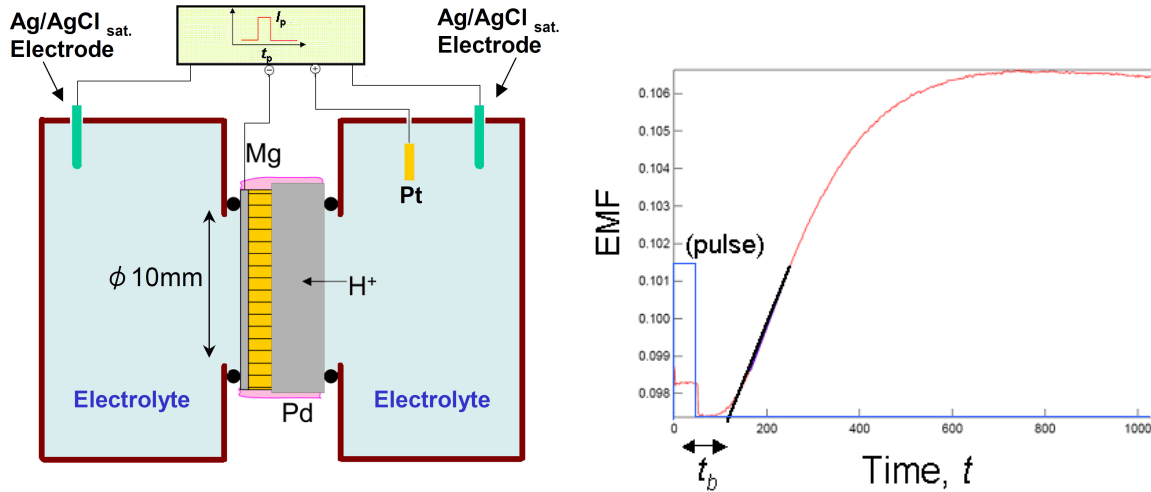
Fig. 3.20 Schematic figure of the setup for electrochemical hydrogen permeation measurements with time-lag method (shown on the left side), and an example of measured time change of the output EMF potential (red line) with applied current-controlled pulse (image, blue), on the right side. Pt was used as the counter electrode, and the edge of sample was polymer-coated. Current was loaded from back side with $i = 10^{-7}\text{-}10^{-3}$ A/cm^2, and break through time t_{b} was determined as a difference time between the start of applied current and the point of deflection with a line, being determined by linear fitting for the rising EMF potential.

3.8.2 Potentiostatic loading condition

Permeation measurements with potentiostatic loading condition are done in the electrochemical double cell [Kest00]. A schematic figure for the setup is shown in **Fig. 3.21**. During potentiostatic loading, the time change of the current density was monitored. Diffusion constant $D_{\text{H}}^{\text{tot}}$ from potentiostatic loading measurements were calculated by [Cran75]

$$D_{\text{H}}^{\text{tot}} = \frac{s^2}{6 \cdot t_{\text{b}}} \qquad (3.17)$$

where s is the total thickness of the membrane, and t_b is the breakthrough time. The t_b for potentiostatic loading measurements was determined as the time taken for the current density to reach 0.6299 of its constant value [Deva64], as shown in **Fig. 3.21**. The time change of the voltage between both ends of electric resistance, which is inserted in series in the circuit, were also monitored to calculate the amount of loaded hydrogen by using Eq.(3.3).
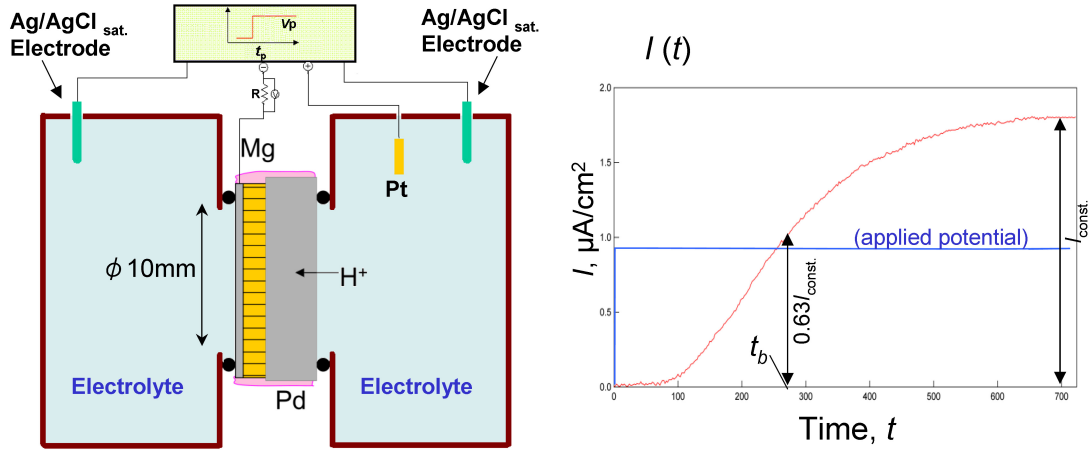

Fig. 3.21 Schematic figure of the setup for electrochemical hydrogen permeation measurements with potentiostatic condition (shown on the left side), and an example of measured time change of the current density (red line) with applied current-controlled pulse (image, blue), on the right side. Pt was used as the counter electrode, and the edge of sample was polymer-coated. Current was loaded from the backside with constant voltage (V_p = 0.1 V), and break through time t_b was determined from the current change during loading.

In steady state, the permeation rates of hydrogen in each layer are the same and constant. In this case, the diffusion constant of hydrogen in Mg layer, D_{Mg}, was calculated by using the following relationship [Cran75]

$$\frac{a^{Pd\text{-}Sub}}{c_{Pd\text{-}Sub} \cdot D_{Pd}} + \frac{a^{Mg}}{c_{Mg} \cdot D_{Mg}} + \frac{a^{Pd\text{-}Cap}}{c_{Pd\text{-}Cap} \cdot D_{Pd}} = \frac{s}{c^{tot} \cdot D_H^{tot}} \tag{3.18}$$

where $a^{Pd\text{-}Sub}$ and $c_{Pd\text{-}Sub}$ are the thickness and the hydrogen concentration in the Pd substrate, as well as a_H^{Mg} and c_{Mg} are the thickness and the hydrogen concentration in the Mg layer, $a^{Pd\text{-}Cap}$ and $c_{Pd\text{-}Cap}$ are the thickness and the hydrogen concentration in the Pd capping layer, a^{tot} and c^{tot} are the thicknesses and the hydrogen concentration for whole layers. D_H^{tot} and D_{Pd} were determined by Eq.(3.17). Applying approximations of $c_{Pd\text{-}Sub} \approx c_{Pd\text{-}Cap}$, $c_{Pd\text{-}Sub} \approx c^{tot}$ and $k = \left(c_{Mg} / c_{Pd} \right) = 10^{-3}$ (see Eq.(3.16)) yields

$$D_{Mg} = \frac{a^{Mg}}{k} \left(\frac{s}{D_H^{tot}} - \frac{a^{Pd\text{-}Sub} + a^{Pd\text{-}Cap}}{D_{Pd}} \right)^{-1} \tag{3.19}$$

$$\text{with } k = \left(c_{Mg} / c_{Pd} \right) = 10^{-3}$$

4. Sample characterization of the as-prepared Mg-films

The characterization of as-prepared Mg-films will be presented in this chapter, changing Mg-layer thickness and substrates. The dependency of the in-plane stress on the prepared film thickness, and the out-of-plane grain size difference by annealing condition will be shown.

4.1 Mg films on: Si-substrate

4.1.1 As deposited Mg films

Mg films with thicknesses ranging from 20 nm to 2800 nm deposited on Si (100) substrates were characterized by means of XRD. **Fig.4.1a** exemplarily shows the XRD pattern for an as-prepared Mg film with the thickness of 160 nm, deposited on Si (100) with the 20 nm thick Pd buffer layer. A strong reflection of the Mg(0002) is observed.
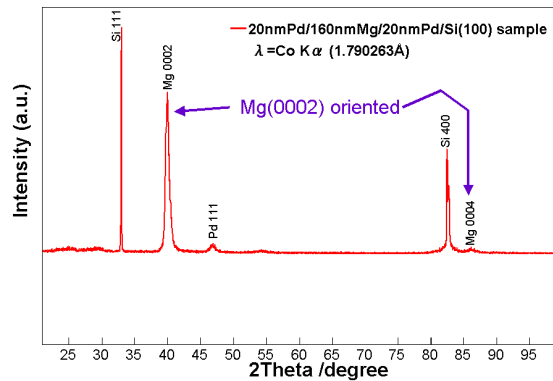
Fig.4.1a XRD pattern of the as-prepared sample of 20 nm Pd-capped Mg film with the thickness of 160 nm, deposited on Si (100) substrate at room temperature and with the Pd buffer layer thickness of 20 nm.

The vertical grain size for the same sample was evaluated by applying the Scherrer formula (Eq.(3.5), [Sche18]) to the Mg(0002) peak width, and calculated to be 30 nm. Cross-sectional TEM observation for this sample show a columnar structure in the Mg-layer with the lateral grain size about 30 nm and vertical grain size in a range of 30-80 nm, as is shown in **Fig. 4.1b**.
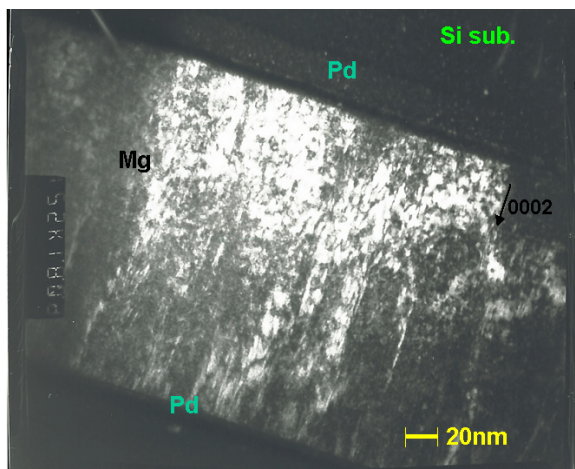

Fig. 4.1b A cross-sectional picture from TEM observation for as-prepared Mg-film (160nm), sputtered at room temperature.

Fig. 4.2a shows the XRD peaks of the α-Mg(0002), measured for as-deposited samples with various Mg-thickness from 20 nm to 2800 nm, deposited on the Si(001) substrates. The initial in-plane stresses, calculated from the peak shift by using Eq.(3.8), are plotted in **Fig. 4.2b**. The vertical grain sizes are also calculated by Eq.(3.5), and plotted in **Fig. 4.2b**. The peak intensity in **Fig. 4.2b** is almost proportional to the sample thickness.

The peak position shifts to higher angles for smaller film thickness, as shown in **Fig. 4.2a**. This shows the tendency of compressive biaxial stress increase with increase of the sample thickness (**Fig. 4.2b**). The dependency of the stress increase on the thickness is significant for samples with $d < 200$ nm, compared to samples with $d > 1000$ nm.
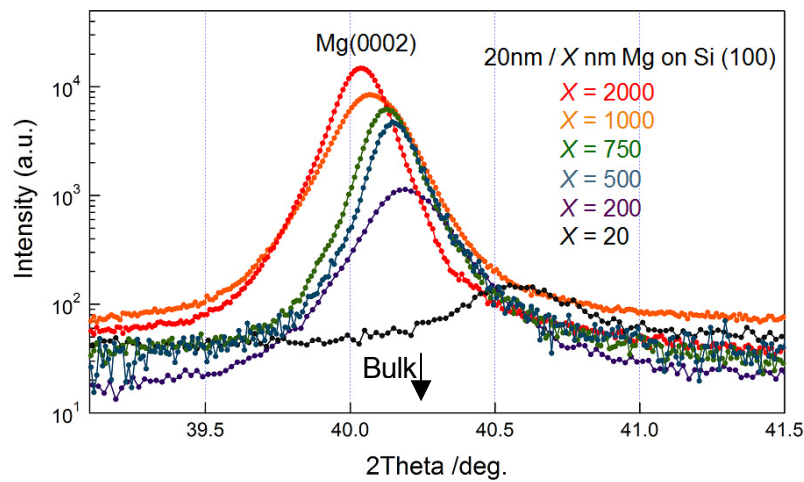
Fig. 4.2a A series of Mg(0002) Bragg peaks measured by same XRD condition for as-prepared nc-Mg films sputtered on Si (100) substrate with thickness of X [nm]; X = 2000 (red), 1000 (orange), 750 (green), 500 (blue), 200 (violet), and 20 (black). As a reference, 2θ value which corresponds to atomic plane distance for the bulk Mg(0002) is marked with black arrow in the figure.
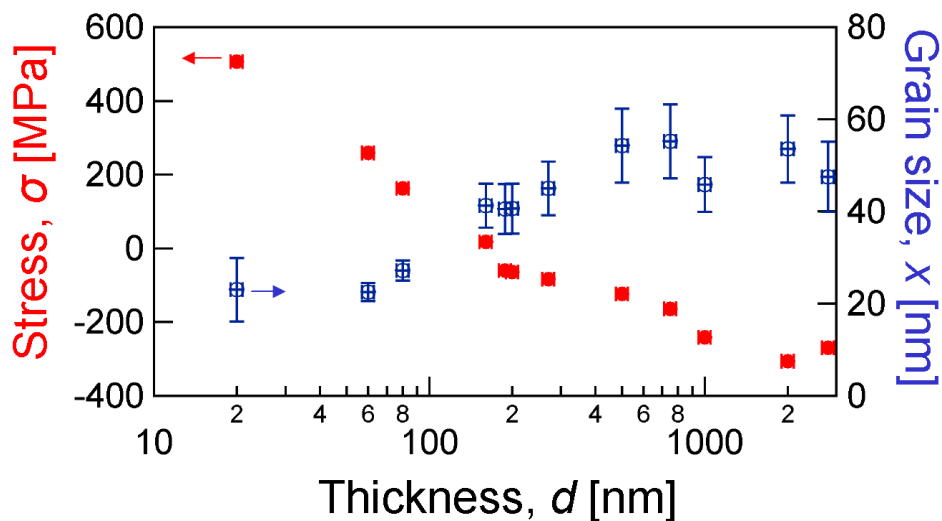

Fig. 4.2b Calculated in-plane stress σ (filled red markers, left axis) and vertical grain size x (hollow blue markers, right axis) plotted versus Mg film thickness d, obtained for as-prepared samples from XRD peak position and peak width (FWHM), respectively.

The vertical grain size corresponds to the sample thickness for a thin film at $d = 20$ nm, and increases to 40 ± 5 nm at $d = 200$ nm. No thickness dependency was visible for samples with $d > 500$ nm.

The texture measurement at the 2θ position of the Mg(0002) peak, shown in **Fig.4.2c**, show the (0002)-texture of Mg in the out-of-plane direction. This preferential growth of Mg(0002) direction [Higu02,Leon02,Isido03,Chec04] is recognized for all samples.
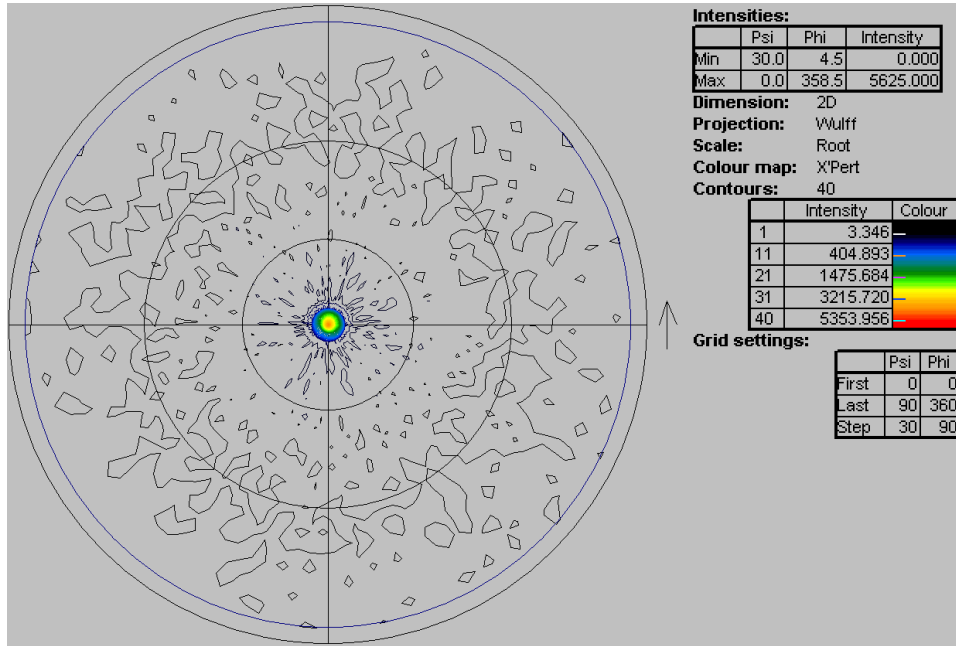

Fig.4.2c A result of the texture measurement at the Mg(0002) peak position, measured for the as-prepared sample (20 nm Pd-capped Mg film with the thickness of 500 nm, deposited on Si (100) substrate at room temperature and with the Pd buffer layer thickness of 20 nm).

4.1.2 Annealed Mg films

In this section, results from properties of annealed Mg films will be shown. Mg films of 60 nm - 2100 nm were prepared and characterized by means of XRD.

Fig. 4.3a exemplarily shows the XRD pattern for the as-prepared sample of an Mg film of the thickness of 100 nm, deposited on Si (100) after annealing at $T = 453$ K for 30 minutes. A strong reflection of the Mg(0002) is observed. At high temperature, formation of intermetallic compounds might occur. However, these phases are not visible in the XRD pattern, for all samples.

The lateral grain size for the same sample was evaluated by applying the Scherrer formula (Eq.(3.5), [Sche18]) to the Mg(0002) peak width, and calculated to be 35 ± 4 nm.
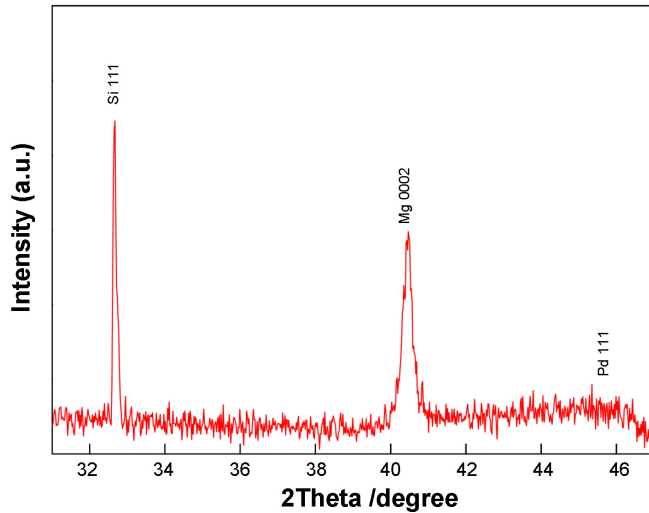
Fig. 4.3a XRD pattern of the as-prepared annealed sample of 20 nm Pd-capped Mg film with the thickness of 100 nm, deposited on Si (100) substrate.

Fig. 4.3b shows the XRD peaks of the α-Mg(0002), measured for as-deposited samples with various Mg-thickness from 20 nm to 1400 nm, deposited on the Si(001) substrates, with the annealing condition of $T = 453$ K for 30 minutes. It is noted that these measurements were performed by different conditions, and therefore they have different maximum intensities.
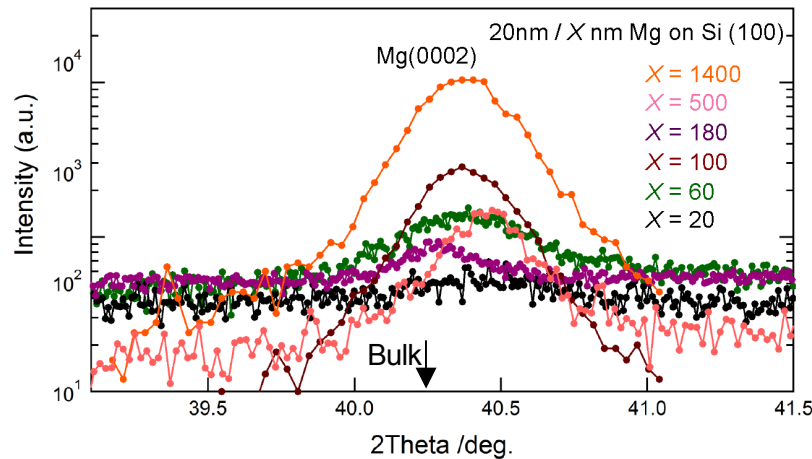

Fig. 4.3b A series of Mg(0002) Bragg peaks measured by same XRD condition for as-prepared annealed Mg films sputtered on Si (100) substrate with thickness of X [nm]; X = 1400 (orange), 500 nm (pink), 180 (violet), 100 (brown), 60 (green) and 20 (black). As a reference, 2θ value which corresponds to atomic plane distance for the bulk Mg(0002) is marked with black arrow in the figure.

The initial in-plane stresses, calculated from the peak shift by using Eq.(3.8), are plotted in **Fig. 4.3c**. The peak positions showed no clear correlation with the film thicknesses, showing that the stress state is thickness independent. Stress values ranging from $\sigma \approx +50$ MPa to $\sigma \approx +300$ MPa were obtained for all whole sample thickness range, which reveals tensile stressed state. These results differ from the case of the samples, which were not annealed (See **Fig. 4.2b**).

The vertical grain sizes are also calculated by Eq.(3.5), and plotted in **Fig. 4.3c**. The grain size reduces from about 60 nm to 40 nm, with reduction of the film thickness. No clear grain size changes can be seen in annealed samples and the samples without annealing process.

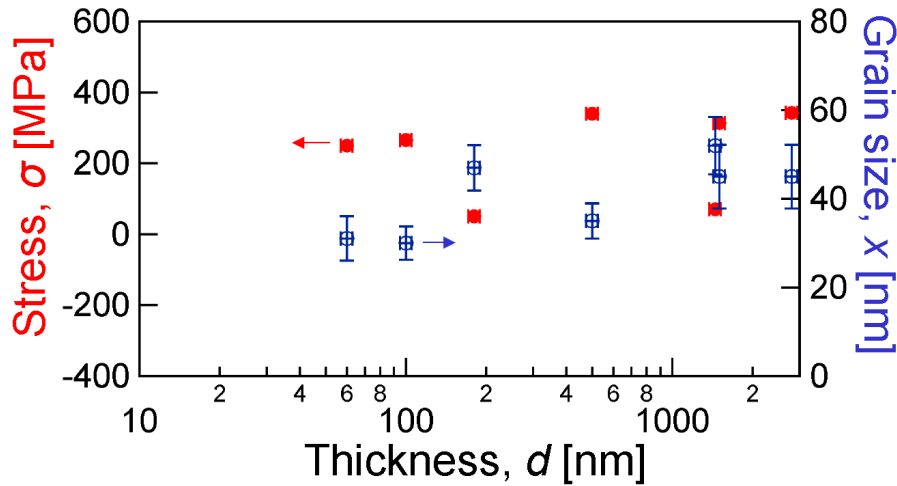The sample showed a strong αMg-(0002) texture. A pole figure for this peak is shown in **Fig. 4.3d**.

Fig. 4.3c Calculated in-plane stress σ (filled red markers, left axis) and vertical grain size *x* (hollow blue markers, right axis) plotted versus annealed Mg film thickness *d*, obtained for as-prepared samples from XRD peak position and peak width (FWHM), respectively.
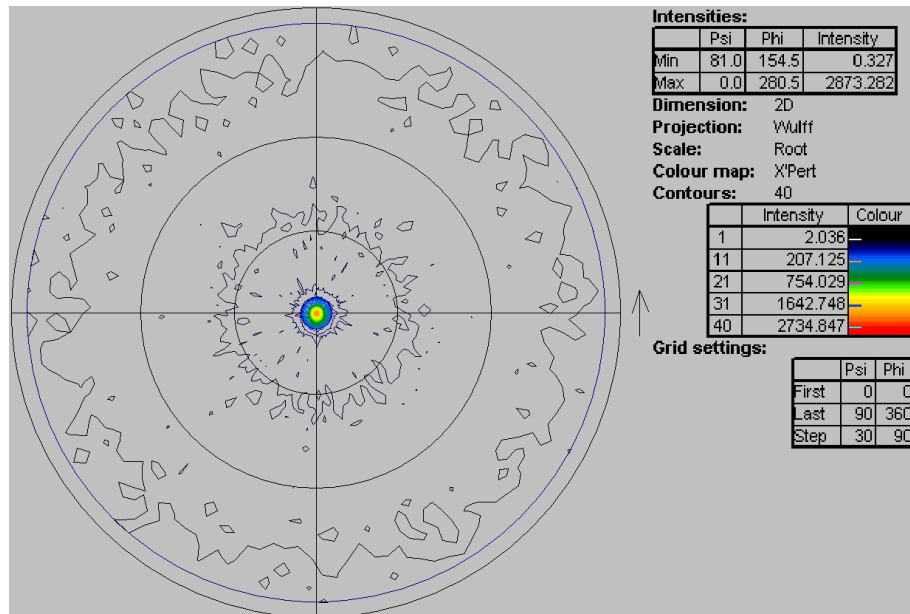

Fig. 4.3d The XRD peak of αMg-(0002) (left) and corresponding texture measurement (right), obtained from the annealed 2800 nm Mg film, annealing at *T* = 453 K for 30 min., measured at *T* = 300 K with the wavelength of CoKα (λ = 1.790263 Å). Fully hydrogenated state by p_H= 20 mbar will be shown later in **Fig. 5.1b**, and *in-situ* loading results about this experiments will be shown in **Fig. 5.15a** in **Chap. 5.2.2**.

4.2 Mg films on: Pd-substrate

Results for Mg-films of 80 nm, 200 nm, 300 nm and 2088 nm deposited on Pd foil will be shown in this section.

The XRD pattern obtained for a 2088 nm-thick Mg-film on a 250 µm thick Pd foil at room temperature is shown in **Fig. 4.4a** with red lines. The wavelength of CoKα is used in these XRD measurements. The strong αMg-(0002) texture perpendicular to sample plane is observed by the 2θ-θ scan. Using Eq.(3.5), grain size of α-Mg was calculated to be 38 ± 4 nm, which is similar to the grain sizes of films deposited on Si. Using Eq.(3.8), in-plane stress in α-Mg matrix was calculated to be $\sigma^p = -120$ MPa. The result of the texture measurement at the 2θ position for the α-Mg(0002) peak is also shown in **Fig. 4.4b.** XRD pattern in hydrogen-loaded state will be described in **Chap. 5.1.2**, and also results of *in-situ* measurement in **Chap. 5.2.3**.

For the 200 nm film, Scherrer formula (Eq.(3.5)) gives a grain size of 19 nm and a stress of $\sigma^p = +155$ MPa, applying Eq.(3.8). Likewise, a grain size of 25 nm and a stress of $\sigma^p = +56$ MPa were obtained for 80 nm film. Those values are plotted in **Fig. 4.4c**.

The obtained stress states for Mg films sputtered on Pd-foil were thickness independent. Furthermore, an effect of the Pd-foil bending on the film stress state is expected.
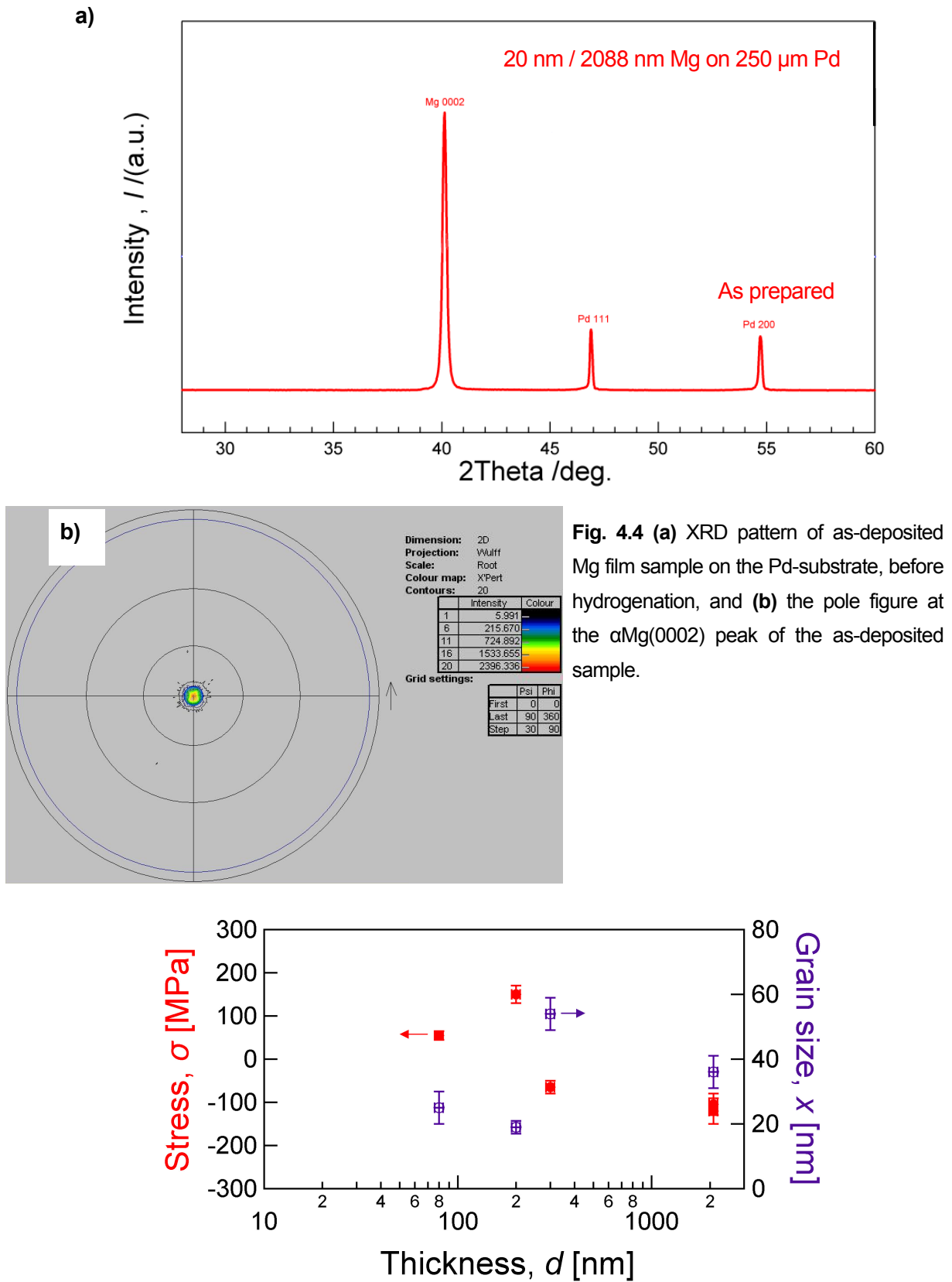
a)

b)

Fig. 4.4 (a) XRD pattern of as-deposited Mg film sample on the Pd-substrate, before hydrogenation, and **(b)** the pole figure at the αMg(0002) peak of the as-deposited sample.

Fig. 4.4c Calculated in-plane stress σ (filled red markers, left axis) and vertical grain size x (hollow violet markers, right axis) plotted versus Mg film thickness d, obtained for as-prepared samples from XRD peak position and peak width (FWHM), respectively.

5. Hydrogen loaded Mg films

In this section, the results of XRD measurements of Mg-films used for electrochemical- and gaseous hydrogenations will be presented. At first, samples with fully hydrogen-loaded states are briefly compared with those in the as prepared state. Then, the development of film properties (stress, thickness, EMF potential, and electrical resistivity) will be shown. Diffusivity of hydrogen will be discussed resulting from gas loading measurements, and subsequently also from permeation measurement. In the end, results of the *in-situ* measurements, performed at elevated temperatures, will be shown.

5.1 Comparison: as prepared-hydrogen loaded Mg films

5.1.1 Mg films on: Si-substrate

Fig. 5.1a shows the XRD peak of α-Mg(0002) for films deposited on a Si(001) substrate at T = 300 K without annealing process, before and after hydrogen loading cycle in the unloaded state. Decrease of α-Mg (0002) peak area and narrowing of the peak width is observed. The pole figure of the remaining α-Mg (0002) shows smaller intensity, keeping the original texture, which is also shown in **Fig. 5.1a** for a 2800 nm Mg film. *In-situ* measurement for this sample will be shown later in **Chap. 5.2.1.3**.
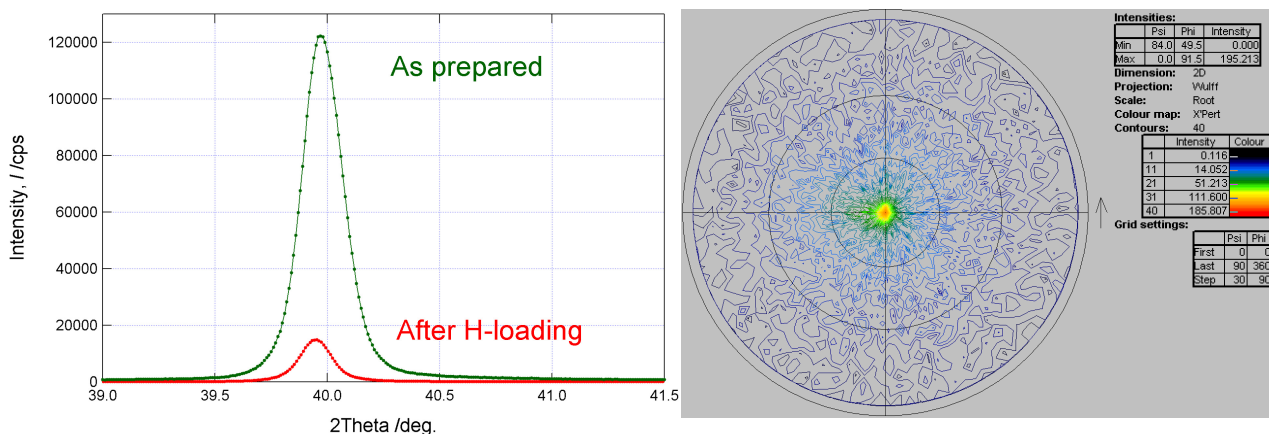

Fig. 5.1a XRD Bragg peak of αMg(0002) for the 2800 nm thickness Mg film, before and after hydrogen loading with the constant gas pressure of p_{H2} = 20 mbar for t = 33300 s (= 9.25 hours) at T = 300 K. Pole figure for loaded state is also shown in right picture.

The XRD peak change can be compared with that of an annealed sample, with same thickness. **Fig. 5.1b** shows the α-Mg(0002) peak of a 2800 nm Mg-film, annealed at T = 453 K for 30 minutes. The related as prepared state is shown in **Fig. 4.3c**. By hydrogen loading, the peak
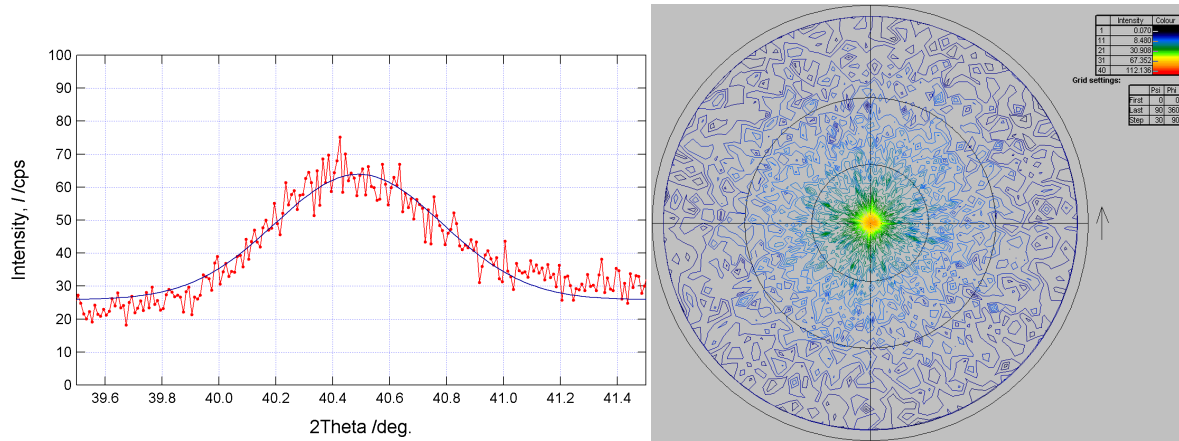
Fig. 5.1b The XRD peak of αMg-(0002) (left) and the corresponding texture measurement (right), obtained for the annealed 2800 nm Mg film, measured at $T = 300$ K (measured by the wavelength of CoKα, λ = 1.790263 Å). Fitting curve for the peak is also appended in the figure. The prepared state of this sample is shown in **Fig. 4.3b**.
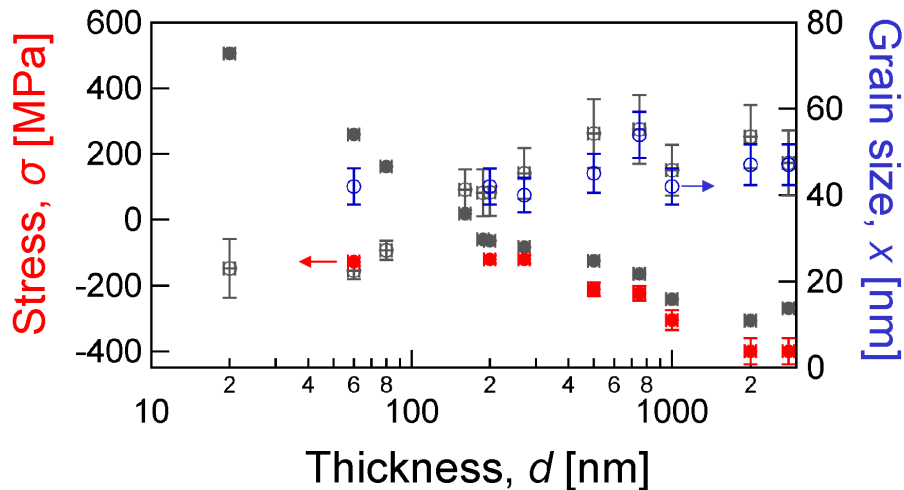

Fig. 5.1c Calculated in-plane stress σ (filled red markers, left axis) and vertical grain size x (hollow blue markers, right axis) for hydrogenated Mg film, plotted versus initial film thickness d, obtained for as-prepared samples from XRD peak position and peak width (FWHM), respectively. The σ-values before hydrogenated states (filled grey markers, left axis) and corresponding vertical grain sizes (hollow grey markers, right axis) are plotted together, for comparison.

maximum intensity decreased about 20 times. The α-Mg(0002) peak position shifted from $2\theta = 40.254$ degree to $2\theta = 40.494$ degree during hydrogen loading, which reveals an increase of the in-plane tensile stress of $\Delta\sigma^p = 362$ MPa (σ^p from 26 MPa to 388 MPa), using Eq.(3.8). Grain size decreased by gas loading from 45 ± 6 nm to 13 ± 2 nm, using Eq.(3.5).

Fig. 5.1c shows an overview of the obtained in-plane stress and grain sizes of partially hydrogenated Mg films with different thicknesses, measured in this work. Comparing with the as-prepared state, the in-plane stress decreases upon hydrogenation for all samples. Also, slight

decreases of the vertical grain sizes are visible.

Likewise, an overview of the in-plane stress and grain sizes of partially hydrogenated films obtained in this work are plotted in **Fig. 5.1d**. It clearly shows that the in-plane stress increases upon hydrogenation, for all of the annealed samples. This behavior differs from the stress development for films which were not annealed. Also, the decrease of the vertical grain sizes upon hydrogenation was larger than that for films without annealing process.

Thus, the stress development in Mg film also depends on the hydrogen loading process, such as hydrogen loading current conditions or the loading gas pressures, which will be shown later in this work. (see **Chap. 5.2.1.3.1** and **Chap. 5.3.2**)
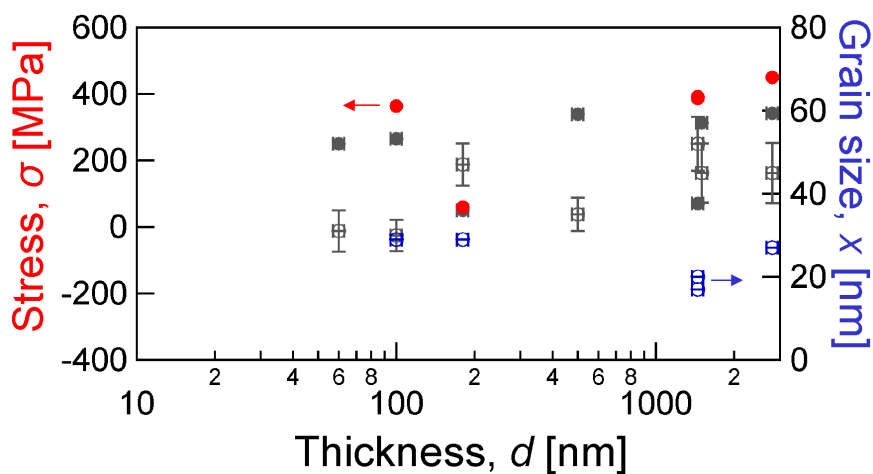

Fig. 5.1d Calculated in-plane stress σ (filled red markers, left axis) and vertical grain size x (hollow blue markers, right axis) for hydrogenated Mg film, plotted versus initial film thickness d, obtained for annealed samples from XRD peak position and peak width (FWHM), respectively. The σ-values before hydrogenated states (filled grey markers, left axis) and corresponding vertical grain sizes (hollow grey markers, right axis) are plotted together, for comparison.

5.1.2 Mg films on: Pd-substrate

In-plane stress and vertical grain size upon partial hydrogenation of Mg-films deposited on annealed Pd-foils were calculated and plotted as functions of film thickness in **Fig. 5.1e**, applying Eq.(3.8) and Eq.(3.5) to the results of *ex-situ* electrochemical hydrogen loading XRD measurements. Upon hydrogenation, the decreasing of α-Mg (0002) peak area and the broadening of the peak width were observed for all films. At the same time, a peak near $2\theta = 32.83$ appeared, increasing with hydrogenation state. This new peak was indexed as (110)-reflection of the β-MgH$_2$ phase. Further peaks of other magnesium hydrides were not obtained.

Fig. 5.1f exemplarily presents the XRD patterns for the 2088 nm sample, before and after

hydrogen loading. The grain size of α-Mg was calculated to be $36 \pm 3\,\text{nm}$, exhibiting a slight decrease compared with the as-prepared state. In-plane stress of the Mg-film calculated by Eq.(3.8) yielded $\sigma^p = -120\,\text{MPa}$ for α-Mg grains, which stays almost constant. The change
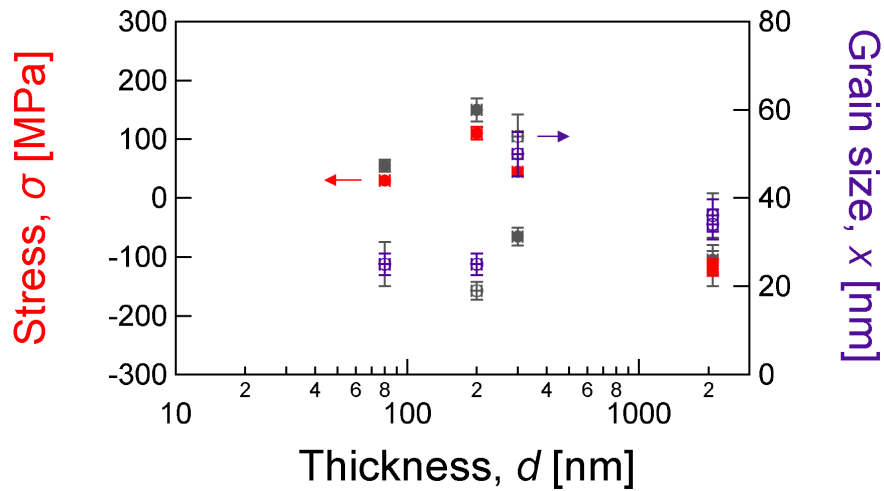

Fig. 5.1e Calculated in-plane stress σ (filled red markers, left axis) and vertical grain size *x* (hollow violet markers, right axis) for hydrogenated Mg film on Pd substrate, plotted versus Mg film thickness *d*, obtained from XRD peak position and peak width (FWHM), respectively. The σ-values before hydrogenated states (filled grey markers, left axis) and corresponding vertical grain sizes (hollow grey markers, right axis) are plotted together, for comparison.
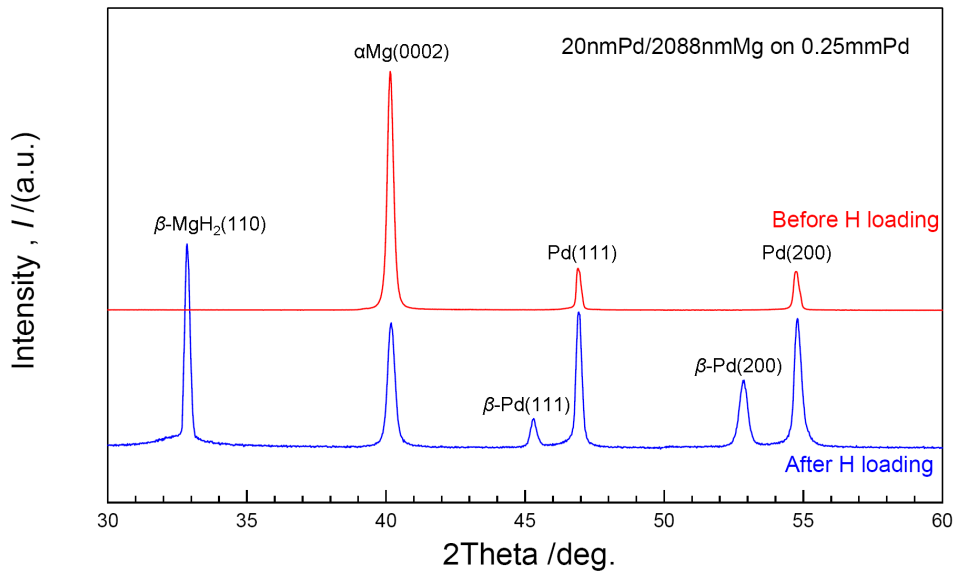

Fig. 5.1f Obtained XRD patterns for 2088 nm thick Mg film prepared on a Pd-substrate, before (red) and after hadrogen loading (blue). Identified phase is indexed for each reflection peak.

of in-plane stress and the vertical grain size were independent of the thickness of the Mg film.

Comparing equilibrium pressures (see **Fig. 2.3**), $PdH_{0.6}$ is more instable than MgH_2, and also diffusivity of hydrogen in Pd is more than 3 orders faster than in α-Mg, at room temperature (see

Fig. 2.4). Therefore, decomposition of Pd hydride is suggested to proceed preferentially, yielding no clear hydrogen induced expansion in this *ex-situ* XRD measurement. Therefore, an *in-situ* XRD measurement will be conducted for Mg films sputtered on Pd substrate in **Chap. 5.2.3**.

5.2 In-plane stress evolution upon hydrogen absorption

In this section, the results of the inner stress evolution of the Mg-films on hydrogenations will be presented. The in-plane stress changes in the Mg-films were measured and evaluated by three different ways, which are based on evaluations from the substrate curvature changes and on the X-ray techniques. (see **Chap.3.5**)

5.2.1 Mg films on Si-substrate

H-loading for nc- and annealed Mg-films on Si (100) substrate samples have been done by electrochemical- and gaseous hydrogen. The gaseous hydrogen loading condition is divided in two different conditions, which are 1) constant pressure conditions and 2) step-by-step pressure increase method. This section presents the results of electrochemical hydrogen loading, at first. Then, gas loading with the condition of step-by-step pressure increase (2) and with the constant gas loading pressure (1) will be shown. In the end, the results for nc Mg-films will be summarized.

5.2.1.1 Results of step-by-step electrochemical loading

In-situ step-by-step electrochemical hydrogen loading measurements were conducted for 1000 nm thick Mg-sample deposited on Si at room temperature. These measurements were done at the beamline P08 in DESY Petra III. Developments of $c_H = x$ H/Mg ($x = 0$, 0.02, and 0.3) were calculated from the loading condition, assuming solution of hydrogen into Pd surface layer with maximum concentration up to $PdH_{0.6}$ (H/Pd = 0.6).

The bragg peak evolution of the α-Mg(0002) and β-MgH$_2$(110) peaks in equilibrium states at different hydrogen concentrations of $c_H = x$ H/Mg ($x = 0$, 0.02, and 0.7), are shown in **Fig.5.2a**. At $c_H = 0.02$ H/Mg, a drastic intensity decrease of the α-Mg(0002) peak is found. For $x = 0.02$ and $x = 0.7$, the β-MgH$_2$(110) peak is observed, too.

θ-2θ scans at different tilting angle ψ were conducted for α-Mg(0002) peaks in equilibrium states at each hydrogen concentration, as shown in **Fig.5.2b**. The peak positions of all peaks are determined by fitting each curve with gaussian functions, and plotted as functions of $\sin^2\psi$ in **Fig. 5.2c**. By applying linear fitting for obtained d values, different slopes were determined for each state of the Mg films. By using Eq.(3.9), in-plane stress σ^t at $c_H = 0$ H/Mg (as prepared state), $c_H = 0.02$ H/Mg and $c_H = 0.7$ H/Mg were determined to be $\sigma^t = -103$ MPa, $\sigma^t = -251$ MPa and $\sigma^t = -376$ MPa, respectively. Thus, $\Delta\sigma^t = -273$ MPa is obtained as the total stress change upon loading up to $c_H = 0.7$ H/Mg. Therefore, the in-plane stress increases by increasing hydrogen concentration. The stress development is plotted in **Fig. 5.2d**.

Between $c_H = 0$ H/Mg up to $c_H = 0.02$ H/Mg , the slope of the stress change from is calculated to be $d\sigma^t/dc_H = -7.4$ GPa /(H/Mg). It is reduced from $c_H = 0.02$ H/Mg to $c_H = 0.7$ H/Mg to be only $d\sigma^t/dc_H = -183$ MPa /(H/Mg).

Also from the peak position shift of the α-Mg(0002) reflection, this tendency of the stress increase was visible. The peak position change from $2\theta = 22.083$ (at $c_H = 0$ H/Mg) to $2\theta = 22.074$ ($c_H = 0.02$ H/Mg) yields $d\sigma^p/dc_H = -6.58$ GPa /(H/Mg), and from $2\theta = 22.074$ ($c_H = 0.02$ H/Mg) to $2\theta = 22.07$ ($c_H = 0.7$ H/Mg) it yields $d\sigma^p/dc_H = -170$ MPa /(H/Mg), using Eq.(3.8).

Both σ^t and σ^p values change more strongly at lower c_H, compared to high c_H. At smaller hydrogen concentration, relationships of $d\sigma^t/dc_H = -7.4$ GPa /(H/Mg) and $d\sigma^p/dc_H = -6.58$ GPa /(H/Mg) have good correspondence, with the calculated relationships of $d\sigma/dc_H = -5.72$ GPa /(H/Mg), expected from linear elastic theory (see Eq.(2.41) in **Chap. 2.2**). At higher hydrogen concentration, $d\sigma^t/dc_H$ and $d\sigma^p/dc_H$ is in the same order, but contains an error of about 58% in the absolute value.

The curvature change was also measured by profilometer before and after hydrogen loading. The curvature changes from $\kappa = 1.413 \cdot 10^{-3}$ m^{-1} to $\kappa = 3.33 \cdot 10^{-2}$ m^{-1}, which corresponds to a stress change from $\sigma^{St} = -10$ MPa to $\sigma^{St} = -250$ MPa. Thus, the stress change was calculated to be $\Delta\sigma^{St} = 240$ MPa. This is similar to σ^t and σ^p.

Thus, an increase of compressive in-plane stress was observed upon hydrogen loading, by three different methods. An extraordinary large change was obtained at low c_H.

5.2.1.1.1 Reacted hydride fraction

A thickness increase upon hydrogenation to $x = 0.7$ for the same 1000 nm sample was measured to be $\Delta d = d' - d_0 = 102(\pm 15)$ nm, which corresponds to $c_H = 0.76(\pm 0.11)$ H/Mg calculated by Eq.(3.12b). The 8.5% difference of c_H between this value and loading condition of $c_H = 0.7$ H/Mg could result from assumption of a preferential solution of hydrogen in the Pd layer.
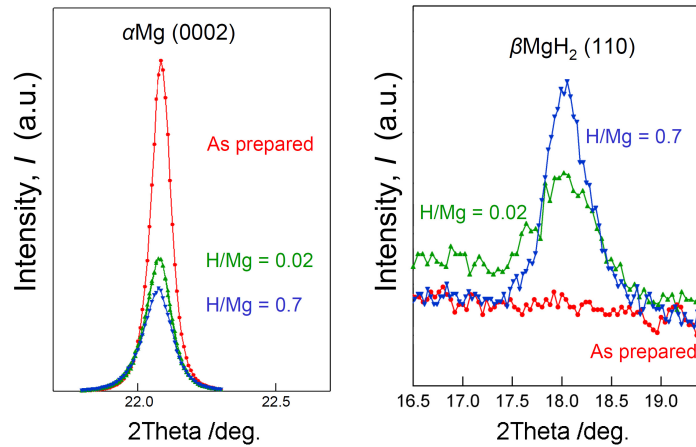
Fig.5.2a Bragg peak change of the αMg(0002) and βMgH$_2$(110) at different hydrogen concentration of $c_H = x$ H/Mg ($x = 0$, 0.02, and 0.7), drawn with red, green and blue, respectively, conducted for 1000 nm Mg film sputtered on Si (100) substrate at room temperature. As prepared state corresponds to $x = 0$, and the state without electrolyte on the surface is shown.
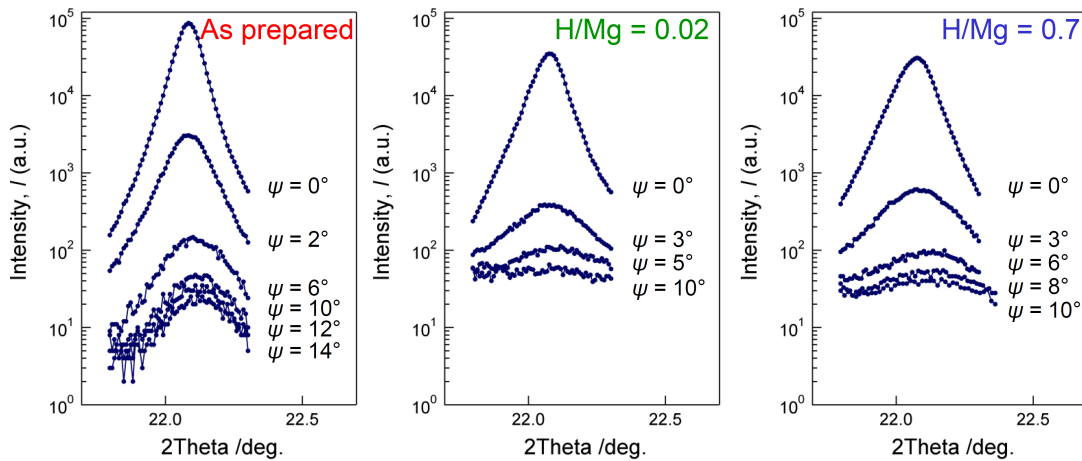

Fig.5.2b αMg(0002) peaks at different tilting angles ψ, at $c_H = 0$ H/Mg (as prepared, left), $c_H = 0.02$ H/Mg (middle), and $c_H = 0.7$ H/Mg (right). The corresponding atomic plane distances for each curve are plotted in **Fig. 5.2c**.

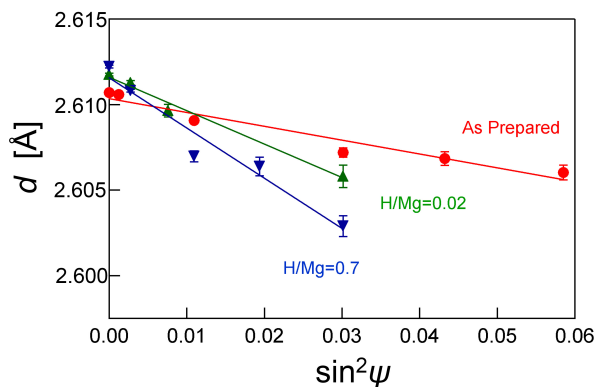**Fig. 5.2c** Obtained atomic distances of (0002) plane (d) from αMg(0002) peaks, as functions of $\sin^2\psi$, at $c_H = 0$ H/Mg (as prepared, red), $c_H = 0.02$ H/Mg (green), and $c_H = 0.7$ H/Mg (blue).
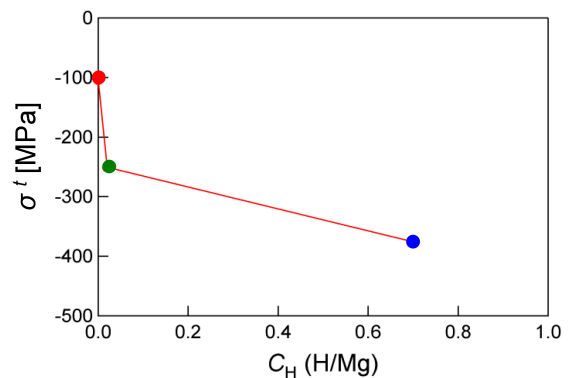
Fig. 5.2d The in-plane stress development during the step-by-step electrochemical hydrogen loading, calculated by Eq.(3.9) from the slope of the d-$\sin^2\psi$ plot, shown in **Fig. 5.2c**.

5.2.1.1.2 Hydride stability in air

The stability of the hydride in the sample was evaluated for the same sample, by comparing the stress change before and after leaving it in air at room temperature.

The film thickness change 1 month after hydrogen loading was measured to be $\Delta d \approx -20$ nm for the 1 μm film, which corresponds to a mean concentration of $c_H \approx 0.55$ H/Mg by Eq.(3.12b). Thus, the decrease of the hydrogen concentration in this sample was calculated to be $\Delta c_H = 0.21$ H/Mg, during leaving the sample in air.

The stress change was also measured by XRD techniques, by the peak shift, and a compressive stress relaxation of $\Delta \sigma^p \approx 50$ MPa was obtained during 1 month. The stress change determination by $\sin^2\psi$ method was also used for this sample (shown in **Fig.5.3a**), and a relaxation of compressive stress by $\Delta \sigma^t \approx 40$ MPa was obtained. Both values of $\Delta \sigma^p$ and $\Delta \sigma^t$ are about 20 % of the maximum relative stress change of the film by hydrogenation (see **Fig. 5.2d**), which explains the existence of a stable hydride phase remaining in Mg film.
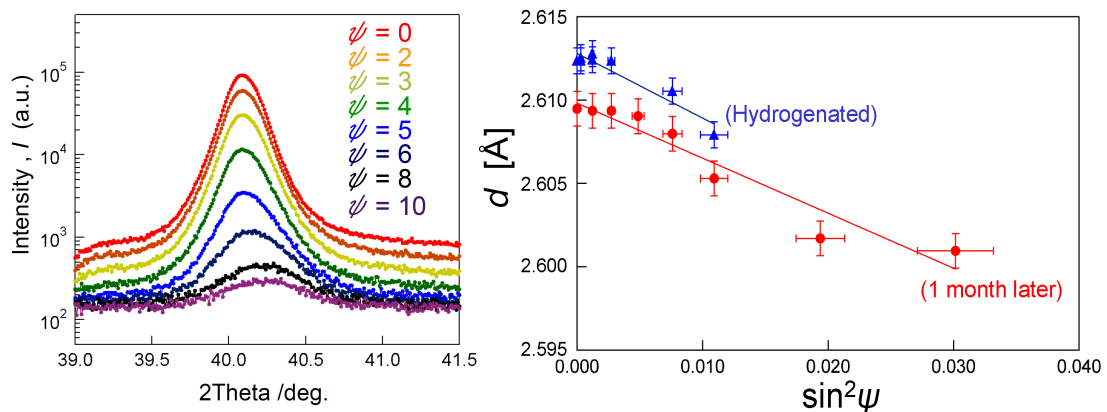

Fig.5.3a Bragg peak of αMg(0002) at different tilting angles ψ (ψ = 0°-10°) (left) and obtained d values of αMg(0002), measured for the sample which was left in air for 1 month after hydrogen loading (right, with red markers). The d values measured for the same sample right after hydrogenation are also plotted (right, with blue triangle), for comparison.

Furthermore, the optical property change due to the hydrogen loading was visible by eyes for all samples, which were prepared on Si-substrates at room temperature. An example will be shown later in **Fig. 5.13**, compared with as prepared state. This clear difference was visible typically for more than 5 hours in the air, at room temperature. After leaving the hydrogenated sample in air for more than 1 week, the appearance of these samples becomes optically metallic, and there were no clear difference by eyes with the as-prepared samples.

5.2.1.2 Results of step-by-step gas loading

Fig. 5.4 and **Fig. 5.5** shows the XRD results in equilibrium state at different hydrogen gas pressure of $p_{H2} = x$ mbar ($x = 0$, 3, 11.9 and 119), by means of step-by-step hydrogen gas absorption applied for nc Mg-films with the thickness of 200 nm and 60 nm sputtered on Si (100) substrate, respectively.
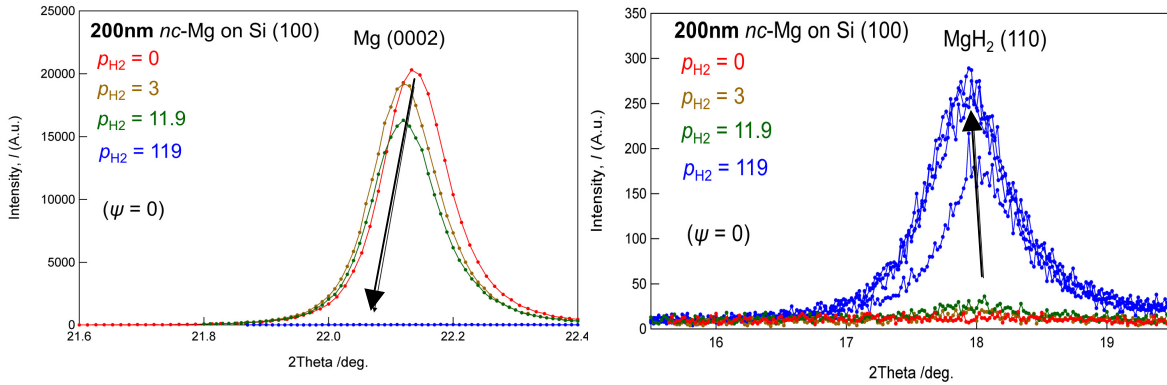

Fig. 5.4 Development of the XRD peaks of α-Mg(0002) (left) and β-MgH$_2$(110) (right) for 200nm thickness nc-Mg film, at p_{H2} = 0 mbar (red), p_{H2} = 3 mbar (brown), p_{H2} = 11.9 mbar (green) , and p_{H2} = 119 mbar (blue). Plots for β-MgH$_2$(110) at p_{H2} = 119 mbar contains additionally non-equilibrium states with proceeding indication. Measurements were conducted at HASYLAB PETRA beamline P08 with λ = 1Å. The black arrows indicate the progress of the peak change during the measurement.

Fig. 5.5 Development of the XRD peaks of α-Mg(0002) (left) and β-MgH$_2$(110) (right) for 60nm thickness nc-Mg film, at p_{H2} = 0 mbar (red), p_{H2} = 3.6 mbar (brown), p_{H2} = 11.9 mbar (green), and p_{H2} = 119 mbar (blue). Plots for α-Mg(0002) at p_{H2} = 119 mbar contain additionally non-equilibrium state. Measurements were conducted at HASYLAB PETRA beamline P08 with λ = 1Å. The black arrows indicate the progress of the peak change during the measurement.

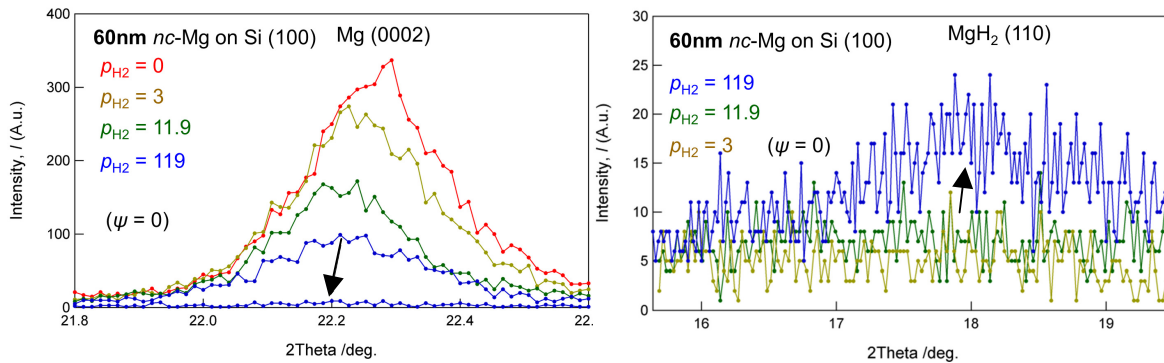The base pressure of the vacuum in the chamber before hydrogen gas introduction was for both sample $p_{H2} = 2 \times 10^{-5}$ bar, and this value is here treated as 0 bar. XRD peaks of α-Mg(0002)

reflection for both films exhibited a peak shift and the peak disappeared at the loading step of p_{H2} = 119 mbar.

For the 200 nm thick film, peak positions of α-Mg(0002) at equilibrium states are fitted to be 2θ = 22.143°, 22.122°, and 22.123° for each hydrogen pressure of p_{H2} = 0 mbar, 3 mbar, and 11.9 mbar, respectively (**Fig. 5.4** left side). Applying Eq.(3.8) for these peak shifts yields in-plane stress development of σ^p = -80 MPa, -141 MPa, and -138 MPa, respectively. The hydrogen concentration in the sample in equilibrium state under loading condition of p_{H2} = 3 mbar was calculated to be $c_H \approx 4 \cdot 10^{-2}$ H/Mg, by using the change of the Bragg peak area for α-Mg(0002) reflection. Therefore, $(d\sigma^p / dc_H) \approx$ -1.53 GPa/(H/Mg) was obtained for the first peak shift from p_{H2} = 0 mbar to p_{H2} = 3 mbar. Also, a slight increase of the tensile stress was visible in a further peak shift from p_{H2} = 3 mbar to p_{H2} = 11.9 mbar. The equilibrium pressure for the Mg-MgH$_2$ transition at given temperature is $p_{H2} \approx 0.1$ mbar (see **Fig. 2.3**). Therefore, the hydride phase is expected to nucleate at p_{H2} = 3 mbar, as is also confirmed by the appearance of the β-MgH$_2$(110) peak in **Fig. 5.4**. The stress development in the solid solution concentration regime was calculated to be $(d\sigma / dc_H)$ = -5.72 GPa/(H/Mg) by linear elastic theory (see Eq.(2.41) in **Chap. 2.2**), and comparable values are obtained in the step-by-step electrochemical loading measurements (described in **Chap. 5.2.1.1**). Therefore, the increase of in-plane stress in α-Mg grains is suggested to happen mainly in the solid solution concentration regime, and later it is relieved by plastic deformation in the early stage of hydride nucleation. The small value of the obtained concentration dependency of the stress change $(d\sigma^p / dc_H) \approx$ -1.53 GPa/(H/Mg) compared to the theoretical value can be explained by this process.

In the same way, the in-plane stresses in equilibrium states were also calculated for the α-Mg (0002) reflection of 60 nm thickness sample. Peak positions of the α-Mg(0002) are fitted to be 2θ = 22.269°, 22.246°, and 22.216° for p_{H2} = 0 mbar, 3 mbar, and 11.9 mbar, respectively (**Fig. 5.5** left side). Applying Eq.(3.8) for these peak shifts yields an in-plane stress development of σ^p = 278 MPa, 214 MPa, and 128 MPa, respectively. From the peak area change of the α-Mg(0002), the equilibrium hydrogen concentrations in the sample at p_{H2} = 3 mbar and p_{H2} = 11.9 mbar were calculated to be $c_H \approx 6 \cdot 10^{-2}$ H/Mg and $c_H \approx 8 \cdot 10^{-1}$ H/Mg, respectively. Therefore, the concentration dependency of stress change for first loading step was calculated to be $(d\sigma^p / dc_H) \approx$ -1.07 GPa/(H/Mg). This stress dependency on the concentration is also smaller compared to the expected value by Eq.(2.41), shown in the results for the 200 nm thickness sample. **Table 5.1** summarizes the concentration dependency of the stress change for each loading step and samples.

Table 5.1 Stress dependency on concentration at each loading step (unit in MPa/(H/Mg)), calculated from peak shift and Bragg peak area change of αMg(0002) for samples with Mg layer thickness of 200 nm and 60 nm. Equilibrium hydrogen pressures p_H (unit in mbar) at each step are also described. αMg(0002) peaks were disappeared after 3rd loading.

Loading steps	Mg-film thickness	
	200 nm	60 nm
($p_H = 0$)		
($p_{H,1} = 3$)	$d\sigma^p/dc_H = -1530$	$d\sigma^p/dc_H = -1070$
($p_{H,2} = 11.9$)	$d\sigma^p/dc_H = 10$	$d\sigma^p/dc_H = -114$
($p_{H,3} = 119$)	---	---

The stress change was also obtained by the $\sin^2\psi$-method. **Fig. 5.6** shows the results of the diffraction measurements conducted for α-Mg(0002) and β-MgH$_2$(110) peaks of 200 nm and 60 nm thickness nc-Mg films, by changing ψ-angle in the range of $\psi = 0^\circ\text{-}10^\circ$. The position of $\psi = 0^\circ$ was previously individually determined, to the maximum peak intensity position, in equilibrium states at each hydrogen loading step. The maximum offset change due to this process was 0.2 degree for the α-Mg(0002) peaks, and 2 degrees for the β-MgH$_2$(110) peaks. The fitting curves to determine the 2θ-positions for each peak are also implemented in those figures.

By fitting all peaks for each ψ-position in **Fig. 5.6**, $\sin^2\psi$-plots are obtained. **Fig. 5.7** summarizes the $\sin^2\psi$-plots for the α-Mg(0002) and the β-MgH$_2$(110) peaks of the 200 nm and 60 nm thickness nc-Mg films. For the 200 nm sample at $p_{H2} = 11.9$ mbar, before hydride nucleation (non-equilibrium state) is plotted with brown line. Increases of the compressive stress by increasing the hydrogen concentration are observed. This is also obtained by calculation of the peak shift.

The atomic plane distance for the β-MgH$_2$(110) was calculated to be 3.216 Å, which is an expansion of about 7.5 % compared to the theoretical value (see **Fig. 3.17**). Applying this expansion to Eq.(2.55) yields $\sigma^p \approx -580$ MPa for a 200 nm sample. Furthermore, the in-plane stress calculation by peak shift (Eq.(3.8)) are also applied for the β-MgH$_2$(110) peak for 200 nm and 60 nm samples, and were calculated to be $\sigma^p = -1.75$ GPa and $\sigma^p = -1.28$ GPa, respectively. $\sigma^t = -1.72$ GPa, is also obtained for the 200 nm sample, applying $\sin^2\psi$-method (shown in **Fig. 5.7**). **Table 5.2** compares the obtained stress values of both samples at each hydrogen loading step.

Table 5.2 Obtained stress by peak shift (σ^{p}) and $\sin^{2}\psi$ method (σ^{t}) at different concentrations (unit in MPa/(H/Mg)), calculated for Bragg peaks of α-Mg(0002) and β-MgH$_2$(110), for 200 nm- and 60 nm samples.

		200 nm sample		60 nm sample	
		αMg(0002)	βMgH$_2$(110)	αMg(0002)	βMgH$_2$(110)
(Vac.)	σ^{p}	-80	------------	278	------------
	σ^{t}	-110	------------	-40	------------
p_{H2} = 3 mbar	σ^{p}	-141	------------	214	------------
	σ^{t}	------------	------------	------------	------------
p_{H2} = 11.9 mbar	σ^{p}	-138	-150	128	------------
	σ^{t}	-120	------------	-40	------------
p_{H2} = 119 mbar	σ^{p}	------------	-1750	-128	-1280
	σ^{t}	------------	-1720	-110	------------

5.2.1.2.1 Reacted hydride fraction

Fig. 5.4 and **Fig. 5.5** show by the complete disappearance of the α-reflection, that the Mg films are completely hydrided. The reacted fraction is also evaluated from the resistivity change. **Fig. 5.8** shows the time change of the resistivity measured for both samples during the step-by-step loading. On one hand, by using Eq.(3.13a) directly for the resistivity results, the hydride content in the last state was calculated as $f_{MgH_2} = 0.237$ for 200 nm film ($R/R_0 = 10$), and $f_{MgH_2} < 0$ for the 60 nm film ($R/R_0 = 2.7$). On the other hand, by using Eq.(3.13b), $d_{MgH_2} = 195$ nm ($f_{MgH_2} = 0.975$) for 200 nm film ($R/R_0 = 10$), and $d_{MgH_2} = 54$ nm ($f_{MgH_2} = 0.9$) for 60 nm film ($R/R_0 = 2.7$). This results supports that using a parallel layer model is a suitable assumption, for the hydrided Mg film.

Additionally, increases of the thickness by hydrogen loading for the 200 nm and the 60 nm Mg film were measured to be $\Delta d = 52(\pm 4)$ nm and $\Delta d = 11(\pm 4)$ nm, which corresponds to $c_{H} = 1.93(\pm 0.08)$ and $c_{H} = 1.36(\pm 0.5)$ respectively, using Eq.(3.12b). This yields a hydride layer with a thickness of 193 nm for 200 nm film and 41 nm for 60 nm film, assuming the parallel layer model (see **Fig. 3.19**).
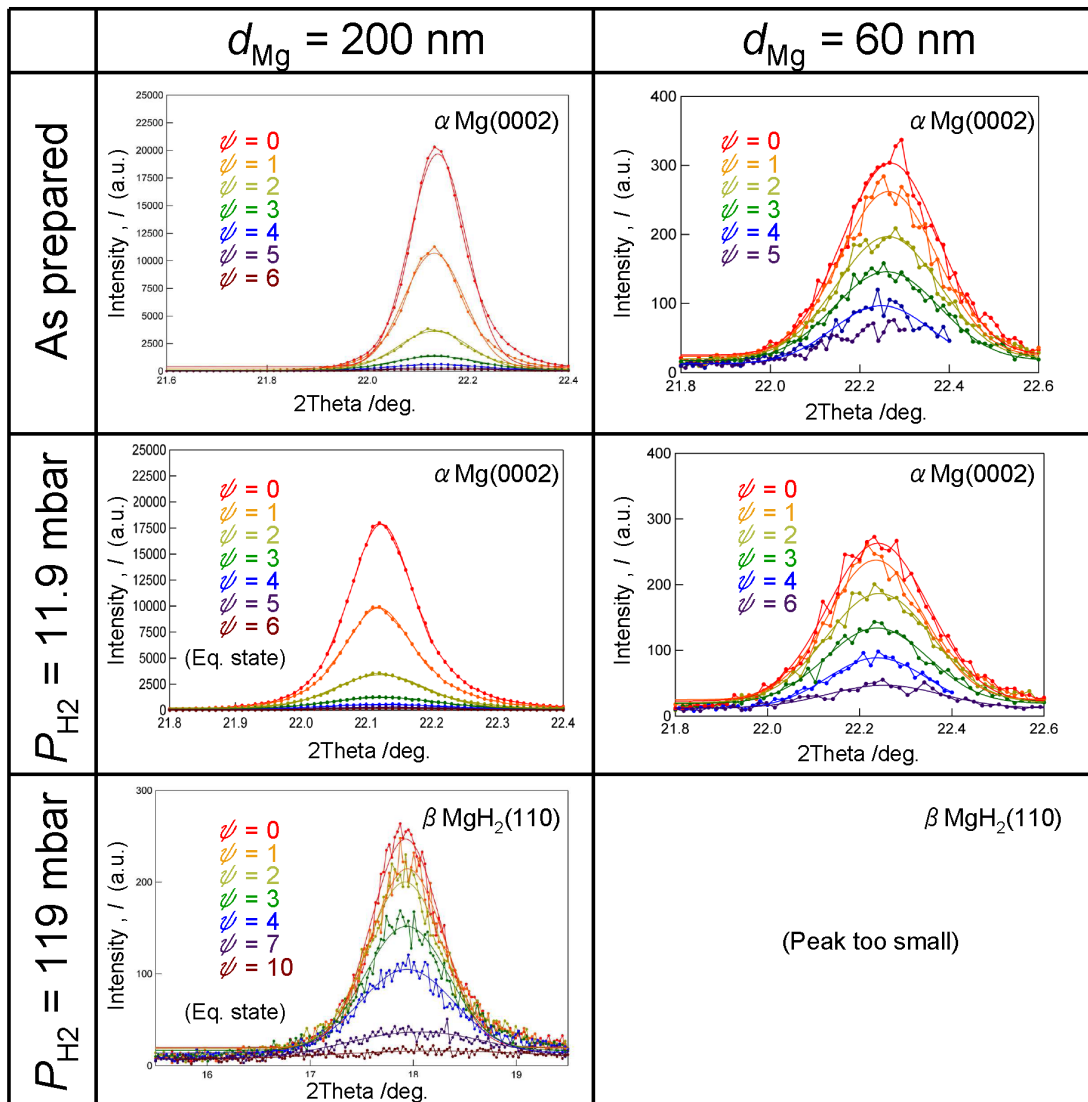
Fig. 5.6 XRD peaks of αMg(0002) and βMgH$_2$(110) at different tilting angle ψ ($\psi = 0°$-$10°$) for d_{Mg} nm thickness nc-Mg film (d_{Mg} = 200, 60) deposited on Si (100) substrate, measured in equilibrium states of each loading pressure steps at p_H mbar (p_H = 11.9, 119) and at vacuum condition (as prepared). Fitted curve to determine peak position is also plotted together as curve without dots.
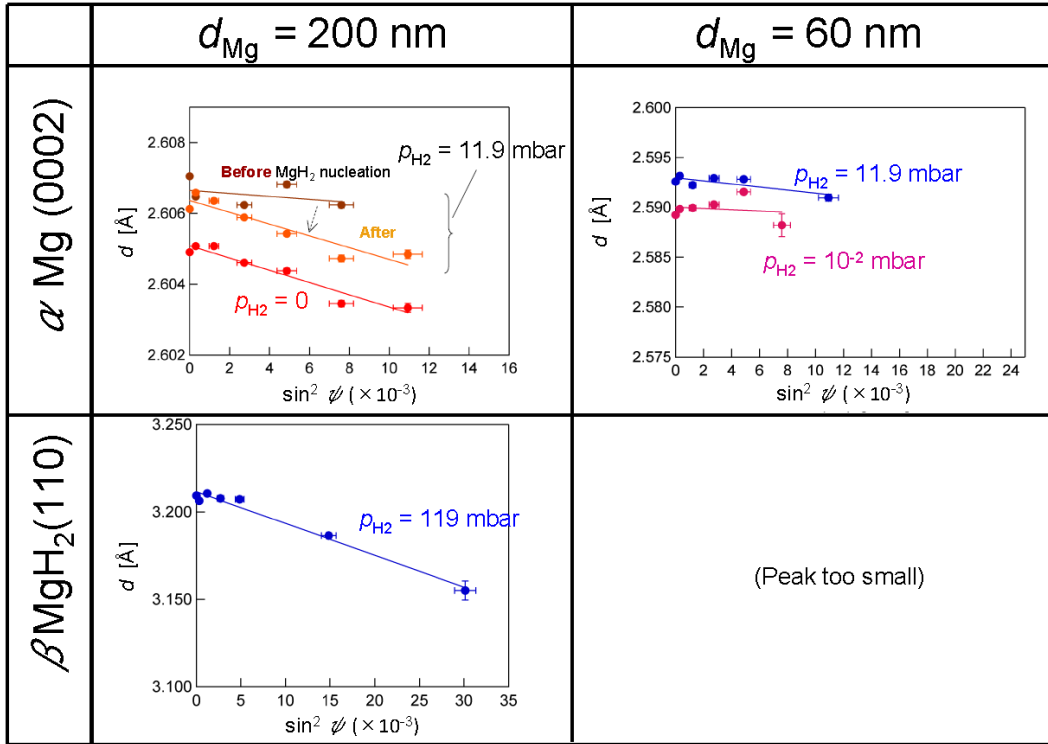
Fig. 5.7 $\mathrm{Sin}^2\psi$ plots for αMg(0002) and βMgH$_2$(110) peaks for d_{Mg} nm thickness nc-Mg film (d_{Mg} = 200, 60) deposited on Si (100) substrate, measured in equilibrium states of each loading pressure steps at p_H = x mbar (x = 11.9, 119) and at vacuum condition (as prepared). Fitting lines to determine slopes are implemented. For 200 nm sample at p_H = 11.9 mbar, before hydride nucleation (non-equilibrium state) is plotted with brown.
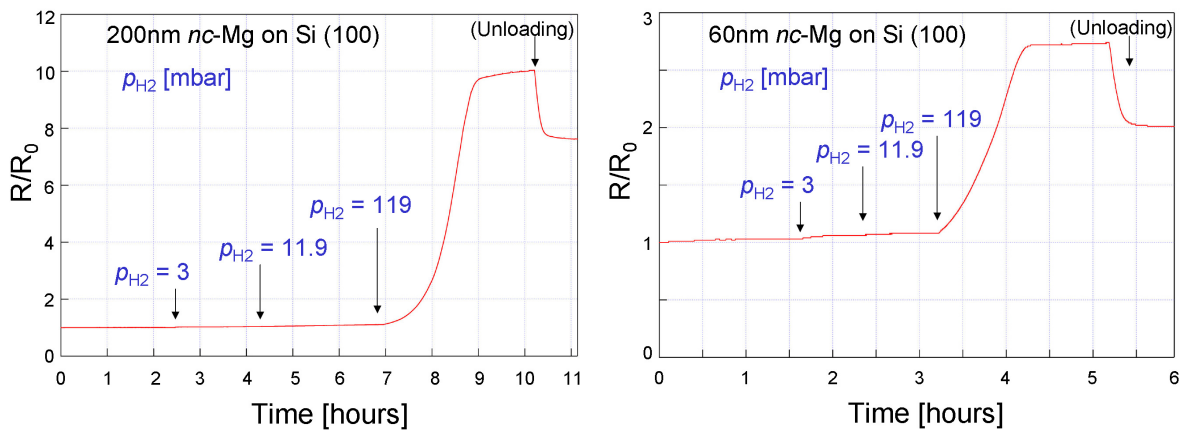

Fig. 5.8 Resistivity change measured for nc-Mg film with thickness of 200 nm (left) and 60 nm, during step-by-step H$_2$ gas loading, measured by means of four-point measurement at room temperature. Loading pressure conditions are written in the picture with blue letters.

5.2.1.3 Results of constant gas-pressure loading: hydride formation kinetics

Fig. 5.9a shows the XRD peak shift of the α-Mg(0002) peak for a 2800 nm thick Mg film, during hydrogen loading with a constant pressure of p_{H2} = 20 mbar at T = 300 K. This loading pressure is far above the hydride formation pressure of β-MgH$_2$ (p_{H2} = 10^{-2}-10^{-1} mbar T = 300 K), see details in **Fig. 2.12** in **Chap. 2.1.5.3**. The sample was deposited on a Si substrate with the thickness of 0.5 mm at room temperature. Reaction time t = 0 indicates the beginning of the reaction, and the averaged value of the beginning and at the end of each scan is used as further values of t. Each reaction time regime was indicated with different colours in this picture. The peak shifts to lower angles almost monotonically, decreasing the peak area as the hydrogenation reaction proceeds. This decrease of the α-Mg(0002) peak can be directly interpreted as the phase transition to the β-phase, since the hydrogen solubility in the α-Mg is almost negligible (see **Chap. 2.1.5.1**). A layer thickness of the β-MgH$_2$ reached almost 2000 nm, as calculated from the peak area change with Eq.(3.6).

The time change of the in-plane stress in the α-Mg phase, calculated from the same measurement for the same sample by Eq.(3.5), is shown in Fig. 5.9b. Colours indicating each time regimes corresponds to the same reaction times, t. The in-plane stress change at each curves is increased by about $\Delta\sigma^p$ = 50 MPa from t = 0 s to t =33300 s (= 9.25 h).
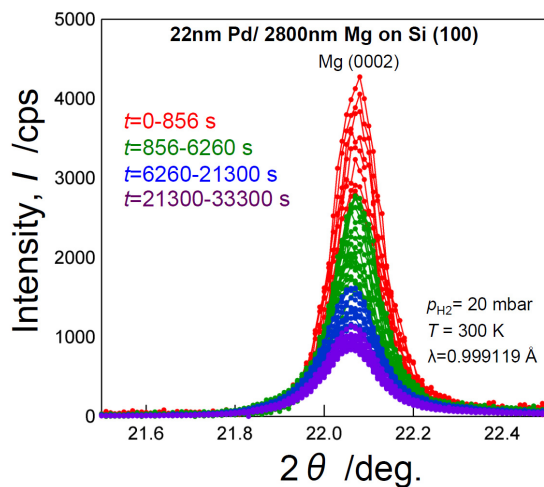
Fig. 5.9a XRD peak shift of the αMg(0002) peak for the 2800 nm thickness Mg film, during hydrogen loading with the constant gas pressure of p_{H2} = 20 mbar at T = 300 K, at different loading time t. Plots are colored by red for t = 0-856s (= 0-0.24hour), by green for t = 856-6260s (= 0.24-1.74hour), by blue for t = 6260-21300s (= 1.74-5.92hour), and by violet for t = 21300-33300s (= 5.92-9.25hour). A constant wavelength of λ = 0.999119 Å was applied at the beamline HASYLAB B2.

Fig. 5.9b Time change of the in-plane stress in the αMg phase, during hydrogen gas loading of 2800nm Mg film with p_{H2} = 20 mbar at T = 300 K, as a function of loading time t, calculated from the XRD peak shift of the αMg(0002), with Eq.(3.8).

The in-plane stress change of the same sample was also calculated by the $\sin^2\psi$ method, using Eq.(3.9), which is shown in **Fig. 5.9c**. This measurement was carried out fo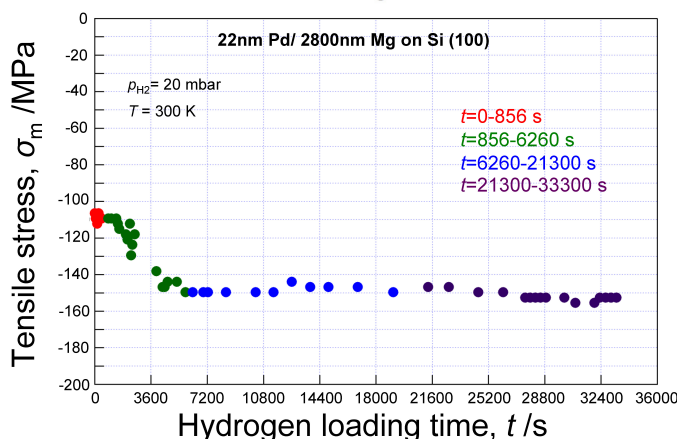r the α-Mg(0002) peak of the as-prepared and the hydrogenated sample, with the Co-Kα ($\lambda = 1.790263$ Å) wavelength at different tilt-angles ψ from 0 to 6 degrees. The compressive stress σ^t, obtained from the slope of the linear fits, increased from $\sigma^t = -705$ MPa to $\sigma^t = -761$ MPa, before and after hydrogenation. The increase of the compressive is therefore obtained as $\Delta\sigma^t = 55$ MPa, which is in good agreement with the value that calculated from the peak shift.
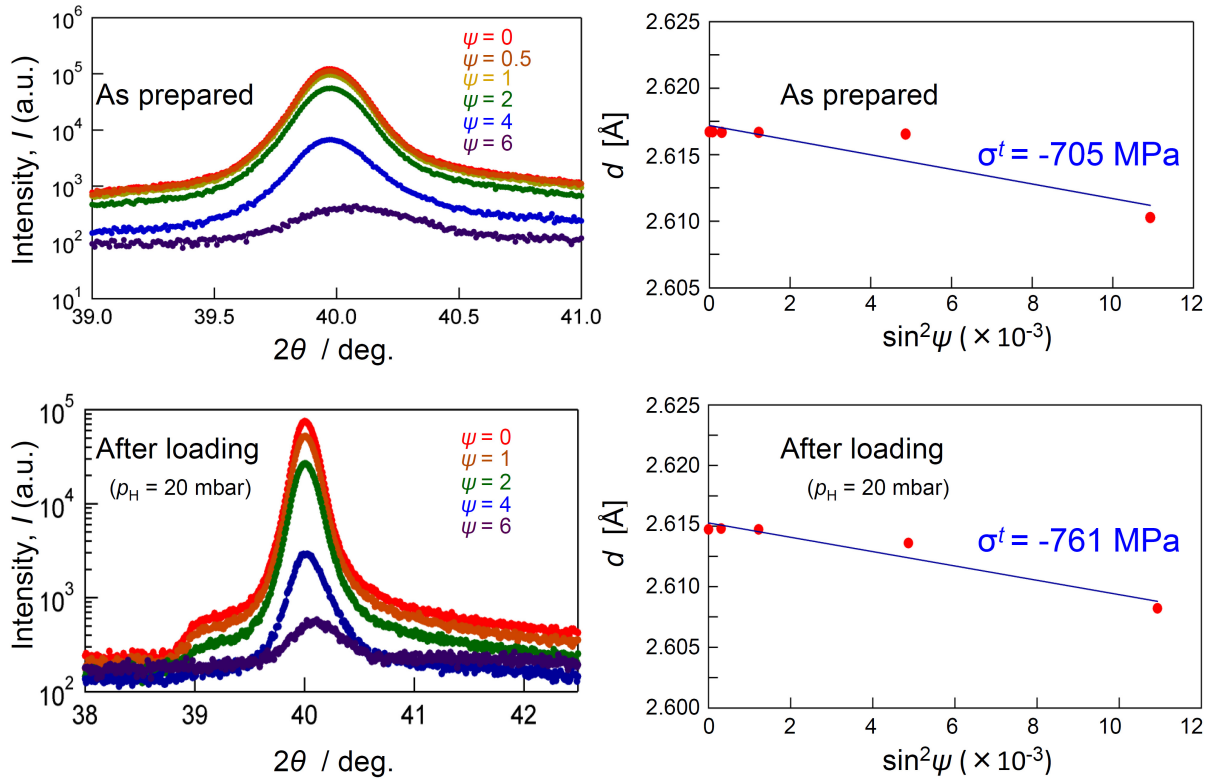

Fig. 5.9c Obtained αMg(0002) XRD peak and calculated atomic plane distance d, at different steps of tilting angle ψ of range from 0 to 6 degrees, before (upper side) and after hydrogenation of 2800nm Mg film with a constant hydrogen pressure $p_{H2} = 20$ mbar at $T = 300$ K. Indicated stress values with blue fonts are calculated from the slope by linear fitting of d against $\sin^2\psi$, applying Eq.(3.9).

Furthermore, the curvature difference of the same sample was measured by the profilometer. The obtained average curvature radius changed from $\kappa = 602(\pm100$) m to $\kappa = 490(\pm80$) m by hydrogenation. This curvature change indicates an increase of the compressive stress in the in-plane direction from $\sigma^{St} = -415$ MPa to $\sigma^{St} = -510.2$ MPa, applying Stoney's equation, which is presented in Eq.(3.10). The change of the in-plane stress is therefore obtained as $\Delta\sigma^{St} = 95$ MPa. This value is in a similar range with $\Delta\sigma^p$ and $\Delta\sigma^t$, since this measurement results contain the whole error of +/- 25 MPa in this case. Their values are involved in **Table 5.3** to compare with other obtained stress values of $\Delta\sigma^p$, $\Delta\sigma^t$, and $\Delta\sigma^{St}$ for different Mg thickness films deposited on Si substrate.

Table 5.3, summarizes the values of stress changes from the as-prepared state to the hydrogenated

Table 5.3 Obtained inner stress change before and after hydrogenation (unit in MPa) in different x nm thick Mg films (x = 60,100,200,500,1000,1400,2800) on Si substrate, sorted by different methods (see **Table 3.5**) and by different hydrogen loading methods, measured at T = 300 K for samples prepared with-/without annealing treatment process. With respect to the gas loaded samples, it is noted that the stress change also depends on the gas loading pressures, as will be described later in this section.

$$\Delta\sigma \text{ upon hydrogenation (unit: MPa)}$$

Sample (As-prepared thickness)		Gas Loading			Electrochem. loading (Step by Step)		
		$\Delta\sigma^t$	$\Delta\sigma^{St}$	$\Delta\sigma^p$	$\Delta\sigma^t$	$\Delta\sigma^{St}$	$\Delta\sigma^p$
2800nm	Dep. at RT	-55	-95	-10~ -50			
	Annealed	~+2500	---	+750~+2000			
1400nm	Dep. at RT	-180		-250			-250~ -400
	Annealed						
1000nm	Dep. at RT				-270~ -320	-240	-125~ -450
	Annealed						
500nm	Dep. at RT	-60	-100	-10~ -80			
	Annealed						
200nm	Dep. at RT	-60	-100	-60			
	Annealed	0±10	---	0±10			
100nm	Dep. at RT	(Peak not available)			(Peak not available)		
	Annealed	+132	---	+125			
60nm	Dep. at RT	(Peak not available)			-100	-200	-60~ -110
	Annealed	(Peak not available)			(Peak not available)		

state, for all Mg films on Si-substrates, as treated in this work. It can be seen that $\Delta\sigma^t, \Delta\sigma^{St}$ and $\Delta\sigma^p$ for films deposited at room temperature has negative values, for all cases, which indicates the increase of compressive stress by hydrogenation, regardless of the hydrogen loading techniques. Also, those different stress values for each film are similar, and the reliability of stress values is ensured. Results for annealed samples will be shown later in **Sec. 5.2.2**.

Focusing on the stress development during hydrogen loading, **Fig. 5.9a** and Fig. 5.9b show that the reaction kinetics and the stress change are larger in the beginning of loading, and smaller in the end. However, the loading hydrogen gas pressure is also known to be a factor to control hydride growth during hydrogenation reaction [Bloch97], for the metal-hydrogen system. The *in-situ* XRD measurements allow to see the effect of the loading hydrogen gas pressure on the reaction kinetics.

Fig. 5.10 presents the diffraction peak evolution depending on the loading time for a 2800 nm Mg-film and for a 500 nm Mg film for 2 different hydrogen loading pressures of p_{H2} = 20 mbar Pa and p_{H2} = 200 mbar, respectively, at T = 300 K. The data contain information about diffusion constants and the related stress development. The stress development in the α-phase with time at

constant hydrogen gas pressure is determined for each film from the peak shift of the α-Mg (0002) lattice reflection. **Fig. 5.11** summarize the stress state as calculated by using Eq.(3.8), for the two different film thicknesses (**a** for 500 nm and **b** for 2800 nm) and the two loading pressure conditions ($p_{H2}=$ 20 mbar and $p_{H2}=$ 200 mbar), as a function of square root of the loading time $\sqrt{t}$. The 2800 nm-thick sample loaded by $p_{H2}=$ 20 mbar corresponds to the sample shown in **Fig. 5.9a, Fig. 5.9b** and **Fig. 5.9c**.

As shown in **Fig. 5.10**, for all measurements the peak area shrinks upon hydrogen exposure, verifying hydrogen absorption in Mg and the hydride formation. **Fig. 5.12** shows the relative peak area change of the α-Mg (0002) plotted as a function of the square root of the hydrogen gas loading time, obtained from the *in-situ* XRD measurements shown in **Fig. 5.10**. The results on Mg films with thickness of 2800 nm (circles) and 500 nm (triangles) are presented, for comparison. The results for the samples loaded at $p_{H2}=$ 200 mbar are marked in bold red, and results for the samples loaded at $p_{H2}=$ 20 mbar are marked with blue open sign.

The time-dependency of the peak area development reveals two different regimes distinguishable by different linear slopes. These regimes are denoted as I and II, and attributed to two different regimes of absorption kinetics. For each film the hydrogen absorption regime change, $\sqrt{t_I}^{200}$ or $\sqrt{t_I}^{20}$ for $p_{H2}=$ 200 mbar or $p_{H2}=$ 20 mbar, respectively, is marked with straight lines.

The time dependency of the stress-state is more complex. As shown in **Fig. 5.11 a)**, the initial
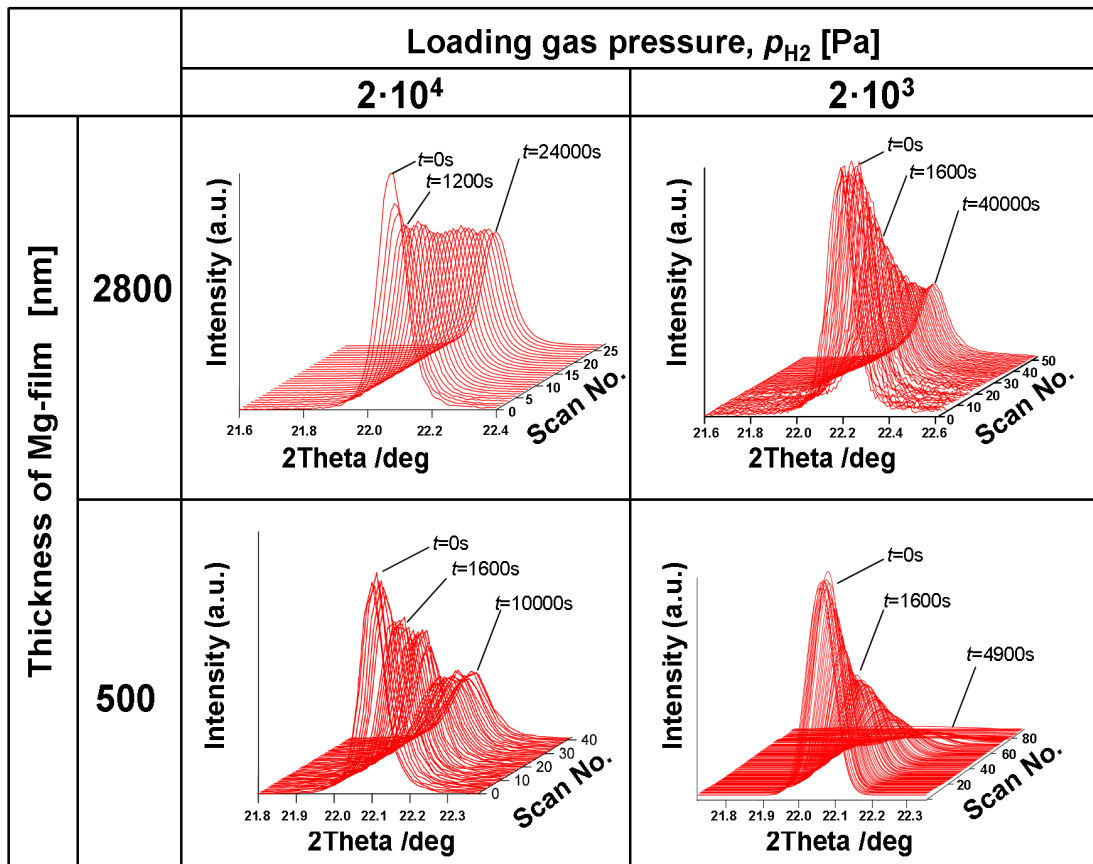

Fig. 5.10 The evolution of the αMg-0002 peaks during hydrogenation, for the sample thickness of 2800 nm and 500 nm, constant hydrogen gas pressures applied with 200 mbar and 20 mbar. Plateau H_2 pressure of Mg at T = 300 K is 10^{-5} mbar.

a)

b)
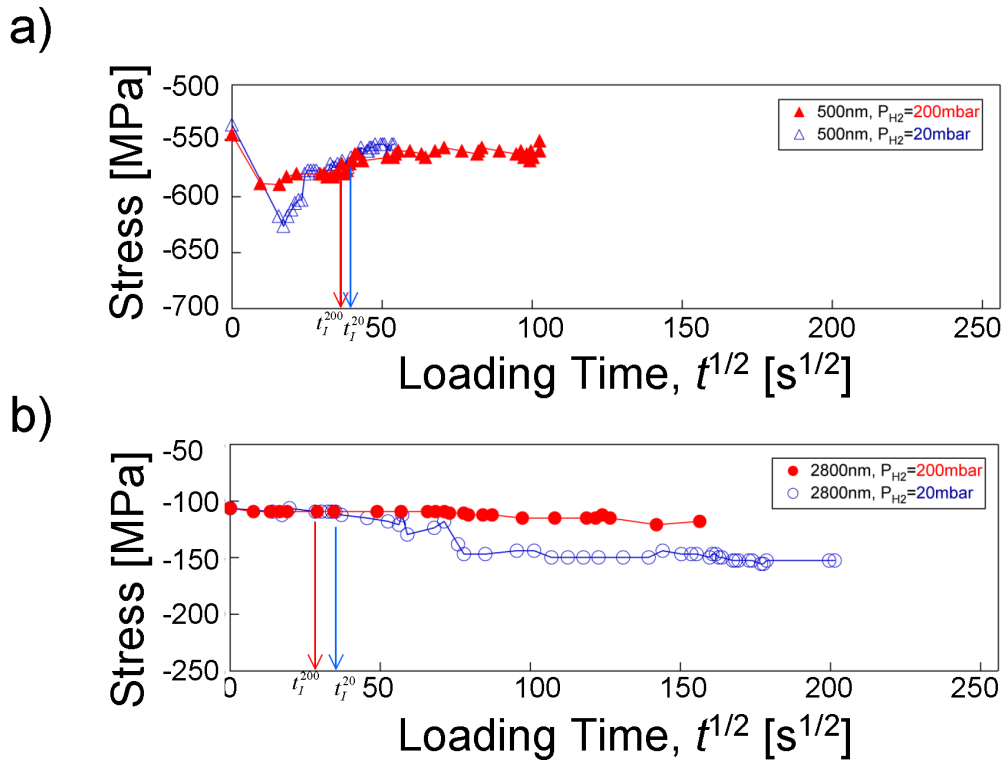
Fig. 5.11 The in-plane stress states as calculated from the peak shift of the α-(0002) lattice reflections for the samples shown in **Fig. 5.10**, with the thickness of **a)** 500 nm films in triangles, and **b)** 2800 nm films in circles, as a function of square root of the loading time $\sqrt{t}$. Arrows mark the transition between different kinetics regimes.
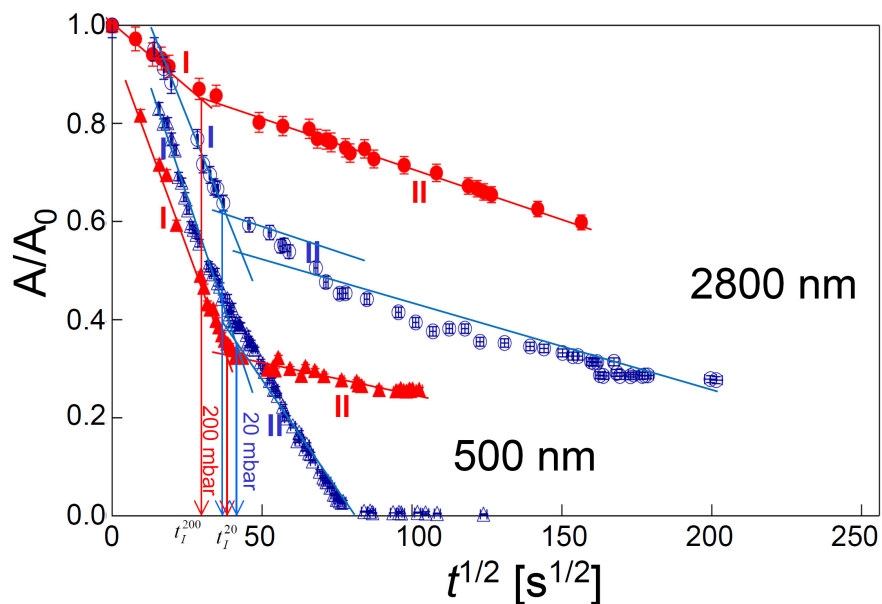
Fig. 5.12 The relative peak area change of the α-Mg (0002) as function of the square root of the hydrogen gas loading time, obtained from the *in-situ* XRD measurements (shown in **Fig. 5.10**), for Mg films of 2800 nm (circles) and Mg films of 500 nm (triangles). For 200 mbar hydrogen loading pressure (bold red) and 20 mbar hydrogen loading pressure (blue open) the hydrided volumes differ strongly. For details see text.

stress of the 500 nm film is about $\sigma^p \approx$ -540 MPa. Upon hydrogen exposure the α-phase turns into an even more compressed state. It reaches $\sigma^p =$ -590 MPa for the sample loaded at $p_{H2} =$ 200 mbar, and even $\sigma^p =$ -635 MPa for the sample loaded at $p_{H2} =$ 20 mbar. Further on, the compressive stress in the α-phase decreases until it reaches a constant value close to the initial stress state. The constant value is reached after a time that corresponds to $\sqrt{t_I}^{200}$ or $\sqrt{t_I}^{20}$, as marked in **Fig. 5.12** by arrows.

The initial stress of the 2800 nm film is about $\sigma^p \approx$ -80 MPa. It stays nearly constant for the sample loaded at $p_{H2} =$ 200 mbar. For the sample loaded at $p_{H2} =$ 20 mbar, it slightly changes to a more compressive state. In total, the effect is much less pronounced for the 2800 nm film.

As discussed in the following, the different stress states during hydrogen loading can be related to the changes of the hydride morphology in the films. With respect to these hydride morphology changes, a model is established to explain hydrogen absorption process. Details will be described in **Chap. 6.3**.

5.2.1.3.1 Reacted hydride fraction

The reacted volume fractions for both of 2800 nm and 500 nm samples were evaluated by different methods. At first, the increases of the film thickness for the 2800 nm thick samples were measured by a profilometer to be $\Delta d = 280(\pm 14)$ nm for the sample loaded at $p_{H2} =$ 200 mbar and $\Delta d = 420(\pm 30)$ nm for the sample loaded at $p_{H2} =$ 20 mbar. Applying Eq.(3.12b), these changes correspond to a mean concentration of $c_H = 0.75(\pm 0.03)$ H/Mg and $c_H = 1.11(\pm 0.08)$ H/Mg, respectively. This yields hydride fractions of $f_{MgH_2} = 0.37$ for the sample loaded at $p_{H2} =$ 200 mbar, and $f_{MgH_2} = 0.55$ for the sample loaded at $p_{H2} =$ 20 mbar, respectively. Second, from the α-Mg(0002) Bragg peak area decay, the volume fractions are calculated to be $f_{MgH_2} \approx 0.4$ and $f_{MgH_2} \approx 0.75$, respectively.

Likewise, increases of thickness by hydrogen loading for 500 nm Mg film were also obtained: They are $\Delta d = 78(\pm 12)$ nm for the sample loaded at $p_{H2} =$ 200 mbar and $\Delta d = 112(\pm 20)$ nm for the sample loaded at $p_{H2} =$ 20 mbar. Applying Eq.(3.12b), these changes correspond to a mean concentration of $c_H = 1.16(\pm 0.18)$ H/Mg and $c_H = 1.67(\pm 0.3)$ H/Mg, respectively. This yields a hydride fraction of $f_{MgH_2} = 0.58$ for the sample loaded at $p_{H2} =$ 200 mbar, and $f_{MgH_2} = 0.89$ for the sample loaded at $p_{H2} =$ 20 mbar, respectively. From the α-Mg(0002) Bragg peak area decay, they are calculated to be $f_{MgH_2} \approx 0.75$ and $f_{MgH_2} \approx 0.89$, respectively.

Calculated values of reacted hydride fractions, and achieved hydride thickness for both of 2800 nm and 500 nm samples are listed in **Table 5.4**.

The f_{MgH_2} values obtained by thickness measurement are 7% up to 25% smaller compared to the values obtained by XRD peak area. The film thickness decrease after 2 weeks was only 5% in maximum, which is almost the error of the thickness measurement with the used profilometer. This supports the adequate stability of the hydride phase if the formation of MgH_2 is assumed.

Therefore, the hydride phase fraction is treated to be constant for these measurements. Instead of hydride phase decomposition, the surface roughness change is due to the existence of volume expanding hydride precipits. This is suggested to make an effect of decreasing α-Mg(0002) peak areas.

Thirdly, the fractions of the hydride phase (f_{MgH_2}) were also calculated from the relative resistivity measurements. The relative resistivity changes of 2800 nm samples were measured to be $R/R_0 = 1.7$ and $R/R_0 = 2.2$, for 200 mbar loading pressure and for 20 mbar loading pressure, respectively. Applying Eq.(3.13b), hydride fractions of $f_{MgH_2} = 0.4$ and $f_{MgH_2} = 0.55$ were obtained, respectively. Likewise, for 500 nm Mg samples, $R/R_0 = 3.6$ and $R/R_0 = 14$ were measured for 200 mbar loaded sample and 20 mbar loaded sample. Applying Eq.(3.13b), hydride fractions of $f_{MgH_2} = 0.75$ and $f_{MgH_2} = 0.95$ were calculated, respectively. These calculated values of hydride fraction are in good agreement with values calculated from α-Mg(0002) Bragg

Table 5.4 Calculated fractions of hydride (f_{MgH2}) for 2800 nm and 500 nm films, upon hydrogen loading by $p_H = 200$ mbar and 20 mbar, from each film thickness change (Δd) by profilometer, from each decay of α-Mg(0002) Bragg peak area and from resistivity measurements. Achieved hydride thicknesses for each loading condition (Δd_{MgH2}) are also listed.

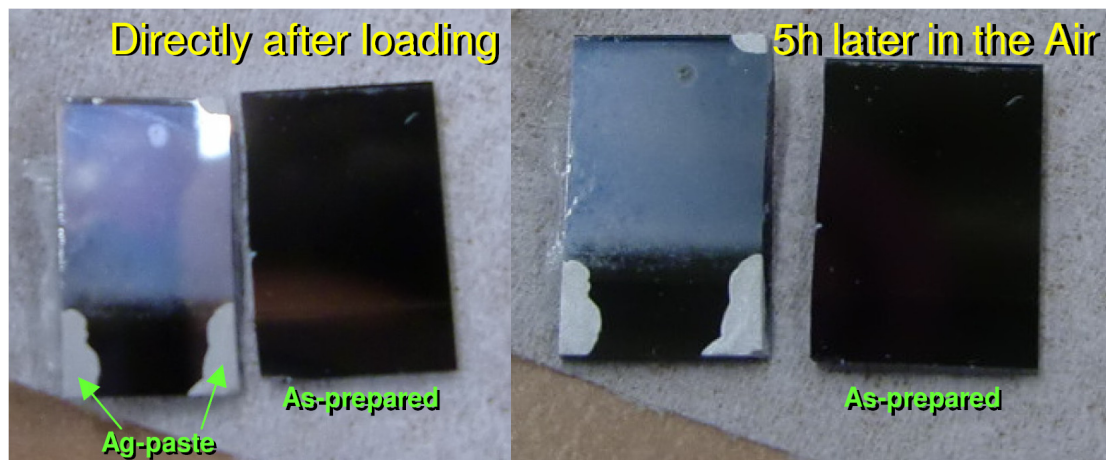|		2800 nm sample		500 nm sample	
		p_H = 200 mbar	p_H = 20 mbar	p_H = 200 mbar	p_H = 20 mbar
Profilometer	Δd	280 (±14) nm	420 (±30) nm	78 (±12) nm	112 (±20) nm
	f_{MgH2}	0.37	0.55	0.58	0.89
Bragg peak	f_{MgH2}	~0.4	~0.75	~0.75	~0.89
Resistivity	R/R_0	1.7	2.2	3.6	14
	f_{MgH2}	0.4	0.55	0.75	0.95
	d_{MgH2}	1080 (±40)	1820 (±280)	333 (±45)	445 (±55)

Fig. 5.13 Optical appearance of the completely hydrogen loaded sample directly after H$_2$ loading and bringing out from the chamber (including 10min. time of evacuation), compared with as-prepared state (left), and its change after 5 hours. The silver spots relate to Ag-paste.

peak area decay and the thickness change (**Table 5.4**).

Fig. 5.13 exemplarily shows the optical property change for 500 nm sample loaded at $p_{H2} = 20$ mbar, compared with the as prepared state (left side). Leaving this hydrogen loaded sample in the air for 5 hours results no clear change by eyes, as shown in the right side in **Fig. 5.13**. Assuming this optical property change due to the transition into the hydride phase, the result supports that the magnesium hydride can be exist in the Mg film at room temperature even in the air.

5.2.2 Mg films on Si-substrate, annealed

Hydrogen loading measurements for annealed samples were also conducted. No formation of oxide or intermetallic compounds was recognized after the annealing treatment at 453 K to 503 K, by XRD measurement for each prepared samples before hydrogen loading. Samples with Mg layer thickness of 180 nm, 1450 nm and 2800 nm were prepared.

Stepwise constant pressure loading at $p_{H2} = x$ mbar ($x = 20, 200, 900$), was done for a 180 nm Mg film annealed at $T = 503$ K for 30 min. **Fig. 5.14** shows the result of XRD measurement. Each loading step was done for a loading time of $t = 3600$ s. The in plane stress (σ^P) was calculated to be $\sigma^P \approx 410$ MPa, and exhibited almost no change during hydrogen loading ($\Delta\sigma^P < 20$ MPa). Moreover, only small peak area change of the α-Mg(0002) peak is visible, after the whole loading process. Thus, hydrogen loading for this sample seems to be very sluggish, already in the α-phase. Oxidation of the Mg-film surface during the sample annealing condition for this sample cannot be excluded. A surface oxide could be the reason for the sluggish kinetics. Therefore, the annealing temperature is lowered to $T = 453$ K for 30 min, for further samples.
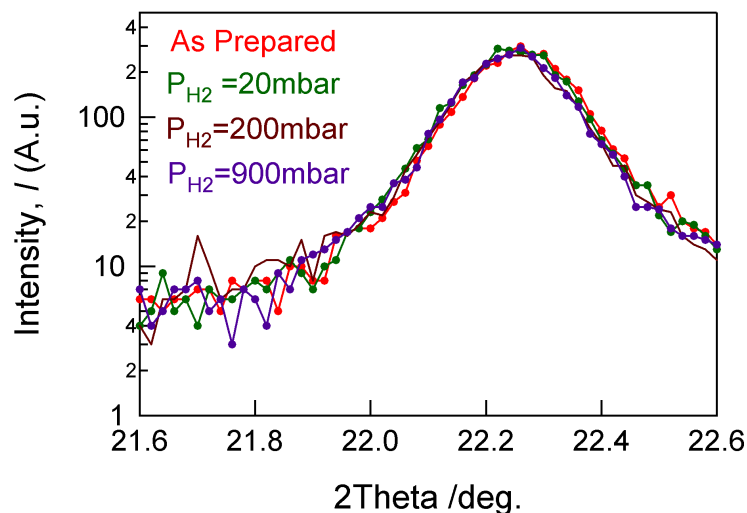
Fig. 5.14 The development of the αMg(0002) Bragg peak for a 180 nm Mg thick sample (annealed at $T = 503$ K), as-prepared state (red) compared with peaks after hydrogen loading at room temperature by a constant pressure of $p_H = 20$ mbar for the loading time of $t = 3600$ s (green) and further loadings by $p_H = 200$ mbar for $t = 3600$ s (brown) and by $p_H = 900$ mbar for $t = 3600$ s (purple). Measured with the wavelength of $\lambda = 0.999119$ Å.

In order to see more pronounced change of peak area and position, thicker Mg-layer sample and longer hydrogen loading time were applied. 2800 nm thick Mg film, annealed at $T = 453$ K for 30 min. was prepared. This sample was loaded by a constant hydrogen pressure of $p_{H2} = 200$ mbar, for 7 hours. **Fig. 5.15a** shows the α-Mg(0002) peak development and the corresponding σ^P. Now, the α-Mg(0002) peak area clearly decreases indicating hydride formation. The change of σ^P was calculated to be $\Delta\sigma^P = 50$ MPa. A slight increase of the compressive stress was visible at the early stage of hydrogen loading. In contrast, an increase of tensile stress was observed in further loaded states. The change of σ^t before and after hydrogen loading was calculated to be $\Delta\sigma^t = 2.4$ GPa (**Fig. 5.15b**).

Stress changes before and after hydrogenation are summerized in **Table 5.3**. Both of the stress changes $\Delta\sigma^P$ and $\Delta\sigma^t$ upon hydrogenation revealed tensile stress. This tendency differs from the result for samples without annealing process.
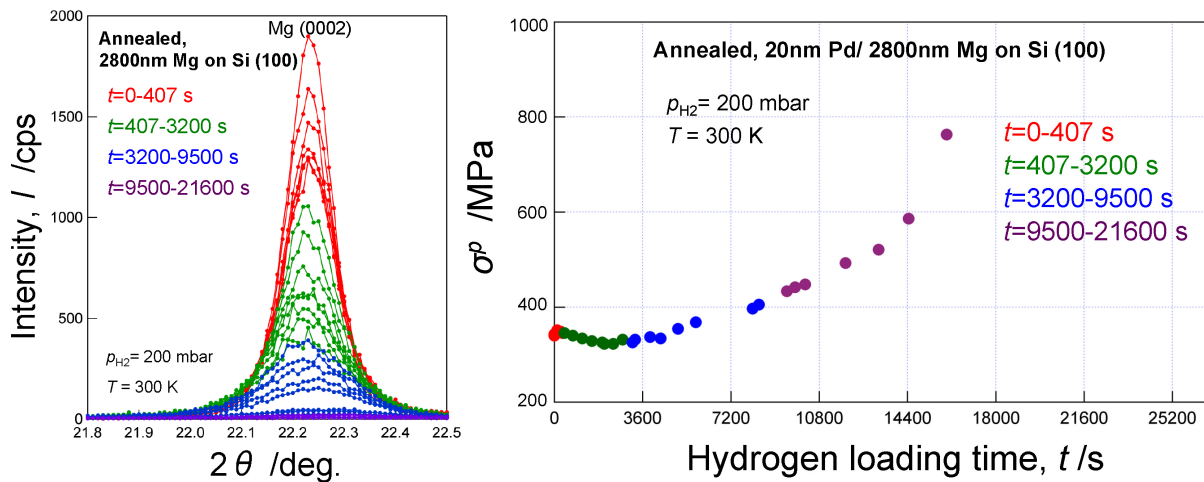
Fig. 5.15a Development of αMg(0002) for annealed 2800 nm Mg film, during hydrogen gas loading with constant pressure at p_{H2} = 200 mbar (left) and the time change of the in-plane stress σ^p obtained from the shift of αMg(0002) XRD peak (right). Plotted markers in both graphs are colored by different degrees of loading time t (unit in s), with red (t = 0 - 407), green (t = 407 - 3200), blue (t = 3200 - 9500) and violet (t > 9500).
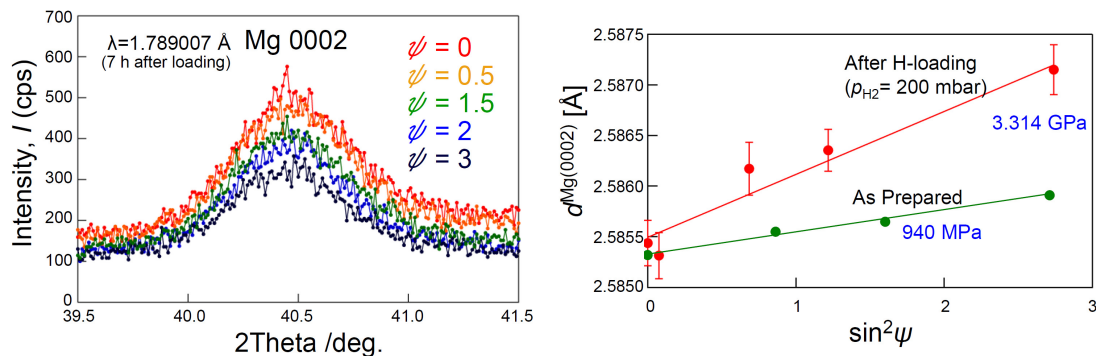
Fig. 5.15b Results of *ex-situ* XRD measurement for αMg(0002) peak, at different tilting angle ψ (ψ = 0, 0.5, 1.5, 2, 3), conducted for annealed 2800 nm Mg film, 7 hours after hydrogen loading (left) and corresponding d values plotted against $\sin^2\psi$, compared with as-prepared state (right). σ^t values obtained from each slope are appended with blue letters.

5.2.3 Mg films on Pd-substrates

Fig. 5.16 shows the peak position and intensity change of the α-Mg (0002) peak during an *in-situ* XRD measurement on a 250 nm Mg sample deposited on a 12.5 µm Pd foil, at 300 K.

As the hydrogen concentration increases, the peak shifts to lower angles and the peak area decreases. Hydrogen is dissolved in the α-Mg lattice up to a concentration of $c_H = 10^{-3}$ H/Mg, as the peak only shifts but its area is not changed. Above this concentration, the α-phase peak area decreases, and thus, hydride formation starts. The peak area change in this concentration range is superimposed by a Pd-substrate bending effect, and therefore it is much stronger than expected from the calculated concentrations. The concentrations are, therefore, determined by the loading current and time.

The peak shift of the α-Mg (0002) lattice reflection is mainly due to an increase of in-plane
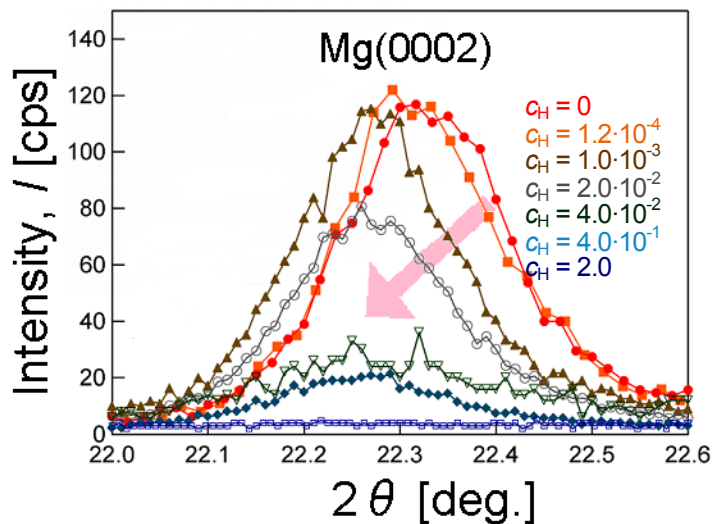
Fig. 5.16 Development of the XRD peak for the αMg(0002) during hydrogen absorption, at the concentration of c_H = 0 H/Mg (red), $1.2 \cdot 10^{-4}$ H/Mg (orange), $1.0 \cdot 10^{-3}$ H/Mg (brown), $2.0 \cdot 10^{-2}$ H/Mg (grey), $4.0 \cdot 10^{-2}$ H/Mg (green), $4.0 \cdot 10^{-1}$ H/Mg (light blue) and 2 H/Mg (blue), measured with λ = 1 Å for a 250 nm Mg sample deposited on an annealed 12.5 µm Pd foil, by means of the step-by-step electrochemical loading with current density $i = 10^{-5}$ A/cm^2 (for $c_H < 2.0 \cdot 10^{-2}$ H/Mg) and $i = 10^{-4}$ A/cm^2 (for $c_H \geq 2.0 \cdot 10^{-2}$ H/Mg) at T = 298 K.
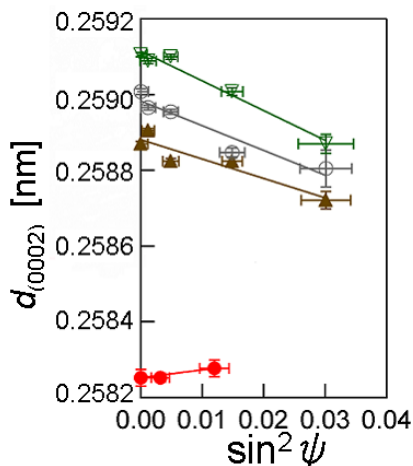
Fig. 5.17 Obtained *d* values of αMg(0002) plane, as functions of sin$^2\psi$, measured in equilibrium at each hydrogen concentration, from $c_H = 0$ H/Mg up to $c_H = 4.0 \times 10^{-2}$ H/Mg Expressions are same as shown in **Fig. 5.16**.

compressive stress during hydrogen absorption. The α-Mg peak clearly shifts also in the two-phase region. The shift of the α-Mg in the two-phase region is assumed to originate purely from the stress by the surrounding hydride phase.

Applying Eq.(3.8), the stress change in the α-Mg phase at mean concentrations between $c_H =$ 0 H/Mg and $c_H = 4.0 \cdot 10^{-2}$ H/Mg was calculated to be $\Delta\sigma_m^p \approx$ -150 MPa.

Fig. 5.17 shows the change of atomic plane distance d in the α-Mg phase for the same sample, as a function of $\sin^2\psi$ at the given hydrogen concentration, measured in quasi-equilibrium states. The slope of this curve is positive for the as prepared Mg film on the Pd-substrate, yielding tensile stress of +30 MPa by Eq.(3.9). For the electrochemically hydrogen loaded films, the slope changes to negative, yielding compressive stress of $\sigma^t =$ -16 MPa for $c_H = 1 \cdot 10^{-3}$ H/Mg, $\sigma^t =$ -40 MPa for $c_H = 2 \cdot 10^{-2}$ H/Mg, and finally $\sigma^t =$ -120 MPa for $c_H = 4 \cdot 10^{-2}$ H/Mg. Applying equation Eq.(3.9), the stress change between $c_H = 0$ H/Mg and $c_H = 4.0 \cdot 10^{-2}$ H/Mg is $\Delta\sigma_m^t \approx$ -150 MPa. This value correlates well with $\Delta\sigma_m^p$ calculated from the result of **Fig. 5.16**.

In total, -150 MPa hydride-related stress at $c_H = 4.0 \cdot 10^{-2}$ H/Mg is acting compressively on the α-Mg grains. This correlates to a compressive stress increase of -3.5 GPa/$c_{H/Mg}$. This value is comparable with the stress increase expected from Eq.(2.41).

The obtained EMF-values of corresponding measurements will be shown (**Fig. 5.29b**) and discussed in **Chap. 5.5.2**.

5.3 Chemical potentials of hydrogen in Mg-H films

The results of electrochemical loading measurements will be presented in this section.

5.3.1 Chemical potentials of hydrogen in Pd films and foils

Fig. 5.18 presents the results of electrochemical hydrogen loading measurements for the 2 μm thick foil- and 20 nm thick film Pd samples sputtered on Si (100) substrate, as references for the substrate and the capping layer. The solubility limit of hydrogen for the film 20 nm Pd is about $c_H = 7 \cdot 10^{-2}$ H/Pd. It is much larger than that for the Pd foil which is about $c_H = 10^{-3}$ H/Pd.

Comparing at the two-phase region, the plateau position for the thin film sample corresponds to the hydrogen partial pressure of $p_H \approx 3 \cdot 10^{-2}$ bar. It is nearly 4 times higher than the value for foil sample which is $p_H \approx 7 \cdot 10^{-3}$ bar. Extrapolated value of bulk Pd-PdH$_{0.6}$ transition at room temperature in the van't Hoff Plot (**Fig. 2.3**) yields $p_H \approx 10^{-2}$ bar.
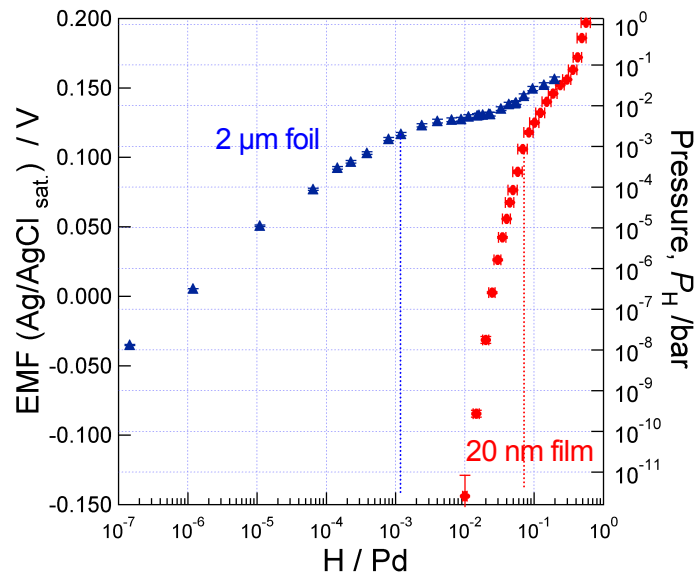
Fig. 5.18 Development of the EMF values (left axis) and corresponding hydrogen partial pressure (right axis) for 25nm thick Pd film on Si (100) substrate (red circle) and 2μm Pd foil (blue triangle), during step-by-step electrochemical hydrogen loading with constant current density of $i = 10^{-4}$ A/cm^2 at room temperature, plotted as a function of hydrogen concentration (bottom axis).

5.3.2 Chemical potentials of hydrogen in Mg films: effect of loading current

Chemical potentials were determined for Mg films on Si, for thicknesses ranging from 80 nm to 500 nm. The loading current density was varied for the different films.

The results of the EMF measurements are presented in **Fig. 5.19**. Parts of these results are published in ref.[Uchi11]. Samples and loading conditions are listed in **Table 5.4**. For all films, the α-phase solubility limit is about $c_H = 2 \cdot 10^{-4}$ H/Mg. This is larger than the bulk value of $c_H = 1 \cdot 10^{-7}$ H/Mg [Sanma87] or $c_H = 3 \times 10^{-6}$ H/Mg [Koen59]. But, such an α-phase solubility limit increase is well-known for other thin films systems [Stei94,Laud98,Wagn08,Wagn11]. For many EMF-curves two plateaus are detected. One at the pressure range of the Mg-MgH$_2$ transition and one at the equilibrium pressure range for the Pd-PdH$_{0.6}$ formation (between $p_H = 3 \times 10^{-3}$ bar and $p_H = 1 \times 10^{-2}$ bar).

The shapes of EMF curves strongly depend on the current densities. The maximum mean solubilities c_H differ between 0.01 H/(Mg+Pd) to 1.55 H/(Mg+Pd). Only one plateau of Pd-PdH$_{0.6}$ can be seen for samples hydrogenated by high current densities $i > 3 \times 10^{-6}$ A/cm^2. Also, the maximum achieved hydrogen concentration of $c_H = 0.01$ H/Mg is very small. This indicates a strong blocking effect. The second plateau related to Mg-MgH$_2$ appears for the samples hydrogenated by lower current densities of $i < 3 \times 10^{-7}$ A/cm^2. The maximum hydrogen

concentration in these Mg-films is large (about $c_H = 1.55$ H/(Mg+Pd)). The width of the Mg-MgH$_2$ plateaus strongly differs by the loading conditions. The different widths show that the samples are not in true equilibrium even though the potential is constant. The applied smallest current density condition is even less than that reported by Vermeulen $et\ al$ [Verm06].

Table 5.5 The Mg-layer thicknesses and applied loading current conditions of the samples, prepared for the step-by-step EMF measurements. Achieved MgH$_2$ thickness estimated from the hydrogen content (N) and from the XRD peak ratio (X) are also given.

Sample		A	B	C	D	E	F
Mg thickness [nm]		200	80	270	250	500	165
Current density [A/cm^2]		1 x 10^{-3}	2 x 10^{-4}	1.2 x 10^{-6}	3 x 10^{-6}	1.2 x 10^{-7}	3 x 10^{-7}
Achieved hydride-thickness [nm]	N	<25	<25	160	155	195	160
	X	---	---	150	150	200	150
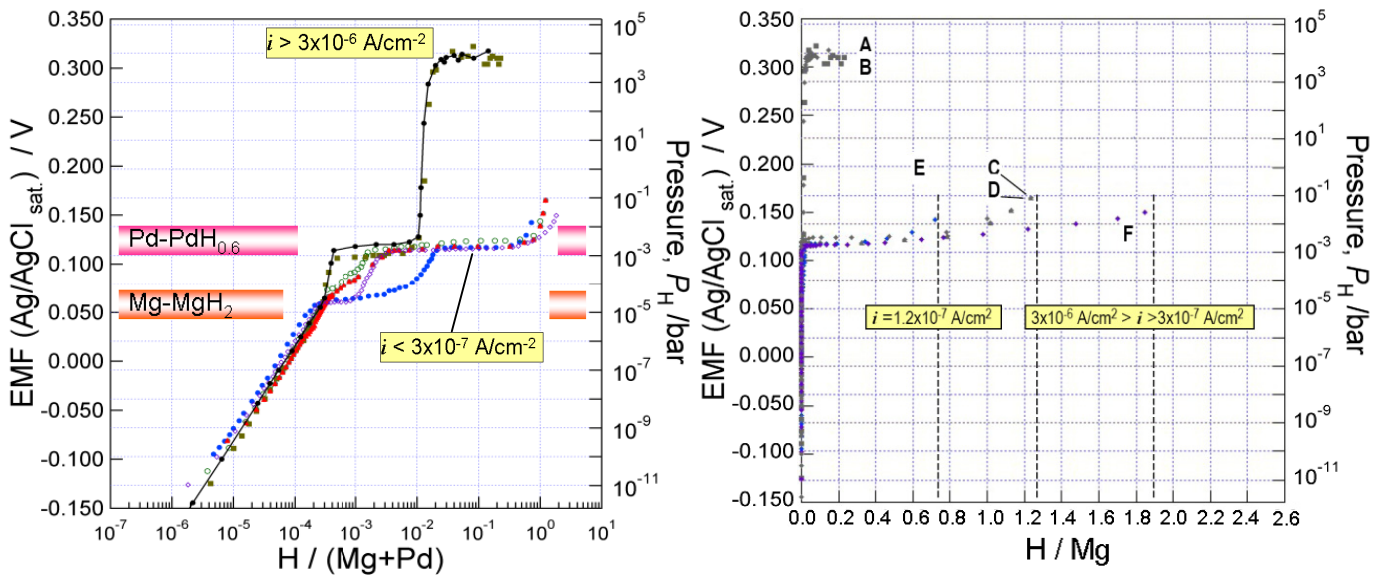
Fig. 5.19 EMF curves for Pd capped Mg film on Si (100) substrate, during step-by-step electrochemical hydrogen loading at various current densities i (unit in A/cm^2), plotted as a function of total hydrogen concentration with logarhysmic scale (left picture) and concentration in H/Mg with linear scale (right picture): Sample A (black) and B (brown) ($i = 1.0$ x10^{-3}-2x10^{-4}), Sample C (green) and D (red) ($i = 1.2$x10^{-6}-3x10^{-6}), E (blue) ($i = 3$x10^{-7}) and F (violet) ($i = 1.2$x10^{-7}). The Mg thicknesses of the samples, and the estimated values of the MgH$_2$ thickness from the hydrogen content and from the XRD peak ratio are given in **Table 5.5**. Equilibrium hydrogen pressure at room temperature corresponding to the Mg-MgH$_2$ and Pd-PdH$_{0.6}$ transitions are appended in the figure.

With respect to the EMF plateau potential appearing at low current densities, the hydrogen pressure calculated from the obtained potential reveals good agreement with extrapolated data from a collection of literature data (see **Fig. 2.12**).

The right picture of **Fig. 5.19** refers to the hydrogenation of Mg by subtraction of a 20 nm surface Pd-hydride with c_H = 0.6 H/Pd. Thus, the x-axis gives the mean H concentration in the Mg films. This can be split into one part of a MgH$_2$ layer and a remaining layer of Mg with a negligible amount of hydrogen. For the 500 nm thick film with the observed maximum mean concentration of c_H = 0.72 H/Mg, a maximum MgH$_2$ layer thickness of 195 nm is detected for a low current density of i = 1.2×10^{-7} A/cm^2. About the same thickness of 200 nm is obtained using the measured XRD peak area ratio of $A^{\beta Mg(110)} \big/ A_0^{Mg(0002)}$ = 40% and Eq.(3.6') of the 500 nm film.

For the slightly higher loading current density, a layer of about 160 nm is hydrided which corresponds to the value of 150 nm obtained from the XRD intensity peak ratio. The MgH$_2$ layer thickness depends on the loading current density and is nearly independent of the total film thickness, as shown for 270 nm to 165 nm thin Mg-films. For higher loading current density, a blocking hydride layer of the thickness of about 30 nm builds up on the Mg-layer surface.

The achieved hydride thicknesses for each sample are listed in **Table 5.5**. The evaluated thicknesses from the loaded hydrogen content and from the XRD peak ratio are shown with N and X, respectively. Both evaluated hydride thickness values have good agreement for each sample. Furthermore, it is clear that the smaller loading current density condition yields larger hydride thickness. The maximum layer thickness of MgH$_2$ in this result (up to 195 nm) is already larger than the maximum reported hydride thicknesses. (See **Chap. 2.1.5.2**).

In conclusion, the hydrogenated volume depends on the loading current: for a large loading current density density i > 2×10^{-4} A/cm^2, a blocking layer with a thickness of 30 nm MgH$_2$ builds up on the Mg-layer surface. For a small loading current i < 4×10^{-7} A/cm^2, further growth of hydrides is possible.

5.4 Hydrogen solubility and hydride nucleation observation in Mg films

The beginning of hydride nucleation can be seen by the beginning of the plateau region for ex. in **Fig. 5.19**. Regarding to the hydrogen concentration axis, hydrogen atoms are expected to exist mainly in α-Mg grains and at grain boundaries, in a grain boundary-rich Mg layer. To obtain precise hydrogen solubility in Mg grains, it is necessary to divide hydrogen content which solves into the α-Mg grains and which residess at grain boundaries.

A rough estimation of the hydrogen concentration in grain boundaries were applied in this work, using the measured apparent solubility limit. (See **Appendix A4** for details). The sample E

in **Table 5.5**, which has the largest thickness (500 nm) and with smallest loading current density condition, has the apparent solubility limit at $c_{\text{H-Sol}}^{\text{nc}} \approx 10^{-4}$ H/Mg (see **Fig. 5.19**). Applying these values for Eq.(A4.8) yields $c_{\text{H}}^{\text{GB}} \approx 10^{-2}$ H/Mg. In the solubility of H in Mg-grains is that the bulk sample and, thus, about $c_{\text{H}}^{\text{G}} = 3 \times 10^{-6}$ H/Mg (see **Sec. 2.1.5.1**), $\left(c_{\text{H}}^{\text{GB}} / c_{\text{H}}^{\text{G}} \right) \approx 3500$ is obtained.

Apart from the EMF plot, a direct method to see hydrogen solution into α-Mg lattice is the XRD peak shift, by increasing hydrogen concentrations up to that concentration where a rapid decrease of peak reflection area starts. The XRD peak contains information about the grain while grain boundaries are not visible. To see the precise hydrogen solubility in Mg-grains, *in-situ* XRD measurements have been conducted at beamline BM20 in ESRF Grenoble.

At first, Mg films with two different thicknesses of 60 nm were prepared on a Si(100) substrate at room temperature, and Pd-capping and polymer coating were added as shown in **Chap. 3.2**. Maximum loading current densities of $i < 4 \times 10^{-4}$ A/cm^2 is applied for these samples.

Fig. 5.20 shows the result for the 60 nm sample. For the Mg(0002) peak, a rapid decrease of peak intensity and peak shift was observed. Clear peak area decrease of α-Mg(0002) is obtained, at $c_{\text{H}} = 5 \cdot 10^{-3}$ H/Mg. This peak area decrease was expected for nucleation of the β-MgH$_2$ phase. However, the nucleation of the β-MgH$_2$(110) peak was not observed at this concentration. The hydride peak was eventually observed at further hydrided state of $c_{\text{H}} = 2.5 \cdot 10^{-1}$ H/Mg, at sample tilting angle ψ of $\psi = 4.5$ degrees.
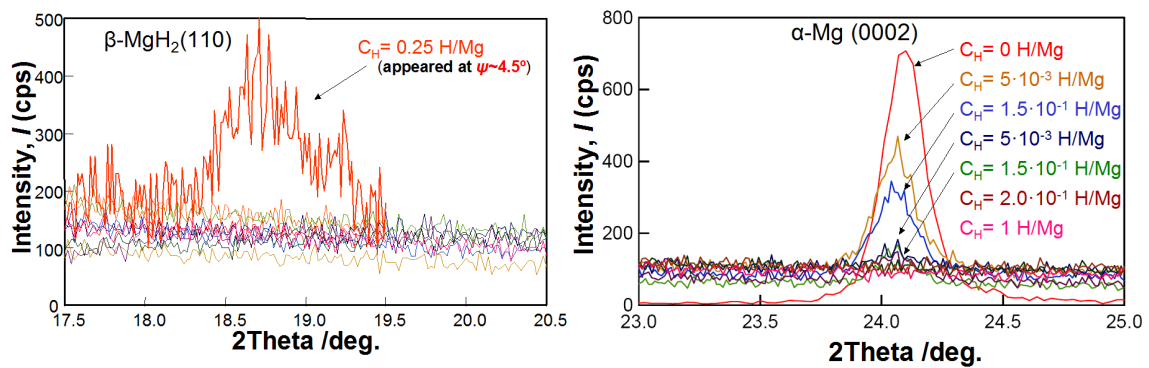
Fig. 5.20 Appearance of the βMgH$_2$(110) peak (left), and development of Mg(0002) peak (right) from XRD measurements for 60nm Mg film at different hydrogen concentration c_{H} from c_{H} = 0 H/Mg up to c_{H} = 1 H/Mg. Both picture are drawn with same color for same conditions of c_{H}. Maximum peak intensity for βMgH$_2$(110) peak appeared at the sample tilting angle of ψ = 4.5 degrees at c_{H} = 4.3 $\cdot$ 10^{-4} H/Mg.

From both results of 60 nm and 188 nm samples, hydride peak nucleation was clearly observed at c_{H} in the order of 10^{-1} H/Mg. However from the peak decrease of α-Mg(0002) for the 60 nm Mg film sample, the solution limit of hydrogen in Mg grains, was expected to be smaller than $c_{\text{H}} = 5 \cdot 10^{-3}$ H/Mg.

To see smaller hydrogen concentration regions, further *in-situ* measurements have been conducted with smaller current densities and thicker samples. Two Mg films with thickness of

1400 nm were prepared on Si(100) substrates, at room temperature. Two different hydrogen loading conditions of the maximum current density i were applied, $i < 4 \cdot 10^{-6}$ A/cm^2 for Sample 1 and $i < 2 \cdot 10^{-5}$ A/cm^2 for Sample 2, respectively. Due to small current density and limited measuring time at beamline, loading was prepared externally for larger concentration steps. Schematic diagrams of loading conditions for both samples are described in **Fig. 5.21**.

Fig. 5.22 shows the result of XRD scans on the change of the Mg (0002) peak at different hydrogen concentrations in equilibrium states. Both samples revealed increasing compressive stress change to the initial state up to $\Delta\sigma = -400$ MPa (Sample 1) and $\Delta\sigma = -250$ MPa (Sample 2) in the hydrogen loading processes, being charged up to $c_H = 5 \cdot 10^{-3}$ H/M (Sample 1) and $c_H = 7 \cdot 10^{-3}$ H/M (Sample 2). Both sample revealed a decrease of the in-plane compressive stress for further hydrogenation. This is attributed to a detachment of the films, optically observed after the loading (**Fig. 3.5 right**). With respect to hydride peaks, peak tiltings between $\psi = 1.0°$ and $\psi = 3.5°$ against the α-phase are also observed for Sample 1.

The most visible stress change happens in the concentration range of 10^{-3} H/M (see peak shift of Sample 2 from $c_H = 5 \cdot 10^{-3}$ H/M to $c_H = 7 \cdot 10^{-3}$ H/M.). Just prior to this large stress increase, the development of the β-MgH$_2$(110) peak was observed for both samples. For example, Sample 1 showed nucleation of hydride peak between $c_H = 2.5 \cdot 10^{-4}$ H/Mg and $c_H = 4.3 \cdot 10^{-4}$ H/Mg, which is presented in **Fig. 5.23**. This concentration range is in good agreement with the EMF result shown in **Fig. 5.19**. Applying rough estimation of apparent solubility limit $c_{H-Sol}^{nc} \approx 2.5 \times 10^{-4}$ H/Mg (see **Fig. 5.19**) and $c_H^G = 3 \times 10^{-6}$ H/Mg for Eq.(A4.8) yields $c_H^{GB} \approx 5 \times 10^{-2}$ H/Mg, thus, $\left(c_H^{GB} / c_H^G \right) \approx 2 \times 10^4$ is obtained for 1400 nm sample. In the end, a thickness of 1300 nm hydride layer was achieved for this sample.

The stress development due to hydrogen induced expansion in alpha solid solution region was expected to be $d\sigma / dc_H = -5.72$ GPa/(H/Mg) from linear elastic theory, as is shown in Eq.(2.41). In the concentration range up to $c_H = 5 \cdot 10^{-3}$ H/Mg for sample 1 (before buckling), the stress development was calculated to be $d\sigma^p / dc_H = -7.9 \pm 1$ GPa/(H/Mg). This value could have been affected by hydride nucleation, however, is in agreement with experiment. This agreement explains that hydrogen resides not only in grain boundary, but also dissolves in the α-Mg grains, at $c_H = 5 \cdot 10^{-3}$ H/Mg.

The maximum intensity of the β-MgH$_2$(110) peak was achieved at a sample tilting angle ψ (rotation by axis vertical to the plane which the beam progressing) from $\psi = 1.0°$ to $\psi = 3.5°$, which is shown in **Fig. 5.24**. Since buckling of the film [Niki08] makes intensity disappear, this tilting was attributed to the grain rotations.

Furthermore, *ex-situ* electrochemical loading XRD measurements have been also performed in the Institut für Materialphysik, University Göttingen. Surprisingly, the hydride reflection does not occur in the diffraction pattern, as can be seen in **Fig. 5.25**, showing the case for 300 nm thick Mg film. This clearly hints on a tilting of the lattice during phase transformation towards the main axis of the used Bragg-Brentano geometry, thereby moving the reflection away from the
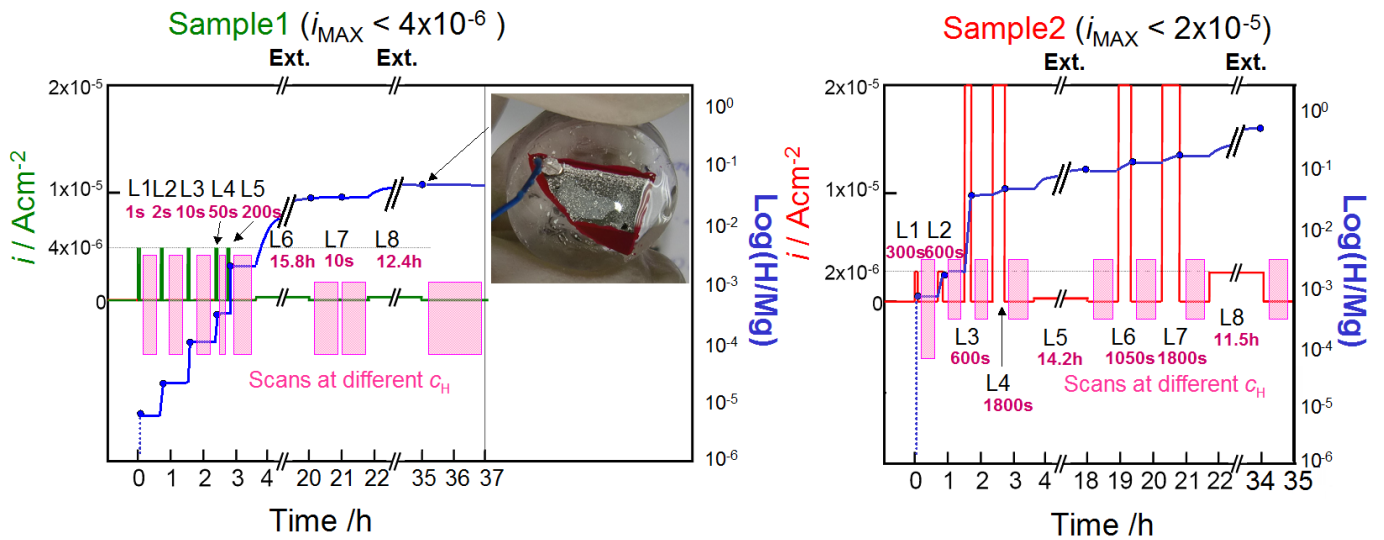
Fig. 5.21 Schematic diagrams of loading conditions for sample 1 (left) and sample 2 (right). Current densities are plotted in left axis with green and red for sample 1 and 2, respectively. Corresponding hydrogen concentrations (right axis for both graphs) are schematically plotted by blue lines. Concentration conditions for each scan are appended with pink areas in both figures. A picture for loaded sample up to $c_H = 9 \cdot 10^{-2}$ H/Mg (Buckled) is involved in left picture for sample 1. A picture for Sample 2 (loaded state) with light microscope is shown in the right side of **Fig. 3.5**.
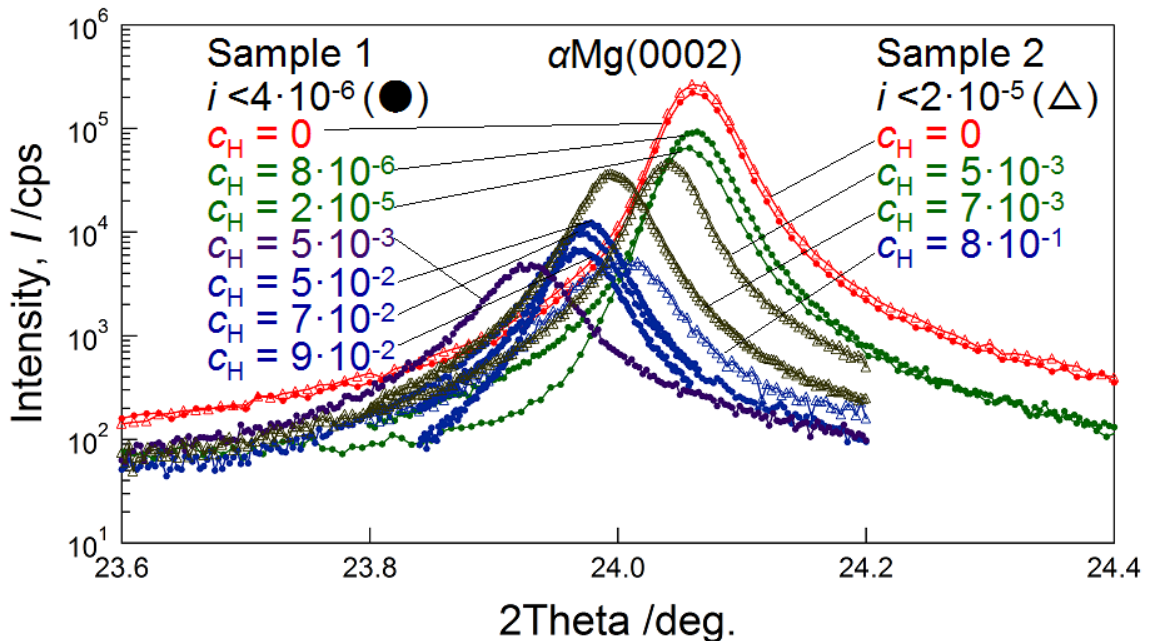
Fig. 5.22 XRD peaks of αMg (0002) for sample 1 (circle) and sample 2 (triangle) at different hydrogen concentrations c_H (in H/Mg), described in the left side and the right side, respectively.

detector-position. Thus, sample tilting should result in the appearance of the hydride reflection. This was checked in this work by performing ψ-tilts of the sample and, indeed, found the missing hydride reflection, as shown in **Fig. 5.26**. An explanation of this plane relationship is given in **Fig.**

5.27.

Because the hydride-peak intensity strongly depends on the correct detector position, the hydride concentration was fundamentally evaluated not by peak area of the β-MgH$_2$(110) reflection but by the area of the α-Mg(0002) reflection, for further measurements. According to the conventional detector position, this area is more reliable than that of the hydride reflection, which needs the sample to be tilted.

Taking this peak tilting into account, an *in-situ* XRD measurement has been performed for a 188 nm thick Mg film, as results shown in **Fig. 5.23**. Each scan for hydride peaks is measured at different sample tilting angle ψ at the maximum peak intensity ($\psi = 0°$-0.5° for scans of $c_H < 0.48$ H/Mg and, $\psi = 0.5°$ and 3.0° for $c_H = 1.17$ H/Mg and 1.43 H/Mg, respectively).
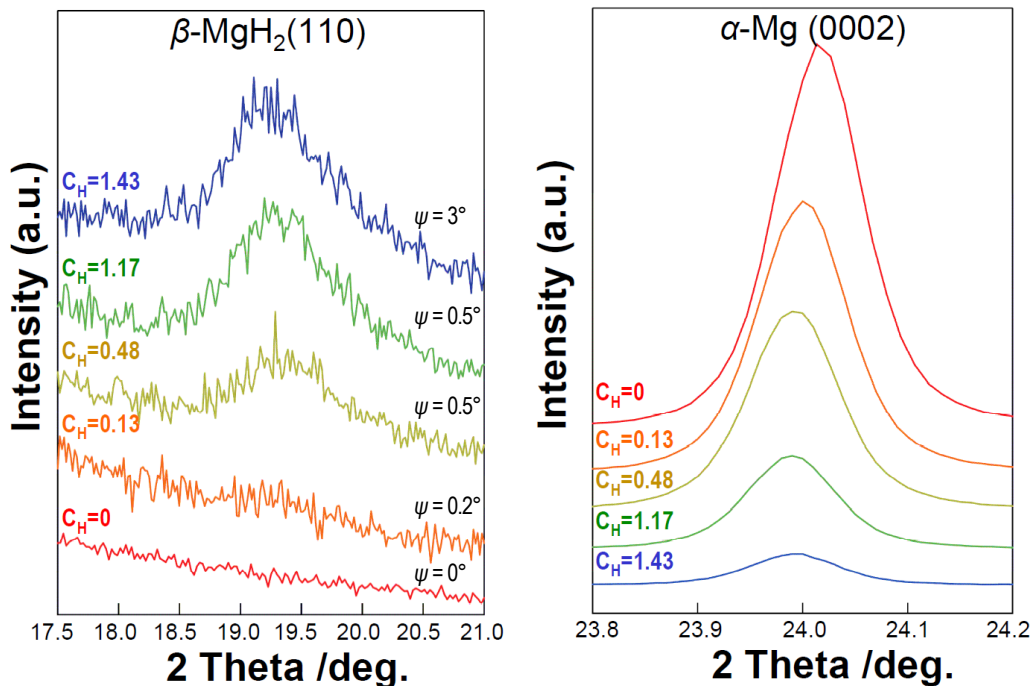
Fig. 5.23 Peak development of the βMgH$_2$(110) peak (left), and αMg(0002) peak from XRD measurements for 188 nm Mg film at different hydrogen concentrations of $c_H = 0$ H/Mg (red), $c_H = 0.13$ H/Mg (orange), $c_H = 0.48$ H/Mg (light green), $c_H = 1.17$ H/Mg (green), and $c_H = 1.43$ H/Mg (blue). Each scan for hydride peaks are measured at the sample-tilting angle of ψ at the maximum peak intensity ($\psi = 0°$-0.5° for scans of $c_H < 0.48$ H/Mg, and $\psi = 0.5°$ and 3.0° for $c_H = 1.17$ and 1.43, respectively).
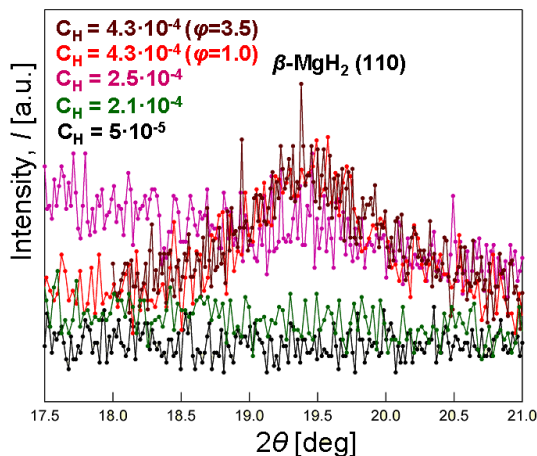
Fig. 5.24 Development of the βMgH$_2$(110) peak, from XRD measurements for the Sample 1, at different hydrogen concentration c_H. Peaks at sample tilting angle of $\psi = 1.0°$ and $\psi = 3.5°$ are also plotted, scans in order to find the maximum peak intensity at $c_H = 4.3 \cdot 10^{-4}$ H/Mg.
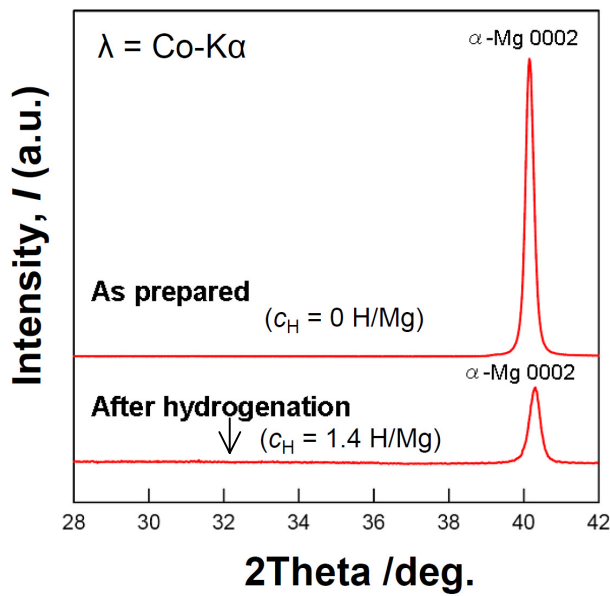
Fig. 5.25 XRD pattern of the αMg(0002) reflection after hydrogen loading (c_H = 1.4 H/Mg). The hydride reflection is invisible in this scale and geometry (shown by an arrow).
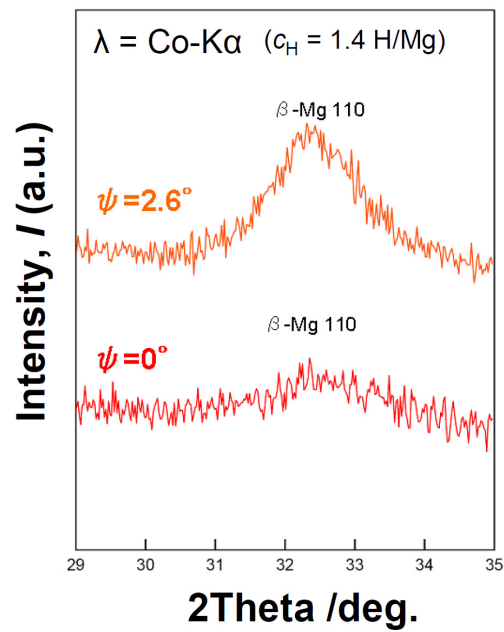
Fig. 5.26 XRD pattern of the α-reflection after hydrogen loading up to c_H = 1.4 H/Mg, at two different Ψ positions (Ψ = 0° and Ψ = 2.6°). The weak hydride reflection becomes more intense by tilting.
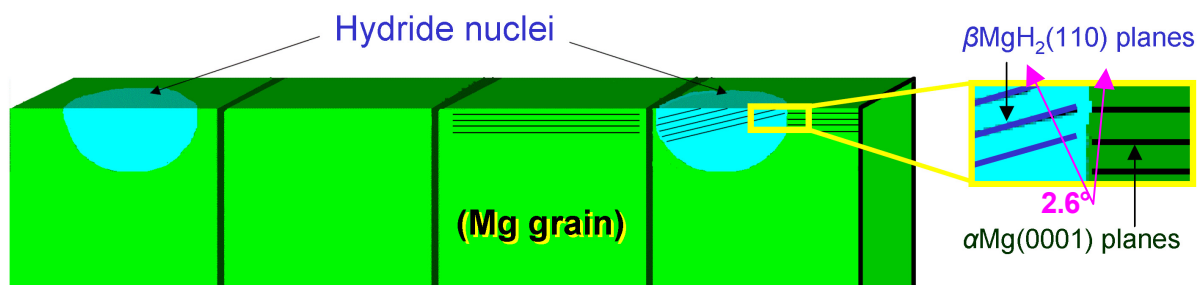
Fig. 5.27 Schematic figure with the cross-sectional view of the columnar shaped sample at the early stage of hydride nucleation, showing the lattice plane tilting between (0001) planes in the textured parent αMg phase (green) and the (110) plane in randomly nucleated βMgH₂ phase (blue). Zoomed picture of the selected area with yellow separator lines are shown in right side. The expression of tilting angle ψ, which is the angle of difference between perpendicular lines of both planes, is emphasized in this figure.

5.5 Determination of hydrogen diffusion constants

Permeation measurements have been conducted to probe the hydrogen distribution in grain boundary rich Mg films. In this Chapter, the results of electrochemical hydrogen loading measurements will be presented.

The diffusion coefficient depends on the concentration strongly for both layers of Pd and Mg. Therefore, in this work, the diffusion coefficient of pure palladium at each concentration was measured first, and those values were applied to calculate the hydrogen diffusion coefficient for each concentration, applying the pulse-loading method with small concentration steps. Afterwards, the diffusivity through the Pd/Mg package is determined. In the end, the hydrogen diffusivity at higher hydrogen concentrations will be discussed using results of constant pressure gas loading measurements (see **Sec. 5.2.1.3**).

5.5.1 Hydrogen diffusivity in Pd foils

In order to see the hydrogen concentration dependency on hydrogen diffusivity in Pd, electrochemical hydrogen permeation measurements have been performed on the annealed 250 μm Pd-foil at T = 298 K, using the electrochemical double cell. **Fig.5.28a** presents the EMF change and the obtained hydrogen diffusion coefficients as a function of the hydrogen concentration, with green triangles and blue triangles, respectively. Reported values of Kirchheim [Kirch80] and of de Ribaupierre and Manchester [Riba73] are also implemented as references in this figure.

In case of hydrogen permeation through a membrane, it is known that additional activation energy for dissociation is needed upon the solution from the entry surface. However, the thickness dependency on the break through time with same hydrogen concentration showed a proportional dependence (**Fig. 5.28b**) which shows that the process of hydrogen permeation was not affected by any surface effects, according to the Fick's 1st law. Hence, surface effects of this Pd-foil on hydrogen permeation are neglected, for further measurements in this work.

5.5.2 Hydrogen diffusion through Pd/Mg/Pd films

The chemical potential and the related diffusion constants are obtained for two Mg films by means of electrochemical permeation measurements, focusing on the α-phase and the two-phase region. **Fig. 5.29 a)** shows the equilibrium EMF values (plus-signs) with respect to a Ag/AgCl-standard electrode and the related total hydrogen diffusion coefficients D_H^{tot} (cross-sign) as determined by the time-lag method for a 20 nm Pd / 2088 nm Mg / 250 μm Pd sample (cf. Eq.(3.14)), as a function of the hydrogen concentration of up to c_H = $3 \cdot 10^{-1}$ H/(Pd+Mg) and c_H = $8 \cdot 10^{-2}$ H/(Pd+Mg), respectively. Pulse loading current densities in the order of i = 10^{-5} A/cm^2 were applied, here. Thereby, a blocking layer should be formed, for higher

hydrogen concentrations. For comparison, the measured diffusion coefficient of hydrogen in the annealed Pd substrate $D_{\mathrm{H}}^{\mathrm{Pd}} = 3.1(\pm 0.1) \times 10^{-11}\ \mathrm{m}^2\mathrm{s}^{-1}$ is implemented, as determined in the concentration range between $c_{\mathrm{H}} = 7\cdot 10^{-7}$ H/Pd and $c_{\mathrm{H}} = 1\cdot 10^{-2}$ H/Pd (marked with black line in **Fig. 5.29 a)**). The positions of the hydride formation plateaus of Mg-MgH$_2$ films and the
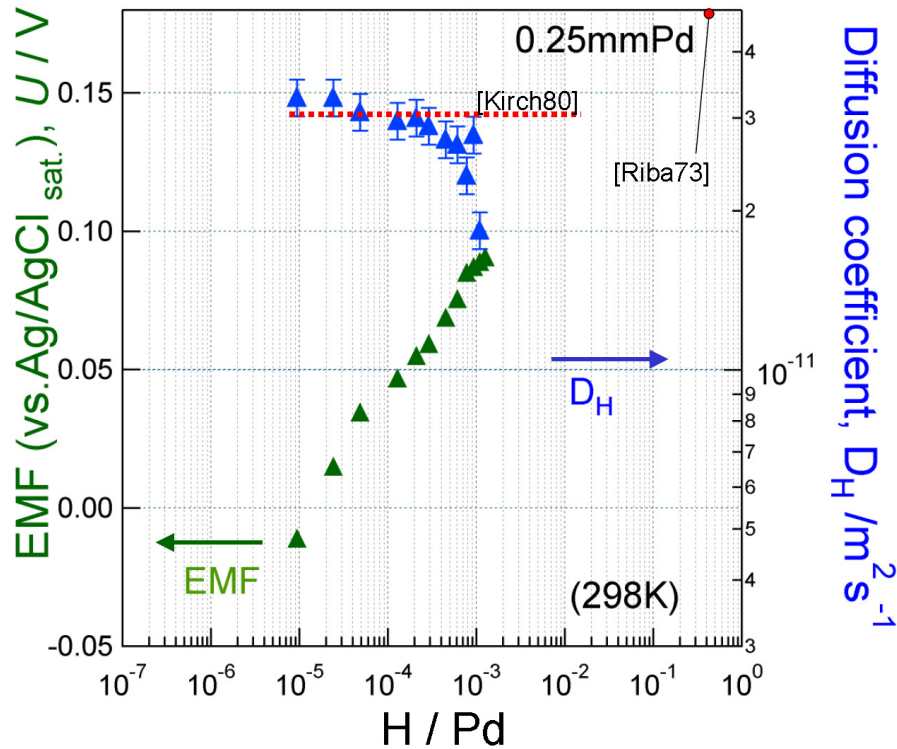
Fig.5.28a Obtained hydrogen diffusion coefficients for Pd-foil (right axis), plotted as a function of concentration with equilibrium EMF values (left axis). Values of diffusion coefficients by Kirchheim [Kirch80] and de Ribaupierre and Manchester [Riba73] are also implemented in the figure with red line and red marker, respectively.
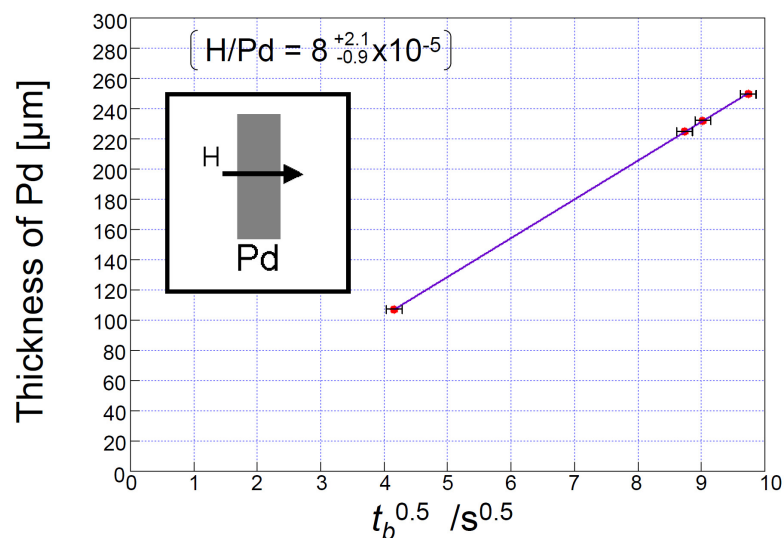
Fig. 5.28b Thickness dependency of hydrogen diffusion coefficient compared at the same hydrogen concentration ($c_{\mathrm{H}} \sim 8\mathrm{x}10^{-5}$ H/Pd), marked with red markers. The proportionality proves diffusion control in the experiment.

Pd-PdH$_x$ substrate (as shown in **Fig. 5.19**) are marked in shaded green in **Fig. 5.29 a)**. The position of the Mg-MgH$_2$ plateau is determined by slow loading on similar films, using current densities in the order of $i = 10^{-7}$ A/cm^2 (See **Chap. 5.3.2**). In **Fig. 5.29 a)**, the Mg-MgH$_2$ plateau is only visible in a change of the slope which is attributed to the slow kinetics in the system. The EMF curve in **Fig. 5.29 a)** shows that the Mg film starts to form the hydride at a concentration of $c_H = 1 \cdot 10^{-5}$ H/(Pd+Mg). Here, the measured EMF-value crossed the hydride formation plateau of MgH$_2$. At this stage, hydrogen predominately dissolves in the Mg film because of its lower hydrogen solution enthalpy compared to that for Pd.
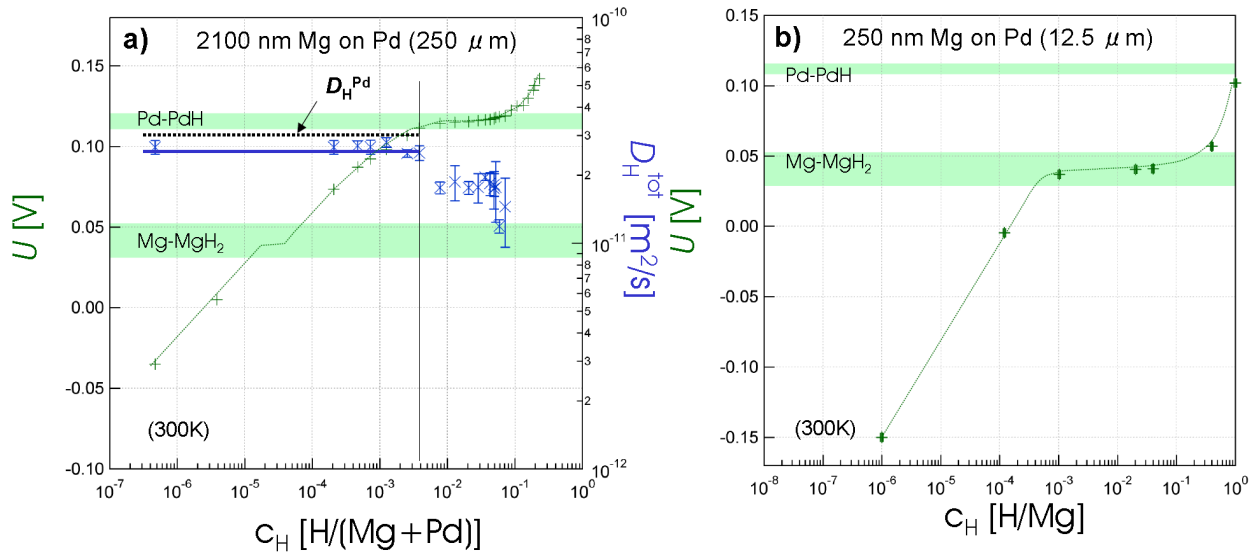
Fig. 5.29 a) Total hydrogen diffusion coefficients D_H^{tot} (cross symbol and black line) as determined by the time-lag method as a function of the total hydrogen concentration c_H in H/[Mg+Pd], for a 20 nm Pd / 2088 nm Mg / 250 µm Pd sample at 300 K. The related EMF values U are shown. Loading current densities were 10^{-6}-10^{-5} A/cm^2 for $c_H < 3 \cdot 10^{-3}$ H/(Mg+Pd), 10^{-5}-10^{-4} A/cm^2 for $c_H > 3 \cdot 10^{-3}$ H/(Mg+Pd). The gray line gives the hydrogen diffusion coefficient in the annealed Pd substrate D_H^{Pd}. The positions of the hydride formation plateaus of Mg-MgH$_2$ films and the Pd-PdH$_x$ substrate are marked by shades. (All EMF values with respect to Ag/AgCl-standard electrode).; **b)** EMF values U for a 20 nm Pd / 250 nm Mg / 12.5 µm Pd sample, as function of the hydrogen concentration c_H in H/Mg. Loading current densities were 10^{-6}-10^{-5} A/cm^2. The positions of the hydride formation plateaus are marked by shadeed areas. The position of the hydride formation plateau of the Mg-MgH$_2$ film is clearly visible by the EMF-curve.

The measured total diffusion constant $D_H^{tot} = 2.7(\pm 0.1) \cdot 10^{-11}$ m^2/s stays constant up to a concentration $c_H = 5 \cdot 10^{-3}$ H/(Mg+Pd). This value is significantly smaller than the diffusion constant of the Pd-substrate $D_H^{Pd} = 3.1(\pm 0.1) \cdot 10^{-11}$ m^2/s, clearly showing the effect of the Mg-film on the breakthrough time. It further shows, that the hydrogen diffusivity through the film package does not change strongly up to $c_H = 5 \cdot 10^{-3}$ H/(Mg+Pd). According to the EMF-values, at this concentration the hydride formation in the Mg film has long started. Thus, the high diffusivity

is kept in the α-β two-phase field of the Mg-H system.

Above $c_H = 10^{-2}$ H/(Mg+Pd) where the EMF value indicates the Pd hydride formation, D_H^{tot} starts to decrease. Because of the thickness of the substrate, the drop of D_H^{tot} is governed by the contribution of Pd-H at this concentration. In the two-phase region of Pd-H, the diffusivity is known to be reduced [Kirch88$^+$].

A breakthrough time of time $t_b = 1033$ s is obtained for a 20 nm Pd / 2088 nm Mg / 250 μm Pd sample by pulse loading method, for concentrations up to $c_H = 10^{-2}$ H/(Mg+Pd). Applying this breakthrough time with the measured diffusion constants of $D_H^{tot} = 2.7(\pm 0.1) \cdot 10^{-11}$ m^2/s and $D_H^{Pd} = 3.1 \cdot 10^{-11}$ m^2/s for the multilayer model (Eq.(3.15)), a hydrogen diffusion constant of $D_H^{Mg} = 7(\pm 2) \cdot 10^{-11}$ m^2/s can be gained.

Fig. 5.29 b) shows the EMF values of a 20 nm Pd / 250 nm Mg / 12.5 μm Pd sample, as a function of the hydrogen concentration in the Mg-film. This EMF-curve is generated by subtracting concentrations of the related EMF-curve of the Pd-substrate. Loading current densities in the order of 10^{-6} A/cm^2 were applied. The hydride formation plateau is more pronounced because of the lower current density. It appears at $c_H \geq 1 \cdot 10^{-3}$ H/Mg. The difference in the plateau widths, illustrated in **Fig. 5.29 a)** and **Fig. 5.29 b)**, is due to a different loading current density of 10^{-5} A/cm^2 and 10^{-6} A/cm^2, respectively (see **Chap. 5.3.2**). The slightly different thickness ratio of the Mg and the Pd-layers in these samples is not responsible for this finding, since the measured
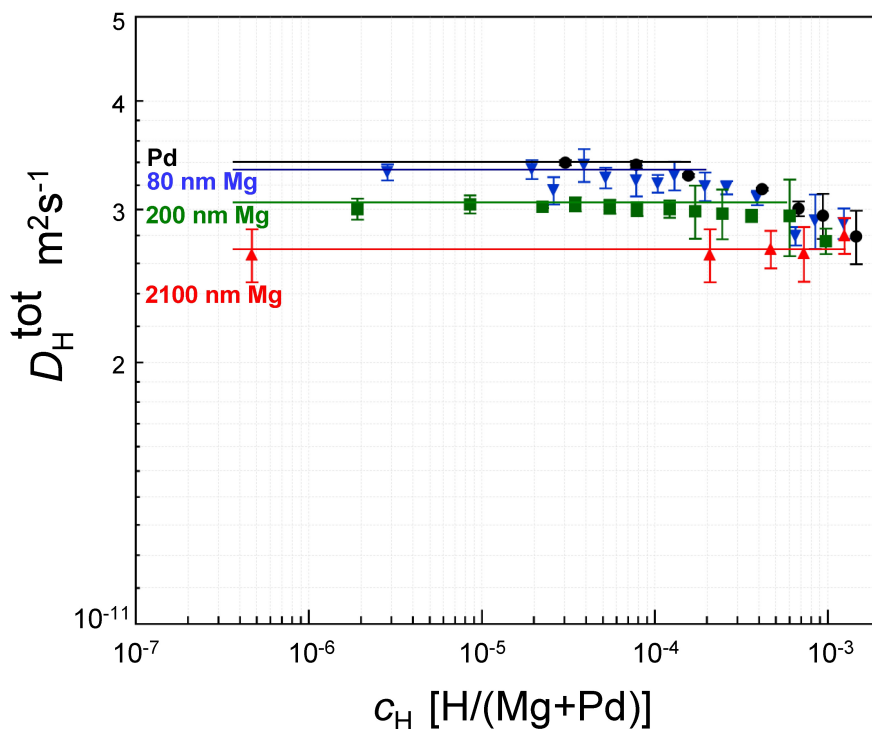
Fig. 5.30 Obtained hydrogen diffusion coefficients for Mg film for the thickness of 0 nm (only Pd substrate, plack dots), 80 nm (blue triangle markers), 200 nm (green quadrilateral markers) and 2100 nm (red triangle markers), plotted as a function of concentration c_H in H/(Mg+Pd). Mg layer were sputtered on the same Pd foil thickness of 250μm, and hydrogen was loaded from the substrate side, as is shown in the schematic figure right side.

plateau width can be tuned by the loading current density [Uchi11].

Fig. 5.30 compares the effect of the Mg-layer thickness on the total hydrogen diffusion coefficient D_H^{tot}, by using the same condition of hydrogen loading current density. Upon thickness increase the total diffusion coefficient D_H^{tot} decreases, clearly showing the impact of the diffusion of hydrogen through the Mg-film. As the diffusivity is smaller in Mg than in Pd, it lowers the total diffusivity.

Permeation measurements by potentiostatic loading condition were also applied for a 20 nm Pd / 2100 nm Mg / 12.5 μm Pd sample. A breakthrough time of $t_b = 57 \pm 2$ s is obtained, for total concentration of $c_H < 10^{-2}$ H/(Mg+Pd). Applying this breakthrough time for Eq.(3.17) yields a total diffusion coefficient of $D_H^{tot} = 5.9(\pm 0.5)\cdot 10^{-13}$ m²/s. Applying this value with $D_H^{Pd} = 3.1\cdot 10^{-11}$ m²/s for Eq.(3.19), a hydrogen diffusion constant of $D_H^{Mg} = 8.5(\pm 1)\cdot 10^{-11}$ m²/s is gained.

5.5.3 Sample bending

After electrochemical hydrogen permeation, self-bending phenomenon was observed for the fully hydrided samples, after leaving the samples for 1 hour in air (shown in **Fig. 5.34**). This effect can be explained by the different stress states between both surfaces, caused by remaining stable hydride in the Mg-layer. At the substrate side, the hydride phase of Pd dissociates faster compared to stable MgH$_2$, which explains directly the existence of in-plane stress in the Mg-film side. Because of the large difference of the hydrogen diffusion coefficients with factor of more than 1000 (**Fig. 2.4**), the hydride dissociation rate is controlled by the slower hydrogen diffusion coefficient in the Mg layer, and therefore such bending effect is expected to happen. In case of MgH$_2$, decomposition from high c_H state needs additional process of α-Mg nucleation in the hydride phase, which could make the over-all dissociation energy of MgH$_2$ higher [Evar10].

Fig. 5.31 Bulged Pd/Mg/Pd-substrate sample after electrochemical hydrogen loading. (A picture from the Pd-substrate side). The shape of the film remained stable.

5.5.4 Hydrogen diffusivity at higher c_H

In this Chapter, the reaction kinetics of gas-loaded samples will be presented. **Fig. 5.10** and **Fig. 5.12** show the time dependency of the peak areas development. In those graphs, two different regimes of kinetics with a linearity in $t^{1/2}$ can be observed upon hydrogen absorption of Mg-films.

First, the estimation of the different apparent diffusion constants for the different regimes is intended. Assuming the one-dimensional diffusion Eq.(3.7), which is motivated by the measured $t^{1/2}$ - dependency of each regime, the mean effective hydrogen diffusion constants can be obtained: $D_H^{Mg,I} = 2.5(\pm1.0)\times10^{-16}$ m^2s^{-1} , $D_H^{Mg,II} = 5.5(\pm0.5)\times10^{-18}$ m^2s^{-1} , and $D_H^{Mg,II\text{-}END} = 1.0(\pm0.5)\times10^{-18}$ m^2s^{-1} in the first, second, and at the end of the second regime, respectively. These values are determined nearly independent on the different film thickness and gas pressures. The apparent diffusion constant drops by two orders of magnitude between regime I and the end of regime II. The diffusion in the beginning and the end of regime II differs only by a factor of 5. Thus, regime II can be regarded as a transition regime.

Fig. 5.32 compares the calculated diffusion coefficients with literature data, extrapolated from high temperatures values [Stan77,Renn78,Sime80,Toep82,Stio84,Nish99,Yao08] or measured at 300 K [Spatz93,Qu10], with theoretical calculation [Hao08]. The increase of the hydride volume fraction (as marked by an arrow in **Fig. 5.32** right side) leads to a drop in the apparent diffusion constant. The hydrogen diffusion constant $D_H^{Mg} = 7(\pm2)\cdot10^{-11}$ m^2/s, as obtained from the permeation experiment at 300 K using the multilayer model, is shown as a blue circle in the figure and marked with 'P'. It matches to the low-temperature extrapolation of the hydrogen diffusion coefficients obtained by Nishimura *et al.* [Nish99] in pure α-Mg, in the temperature range 473-493 K. This confirms that the hydrogen diffusion in the n-Mg-films at 300 K is equivalent to that of the α-phase. However, this value was still measured in our experiment on n-Mg, when the EMF curve and the hydrogen concentration reveal the existence of MgH$_2$ phase. It is found up to $c_H = 6\cdot10^{-3}$ H/(Mg+Pd), as shown in **Fig. 5.29 left** in **Chap. 5.5.2**.

The value of $D_H^{Mg} = 7(\pm2)\cdot10^{-11}$ m^2/s obtained for the n-Mg films is higher than the extrapolated values measured by Stander [Stan77] under 3 MPa hydrogen loading pressures, and even higher than those for Mg-alloys reported by Renner and Grabke [Renn78] and Simensen [Sime80]. It is about 10 orders of magnitude higher than the reported hydrogen diffusion constant in MgH$_2$, as determined by Spatz *et al.* [Spatz93].

The fast hydrogen diffusion in the α-Mg phase confirms the presence of α-Mg phase diffusion paths through the film even when Mg-dihydride is already formed. It allows excluding the presence of a closed Mg-dihydride layer at the film's loading side.

Further diffusion constants, as measured by changes of the relative peak area with XRD and using Eq.(3.6) and Eq.(3.7) are added as triangles for the 500 nm films and as circles for the 2800 nm films, in **Fig. 5.12**. They are labelled I and II.

The diffusion coefficients obtained in this work at each regime are compared with other values in **Fig. 5.32**.
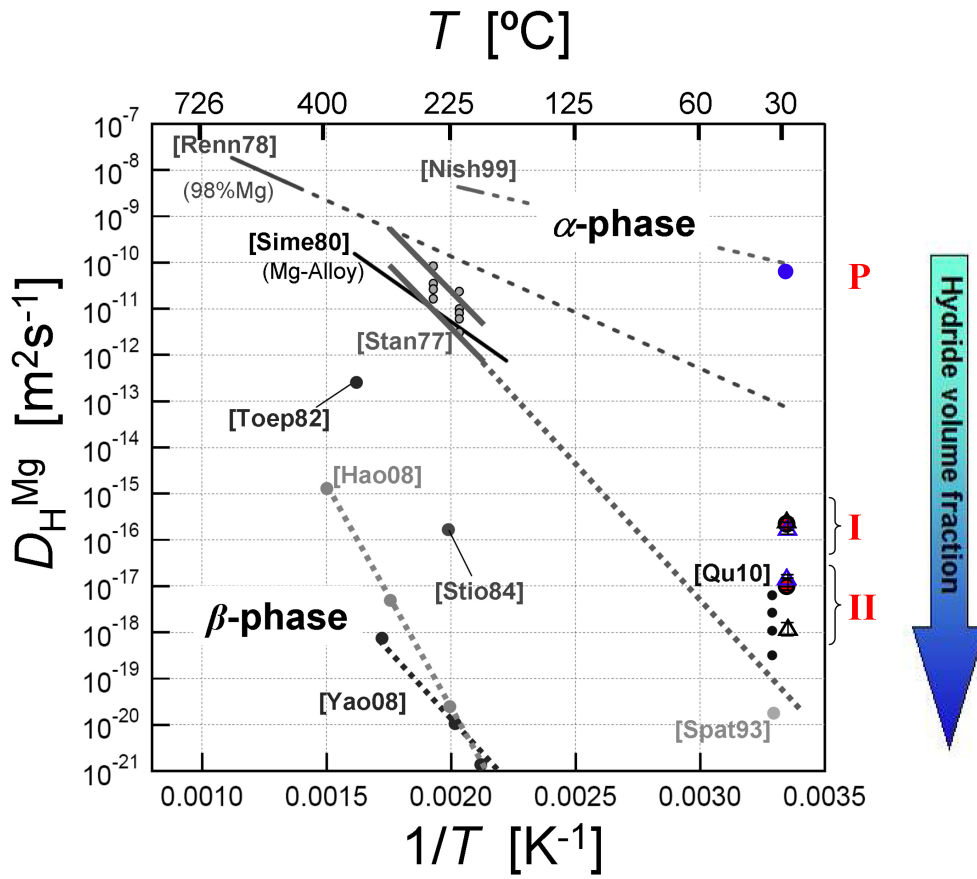
Fig. 5.32 Obtained hydrogen diffusion constants from this work at T = 300 K from the electrochemical hydrogen permeation measurement (blue circle), and from gaseous hydrogen loading measurements (regime I and II, hollow blue triangles relate to 500 nm Mg and loading hydrogen pressure of 20 mbar; hollow black triangles and red circles relate to samples of 500 nm and 2800 nm thickness, with loading hydrogen pressure of 200 mbar, respectively). For comparison, extrapolations of literature data are plotted. (See **Fig. 2.5** in **Chap. 2.1.4.4** and **Table A3.1** in **Appendix A3** for explanation).

5.6 *In-situ* gas-loading measurement at elevated temperatures

To investigate the mechanical stress impact on the thermodynamical stability of β-MgH$_2$, equilibrium states of the Mg film-hydrogen system were investigated in the temperature range of 288 K-343 K under the constant-flow hydrogen gas atmosphere with the pressure conditions up to $p_{H2} = = 35$ mbar.

Temperature changes change the free energy. It affects the mechanical properties of the material and the hydrogen sorption properties. The effect of temperature on the mechanical properties and on the thermodynamic change of the H-Mg and the H-Pd system will be shortly discussed in this section.

5.6.1 Temperature effect on in-plane stress and solubility ratio

Because of the difference in the thermal expansion coefficient between Mg and Si, Mg films reveals not only the stress due to hydride nucleation, but also thermal stress due to temperature change. To divide these contributions, the temperature effect on the inner stress for the Mg film was investigated at different temperatures, before hydrogen loading.

Due to the temperature change of $\Delta T = 343$ K - 288 K $= 55$ K, a contribution of the thermal expansion stress $\sigma_{therm.}$ on the biaxial in-plane stress change is calculated by Eq.(2.60) as $\sigma_{therm.} = (1.661 \cdot 55)$ MPa $= 91.36$ MPa .

Recently Pivak *et al.* [Pivak12] reported a temperature dependency of Young modulus E on temperature T, to be proportional at $T > 273$ K and the slope of $dE/dT = -18.49$ MPa/K , using Varshni's theoretical model [Vars70]. According to this temperature dependency, E decreases about 2.5 % from 45 GPa to 44 GPa, as the temperature increases from $T = 343$ K to 288 K. Because this change is small compared to the expected error due to angular anisotropy (up to 11%), as shown in **Chap. 2.2.2**, E was treated as a constant in the used temperature range in this work. Moreover, the temperature change also affects the hydrogen solubility change in metals (see **Chap. 2.2.1** or ref. [Fukai05]), thereby the stress is also affected. However, these effects are here ignored, because of the small solubility limit of H in Mg, also in the used temperature range. (See **Fig. 2.8**).

In the α-phases, hydrogen dissolves into Pd and Mg, according to the solubility ratio of hydrogen in both layers. This can be estimated by the solution energy of hydrogen for each material, as shown in Eq.(3.16), assuming equilibrium states of bulk material. **Fig. 5.33** presents the temperature dependence of the solubility ratio, $k = \left(c_{H\,in\,Mg} / c_{H\,in\,Pd} \right)$. The k changes by about 1 order of magnitude by increasing T from $T = 273$ K to $T = 373$ K, however this is still large deviation of $k \approx 10^{-2}$ at $T = 373$. This increase of k is mainly dominated by the increase of $c_{H\,in\,Mg}$. The solubility of hydrogen in Mg at $T = 373$ is roughly estimated to be $c_H \approx 10^{-5}$ H/Mg by Eq.(2.23a).

The transition of Mg-MgH$_2$ is expected at lower p_H, compared to that of Pd-PdH$_{0.6}$ transition in the temperature range of $T = 293\text{-}363$ K, which is treated in this work.
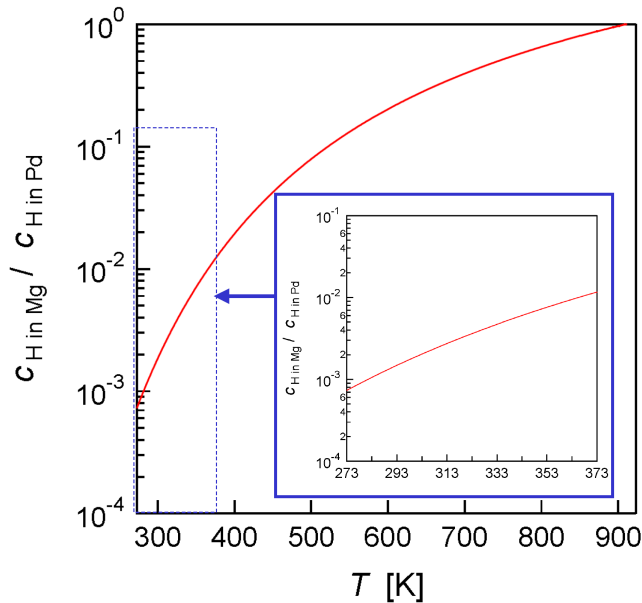
Fig. 5.33 The solubility ratio of hydrogen concentration in Mg and in Pd ($c_{H\,in\,Mg}$ and $c_{H\,in\,Pd}$, respectively), as a function of temperature T, up to the melting point of bulk-Mg. An extended figure is inserted, which corresponds to the temperature range treating in this work. Data of [Bohm99] and [Flan91,Wick64] are used for solution energy of H in Mg and Pd.

5.6.2 Transition pressure at different temperatures

Transition pressures of the Mg-MgH$_2$ system were investigated for Mg films on Si-substrates, at different temperatures. Especially in this measurement, the effect of temperature on the hydride stability is of interest. The hydride stability in annealed Mg film was evaluated at room temperature as a reference, because grain coarsening during the measurements at elevated temperature is expected, for nc-Mg films. Two annealed 1450 nm Mg-film were prepared for the measurements here, at the same time: one for a preliminary experiment at room temperature, and another for measurements at elevated temperatures.

Fig. 5.34 shows an example for the β-MgH$_2$(110) peak shift during unloading, for an annealed
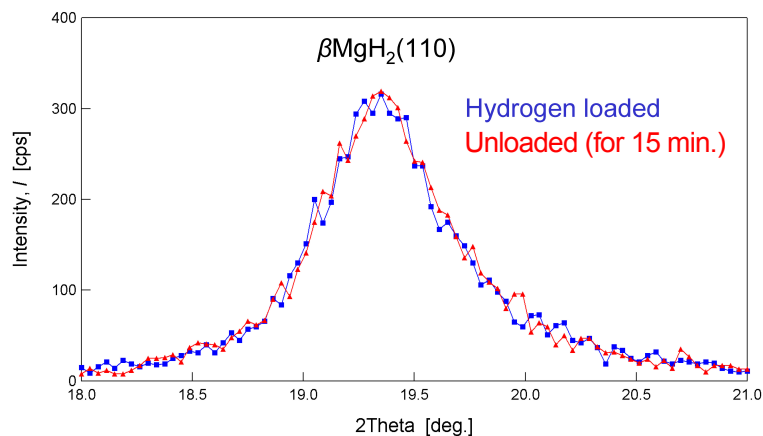
Fig. 5.34 Results of *in-situ* XRD peak change of β-MgH$_2$(110) conducted for 1400 nm Mg film on Si-substrate (annealed at $T = 453$K for 30 min.), in loaded state and after unloading for 15 minutes at $T = 293$ K.

1450 nm Mg-film, previously loaded by hydrogen gas with $p_{H2} = 20$ mbar. The stability of the β-MgH$_2$ phase at room temperature is obviously confirmed by the few changes of the Bragg reflection of β-MgH$_2$(110). A swift decomposition at $T = 293$ K by hydrogen gas evacuation was not possible.

For another annealed 1450 nm Mg-film, decomposition pressures p_H were investigated for a hydrogen gas loaded Mg-film at different temperatures ($T = 313$ K, 323 K, 333 K and 363 K) by observing increase and decrease of α-Mg(0002) and β-MgH$_2$(110) peaks. **Fig. 5.35** shows a
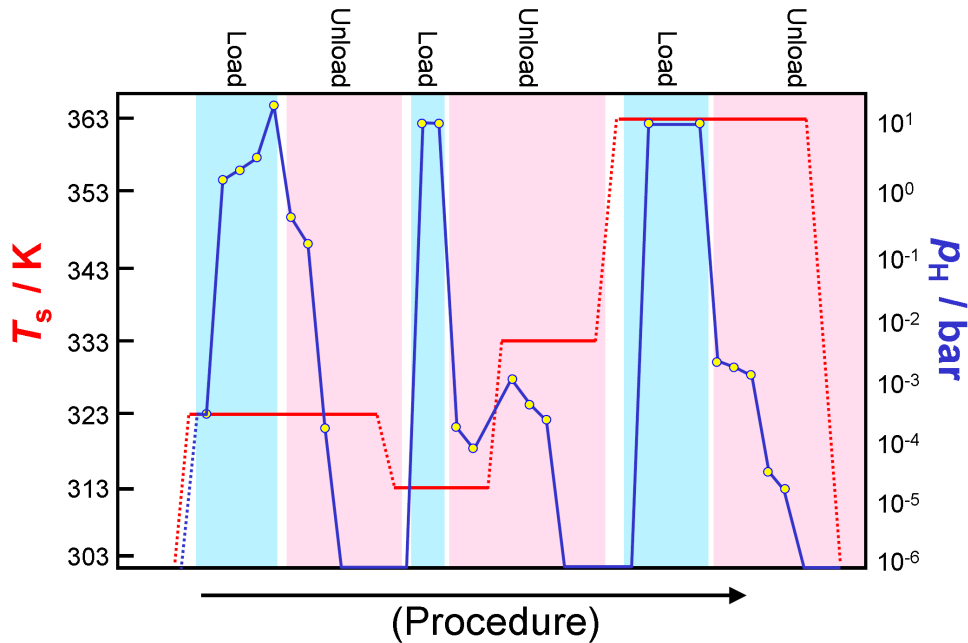
Fig. 5.35 A schematic diagram of the sample temperature (T_s, left axis) and hydrogen pressure (p_H, right axis) controlled during *in-situ* XRD measurement performed in this work at elevated temperatures. Yellow markers correspond to the equilibrium conditions for the executed XRD scans. Blue and pink areas indicate the loading- and unloading process, respectively.
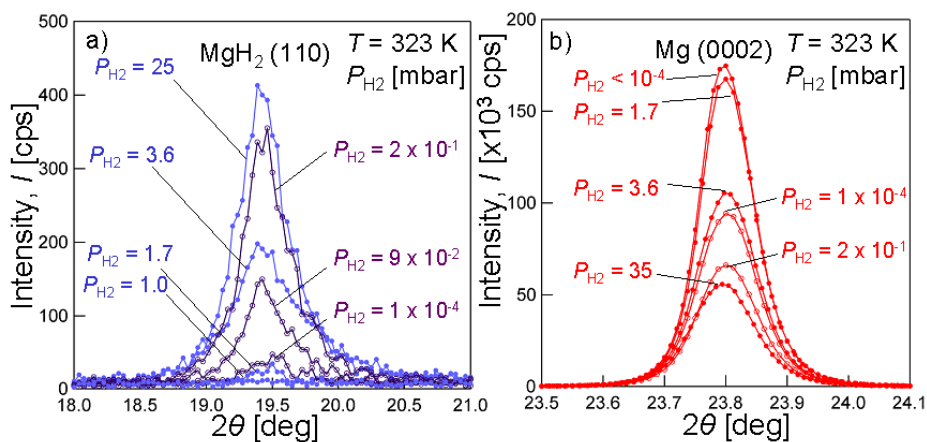
Fig. 5.36 XRD peaks for βMgH$_2$(110) (left, **a**) and αMg(0002) (right, **b**) in equilibrium states at $T = 323$ K under several hydrogen pressures of loading /unloading directions.

schematic diagram of the sample temperature and hydrogen pressures controll during this measurement.

Fig. 5.36 exemplarily shows the results of XRD peaks for α-Mg(0002) and β-MgH$_2$(110) measured at each quasi-equilibrium step at $T = 323$ K, as an example. Nucleation and increase of β-MgH$_2$(110) and decrease of the α-Mg(0002) were observed in the 1st loading and 1st unloading process.

Further on, the decomposition pressures were also determined in the 2nd cycle at $T = 313$ K and $T = 333$ K, yielding $p_{H2} \sim 9.5 \cdot 10^{-2}$ mbar and $p_{H2} \sim 3 \cdot 10^{-1}$ mbar, respectively. The decomposition pressure at $T = 363$ K was also determined to be $p_{H2} \sim 1.5$ mbar in the 3rd cycle.
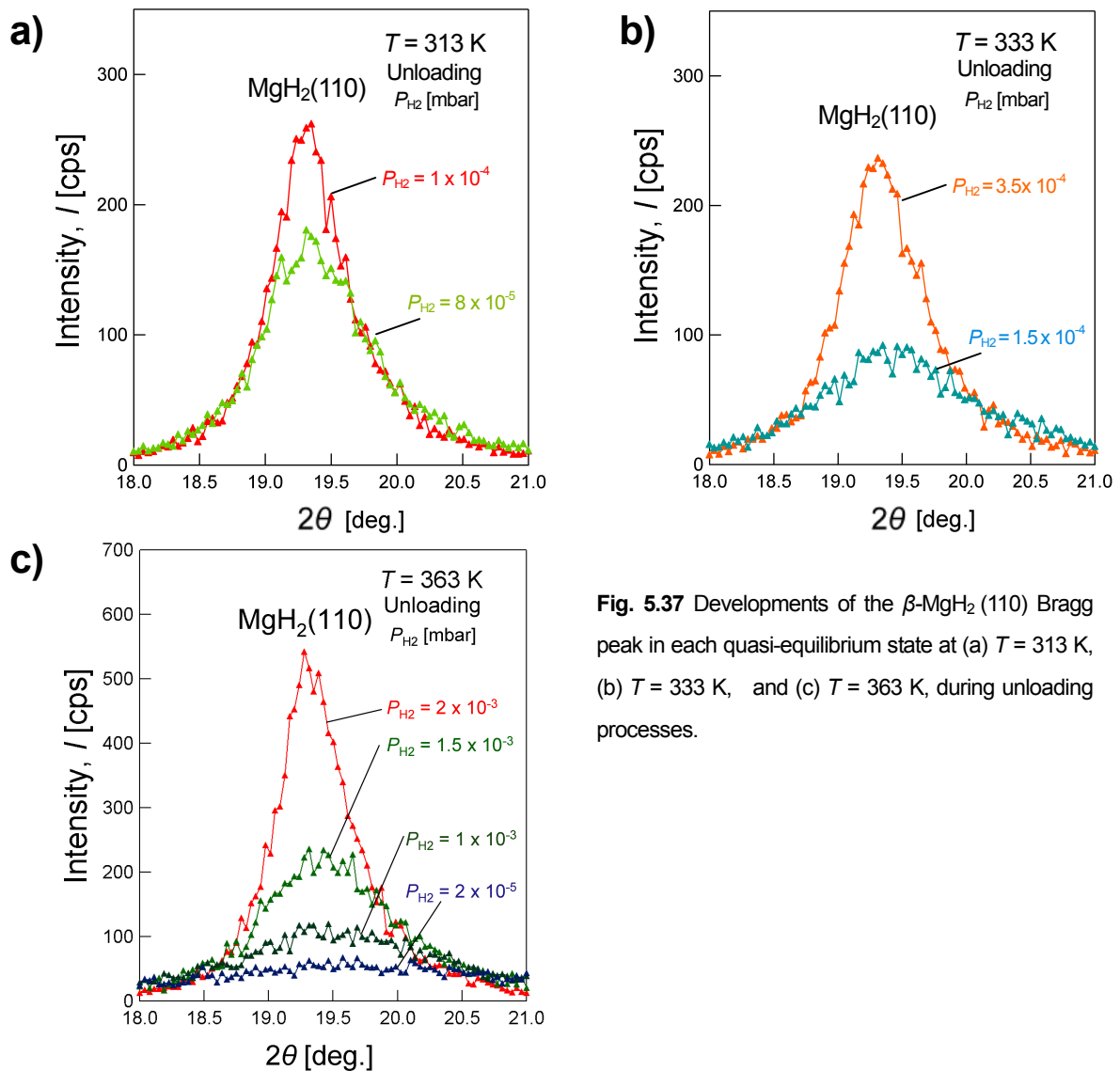
Fig. 5.37 Developments of the β-MgH$_2$ (110) Bragg peak in each quasi-equilibrium state at (a) $T = 313$ K, (b) $T = 333$ K, and (c) $T = 363$ K, during unloading processes.

The peak changes of β-MgH$_2$(110) during each unloading step are shown in **Fig. 5.37**.

In-plane mechanical stress change in the Mg films before and after hydrogen loading is evaluated from the αMg-(0002) peak shift to be $\Delta\sigma^P \approx +0.4$ GPa, using Eq.(3.8).

The tendency of increasing decomposition reaction rate by elevation of the reaction temperature was clearly visible. For example, evacuation for 15 minutes is adequate for

decomposition from $c_H \sim 2$ H/Mg to $c_H \sim 0.2$ H/Mg at $T = 363$ K, meanwhile the evacuation for 15 minutes yielded almost no peak change at $T = 293$ K for the same sample.

During the measurement, no peak nucleation of the γ-MgH$_2$ phase was observed. Thus, the decrease of the β-MgH$_2$ phase was directly treated to transform into the α-Mg phase. The mass ratio of both phases upon transition were roughly estimated from the peak area change of the β-MgH$_2$(110) at each temperature, and plotted as function of the hydrogen concentration to generate isotherm curves, shown in **Fig. 5.38**.

Based on the obtained result, the *p-c-T* curves are plotted in **Fig. 5.38** for Mg-film at different temperatures ranging from 313 K up to 363 K. The directions of the reaction are indicated by arrows in the figure. The plateau pressures on the decomposition reactions were adopted for the van't Hoff plot in **Fig. 5.39**. which will be shown in the next Chapter. Strictly speaking, these plots are from the results of each steady state, however they could be a value in quasi-equilibrium. Therefore, it is remarked that errors are possible in both of the concentration axis and the pressure axis in **Fig. 5.38**.
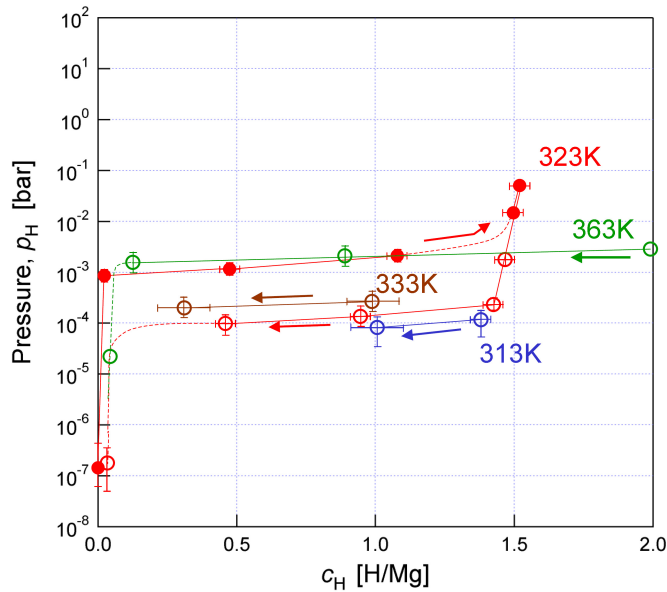
Fig. 5.38 *p-c-T* isotherm curve obtained by this work for Mg-film, 1st cycle at $T = 323$ K (red), part of 2nd desorption cycle at $T = 313$ K (blue) and $T = 333$ K (brown), and 3rd desorption cycle at $T = 363$ K (green).

5.6.3 Hydride decomposition enthalpy of Mg films: stress impact

The obtained plateau pressures for the decomposition reactions at elevated temperatures are plotted in a van't Hoff plot with error bar by purple markers, compared with referential data in **Fig. 5.39**.

The hydride decomposition enthalpy calculated from these measurements was calculated as 62 ± 7 kJ/mol from desorption plots. Those values contain large errors; stricktly speaking, the conditions at each hydrogen loading step could be not in the true equilibrium conditions, because

of the blocking effect. It is remarked that the plateau pressures obtained in this measurement were values in quasi-equilibrium states.

A MgH$_{2-\delta}$ phase is reported in this system by Borgschulte *et al.*, as an intermediate phase, from their DSC study [Borg07]. Formation of this phase could be possible, by such as stress-induced vacancy deviation. However it is difficult to clarify the existence of this MgH$_{2-\delta}$ phase, from just one single peak in the diffraction pattern.

Baldi *et al.* reported that the plateau pressure depends on the loading cycle, and this effect can be reduced by applying Ti buffer layer, in their hydrogenography study [Baldi09++]. Strictly speaking, results of this work could contain an effect of interdiffusion at Pd/Mg boundaries, which increases equilibrium pressure according to Baldi *et al.* [Baldi09++]. This point will be discussed later in **Chap. 5.7.5**.

In this work, a peak separation of the *β*-MgH$_2$(110) peak was expected in case of existence of MgH$_{2-\delta}$ phase. However, due to broad peaks, this effect was not recognized. No peaks of obtained XRD pattern were indexed by intermetallic compounds or hydrides in the Mg-Pd system or in the Mg-Pd-H system, however, solution of Mg into Pd layer, or formation of intermetallic compounds at interlayer with Pd is possible. During long waiting time at high temperature which changes thermodynamic property of the film Mg-H system. Therefore, strictly speaking, the obtained pressure values could contain large error.
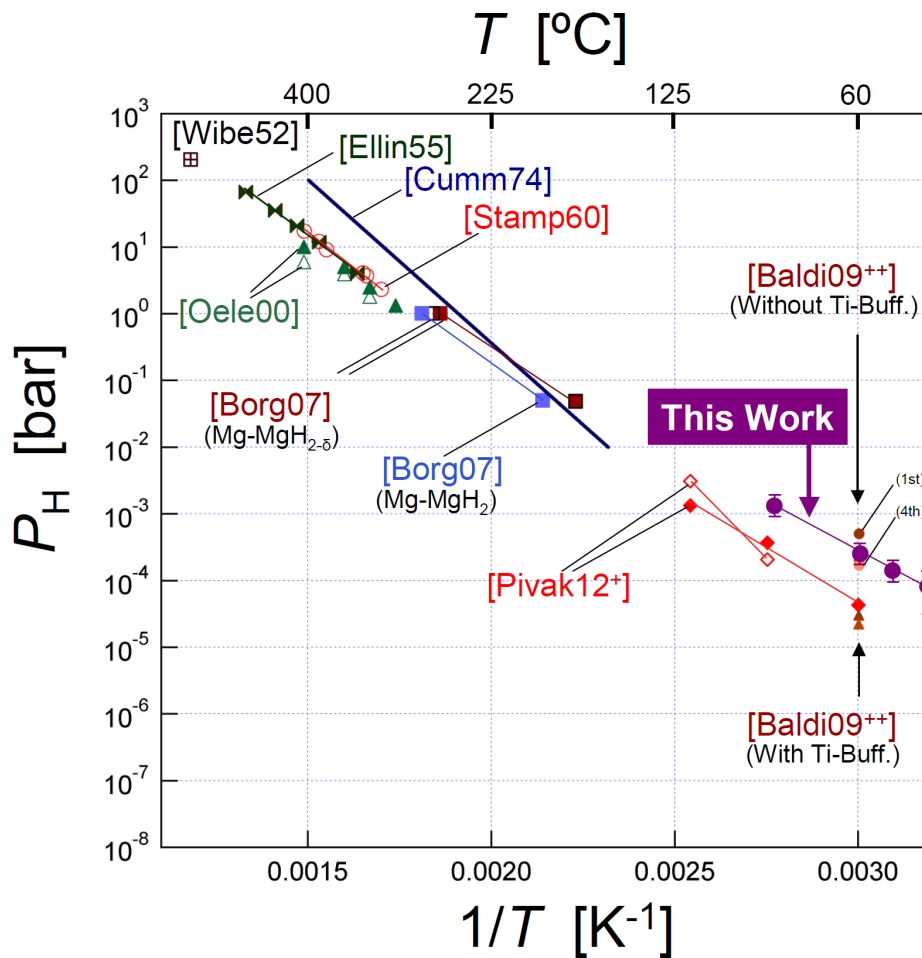
Fig. 5.39 Van't Hoff plots obtained this work (marked in purple circles) compared with reference values [Wibe52,Ellin55,Stamp60,Cumm74,Oele00,Borg07,Baldi09^{++},Pivak12^{+}]. Hollow/filled symbols are in the desorption/absorption reaction, respectively.

However, taking errors into account, the obtained absolute enthalpy values are smaller than that of bulk Mg, reported by Stampfer *et al.* (-70.8 kJ/molH$_2$ to -72.6 kJ/molH$_2$) [Stamp60] or by Kennelly *et al.* (-74.1 ±2.9 kJ/molH$_2$)[Kenn60], as is visible in the difference of slope in **Fig. 5.39**. The influence by the in-plane compressive biaxial stress, mainly due to the clamping by the substrate is suggested for this smaller hydride formation enthalpy compared to the bulk material.

About this high equilibrium pressures, some possible reasons are discussed.

At first, an increase of sample temperature due to the high enthalpy change upon the transition into β-MgH$_2$ is suggested. An increasing temperature yields a higher partial pressure of hydrogen in equilibrium, as is shown in **Fig. 5.38**. However, a temperature change during hydrogen loading was not observed (with error smaller than 1 K by directly installed thermocouple on the sample.) Therefore, further possibilities are discussed, assuming no temperature change due to the reaction.

Now, the contribution of the elastic term on the free energy change upon the hydrogen loading reaction is discussed [Laud98,Dorn02,Pundt06]. It is known that the increase of stress

affects the chemical potential of hydrogen [Li66,Kirch86]. In order to calculate the free energy change due to the increase of compressive inner stress, an estimation is introduced. Assuming an isotropic film clamped on a substrate (**Fig. 2.15**), the change in the free energy ΔF can be expressed for this case by [Dorn02]

$$\Delta F = \sum_i \int V \sigma_i \varepsilon_i = \sum_i \int V (M \cdot \varepsilon_i) d\varepsilon_i \tag{5.1}$$

where V is the volume (treated to be constant), $\sigma_{i,i=xx,yy} = -M \cdot \varepsilon_{0,xx,yy}$ is the biaxial stress (principal stress), ε the expansion which would occur in a free film, M the biaxial modulus, and $i = x, y$. Then $\Delta F \approx V \alpha_H^2 M \sum_{i=xx,yy} \int c_H dc_H$, therefore, the following relationship is obtained

$$\Delta F \approx V \alpha_H^2 M c_H^2 \tag{5.2}$$

where $V = 14.0$ cm^3/mol is the molar volume of the α-Mg [Aved99], $M = 70.63$ GPa and $\alpha_H = 0.081$ are already obtained for (0001)- oriented hexagonal Mg film by Eq.(2.37) and Eq.(2.39), respectively. The contribution of the biaxial stress to the free energy ΔF (unit in kJ/(mol Mg)) is calculated to be

$$\Delta F \approx (14 \cdot 10^{-6}) \cdot (0.081)^2 \cdot (70.63 \cdot 10^9) \cdot c_H^2 = 6.487 \cdot c_H^2$$

$$\text{with } 0 < c_H < 2 \tag{5.3}$$

According to this estimation, MgH$_2$ laterally fixed on a hard substrate could be destabilized by up to $\Delta F = 24$ kJ/(mol Mg) $\approx$ 0.25 eV/(Mg atom). This result has also good agreement with the rough calculation by Dornheim (calculated to be $\Delta F \approx 4.4 \cdot c_H^2$ kJ/(mol Mg)) for Mg film, assuming isotropic material [Dorn10]. Similar influence of the biaxial stress on the thermodynamical peroperties is also reported for Pd by Wagner *et. al.* [Wagn08,Wagn15].

On one hand, this contribution of the biaxial stress to the free energy could cause smaller enthalpy for absorption reaction of Mg with hydrogen, compared to Bulk sample. On the other hand, for decomposition reaction from fully hydrided state needs further discussion about the instability of the hydride phase.

Recently, Zhang *et al.* [Zhan13] reported on the effect of biaxial stress on the thermodynamical stability of β-MgH$_2$ using first-principles calculations based on the density functional theory (DFT). In their study, the structural deformation and energy of β-MgH$_2$ crystal due to the biaxial stress is calculated as a function of biaxial strain, and involving this energy term into the energy term of phase transition, they concluded decrease of decomposition temperature for β-MgH$_2$ phase, under negative strain of ε_{zz}. **Fig. 5.40a** shows the β-MgH$_2$ structure with (110) plane, and **Fig. 5.40b** shows the reported strain energy of β-MgH$_2$ phase as a function of strain [Zhan13].

From the XRD peak shift, atom plane of the β-MgH$_2$(110) has strain of ((3.21Å-3.19Å)/3.19Å=) +0.7%, at hydrided state at 323 K. This strain corresponds to about -1 % strain in (100) direction of the β-MgH$_2$ structure, applying rotation matrix (see Eq.(2.50)-Eq.(2.55) in **Chap. 2.2.1**). From this strain, destabilization of the hydride phase is evaluated.

According to this, -1 % of strain change induces 0.23 eV destabilization of the strain energy. This value has good agreement with the calculated value, $\Delta F \approx 0.25$ eV/(Mg atom), as obtained in this work.
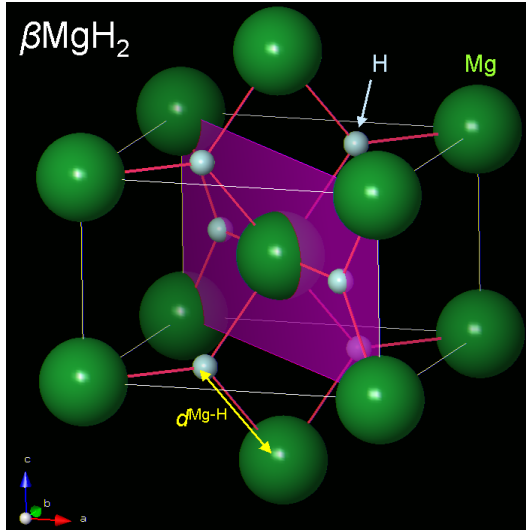
Fig. 5.40a The crystal structure of tetragonal βMgH$_2$. Bonds between Mg atom (green) and H atom (blue) are expressed by pink solid line, and the (110) plane is shown with plane.
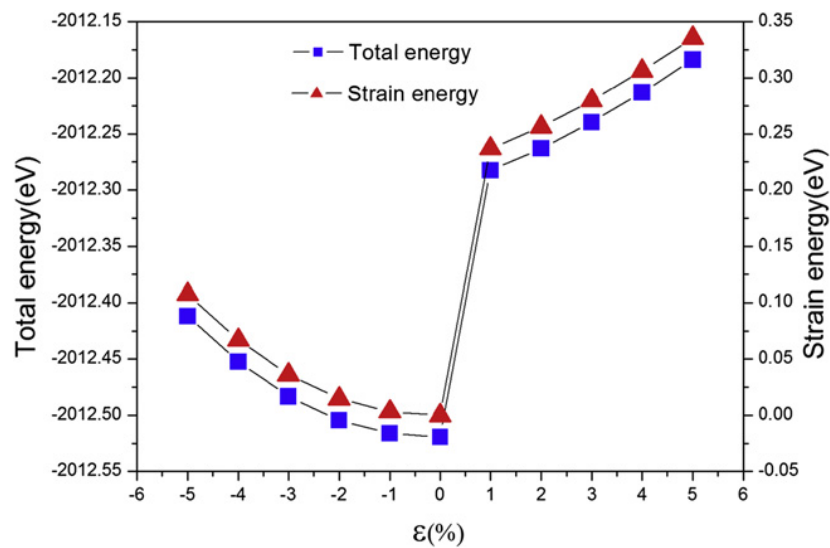
Fig. 5.40b Calculated total energy and strain energy as a function of biaxial strain ε in βMgH$_2$ unit cell, calculated by DFT by Zhang *et al.*. [Zhan13]

5.6.4 Alternative explanation

Additional possible side effects are discussed, apart from the previous discussions above. For powder samples, Vajo *et al.* [Vajo04] showed that Si can destabilize MgH$_2$ by setting up a competing reaction (given by MgH$_2$ + Si $\Leftrightarrow$ Mg$_2$Si + H$_2$) which decreases the enthalpy change

of magnesium hydride ($\Delta_f H$ and $\Delta_d H$) for pure Mg from $\Delta H = 75.3$ kJ/(mol H$_2$) to $\Delta H = 36.4$ kJ/(mol H$_2$) for the silicide. In that process, Mg$_2$Si forms as an intermediate compound which might be possible at the interface between the Mg-film and the Si substrate. However, this aspect can be neglected, because of the enough thickness of the Mg-layer (> 1μm). A solution of Si in Mg can be also neglected (see **Chap. 2.1.8**).

Instead of the effect of forming Mg$_2$Si at the interface, oxygen atoms that originally exist on the substrate surface as SiO$_x$, are able to destabilize MgH$_2$ phase. Comparing the stability of MgO and SiO in the Ellingham diagram [Ellin44], MgO$_x$ is thermodynamically more stable than SiO$_x$. Therefore, it is thermodynamically preferred for O atoms to exist as MgO$_x$ rather than SiO$_x$ at the interface between Mg and the Si substrate.

With respect to MgO$_x$, partially oxidized magnesium formed on the Mg surface of up to ~14 Å thickness is reported to be able to increase the reaction of Mg with H$_2$, by being a trapping and hydride nucleation centre, as Hjort *et al.* reported [Hjort96]. Yoshimura *et al.* [Yosh04] also reported a similar effect. Oxygen effect on the stability of MgH$_2$ is still not clear, however, it is suggested not to be the dominant effect for destabilization of MgH$_2$ phase in this case, because of the low mobility of oxygen in Mg. Wriedt [Wrie87] reported that the solubility of oxygen is quite small, including elevated temperatures, and there is no possibility for dissolved oxygen atoms to diffuse in solid Mg. This fact suggests that oxygen atoms diffusing through the Mg layer are not a realistic reaction. Most probably, MgO$_x$ stays stable at interlayer between Mg and Si substrate.

A further suggested effect that is more realistic and that could characterize the MgH$_2$ is the effect of intermixing between Mg and Pd capping layer, which is reported by Baldi *et al* [Baldi09^{++}]. This effect could increase the electrical resistivity, or result in other intermetallic compounds [Call10,Pasq11], which were not clearly observed by a resistivity change or by nucleation-related XRD peaks, in this work. However, a Pd solution effect on Mg-H thermodynamics is possible, as is reported in case of a Fe solution effect, which is known to destabilize the β-MgH$_2$ phase of Mg-film samples, as reported by Tan *et al.* [Tan11]. To determine these intermixing effects, further measurements with a buffer layer could be a solution, with material which prevents not only interdiffusion of Mg and Pd, but also has the character not to form intermetallic compounds with Pd or Mg. Ti, which has almost no solid solution regime with Pd and Mg, or Ta (as reported by Pivak *et al.* [Pivak12]) could be candidates for such buffer layers.

5.6.5 Conclusion for measurements at elevated temperatures

Higher decomposition pressures compared to that of bulk samples were measured for the studied Mg film samples. No evidence of metastable hydride phases was obtained. Intermetallic compounds are not expected to be formed during the measurements. Calculation of in-plane stress showed the possibility of mechanical impact on the β-MgH$_2$ phase destabilization, which is in good agreement with DFT calculation result by Zhang *et al.* [Zhan13]. Nevertheless, the

intermixing effect between the Mg and the Pd capping layer is also suggested as a possible factor for destabilization of the MgH_2 phase. To divide these factors or eliminate a solution effect, further experiments with buffer-layers [Baldi09^{++},Pivak12] are needed. Also, further measurements with more thinner films are needed to clarify the mechanical impact on the hydride phase stability.

6. Global discussion

In this chapter, the results obtained in different measurements are synthesized and discussed.

6.1 Thermodynamic discussion of hydride nucleation

Fig. 6.1 shows a schematic drawing of the free energy curves in the Mg-H binary system at a constant temperature T, showing Gibbs energies of both α-phase (G^α) and β-phase (G^β). The liquid phase (G^β) is ignored at room temperature. The chemical potential of hydrogen in the α-phase
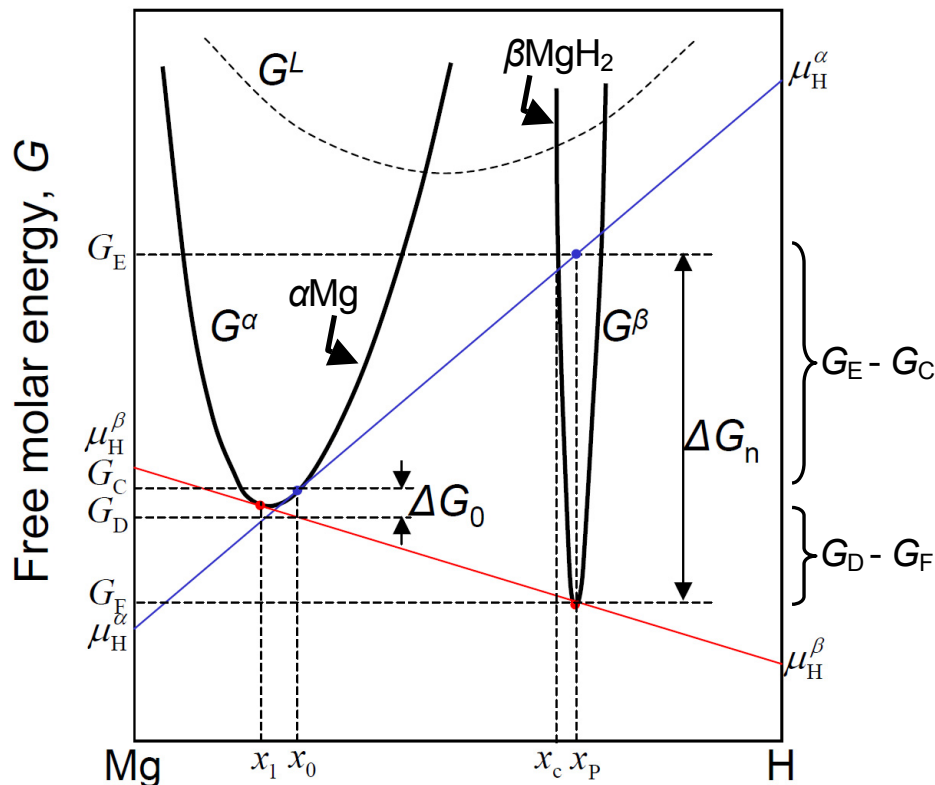
Fig. 6.1 Schematic draw of the free energy curves in the Mg-H binary system at a constant temperature T, for ideal liquid phase (G^L), α-Mg phase (G^α) and for the β-MgH$_2$ phase (G^β). Both curves of G^α and G^β are expanded with respect to the concentration change. The Gibbs energy change of a system by the α-β transition ($\Delta G_0 = G_C - G_D$:driving force) and the Gibbs energy change by nucleating β-MgH$_2$ ($\Delta G_n = G_E - G_F$) are shown in figure. Upon the transition, the concentration of H in α-Mg phase jumps from x_0 to x_1, whereas the concentration of H in β-MgH$_2$ phase is assumed to be constant value of x_P. Supersaturated state of H in α-Mg during hydrogen loading before nucleation (shown with blue line) has a chemical potential of μ_H^α, which is determined by hydrogen pressure in this case. Since β-MgH$_2$ is almost a line compound, an approximation of $x_C = x_P$ is justified. In equilibrium after hydride nucleation, the chemical potential of hydrogen is the same in both phase, therefore $\mu_H^\alpha = \mu_H^\beta$ (shown with red line).

before the nucleation of the β-phase loaded from the gas phase (shown by the blue line in **Fig. 6.1**) is determined by the concentration at $c_H = x_0$, which is determined by a hydrogen loading pressure p_H (see Eq.(2.11)). The hydrogen concentration in the α- and the β-phase after the hydride nucleation are assumed to be at $c_H = x_1$ and at $c_H = x_P$, respectively. The red line shown in **Fig. 6.1** indicates the chemical potential of hydrogen, after the hydride nucleation triggered by the driving force of ΔG_0. The total Gibbs energy change of nucleating β-MgH$_2$ (ΔG_n) is shown in **Fig. 6.1** by

$$\Delta G_n = G_E - G_F \tag{6.1}$$

with

$$G_E = \mu_H^\alpha c_H^\beta + \mu_{Mg}^\alpha c_{Mg}^\beta \tag{6.2a}$$

$$G_F = \mu_H^\beta c_H^\beta + \mu_{Mg}^\beta c_{Mg}^\beta \tag{6.2b}$$

where μ_H^α and μ_H^β are the chemical potential of hydrogen in the α-Mg phase before the hydride nucleation and that in the β-MgH$_2$ phase after the hydride nucleation, respectively, μ_{Mg}^α and μ_{Mg}^β are the chemical potential of magnesium in the α-Mg and β-MgH$_2$ phase after, respectively, c_H^β and $c_{Mg}^\beta (= 1 - c_H^\beta)$ are concentration of hydrogen and magnesium in the β-MgH$_2$, respectively. c_H^β, ΔG_1 and ΔG_2 corresponds to x_P, $(G_E - G_C)$ and $(G_D - G_F)$ in **Fig. 6.1**, respectively. Here, the G^α curve is narrow enough for Mg at room temperature, to assume $G_C \approx G_D$.

Using $\mu_{Mg}^\alpha = \mu_{Mg}^\beta$,

$$\Delta G_n = c_H^\beta (\mu_H^\alpha - \mu_H^\beta) \quad \text{therefore} \quad \Delta G_n \propto (\mu_H^\alpha - \mu_H^\beta) \tag{6.3}$$

is obtained. Taking this conclusion into account, further section describes the nucleation model.

6.2 Hydride nucleation model in the Mg-H system

Hydride nucleation behavior in the Mg-matrix upon hydrogen absorption is explained from classical nucleation and growth theory [Verh75].

The free-energy change ΔG can be expressed by the bulk free-energy change ΔG_B, the surface tension γ and the elastic strain energy $\Delta G_{El.}$ as follows:

$$\Delta G = \frac{4}{3} \pi r^3 \Delta G_B + 4\pi r^2 \gamma + \frac{4}{3} \pi r^3 \Delta G_{El.} \tag{6.4}$$

Between ΔG_B in Eq.(6.4) and ΔG_n in Eq.(6.3) follow a relationship as

$$\Delta G_B = \frac{\Delta G_n}{v_{mol.}^{\beta MgH2}} \tag{6.5}$$

where $v_{mol.}^{\beta MgH2}$ is the molar volume of the nucleated β-MgH$_2$ phase.

The total free energy change expressed in Eq.(6.4) can be plotted as shown in **Fig. 6.2**. To simplify the model, the elastic energy term $\Delta G_{El.}$ which is anisotropic for the Mg-MgH$_2$ transition, is here neglected.
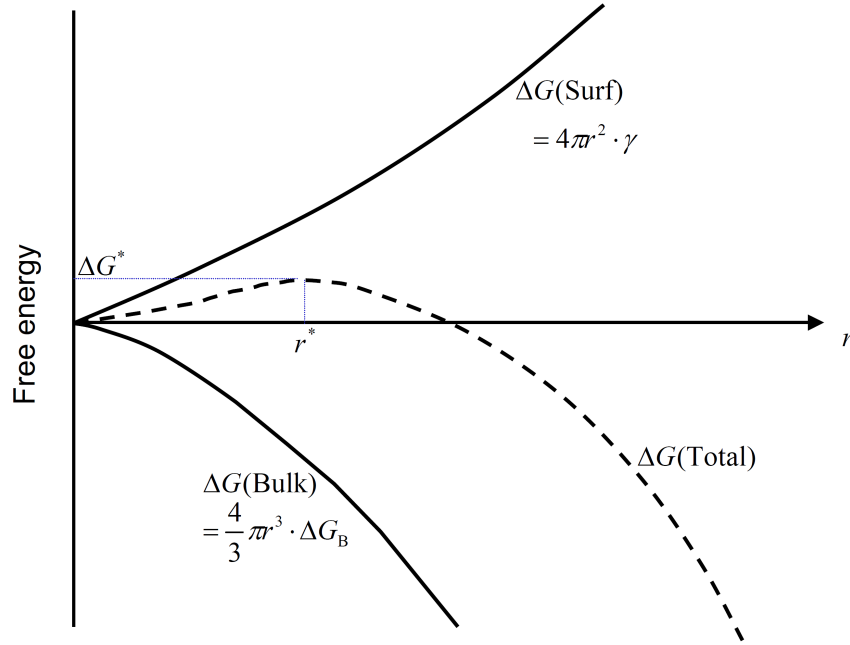
Fig. 6.2 Conceptual diagram of the free energy of nucleus formation and growth, as a function of its radius.

The ΔG reaches a maximum value of ΔG^* at a critical radius r^*, which is expressed as

$$r^* = \frac{-2\gamma}{\Delta G_B} \tag{6.6}$$

Here, for the simplest models and by neglecting the elastic energy terms [Schw06], the radius of the critical nucleus r^* scales inversely with the driving force $\Delta(\mu_{load} - \mu_\beta) \cdot \Delta c$:

$$r^* = \frac{2\gamma}{\Delta(\mu_{load} - \mu_\beta) \cdot \Delta c} \tag{6.7}$$

Here, μ_{load} and μ_β represents the chemical potential of hydrogen atoms during hydrogen loading and that in the β-hydride phase respectively, and Δc is the whole hydrogen concentration change upon absorption.

The driving force depends on the loading gas pressure. Since the chemical potential can be expressed as $\mu = \mu_0 + RT \ln(p/p_0)$, this means that upon higher overpressure p the size of the critical nucleus shrinks. Thereby, also smaller nuclei become stable. The critical size also depends on the interfacial energy γ between the α-phase and the β-nucleus. It is typically of the order 500 mJ/m^2 for incoherent solid/solid interfaces [Balu05].

The nucleation rate $\dot{N}$ depends on the related nucleation barrier ΔG_0:

$$\dot{N} \propto \exp\left(-\frac{\Delta G_0}{RT}\right) \tag{6.8}$$

For smaller nucleation barriers ΔG_0, larger nucleation rates occur at a constant temperature T. This nucleation barrier ΔG_0 itself depends inversely on the square of the driving force $\Delta(\mu_{load} - \mu_\beta) \cdot \Delta c$:

$$\Delta G_0 = \frac{16}{3}\pi \frac{\gamma^3}{\left(\Delta(\mu_{load} - \mu_\beta) \cdot \Delta c\right)^2} \tag{6.9}$$

In total, the increase of the driving force results in a strong increase of the nucleation rate and thereby, in a large number of small nuclei. In this case, the distance between the growing particles is small.

With respect to the hydride nucleation behavior in the α-Mg phase, Rydén *et al.* applied the ^{15}N method and obtained unusual pressure dependence for the hydrogen uptake of 600-1300 nm thick Mg-films sandwiched by Pd at $T = 260$-403 K, which increases with decreasing pressure, [Ryde89]. The hydride nucleation from the Pd/Mg interface was suggested. Furthermore, Mooij *et al.* [Mooij13] recently reported two-dimensional nucleation and growth of single hydride domains of up to several millimeters in diameter with low density of nuclei points. From an analysis of the growth kinetics they deduce an extremely large edge boundary energy, which they relate to the plastic deformations inherent to the 30% volume expansion of the MgH$_2$.

In this work, a model is suggested that describes the different stages for hydride nucleation and growth in poly-crystalline Mg-films, based on the *in-situ* hydrogen gas-loading results (**Chap. 5.2.1.2**). It includes a spatial distribution of half-spherical hydrides and their growth. Many of the experimental findings can be explained with these hydride morphologies. **Fig. 6.3 a)-d)** show a schematic drawing of this model, for four subsequent situations.
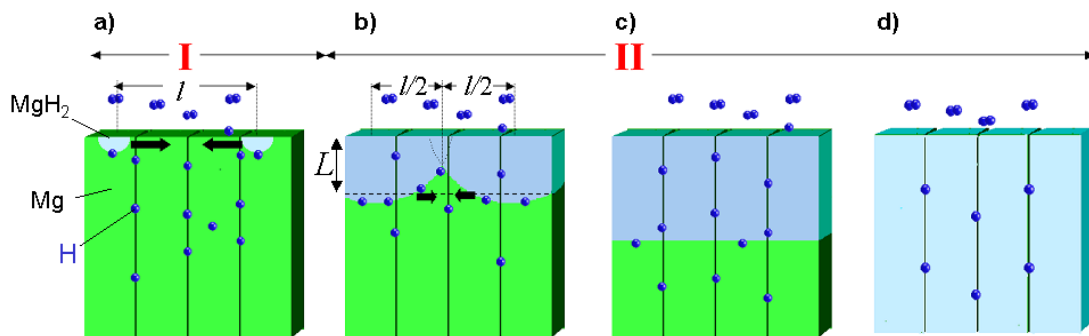
Fig. 6.3 Schematic drawing of the hydride nucleation and growth model suggested for the Mg-films with grain boundaries [Uchi15]. The hydride phase (β-MgH$_2$, blue) nucleation takes place at the film surface with a mean distance of l. It grows like half-spheres into the α-Mg phase (green). Fast diffusion through the α-Mg phase is possible until neighbouring half-spheres meet each other (Regime I). **b)** Further growth of the hydrides close the diffusion paths through the α-phase. A blocking layer of thickness L forms. **c)- d)** Hydrogen supply is limited by the flux along the grain boundaries and interfaces. (Regime II).

It presents a cross section of a thin film with columnar grains where the hydride phase is marked in blue shading and the α-Mg phase in green. The grain boundaries are given by dark vertical lines. Hydrogen is supplied from the upper film surface. Hydrogen atoms are sketched with dots. Half-spherical hydrides nucleate at the sample surface [Vige87,Mooij13]. The distance between the hydride precipitates is marked with l. They grow first isolated from each other, but touch each other after reaching a critical diameter of $d = l/2$. Upon further growth, a hydride layer of thickness L is formed. This hydride layer afterwards propagates until the complete film is hydrided.

The local mechanical stress calculated from the finite element method (FEM) is mapped in **Fig. 6.4**. It arises when the half-spherical hydrides form in the Mg-film, for a situation like that in **Fig. 6.3 a)**. The FEM calculations using the COMSOL Multiphysics program package (ver. 4.6, COMSOL Inc.) was performed by M. Hamm [Uchi15]. It shows an example from a series of simulations performed at 5 half-circular particles of 800 nm distances, at a size of 300 nm.

In the example of **Fig. 6.4**, the compressive stress arises in the hydride half-spheres, with maximum stress of -4 GPa at the upper film edges. The hydride surface is slightly lifted above the film level, because of the local vertical expansion of the hydride. In this region the local stress is, therefore, reduced when compared to the inner regions of the hydride. The compressive stress also arises between the hydride half-circles in the α-Mg-phase. The local magnitude is of the order of -3 GPa, decreasing from the film surface into the bulk. Below the hydride, a small tensile stress of about +400 MPa builds up that is related to the lateral hydride expansion into the film matrix. In contrast to the former results on columnar Nb-H precipitates in Nb-films, lateral expansion is possible, as the hydride is not reaching the substrate [Nört08].

The FEM calculations were executed on two-dimensional Mg-films of 500 nm thickness fixed to a stiff substrate. The elastic properties of Mg were implemented from the COMSOL material database. For simplicity, the films were assumed to behave isotropically and the elastic properties of Mg-matrix and its hydride were treated the same. Film expansion was not allowed at the substrate borders in lateral directions, which accounts for the film clamping condition to the substrate. The lateral size of the matrix was set to be sufficiently large to exclude border effects. It was set by summing up 5.2× the distance between the hydrides with 6× the hydride radius. The thermal expansion package was used to model the hydrogen induced expansion [Nört08]. A value of the one dimensional expansion coefficient (0.103) was assumed, which was calculated from the volume expansion upon the phase transition from Mg into MgH$_2$ ($V_{MgH2}/V_{Mg} \approx 0.31$, see Eq.(2.38)). Only the hydride parts were assumed to expand actively. The sliding between the precipitates and the film was not allowed. Therefore, these calculations only deal with coherent precipitates.

FEM calculation series of different situations give the local mechanical stress development. For each situation a stress map like that in **Fig. 6.4** can be deduced. From these stress maps, the "mean stress of the α-phase" can be calculated by excluding the precipitates. It arises in the not-hydrided part of the film and only accounts for the α-Mg matrix. This treatment allows for comparison with the experimental stress data that are obtained from the XRD diffraction α-phase peak, as shown in **Fig. 5.11**.
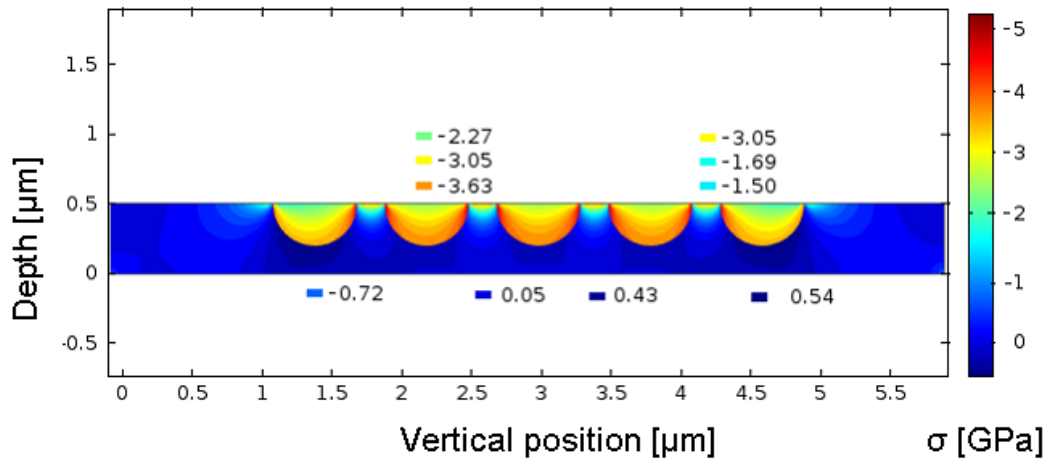
Fig. 6.4 2D-FEM-simulations (COMSOL multi-physics) on a Mg-film containing five half circular hydride particles with radii of r = 300 nm and a distance of d = 800 nm [Uchi15], performed by M. Hamm. The local stress colour map shows that the compressive stress (light blue to red) arises in the particles and, also, in the α-phase Mg-film between the hydride particles. The colour-scale (right side) gives the local stress intensity. It appears mostly in compression; only below the particles tensile components (dark blue) are found.

With respect to the influence of the hydride distance l on the mean stress, a FEM series of the local stress was calculated for particles of 300 nm radii with distances l ranging from 0 to 4800 nm. The mean stress evolution versus the particle distance l is shown in **Fig. 6.5 a)**. The compressive stress of $\sigma = -210$ MPa builds up by the presence of the hydrides. For precipitate distances below l = 600 nm (marked with dashed line), particle overlap occurs. The particle overlap is only an artificial construction in performing FEM calculations. It does not generally affect the local stress map. However, it reduces the mean stress. Slightly above that size the mean stress decreases upon distance enlargement. This is related to the shrinking volume content of the hydrides compared to the film.

For studying the influence of hydride growth on the mean stress in the α-phase, a FEM series of the local stress on 5 particles with increasing size (from r = 0 to r = 600 nm) and a constant inter-particle distance of l = 800 nm were studied. **Fig. 6.5 b)** shows the calculated mean stress

versus the hydride size r. Compressive stress builds up to $\sigma = -170$ MPa. Thereafter, the mean stress decreases, leaving a maximum compressive stress state at a hydride radius of $r = 0.3$ µm. Local stress maps show that further growth of the hydrides enhances the tensile component below the hydrides. Two adjacent hydrides get in contact when their radii reach $r = 0.4$ µm.

For $r_{Hydride} > 0.4$ µm the mean stress turns in compression again, in the simulation of **Fig. 6.5 b)**. On one hand, this is due to the matrix regions bordering the five hydrides in the performed calculation. This border region is compressed. On the other hand it should be considered that, for
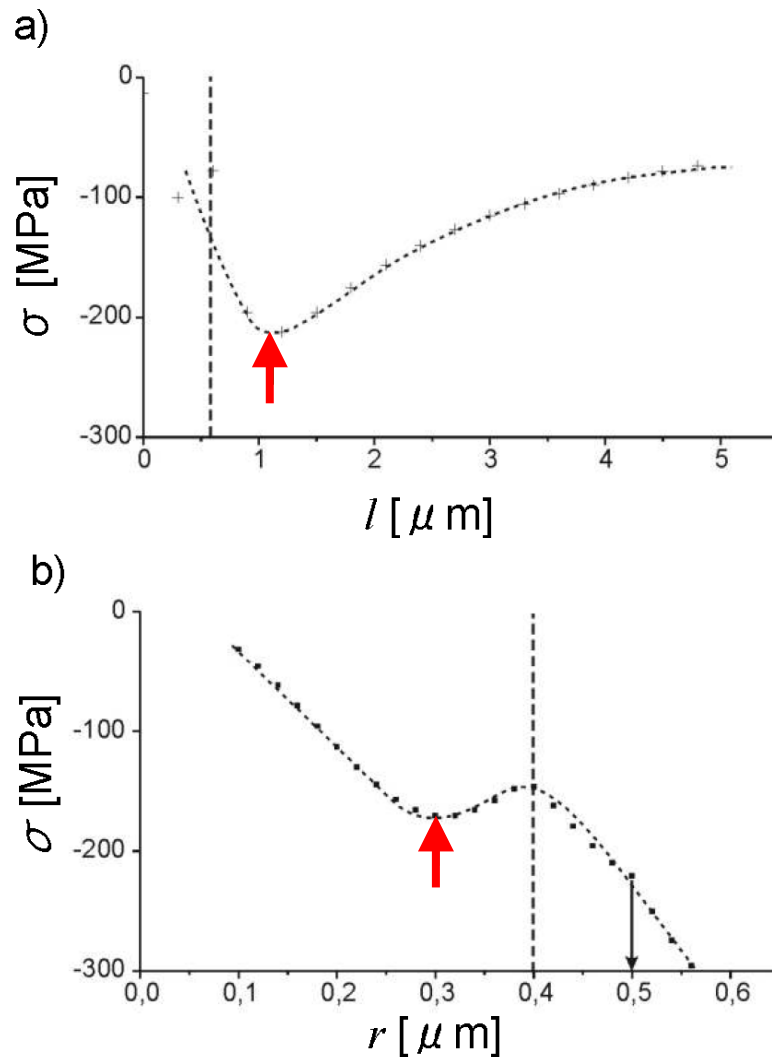
Fig. 6.5 Mean stress in the α-Mg-matrix (between, below and beside the Mg-hydride particles), resulting from 2D-FEM-simulations on Mg-films containing half circular hydride particles, performed by M. Hamm [Uchi15]. The splines are included to guide the eye. **a)** For increasing hydride distances l (with r = 300 nm) of up to 1.2 µm compressive stress of -210 MPa builds up (indicated with red arrow). Hydrides are separated for l > 0.6 µm (dashed line). For larger distances the mean compressive stress decreases. **b)** For increasing hydride radii r (with l = 800 nm), growth results in a compressive stress increase of up to -170 MPa at r = 300 nm (indicated with red arrow). This is followed by a mean compressive stress decrease, leaving a minimum stress state. This resembles the results of **Fig. 5.11** for the 500 nm film (indicated with black arrow). The minimum appears before adjacent particles touch each other (dashed line). Also, the mean stress turns compressive because of border effects. For r > 0.5 µm the substrate is reached.

$r_{Hydride}$ = 0.5 µm, the hydride reaches the film/substrate interface. Thus, the tensile stress contribution, which was present below the hydrides, is reduced or even vanishes. By these border effects, the mean stress turns in compression again.

The model given in **Fig. 6.3 a)-d)** suggesting a spatial distribution of half-spherical hydrides and their growth in combination with the FEM calculations of **Fig. 6.4** and **Fig. 6.5** now allows describing the found dependencies on diffusion values, phase volume fractions time dependencies and stress states. This will be shown in the following:

At low concentrations (and chemical potentials well below 0.025 V, **Fig. 5.29 a)** hydrogen diffuses in the α-Mg phase with the α-phase diffusion constant. This happens before regime I and is, therefore, not shown in **Fig. 6.3**.

By crossing the phase boundary for Mg-hydride formation, in regime I and for times < t_I, the Mg-hydride phase nucleates at the surface of the Mg-film (**Fig. 6.3 a)**). The hydride nuclei are known to form easily at the sample surface, due to the lower total strain energy at the sample surface compared to the bulk [Ryde89]. In this regime, there are still diffusion paths through the α-Mg phase at this stage in accordance with the measured relatively fast hydrogen diffusion (**Fig. 5.29a)**).

Between the Mg-hydrides, the remaining α-phase regions will be compressed, as presented in **Fig. 6.4**. The compressive stress in the α-phase first increases upon hydride growth. This was calculated in **Fig. 6.5 b)** for radii $r_{Hydride}$ < 0.3 µm (hydride distance 0.8 µm) where the stress drops to σ = -170 MPa for $r_{Hydride}$ = 0.3 µm. A compressive stress increase was also determined from the XRD peak shifts (**Fig. 5.9a** and **Fig. 5.10**) and ψ-scans on the α-phase Mg lattice reflection (**Fig. 5.2c**). As shown in **Fig. 5.11** for the 500 nm film, the stress goes from initially σ = -550 MPa to σ = -630 MPa in maximum compression.

Upon further hydride growth, the compressive stress in the α-phase reduces again. In the FEM calculations of **Fig. 6.5 b)**, the compressive stress of σ = -170 MPa reduces to σ = -150 MPa before the neighboring hydrides meet at r = 0.4 µm. This point of contact is marked by a dashed vertical line in **Fig. 6.5 b)**. This resembles the experimental findings of **Fig. 5.11** for the 500 nm film (open triangles). There, the stress reduces from σ = -630 MPa to about σ = -590 MPa. This stress reduction happens before the hydrides get in contact, as this situation is marked with t_I in **Fig. 5.11**. The sample is still in the fast diffusion regime I. To summarize, there is a compressive stress turning point that appears before the hydrides get in contact. This presence of a turning point vice versa supports the suggested model of half-spherical hydrides growing from the film surface into the film.

Upon further hydride growth the mean stress in the α-phase stays constant, even until the film is completely hydrided. This differs from the simulations results of **Fig. 6.5 b)** which showed an increase of compressive stress. This difference is partially attributed to the border effects.

On top of this it should be also considered that the interface coherency also contributes. This is not included in the FEM calculations. Coherent interfaces strain the α-phase lattice and

compress the hydride-phase lattice in the vicinity of the interface [Wagn11^{+}]. Thereby, the coherent interfaces affect the position of the measured α-phase XRD lattice reflection. This contribution scales with the coherent interface content: It is large for small coherent hydride precipitates and vanishes when the precipitates become incoherent. For the incoherent precipitate only the hydride induced stress related to expansion remains, in the α-phase. This additional effect results in further compressive stress reduction. At the end of regime I a steady state of stress and strain is established.

FEM calculations on the dependence of the mean stress on the hydride distance l, show an increase in compressive stress with increasing the distance, in **Fig. 6.5 a)**, for distances up to $l = 1.2$ µm between the hydrides (for 0.3 µm hydrides). For the experiments, large distances corresponding to low nucleation densities appear for the films loaded with the low hydrogen pressure ($p_{H2} = 2 \cdot 10^3$ Pa, the open triangles in **Fig. 5.11**). The effect is mainly visible for the 500 nm film. The compressive stress reaches a high value of $\sigma = -630$ MPa. For the film loaded with high hydrogen pressure ($2 \cdot 10^4$ Pa, bold triangles in **Fig. 5.11**) the distance between the hydride nuclei is expected to be smaller. The maximum compressive stress reaches only $\sigma = -590$ MPa. This trend is in good agreement with the FEM calculations.

However, the discussed complex stress dependency is not visible for the 2800 nm film in **Fig. 5.11**. With respect to this point, it should be considered within the time span of conducted measurements only a part of the 2800 nm film could be hydrided. Furthermore, the volume fraction A/A_0 of the compressed α-phase between the hydrides stays small for the 2800 nm film (see **Fig. 5.12**). This might explain why all the stress-related results are more visible for the 500 nm films.

Regime I ends when the hydride half-spheres encounter each other and the diffusion paths through the α-phase close. Regime II is reached. Upon the presence of a closed hydride layer at the surface, the effective hydrogen diffusion becomes very slow. The measured diffusion constant actually drops to values close to that of the Mg-hydride (see **Fig. 5.32**). This change in the diffusion regime is marked with t_I in **Fig. 5.11** and **Fig. 5.12**.

In regime II, the related hydride layer thickness L thereby depends on the size and density of the hydride nuclei. According to the nucleation and growth considerations presented above, the number density is larger for samples loaded at $p_{H2} = 2 \cdot 10^4$ Pa and the distance between adjacent hydride precipitates l is small. Thus, the growing hydride half-spheres get in contact more early and form a closed layer of thickness L ('blocking layer') during the hydrogen loading. This penetration depth is expected to be correlated with the mean nucleation interval l by $L \approx l/2$. As the interface is possibly not flat, L might be smaller than $l/2$.

This describes the experimental finding, that the mean hydride penetration depth L is calculated to be large with $L = 340$ nm at $\sqrt{t_I}^{20}$ and for the low loading pressure of $p_{H2} = 2 \cdot 10^3$ Pa, according to the relative change of Mg (0002) XRD peak area for the 500 nm Mg-film. Thus, a mean distance between hydride nuclei of $l \approx 680$ nm is expected. For the high hydrogen loading

pressure of $p_{H2} = 2 \cdot 10^4$ Pa, the distance between adjacent hydrides is small, a mean hydride penetration depth L is calculated to $L = 200$ nm, for the 500 nm Mg-film. This suggests a mean distance between hydride nuclei of $l \approx 400$ nm.

In regime II, only hydrogen diffusion via grain boundaries and along the strained or incoherent α-β interfaces allows further growth of the β-MgH$_2$ phase. The calculated compressive stress in the α-phase further decreases by reducing the area of the stained α-β interface and by reducing the α-phase volume remaining between the hydrides. This is in accordance with the behavior of the 2800 nm film in **Fig. 5.11 b)** showing a slight increase of the compressive stress for long times.

At the end of regime II, the growth of the hydride in vertical direction will be dominant, and the supply of hydrogen is limited by the hydrogen flux along the grain boundaries. The diffusivity is now at its minimum value, but larger than that of bulk MgH$_2$ (cf. **Fig. 5.32**). This is attributed to the grain boundaries in the film sample. As the Mg-grains in the films grow with columnar shape, their grain boundaries connect the upper and the lower film side. By this, grain boundary diffusion paths are present.

To conclude, the spatial distribution of hydrides and the hydrogen diffusion in Mg thin films strongly depends on the driving force. A small driving force allows hydriding a larger film volume when compared to a high driving force, in the same time. This can be explained by the theory of nucleation and growth that directly links an increase of the nucleation rate with an increase of the driving force. A high nucleation rate or a small distance between neighboring hydrides yields a closed hydride layer in short time. Vice versa, a low nucleation rate or a large distance between neighboring hydrides yields a closed hydride layer in long time.

The experimentally measured mean stress developments upon hydride formation and the related hydrogen diffusion constants can be explained by assuming a spatial distribution of half-spherical hydrides developing at the film surface. The smallest diffusion constant is still larger than that of the pure bulk hydride because of grain boundaries, acting as pathways for faster hydrogen diffusion in poly crystalline Mg-films.

With respect to the hydride nucleation models in the Mg-H system, similar nucleation and growth models were suggested in the former works, for thin films or also for particles. In former
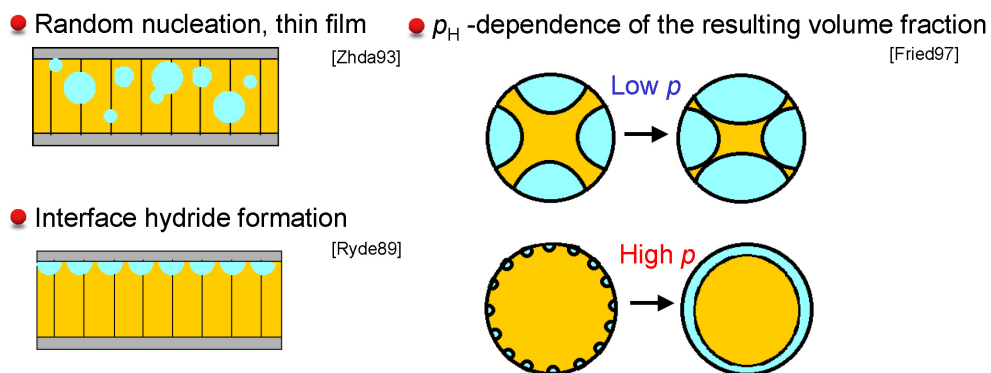
Fig. 6.6 Schematic drawing of the hydride nucleation and growth model suggested in former studies for the Mg-films and Mg-particles [Zhda93,Ryde89,Fried97]. Blue part in figures indicates the nucleating- and growing Mg hydride.

studies, a random nucleation model for thin film by Zhdanov *et al.* [Zhda93], an interface hydride formation model for thin film by Rydén *et al.* [Ryde89], or a pressure-dependence of the resulting volume fraction model for particles by Friedlmeier and Groll [Fried97] are known, as shown in **Fig. 6.6**. Those models also conclude that the inverse effect of the driving force on the kinetics. However, the large volume expansion of about 30% per Mg unit cell taking place upon the phase transition into the hydride phase, is still not correlated in those models for now.

By performing FEM calculations, the hydride morphology changes suggested in this work are nicely correlated with the experimentally measured stress evolution during hydrogen loading. Thus, a new model is suggested in this work, to explain both of the two-different reaction kinetics regimes and stress development, during hydrogen loading (**Fig. 6.3**) : At first, the hemispherical hydrides nucleate on the sample surface, and grow independently. As they grow, the compressive stress increases. At this moment, the reaction kinetics is still fast, because hydrogen can permeate through the α-matrix (the left picture in **Fig. 6.3**). For further loading, maximum compressive stress is achieved, before the hydrides encounter. Then the hydrides begin to touch each other, the slower kinetic regime II starts. In the regime II, hydrogen permeates through grain boundaries and the hydrides (the second picture in **Fig. 6.3**). As a result, the hydride layer (blocking layer) is formed. For further hydrogenation, the front of the hydride layer propagates into the film, and the resulting volume depends on the driving force, because it correlates to the initial hydride distance.

6.3 Hydrogen permeation in GB-rich Mg film

In this chapter, the diffusion, solution and permeation of hydrogen in GB-rich Mg-film will be discussed. The over-all diffusion constant of hydrogen in Mg depends on the hydride fraction [Stan77]. This tendency was also recognized in the obtained diffusion constants of hydrogen in Mg-films (see **Fig. 5.32**). It should be taken into consideration that all these diffusion constants contain mixed information. They include hydrogen diffusion through the α-phase and along grain boundaries (GBs), hydrogen diffusion along the strained α/β- interface and the formation of the hydride phase. An arrow in **Fig. 5.32** indicates the increase of the hydride volume fraction in the related sample. The diffusion constants can be further reduced by gas adsorption kinetics that becomes more pronounced in gas phase loading experiments. All diffusion data for hydrogen diffusion in GB-rich Mg films are are much larger than the value for hydrogen diffusion in MgH$_2$ ($D_{\mathrm{H}}{}^{\mathrm{MgH_2}}$), reported by Spatz *et al.* [Spatz93] and they are well below the low-temperature extrapolation of the data of Nishimura *et al.* [Nish99]. The diffusion constants for all films get smaller upon increasing hydride volume fraction.

However, there are 2-10 orders of magnitude difference between the obtained effective hydrogen diffusion coefficients $D_{\mathrm{H}}{}^{\mathrm{eff}}$ and thermodynamically extrapolated coefficient of $D_{\mathrm{H}}{}^{\mathrm{MgH_2}}$, compared at room temperature (**Fig. 5.32**), even for the reaction in the end of regime II. According to the new model (shown in **Fig. 6.3**), only hydrogen diffusion via grain boundaries and along the strained or incoherent α-β interfaces allows further growth of the β-MgH$_2$ phase. Also, the sample prepared at room temperature contains abundant GBs with fiber texture (see **Chapter 4.1.1**). The grain sizes were found to decrease by hydrogen absorption (**Fig. 5.1c**).

6.3.1 Hydrogen permeation through Pd/Mg film: without GB

Permeability can be estimated from the diffusivity and solubility (see **Appendix A4** in details). Hydrogen flux in α-Pd and α-Mg are compared in this section, using Eq.(A4.5). In case of H in Pd at dilute concentration, $H_S \approx$ = -10 kJ/(molH) for solution [Fukai05] (see **Fig. 2.2**) and $H_D \approx$ +24 kJ/(molH) for diffusion (see **Table A3.4**) are known values. Applying these values in Eq.(A4.6), a value of $H_\Phi \approx$ 14 kJ/(molH) is obtained for Pd. Likewise, H_S for defect-free Mg is theoretically calculated to be H_S = +13.5 kJ/(molH) [Bohm99] and also $H_D \approx$ 24.1 kJ/(molH) [Nish99] is experimentally reported (see **Chap. 2.1.4.4**). Thus, $H_\Phi \approx$ 37.6 kJ/(molH) is obtained for Mg. Both of Pd and Mg have positive enthalpy values, pointing out that the hydrogen can permeate faster in bulk-Pd, compared to bulk-Mg. Also, the difference of permeability increases by increasing temperature.

From another point of view, permeabilities of both materials are compared. At T =300 K, the diffusion constant of H in α-Mg is expected to be $D_{\mathrm{H}}^{\alpha\mathrm{Mg}} \approx 10^{-10}$ m^{2}s^{-1} [Nish99] (see **Fig. 5.32**), whereas the diffusion constant of H in α-Pd is known to be $D_{\mathrm{H}}^{\alpha\mathrm{Pd}} \approx 8\cdot10^{-11}$ m^{2}s^{-1} (see **Fig. 2.7**). Thus, a diffusivity ratio of $k_D = \left(D_{\mathrm{H}}^{\alpha\mathrm{Mg}} / D_{\mathrm{H}}^{\alpha\mathrm{Pd}}\right) \approx 1.25$ is obtained. Furthermore, solubility ratio at

$T = 300$ K is already calculated to be $k = \left(c_{\text{H in Mg}} / c_{\text{H in Pd}} \right) = 10^{-3}$ (see **Fig. 5.33**). Thus, the permeability ratio k_Φ can be roughly estimated to be $k_\Phi = \left(\Phi_{\text{H}}^{\alpha\text{Mg}} / \Phi_{\text{H}}^{\alpha\text{Pd}} \right)$ $= \left(D_{\text{H}}^{\alpha\text{Mg}} \cdot c_{\text{H in Mg}} \right) / \left(D_{\text{H}}^{\alpha\text{Pd}} \cdot c_{\text{H in Pd}} \right) = k_D \cdot k \approx 1.25 \cdot 10^{-3}$. This result also supports that the hydrogen can permeate faster in bulk-Pd, compared to bulk-Mg.

In conclusion, the hydrogen flux is limited by the Mg-layer upon the permeation through a defect-free Pd/Mg multilayer.

6.3.2 Hydrogen permeation through Pd/Mg film: GB-rich film

The hydrogen diffusivity, solubility and permeability in GB-rich material are discussed in this section. A GB-rich sample is assumed; such as the grain boundary diffusion of hydrogen (D_{H}^{GB}) is dominant, superior to the contribution of diffusion through α-β interfaces. In this case, the contribution of grain boundary on the effective diffusion in ($D_{\text{H}}^{\text{eff}}$) is estimated by applying the model of Kaur *et al.* [Kaur95], which is written as

$$D_{\text{H}}^{\text{eff}} = \tau D_{\text{H}}^{\text{GB}} + (1 - \tau) D_{\text{H}}^{\alpha\text{Mg}} \tag{6.10}$$

where τ and $(1 - \tau)$ are the fractions of time that a diffusing hydrogen spends in the grain boundaries and in the α-Mg grains, respectively. In the presence of boundary segregation these time fractions can be estimated as the corresponding volume fractions of grain boundary (g) and volume fractions of grains $(1 - g)$. Multiplied by the respective equilibrium concentrations of hydrogen yields

$$\tau = \frac{g c_{\text{H}}^{\text{GB}}}{g c_{\text{H}}^{\text{GB}} + (1 - g) c_{\text{H}}^{\alpha\text{Mg}}} \approx \frac{sg}{1 + sg} = \frac{qs\delta/d}{1 + qs\delta/d} \tag{6.11}$$

where $g \approx (q\delta)/d$ is the volume fraction of grain boundaries, q is a geometrical factor which depends on the grain shape, and s is the grain boundary segregation factor.

For a condition of $d \gg (s\delta/2)$ in Eq.(6.11) yields $\tau \approx sg$, and a relationship

$$D_{\text{H}}^{\text{eff}} = sg D_{\text{H}}^{\text{GB}} + (1 - sg) D_{\text{H}}^{\text{bulk}} \tag{6.12}$$

is obtained, which is known as the Hart-Mortlock equation [Hart57]. Assuming a polycrystals with large grains ($d > 50$ μm, $\delta/d > 10^{-5}$ or smaller), yields an approximation with $sg \ll 1$ as

$$D_{\text{H}}^{\text{eff}} = sg D_{\text{H}}^{\text{GB}} + D_{\text{H}}^{\alpha\text{Mg}} \tag{6.13}$$

and can be rewritten in the following form

$$D_{\text{H}}^{\text{eff}} = D_{\text{H}}^{\alpha\text{Mg}} \left(1 + 2q \frac{L''}{d} \right) \quad \text{with} \quad L'' = \frac{s\delta}{2} \cdot \left(\frac{D_{\text{H}}^{\text{GB}}}{D_{\text{H}}^{\alpha\text{Mg}}} \right) \tag{6.14}$$

Rough estimation in **Chap. 2.1.4.6** with Eq.(2.22) is the case of applying $q = 3$ for Eq.(6.14).

In contrast, for an ultrafine crystal, $d << (s\delta/2)$ in Eq.(6.11) yields $\tau \approx 1$, Eq.(6.10) yields $D_H^{eff} \approx D^{GB}$. In this case the total amount of the hydrogen atoms residing in the grain boundaries are much larger than that inside the grains.

From definition of the segregation factor, a relationship of

$$s = \frac{c_H^{GB}}{c_H^{\alpha Mg}} \tag{6.15}$$

is written in the low hydrogen concentration regime, where c_H^{GB} and $c_H^{\alpha Mg}$ are the concentration of H in grain boundaries and grains near boundaries respectively, from its definition [Herz03].

The trapping effect is known to be happen at low hydrogen concentration, making a negative effect on the hydrogen transport [Kirch88,Kirch88+,Aran93]. Increasing the hydrogen concentration higher, the trapping effect by GBs on the total hydrogen transportation can be neglected [Oria70], and could even increase the total hydrogen transportation [Aran93].

In this study, hydrogen solubility ratios of $s = (c_H^{GB}/c_H^G) \approx 3500$ or $s = (c_H^{GB}/c_H^G) \approx 2 \times 10^4$ (see **Chap. 5.4** and **Appendix A4**) are obtained from the apparent solubility limit of $c_H^{eff} \approx 10^{-4}$ H/Mg. In case of low loading conditions, the nucleation of the hydride phase is not assumed to happen at this hydrogen concentration.

From the obtained large s, can Eq.(6.14) yields $d << (s\delta/2)$ and thus, $D_H^{eff} \approx D^{GB}$ is expected. According to increase of c_H, becoming lower contribution of trapping site is expected [Oria70].

When the hydrogen concentration in Mg grain reaches $c_H^G = 10^{-5}$ H/Mg, hydride nucleation starts, according to the loading hydrogen potential. During hydride growth, the hydrogen atoms supplied from the surface are still able to diffuse in the sample by finding α-Mg phase. Therefore, the ratio of the area covered by hydrides of the cross section on the surface will be dominant to control the total hydrogen flux. Further hydrogen uptake results the contact of the hydride nuclei, and the complete occupation of the hydride phase on the surface. This situation corresponds to **Fig. 6.3 b)**.

At $c_H \sim 1$, almost all the pathways for α-Mg-diffusion are closed by the covered hydrides (corresponds to the 2nd and 3rd picture in the half-sphere model illustrated in **Fig. 6.3**). At this concentration, the parallel layer model (**Fig. 3.19**) is applicable. Defining boundary conditions and hydrogen fluxes at each boundary and layer, the time-dependent thickness growth of hydride ($d_{MgH_2} \propto \sqrt{t}$) is expected (see **Appendix A1**), and actually this relationship was obtained in this work (**Fig. 5.12**). Thus, the hydrogen flux is diffusion controlled through the hydride layer. This situation corresponds to regime II (the third picture) in **Fig. 6.3**. The pathways through grain boundaries are evaluated here. Assuming a simple hydrogen diffusion model, applying $D_H^{bulk} = D_H^{MgH_2} \approx 10^{-20}$ m²s⁻¹ [Spatz93], d = 35-55 nm and $\delta \approx 0.75$ nm (2-3 monolayers) for Eq.(2.22) yields a diffusivity ratio of $(D_H^{GB}/D_H^{bulk}) \approx 2 \cdot 10^3$ for the regime II. This ratio is under rough assumption, however helpful to understand that grain boundaries contribute to the hydrogen transport in the high concentration regime. The hydrogen atoms in the MgH₂ grains have almost

no chance to diffuse, due to their large affinity to the Mg atoms. Taking this fact into consideration, the permeation through the grain boundaries is expected to dominate the total hydrogen flux. Actually, the obtained effective hydrogen diffusion constant at the end of the regime II was still about 50 times larger than the expected value of $D_{\mathrm{H}}^{\mathrm{MgH_2}} \approx 10^{-20}\,\mathrm{m^2s^{-1}}$ [Spatz93] (see **Fig. 5.32**).

With respect to the hydrogen transport in such high hydride fraction state, Tan *et al.* [Tan11] suggested that hydrogen diffusion along GBs of MgH$_2$ at low temperatures is the mechanism controlling the expansive growth of the hydride layer, from their obtained reduced activation energy of 56 kJ/molH$_2$ for the hydrogen absorption reaction of Mg-4at.%Fe thin film. The results of this work imply also that the grain boundaries could be pathways for hydrogen transport, at the regime II in the model suggested in this work.

In this thesis, the rate-determining process of hydrogen transport in the magnesium film in each degree of hydrogenation was evaluated. However, there are further aspects, which should be kept in mind to evaluate hydrogen transport in Mg films. At first, the effect of stress change, which is caused by the large volume expansion upon the phase transition and its possible influence on the reaction. Also, the temperature change, which occurs due to the large exothermal heat by transition from *α*-Mg into *β*-MgH$_2$ phase, can affect the hydrogen transport near the α/β boundary or the reaction rate itself, from a microscopic point of view. Furthermore, the effect of loading hydrogen potential affects the flux of hydrogen uptake [Rudm79] or the front velocity of the α/β boundary [Bloch97]. Further studies, such as *in-situ* hydrogen loading measurements with changing loading pressure conditions continuously, are needed to discuss those points.

7. Summary and outlook

The purpose of this study is to investigate hydrogen absorption properties of grain boundary rich pure magnesium film.

X-ray diffraction (XRD) measurements has been carried out to estimate microstructures, texture, lattice expansion and inner strain changes during hydrogen absorption. As-prepared sample showed (0001)-texture of the Mg layer, and columnar grain growth was recognized by TEM observation. Hydrogen was loaded by means of electrochemical method or with gaseous hydrogen. Both loading methods lead to a nucleation of β-MgH_2 phase. They revealed crystallographic orientation of αMg-(0002)//βMgH_2-(110), with 2°-4° tilt of the hydride.

By the electrochemical loading measurements for Mg-films, it was found that loading condition with a 1:2 (vol.) mixture of H_3PO_4 (85%) and Glycerin (85%) as electrolyte, a polymer coating on the sample edges and a Pd capping layer thicker than 20 nm showed a successful and suitable condition for successful loading.

Measured potential versus concentration curves were strongly affected by the hydrogen loading current density. Smaller hydrogen loading current achieved thicker hydride content in the end. At small currents of $i < 4 \times 10^{-7}$ A/cm^2, more than 1300 nm thick MgH_2-layers can be built up. However, using a Pd layer between the Mg sample and the Si substrate leads to buckling of the film, for 1400 nm thick Mg films.

Step-by-step loading of Mg films prepared on Si substrates at room temperature revealed an increase of in-plane compressive stress by increasing hydrogen concentrations. In contrast, for annealed Mg films, an increase of in-plane tensile stress by increasing hydrogen concentrations was measured. These tendencies were clearly observed by three different stress measurements, which are the Bragg peak shift, the $\sin^2\psi$ method, and the curvature measurement, in both cases of electrochemical hydrogen loading measurements and gas loading measurements.

For Mg-films prepared on Pd-substrates, the inner stress developments were succesfully obtained by *in-situ* XRD measurements during the step-by-step electrochemical hydrogen loading from back side, using originally prepared sample stage in this work. The hydrogen solution up to a concentration of $c_H = 10^{-3}$ H/Mg was clearly observed from the Bragg peak shifts. In the higher concentration regime, the increases of the in-plane compressive stress in the α-Mg matrix were otained by the $\sin^2\psi$ method.

The inner stress dependency on the hydrogen concentration, $\left(d\sigma^p/dc_H\right)$, was also evaluated. For the gas-loaded samples, it was in GPa range in the solid solution region, and 1-2 orders of magnitude larger than that in the two phase region. The same tendency was also obtained for the electrochemically loaded samples. The stress dependency in the solid solution concentration range was able to be explained by the linear elastic theory.

The achived hydride thicknesses in the Mg-films loaded by gas were evaluated by three different methods, which are the profilometer, Bragg peak area, and the electrical resistivity

measurements. All of those three measurements result in the larger hydride fraction for the samples loaded at lower gas pressure, with a maximum hydride thickness of 1.8 μm.

The film-Mg-H system was also investigated from the kinetical point of view, at room temperature. Electrochemical hydrogen permeation measurements and *in-situ* gas-loading XRD-measurements have been performed on poly-crystalline Mg-films. Hydrogen diffusion constants, the hydride volume content and the in-plane stress were determined, at $T = 300$ K. For low concentrations, a hydrogen diffusion constant of $D_H^{Mg} = 7(\pm 2) \cdot 10^{-11}$ m²/s was obtained, which is attributed to αMg-H.

For higher concentrations, different kinetic regimes with reduced apparent diffusion constants were observed. The apparent diffusion coefficients D_H^{tot} dropped to about 10^{-18} m²/s. This value is still two orders larger than D_H^{MgH2} of bulk β-MgH$_2$, because of the contribution of grain boundaries in the films, acting as pathways for faster hydrogen diffusion in poly crystalline Mg-films.

The different kinetics regimes are attributed to the spatial distribution of the hydrides. A hydride nucleation and growth model is suggested that relyes on half-spherical hydrides with a nuclei densities depending on the driving force. The model allows explaining the complex stress development, the different diffusion regimes and the blocking-layer thickness. The blocking-layer thickness inversely scales with the driving force.

The spatial distribution of hydrides and the hydrogen diffusion in Mg thin films strongly depends on the driving force. A small driving force allows hydriding a larger film volume when compared to a high driving force. This can be explained by the theory of nucleation and growth that directly links an increase of the nucleation rate with an increase of the driving force. A high nucleation rate or a small distance between neighboring hydrides yields a closed hydride layer in short time. Vice versa, a low nucleation rate or a large distance between neighboring hydrides yields a closed hydride layer after long time.

Further hydrogen loading leads to a growth of hydride grains. For all nanocrystalline films, the increase of in-plane stress was measured by XRD techniques (the peak shift method and the sin²ψ method) and by curvature measurements, at different hydrogenated states. In-plane stress changes, being increased according to higher hydrogen concentrations, reveal a good agreement with the values obtained by other methods and are, thus, considered to be reliable. Furthermore, it was observed that the strain in out-of-film-direction increases with hydrogen loading in the two-phase region.

Increases of thickness in highly loaded states were also directly measured by profilometer measurements, and the increase was comparable to the calculated value applying the double layer model. Corresponding increase of hydride fraction was in good agreement with values obtained by resistivity change and also with the Bragg peak area change .

The hydrogen induced in-plane stress and corresponding strain cause an increase of the elastic energy of the film. This increase of the elastic energy affects the activation energy of the

magnesium film with further hydrogen. This effect is clearly seen in the result of measurements at elevated temperatures, namely in the van't Hoff Plot by a change of the slope. However, solution effect of Mg into Pd cannot be eliminated in these results.

In-situ gas-loading measurements at elevated temperatures up to $T = 363$ K have been performed for Mg-films. Unloading of the hydrided Mg-film at $T = 363$ K was possible within 15 minutes. Furthermore, the hydride decomposition enthalpy was calculated to be 62 ± 7 kJ/mol, which is by 24 kJ/mol smaller compared to that for bulk Mg. The influence by the in-plane compressive biaxial stress is suggested for this detabilisation of the hydride phase compared to the bulk material.

The pure impact of grain boundaries on the hydrogen sorption property was also focused in this study. For the hydrogen concentration at the solid solution limit, solubility ratios of $s = \left(c_H^{GB} / c_H^G \right) \approx 3500$ or $s = \left(c_H^{GB} / c_H^G \right) \approx 2 \times 10^4$ were obtained from the apparent solubility limit of $c_H^{eff} \approx 10^{-4}$ H/Mg. Furthermore, at high hydrogen concentration regime, the apparent diffusion coefficients obtained in this work imply that the grain boundaries act as pathways for hydrogen transport in Mg. Using rough assumptions, a diffusivity ratio of $\left(D_H^{GB} / D_H^{bulk} \right) \approx 2 \cdot 10^3$ can be estimated.

To conclude, the driving force plays a major role on the hydrogen absorption in Mg thin films as it controls the morphologies of the hydrides and the formation of the blocking layer. Introducing grain boundaries lead to a visible increase of the hydrogen permeability and are, therefore, beneficial to reduce the "blocking effect" on the hydrogen absorption reaction of Mg.

Appendix

A1. Time-dependency of the hydride thickness growth

This part introduces the theoretical validity of the time dependency of hydride thickness, which was treated to be proportional to the square root of time, in this work.

Fig. A1 shows the schematic view of a film, being envisioned as a multilayer plane sheet with steady and moving boundaries [Cran75]. Two assumptions are introduced here.

The first assumption is that the hydride phase will be formed by supplied hydrogen atoms coming from surface, permeating through the Pd- and hydride layers. This processes can be divided by: I) approach of hydrogen molecules from the gas phase to the Pd surface; II) permeation through the Pd layer; III) transport across the interface between the Pd and the hydride phase, IV) transport through the MgH_2 layer; and V) formation of hydride at the interface between hydride layer and α-Mg layer.

Second assumption introduced is that Fick's first law is valid for each layer in the sample, during the hydriding process. (in steady state, the flux J is assumed to be constant).

The chemical potential of hydrogen atom in gas phase ($\mu_{\text{H}}^{\text{gas}}$) is

$$\mu_0^{\text{g}} = \frac{1}{2}\left[\mu_{\text{H}}^0 + RT \ln\left(\frac{p_H}{p_0} \right) \right] \tag{A1.1}$$
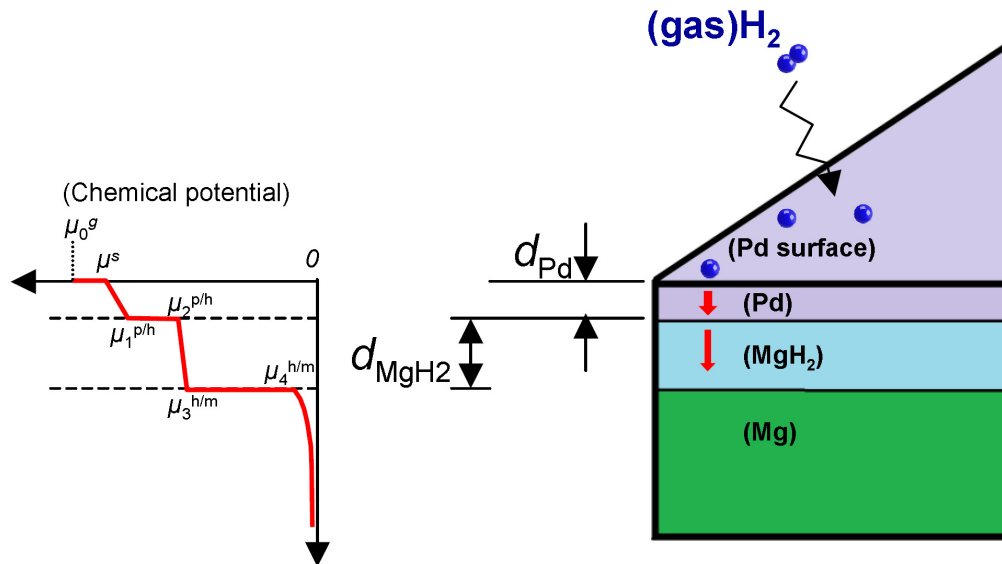

Fig. A1 Schematic draw of parallel layer model for hydride growing in the Mg film (Right) and corresponding chemical potential diagram (Left). Hydrogen gas molecules dissociate on the surface, and permeate Pd layer, go through into the hydride layer, with flux at each layer caused by chemical potential difference.

where p_H and p_0 are the pressure of hydrogen in gas phase and standard pressure respectively, and μ_0^g is the chemical potential of hydrogen atom in gas phase at standard state.

Using a reaction constant (k_1^S) between flux and chemical potential difference at the surface, the surface penetration flux of hydrogen atoms (J_H^S) can be expressed by

$$J_H^S = k_1^S \cdot (\Delta\mu_H) = k_1^S \cdot (\mu_0^g - \mu^S) \tag{A1.2}$$

where μ^S is the chemical potential of hydrogen atom at the surface, and $\Delta\mu_H$ is chemical potential difference of diffusing hydrogen at boundary, and can be also expressed with the hydrogen concentration difference at boundaries (Δc_H), when Δc_H is proportional to $\Delta\mu_H$. However in this work, expression by $\Delta\mu_H$ is used in further part.

Permeation flux of hydrogen atom in Pd layer (J_H^{Pd}) can be expressed as

$$J_H^{Pd} = M_H^{Pd} \cdot \frac{d\mu}{dz} = M_H^{Pd} \cdot \left(\frac{\mu^S - \mu_1^{p/h}}{d_{Pd}} \right) = D_H^{Pd} \left(\frac{d\mu}{dc_H} \right)^{-1} \cdot \left(\frac{\mu^S - \mu_1^{p/h}}{d_{Pd}} \right) \tag{A1.3}$$

where M_H^{Pd}, D_H^{Pd} and c_H are the mobility, the diffusion coefficient and the concentration of hydrogen in Pd layer respectively, and $\mu^{p/h}$ is the chemical potential of hydrogen atom at the interface of Pd/MgH$_2$ layers, d_{Pd} is the thickness of Pd layer, assumed to be a constant.

Likewise, the flux through the interface of Pd/MgH$_2$ layers ($J_H^{p/h}$) is expressed with chemical potential difference ($\Delta\mu_H$) and the reaction constant ($k_2^{p/h}$) at the Pd/MgH$_2$ boundary as

$$J_H^{p/h} = k_2^{p/h} \cdot (\Delta\mu_H) = k_2^{p/h}(\mu_1^{p/h} - \mu_2^{p/h}) \tag{A1.4}$$

The flux of hydrogen atoms through the hydride layer ($J_H^{MgH_2}$) is expressed by the mobility of hydrogen in hydride layer ($M_H^{MgH_2}$), the chemical potentials at both boundaries ($\mu_2^{p/h}$, $\mu_3^{h/m}$), and time-dependent hydride thickness of d_{MgH_2} as

$$J_H^{MgH_2} = M_H^{MgH_2} \cdot \left(\frac{\mu_2^{p/h} - \mu_3^{h/m}}{d_{MgH_2}} \right) \tag{A1.5}$$

The hydrogen flux reaching to the interlayer of MgH$_2$/Mg forming new hydride there ($J_H^{h/m}$) is expressed by chemical potential of hydrogen at the interface of hydride layer side and Mg-layer side ($\mu_3^{h/m}$ and $\mu_4^{h/m}$, respectively) and the reaction constant ($k_3^{h/m}$) at the MgH$_2$/Mg boundary as

$$J_H^{h/m} = k_3^{h/m} \cdot (\mu_3^{h/m} - \mu_4^{h/m}) \tag{A1.6}$$

From assumption of rigid state, the over-all flux J_H^{Rigid} and other flux follow

$$J_H^{Rigid} = J_H^S = J_H^{Pd} = J_H^{p/h} = J_H^{MgH_2} = J_H^{h/m} \tag{A1.7}$$

and also, from Eq.(A1.1)-Eq.(A1.7), following relationships will be obtained

$$J_H^{Rigid} = \mu_0 \cdot \left(\frac{d_{MgH_2}}{M_H^{MgH_2}} + \frac{d_{Mg}}{M_H^{Mg}} + \frac{1}{k_1^S} + \frac{1}{k_2^{p/h}} + \frac{1}{k_3^{h/m}} \right) \tag{A1.8}$$

It is noted again, that d_{MgH_2} is time dependent. Additionally, regarding to the mass balance condition for hydrogen atoms at the moving Mg/MgH$_2$ boundary along z axis,

$$J_H^{Rigid} = c_H \cdot \frac{d}{dt}\left(d_{MgH_2}\right) \tag{A1.9}$$

is needed, where c_H is the mass concentration (atoms/m^{-3}) of hydrogen atoms in the β-MgH$_2$ layer, which can be calculated by crystallographic data.

Now, a condition from Eq.(A1.8) and Eq.(A1.9) from calculation of integration is obtained as

$$d_{MgH_2} = \left(\frac{2\mu_0 M_H^{MgH_2}}{c_H} t + C_0^2\right)^{1/2} - C_0$$

$$\text{with } C_0 = M_H^{MgH_2} \cdot \left(\frac{d_{MgH_2}}{M_H^{Pd}} + \frac{1}{k_1^S} + \frac{1}{k_2^{p/h}} + \frac{1}{k_3^{h/m}}\right) \tag{A1.10}$$

Because the term of M_H^{Pd}, k_1^S, $k_2^{p/h}$ and $k_3^{h/m}$ is large enough and $M_H^{MgH_2}$ is small, therefore

$$d_{MgH_2} \approx \left(\frac{2\mu_0 M_H^{MgH_2}}{c_H} t\right)^{1/2} \tag{A1.11}$$

is obtained. Now it is obvious that thickness of MgH$_2$ is proportional to the $t^{1/2}$. Similar discussion could be found in the book by Gusak *et al.* [Gusa10], in works by Gösele and Tu [Göse82], by Kelly and Clemens [Kelly10], by Cermák and L. Král [Cerm08] or by Belova and Murch [Belo04] introducing further aspects.

It is noted that actually hydrogen can diffuse along grain boundaries and phase boundaries. Permeation through such pathway can increase the effective diffusion coefficient, depending on the hydrogen concentration and solubility. The interlayer could also play a roll as pathway for hydrogen transport, for example as Ham *et al.* [Ham14] recently reported. Negative factor in actual state could be impurities such as oxide on Mg film could make the factor $k_2^{p/h}$ strongly smaller, due to the large energy barrier, reported for example by Wu *et al.* [Wu09].

A2. The error of stress estimation σ^p for hexagonal Mg

In case of the film with hexagonal structure, the elastic behavior is known to be anisotropic, since the stiffness of the lattice depends on the direction. When the film has an epitaxial relationship of (0001) in the out-of -plane direction, the σ^p can be calculated with the following relationship, with the atomic plane distance of the (0001)-direction in a strained state [Ohring91]:

$$\sigma^p = \frac{C_{33}C_{11} - C_{13}^2}{\{C_{33}(C_{11} + C_{12}) - 2C_{13}^2\}(C_{11} - C_{12})}\left(\frac{d_{0001} - d_0}{d_0}\right) \tag{A2.1}$$

for single crystalline sample, where C_{11}, C_{12}, C_{13}, and C_{33} are the elastic constants of the hexagonal lattice (see **Chap. 2.2**). Also, for in-plane random orientated polycrystalline samples [Culli78],

$$\sigma^p = -\frac{E^{0002}}{2\nu^{0002}}\left(\frac{d_\sigma^{0002} - d_0}{d_0}\right) \tag{A2.2}$$

where E^{0002} and ν^{0002} are the Young's modulus and the Poisson's ratio of the hexagonal lattice, respectively.

According the error of σ^p which arises from the use of Eq.(3.8), linear elastic theory calculations on thin (0002) oriented films fixed to rigid substrates reveal a change of the out-of-plane modulus varying between 43 GPa and 51 GPa (see **Fig. 2.18**), depending on the direction of stress. Accounting for the in-plane randomness of grain orientations in our films, yields a mean value of 45.7 GPa is calculated. This ensures the consistency of the value $E = 45$ GPa used in this work (see **Chap. 2.2.2**) within error of 17 %. The Poisson's ratio differs more strongly depending on the direction.

Therefore, the polycrystalline bulk values of E_{Mg} and ν_{Mg} were applied in this work, with the simplified prediction with Eq.(3.8).

A3. Important information

Important remarks are supplementally shown in this part, for figures shown in this work.

Table A3.1 summarises the measurement conditions, methods and the phase conditions in the investigated samples, shown in **Fig. 2.5** in **Chap. 2.1.4.4**.and **Fig. 5.32** in **Chap. 5.5.4**.

Table A3.1 List of experimental conditions for reported hydrogen diffusion coefficients in bulk-Mg, shown in **Fig. 2.5** .

Ref.	Remarks	Region
[Nish99]	Gas permeation measurement for pure Mg at 473-493 K, p_H :0.1-10 kPa.	α-phase
[Renn78]	Hydride thickness growth at 698 K-798 K, Mg-2wt.Ce alloy.	Two-phase
[Sime80]	Interstitial diffusion of H in Mg-Alloy at 723K-873K	Two-phase
[Stan77]	c_H dependency on over-all diffusion for pure Mg, T = 523 K and 490 K, p_H = 3 MPa	Two-phase
[Spat93]	Over-all diffusion at T = 305 K, XPS peak decay, for 20Å-800 Å thick pure Mg-films	Two-phase
[Qu10]	Applying Hagi's model for electrochemical discharging results for 20-100nm Mg films	Two-phase
[Toep82]	Quasielastic neutron scattering technique at T = 623 K	β-phase
[Stio84]	Nuclear magnetic resonance technique at T ~ 503 K	β-phase
[Yao08]	Applying spherical diffusion model with gasloading results for Mg-FeTi-CNT system	β-phase
[Hao08]	Density functional theory, Diffusion of H$^-$ in βMgH$_2$.	β-phase

Table A3.2 summarises the measurement conditions, methods and the phase conditions in the investigated samples, shown in **Fig. 2.5** in **Chap. 2.1.4.5.**

Table A3.2 List of experimental conditions for referential hydrogen diffusion coefficients in bulk-Pd, shown in **Fig. 2.7** in **Chap. 2.1.4.5**.

Ref.	Remarks	H-Concentration
[Seki75]	Frequency response method	α-phase
[Sams73]	Frequency response method	α-phase
[Wick64$^+$]	Permeation method for 99.5% Pd tube	β-phase
[Züch70]	Time-lag method by Electrochemical pulse, 99.9%Pd foils	α-phase
[Kirch80]	Electrochemical Time-lag method on 99.999% Pd foil (annealed)	C_H=0.001-1at.%
[Hase77]	Electrochemical method, 99.95%Pd foil of 0.27mm thickness	α-phase
[Holl67]	Electrochemical method	α-phase
[Riba73]	Quasistatic Gorsky effect method, 99.99%Pd bar	C_H~40 at.%
[Völk71]	Quasistatic Gorsky effect method for Coiled polycrystalline Pd springs	α-phase
[Katl78]	Fitting from literature data	α-phase
[Birn72]	Fitting from literature data	α-phase
[Simo65]	Hydroden absorption method for Pd wires	α-phase
[Koff68]		α-phase

Table A3.3 shows a classification of former works, sorted by targeting phase conditions in the investigated Pd samples, by selected methods.

Table A3.3 A classification of literatures reporting hydrogen diffusion coefficients in αPd ($D_\mathrm{H}^{\alpha\mathrm{Pd}}$) and in βPd ($D_\mathrm{H}^{\beta\mathrm{Pd}}$), by selected methods. $D_\mathrm{H}^{\alpha\mathrm{Pd}}$ values which includes room temperature condition are presented in **Fig. 2.7**, with selected referential $D_\mathrm{H}^{\beta\mathrm{Pd}}$ by Wicke *et al.* [Wick64P+].

	$D_\mathrm{H}^{\alpha\mathrm{Pd}}$	$D_\mathrm{H}^{\alpha\mathrm{Pd}}$ and $D_\mathrm{H}^{\beta\mathrm{Pd}}$	$D_\mathrm{H}^{\beta\mathrm{Pd}}$
Gas permeation measurement	[Toda58] [Katz60] [Koff68] [Holl70] [Davi54]	[Jewe65]	[Wick64+]
Electrochemical permeation measurement	[Deva62] [Züch70] [Hase77] [Earl70] [Simo65] [Holl67] [Kirch80] [Saka81]		[Clea65]
Electrochemical frequency response	[Seki75] [Sams73]		
Electrochemicall absorption method	[Stac64]		
Nuclear magnetic resonance			[Corn75] [Davi76]
Gas volumetric measurement		[Bohm67]	
Gorsky effect	[Riba73] [Völk71]		
Neutron scattering	[Sköl67]		[Neli75]
Fitting from lit. data	[Katl78] [Birn72]		

A series of diffusion data of H in Pd are listed in **Table A3.4**, reported by former studies at different hydrogen concentration and temperatures, obtained by different methods.

Table A3.4 A list of data for hydrogen diffusion in Pd by selected methods at different hydrogen concentrations, reported by former studies. D_0 and ΔG_D indicates the prefactor and the activation energy term for hydrogen diffusion in Palladium.

| c_H range	$D = D_0 \exp(\Delta G_D/RT)$		Temp. Range (min.)-(max) [K]	Remarks	Ref.
	D_0 [10^{-4} m^{2}s^{-1}]	ΔG_D [kJ/molH]			
	$4.3 \cdot 10^{-3}$	23.53	473-973	Permeation method	[Davi54]
	$4.3 \cdot 10^{-3}$	23.45	486-652	99.5% Pd tube, permeation method	[Katz60]
	$1.9 \cdot 10^{-2}$	23.86	303-373	99.5% Pd tube, permeation method	[Wick64+]
alpha	$6.1 \cdot 10^{-3}$	25.08	273-323	Pd wire, hydrogen absorption method	[Simo65]
betha, ~37at%	$5.7 \cdot 10^{-3}$	24.07	293-373	Permeation method, Pd foils, 0.1-0.2 mm thick	[Boes76]
	$1.1 \cdot 10^{-2}$	25.54	273-353	Electrochemical method	[Holl67]
alpha	$5.5 \cdot 10^{-3}$	24.7	533-873		[Knaa68]
alpha	$4.94 \cdot 10^{-3}$	24.05	300-709	Permeation method with low pressure H$_2$ gas	[Koff68]
alpha	$5.25 \cdot 10^{-3}$	26.04	593-923	99.99%Pd, permeation time-lag method	[Golt70]
alpha	$2.94 \cdot 10^{-3}$	22.02	533-913	>99.9%Pd, gas-volumetric time-lag method	[Holl70]
alpha	$4.0 \cdot 10^{-3}$	24.07	273-333	99.9%Pd foils, electrochemical pulse, time-lag method	[Zuch70]
alpha	$2.5 \cdot 10^{-3}$	21.81	233-445	Coiled, polycrystalline springs, quasistatic gorsky effect method	[Völk71]
alpha	$4.5 \cdot 10^{-3}$	24.07	273-1273	Best fit from selected literature data	[Birn72]
40at.%	$2.5 \cdot 10^{-3}$	21.23	100-500	99.99%Pd bar, large grain structure, quasistatic gorsky effect method	[Riba73]
	$2.93 \cdot 10^{-3}$	23.43	453-793		[Puga75]
	$2.1 \cdot 10^{-3}$	21.34	298-298	Frequency response method	[Seki75]
	$1.32 \cdot 10^{-3}$	22.4	296-341	99.95%Pd foil, 0.27mm thick, electrochemical method.	[Hase77],[Hase79]
	$3.44 \cdot 10^{-3}$	22.56	273-313	Frequency response method	[Sams73]
	$6.0 \cdot 10^{-3}$	24.5	273-923	Q and D$_0$ averaged from literature data	[Katl78]
	$2.90 \cdot 10^{-3}$	22.19	473-1548	Best fit from selected literature data for surface-independent methods	[Völk78]
0.001-1at.%			295	99.999% Pd foil, electrochemical time-lag method on annealed specimens	[Kirch80]
alpha	$2.9 \cdot 10^{-3}$	22.2	302-334	Several electrochemical methods	[Kirch80+]
		21.48	279-335	Electrochemical method	[Saka81]
betha, ~37at%		22.29		Mössbauer method	[Wagn84]
betha, ~44at%		22.29		Mössbauer method	[Wagn84]
betha, ~45at%		24.22		Mössbauer method	[Wagn84]
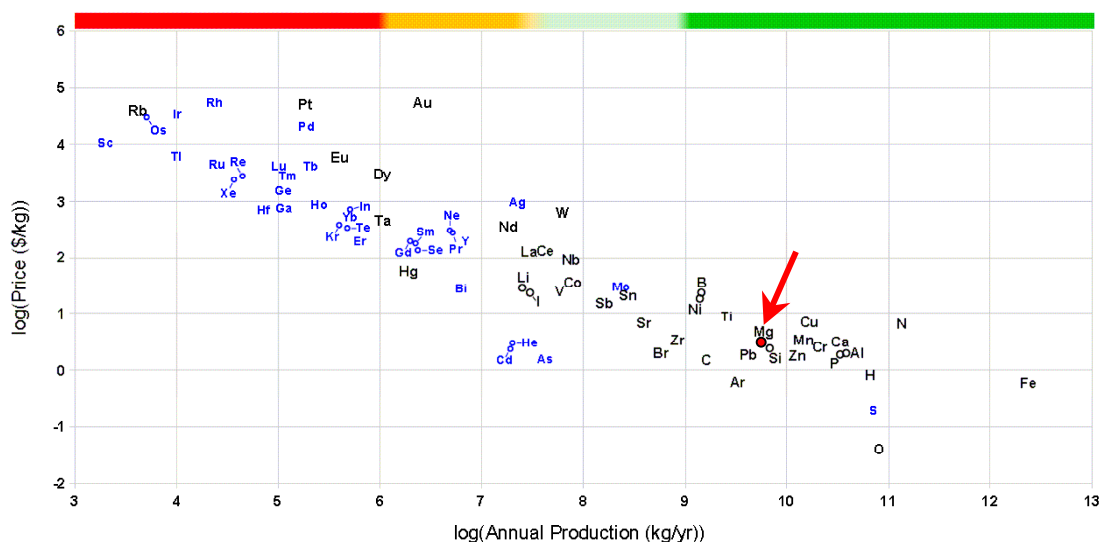
Fig. A3.1 Costs (price in log [$/kg]) plotted versus the annual production (in log [kg/year]), for various elements, quoted from [Vesb12]). An arrow is appended to emphasize position of Mg in figure.

A4. Estimation of hydrogen permeability in GB-rich film

A4.1 Hydrogen permeability in Pd and Mg

Strictly speaking, the effective diffusion constants obtained by hydrogen transport phenomena such as permeation method, contains aspect of hydrogen permeability. Therefore, the effect of GBs on the hydrogen solubility are also included in the discussion.

In case of the diffusion controlled process, the hydrogen permeability Φ is generally defined as the product of the diffusivity D and the solubility S,

$$\Phi = D \cdot S \tag{A4.1}$$

which the units of Φ in $[\mathrm{molH_2 m^{-1} s^{-1} Pa^{-0.5}}]$, D in $[\mathrm{m^2 s^{-1}}]$, and S in $[\mathrm{molHm^{-3} Pa^{-0.5}}]$.

Here, D and S can be expressed in following forms:

$$D = D_0 \exp\left(\frac{-G_D}{RT}\right) \tag{A4.2}$$

$$S = S_0 \exp\left(\frac{-G_S}{RT}\right) \tag{A4.3}$$

where D_0 and S_0 are constants, G_D and G_S are the energies (units in $[\mathrm{J/molH}]$) for the hydrogen diffusion and the hydrogen solution, respectively. S can be experimentally determined by gaseous hydrogen solution into metals, by Sieverts' law [Siev29,From96]:

$$c_\mathrm{H} = S \cdot \sqrt{p_\mathrm{H}} \tag{A4.4}$$

where c_H and p_H are the hydrogen concentration in metal and the pressure of the gaseous hydrogen at the gas/metal interface. This S is the Sieverts constant, and corresponds to the K_p in Eq.(2.6) or in Eq.(2.10).

Thus, Eq.(A4.1) can be rewritten as

$$\Phi = \Phi_0 \exp\left(\frac{-G_\Phi}{RT}\right) \qquad \text{with} \qquad G_\Phi = G_D + G_S \tag{A4.5}$$

where Φ_0 is a constant, G_Φ is the molar activation energy for the permeation and can be expressed in following form:

$$G_\Phi = H_\Phi - TS_\Phi = (H_D + H_S) - T(S_D + S_S) \tag{A4.6}$$

where H_Φ, H_D and H_S are the enthalpies of hydrogen permeation, diffusion and solution respectively, as well as S_Φ, S_D and S_S are the entropies of hydrogen permeation, diffusion and solution, respectively. The relationship of Eq.(A4.5) is valid as far as the Sieverts' law is established. Thus, values at dilute hydrogen concentrations should be chosen for the G_D and G_S. In case of plotting Φ as function of $(1/T)$, $H_\Phi (= H_D + H_S)$ indicates the slope.

A4.2 Hydrogen solution in GB-rich film

The maximum evaluation of the hydrogen solubility limit in nanocrystalline film, $c_{\text{H-Sol}}^{\text{nc}}$, can be obtained by the method by Mütschele end Kirchheim [Muet87^{+}] assuming average cubic grain shape with the length a and the width of grain boundaries b as:

$$c_{\text{H-Sol}}^{\text{nc}} = \frac{1}{V_{\text{Total}}}\left(V_{\text{G}}c_{\text{H}}^{\text{G}} + V_{\text{GB}}c_{\text{H}}^{\text{GB}}\right) = \frac{1}{a^2 d}\left[(a-b)^3 c_{\text{H}}^{\text{G}} + \left\{a^3 - (a-b)^3\right\}c_{\text{H}}^{\text{GB}}\right] \qquad \text{(A4.7)}$$

where V_{Total} is the total volume of the sample, $V_{\text{G}} = a^3$ is the volume of the grain, V_{GB} is the volume of grain boundaries, d is the film thickness. Assuming the columnar grains shape with grain length in out-of-plane direction a', Eq.((A4.1)) can be rewritten as:

$$c_{\text{H-Sol}}^{\text{nc}} = \frac{1}{a^2 d}\left[(a-b)^2(a'-b)c_{\text{H}}^{\text{G}} + \left\{a^2 a' - (a-b)^2(a'-b)\right\}c_{\text{H}}^{\text{GB}}\right]$$

$$\text{with} \quad a < a' < d \qquad \text{(A4.8)}$$

Assumptions of $a = 15$ nm, $b = 0.8$ nm, $a' = 35\text{-}55$ nm (depends on sample, see **Fig. 4.2b**), and $c_{\text{H}}^{\text{G}} = 3 \times 10^{-6}$ H/Mg (see **Sec. 2.1.5.1**) were applied in this work. Thus, the contribution of the grain boundary on the apparent concentration, $c_{\text{H}}^{\text{GB}}/c_{\text{H-Sol}}^{\text{nc}}$, can be obtained as a function of d. The contribution of the hydrogen segregation at the surface or at the subsurface [Kirch14] is neglected in this work.

Bibliography

[Abba08] R. Abbaschian and R.E. Reed-Hill, "*Physical Metallurgy Principles*", (2008), Cengage Learning.

[Aguey08] K.-F. Aguey-Zinsou and J.-R. Ares-Fernández, "Synthesis of Colloidal Magnesium: A Near Room Temperature Store for Hydrogen", *Chem. Mater.*, **20**, (2008), 376-378.

[Aguey10] K.-F. Aguey-Zinsou and J.-R. Ares-Fernández, "Hydrogen in magnesium: new perspectives toward functional stores", *Energy Environ. Sci.*, **3**, (2010), 526-543.

[Akib82] E. Akiba, K. Nomura, S. Ono and Y. Minzuno, *J. Less Common Met.*, **83**, (1982), L43-46.

[Ande54] O.L. Anderson and D.A. Stuart, "Calculation of Activation Energy of Ionic Conductivity in Silica Glasses by Classical Methods", *J. Am. Ceram. Soc.*, **37**, (1954), 573-580.

[Andr06] A. Andreasen, M. Sorensen, R. Burkarl, B. Moller, A. Molenbroek, A. Pedersen, T. Vegge and T. Jensen, "Dehydrogenation kinetics of air-exposed MgH_2/Mg_2Cu and $MgH_2/MgCu_2$ studied with *in situ* X-ray powder diffraction", *Appl. Phys. A*, **82**, (2006), 515-521.

[Anton10] H. Anton, and C. Rorres, "*Elementary Linear Algebra: Applications Version, 10th Edition*", (2010), Wiley.

[Aran93] D.R. Arantes, X.Y. Huang, C. Marte and R. Kirchheim, "Hydrogen diffusion and permeation in micro- and nanocrystalline nickel", *Acta Metallur. Mater.*, **41**, (1993), 3215-3222.

[Ashc76] N.W. Ashcroft and N.D. Mermin, "*Solid State Physics*", (1976), Cengage Learning, ISBN: 9780030839931.

[ASM87] ASM International (American Society for Material), "*Corrosion: ASM Metals Handbook, Ninth Edition, (Vol 13)*", (1987), Gulf Professional Publishing.

[Atkins82] P.W. Atkins and M.J. Clugston, "*Principles of physical chemistry*", (1982), Pitman Books.

[Aved99] M.M. Avedesian and H. Baker (*ed.*), "*Magnesium and Magnesium Alloys (ASM Specialty Handbook)*", (1999), ASM International, ISBN: 9780871706577.

[Baldi09] A. Baldi, M. Gonzalez-Silveira, V. Palmisano, B. Dam, and R. Griessen, "Destabilization of the Mg–H System through Elastic Constraints", *Phys. Rev. Lett.*, **102**, (2009), 226102.

[Baldi09^{+}] A. Baldi, R. Gremaud, D. Borsa, C. Baldé, A. van der Eerden, G. Kruijtzer, P. de Jongh, B. Dam, and R. Griessen, "Nanoscale composition modulations in $Mg_yTi_{1-y}H_x$ thin film alloys for hydrogen storage", *Int. J. Hydrogen Energy*, **34**(3), (2009), 1450-1457.

[Baldi09^{++}] A. Baldi, V. Palmisano, M. Gonzalez-Silveira, Y. Pivak, M. Slaman, H. Schreuders, B. Dam, and R. Griessen, "Quasifree Mg–H thin films", *Appl. Phys. Lett.*, **95**(7), (2009), 071903.

[Baldi10] A. Baldi, G.K. Pálsson, M. Gonzalez-Silveira, H. Schreuders, M. Slaman, J.H. Rector, G. Krishnan, B.J. Kooi, G.S. Walker, M.W. Fay, B. Hjörvarsson, R.J. Wijngaarden, B. Dam, R. Griessen, "Mg/Ti multilayers: Structural and hydrogen absorption properties", *Phys. Rev. B*, **81**, (2010), 224203.

[Balu05] R.W. Baluffi, S.M. Allen, W.C. Carter, "*Kinetics of materials*", (2005), John Wiley & Sons, Inc., pp.459. (ISBN 9780471246893)

[Bara71] B. Baranowski, S. Majchrzak, and T.B. Flanagan, "The volume increase of fcc metals and alloys due to interstitial hydrogen over a wide range of hydrogen contents", *J. Phys. F: Metal Phys*, **1**, (1971), 258-261.

[Bara94] I. Baraille, C. Pouchan, M. Causa, and C. Pisani, "An ab initio Hartree-Fock study of electronic and structural properties of MgH_2", *Chem. Phys.*, **179**(1), (1994), 39-46.

[Bark03] G. Barkhordarian, T. Klassen, and R. Bormann, "Fast hydrogen sorption kinetics of nanocrystalline Mg using Nb_2O_5 as catalyst", *Script. Mater.*, **49**, (2003), 213-217.

[Bast80] J.P. Bastide, B. Bonnetot, J.M. Letoffe and P. Claudy, "Polymorphisme de l'hydrure de magnesium sous haute pression", *Mater. Res. Bull.*, **15**, (1980), 1215.

[Belo04] I. Belova and G. Murch, "The effective diffusivity in polycrystalline material in the presence of interphase boundaries", *Phil. Mag.*, **84**, 17-28.

[Birn72] H.K. Birnbaum and C.A. Wert, "Diffusion of hydrogen in metals" *Ber. Bunsenges. Phys. Chem.*, **76**, (1972), 806.

[Bloch97] J. Bloch and M.H. Mintz, "Kinetics and mechanisms of metal hydrides formation—a review", *J. Alloy. Comp.*, **253-254**, (1997), 529 - 541.

[Bocq96] J.L. Bocquet, G. Brebec and Y. Limoge, "*Diffusion in Metals and Alloys*", written as Chap.7 in: R: Cahn and P. Haasen, (ed.), "*Physical Metallurgy, Fourth Edition*" *(Three Volume Set)*, (1996), North Holland, pp.534-668.
Boes76

[Boes76] N. Boes, H. Züchner, "Electrochemical methods for studying diffusion, permeation and solubility of hydrogen in metals", *J. Less Common Met.*, **49**, (1976), 223.

[Bogd95] B. Bogdanovic, A. Ritter, B. Spliethoff, and K. Straßburger, "A process steam generator based on the high temperature magnesium hydride/magnesium heat storage system", *Int. J. Hydrogen Energy*, **20**, (1995), 811-822.

[Bohm67] G. Bohmholdt and E. Wicke, "Diffusion of hydrogen and deuterium in palladium and palladium alloys. Part. 1. Gas volumetric measurements", *Z. Phys. Chem.*, **56**, (1967), 133-154.

[Bohm99] K. Bohmhammel, U. Wolf, G. Wolf, and E. Königsberger, "Thermodynamic optimization of the system magnesium-hydrogen", *Thermochim. Acta*, **337**, (1999), 195-199.

[Bokh87] B. Bokhonov, E. Ivanov, and V. Boldyrev, "A study of the electron-beam-induced decomposition of magnesium hydride single crystals", *Mater. Lett.*, **5**, (1987), 218-221.

[Borg07] A. Borgschulte, U. Bösenberg, G. Barkhordarian, M. Dornheim and R. Bormann, "Enhanced hydrogen sorption kinetics of magnesium by destabilized $MgH_{2-\delta}$", *Catal. Today*, **120**, (2007), 262-269.

[Bors07] D. Borsa, W. Lohstroh, R. Gremaud, J. Rector, B. Dam, R. Wijngaarden and R. Griessen, "Critical composition dependence of the hydrogenation of $Mg_{2\pm\delta}$ Ni thin films", *J. Alloy. Compd.* **428**, (2007), 34-39.

[Bort98] M. Bortz, B. Bertheville, K. Yvon, E.A. Movlaev, V.N. Verbetsky and F. Fauth, "Mg_3MnH_7, containing the first known hexahydridomanganese (I) complex", *J. Alloy. Compd.*, **279**, (1998), L8-L10.

[Bort99] M. Bortz, B. Bertheville, G. Boettger and K. Yvon, "Structure of the high pressure phase

γ-MgH$_2$ by neutron powder diffraction", *J. Alloy. Compd.*, **287**, (1999), L4-L6.

[Bragg13] W.L. Bragg, "The Diffraction of Short Electromagnetic Waves by a Crystal", *Proc. Cambridge Phil. Soc.*, **17**, (1913), 43-57.

[Burk69] P. Burkhardt, R.F Marvel, "Thermal expansion of sputtered silicon nitride films", *J. Electrochem. Soc.*, **116**, (1969), 864.

[Call10] E. Callini, L. Pasquini, L.H. Rude, T.K. Nielsen, T.R. Jensen, and E. Bonetti, "Hydrogen storage and phase transformations in Mg–Pd nanoparticles", *J. Appl. Phys.* , **108**, (2010), 073513.

[Cant69] R. Cantelli, F.M. Mazzolai, and M. Nuovo, "Internal friction due to Long-Range Diffusion of hydrogen in Niobium (Gorski effect)", *Phys. Stat. sol.*, **34**, (1969), 597.

[Cart13] D. Carter and J. Wing, "The Fuel Cell Industry Review 2013", (2013), Fuel Cell Today.

[Cerm08] J. Cermák and L. Král, "Hydrogen diffusion in Mg-H and Mg-Ni-H alloys", *Acta Mater.*, **56**, (2008), 2677-2686.

[Chec04] R. Checchetto, N. Bazzanella, A. Miotello, R.S. Brusa, and A. Zecca, "Deuterium storage in nanocrystalline magnesium thin films", *J. Appl. Phys.*, **95**, (2004), 1989.

[Chen95] Y. Chen and J. Williams, "Formation of metal hydrides by mechanical alloying", *J. Alloy. Compd.*, **217**, (1995), 181-184.

[Chen04] D. Chen, Y.M. Wang, L. Chen, S. Liu, C.X. Ma and L.B. Wang, "Alloying effects of transition metals on chemical bonding in magnesium hydride MgH$_2$", *Acta Mater.*, **52**. (2004), 521-528.

[Cheu05] S. Cheung, W.-Q. Deng, A.C.T. van Duin, and W.A. Goddard, "ReaxFFMgH Reactive Force Field for Magnesium Hydride Systems", *J. Phys. Chem. A*, **109**, (2005), 851-859.

[Chit13] L.ChitsazKhoyi, S. Raygan, and M. Pourabdoli, "Mechanical milling of Mg, Ni and Y powder mixture and investigating the effects of produced nanostructured MgNi4Y on hydrogen desorption properties of MgH$_2$", *Int. J. Hydrogen Energy*, **38**, (2013), 6687-6693.

[Chris01] C. Christodoulatos, T.L. Su, and A. Koutsospyros, "Kinetics of the alkaline hydrolysis of nitrocellulose.", *Water Environ. Res.*, **73**, (2001), 185-191.

[Chris88] K. Christmann, "Interaction of hydrogen with solid surfaces", *Surf. Sci. Rep.*, **9**, (1988), 1-163.

[Cize13] J. Čížek, O. Melikhova, M. Vlček, F. Lukáč, M. Vlach, I. Procházka, W. Anwand, G. Brauer, A. Mücklich, S. Wagner, H. Uchida, A. Pundt, "Hydrogen-induced microstructural changes of Pd films", *Int. J. Hydrogen Energy*, **38**, (2013), 12115-12125.

[Clea65] H. Cleary and N. Greene, "Electrochemical Energy Conversion in a Palladium-Hydrogen Diffusion Electrode", *Electrochim. Acta*, **10**, (1965), 1107-1115.

[Culli78] B.D. Cullity, "*Elements of X-ray diffraction*", 2nd ed., (1978), Addison-Wesley publishing company.

[Cumm74] D.L. Cummings and G.J. Powers, "The Storage of Hydrogen as Metal Hydrides", *Ind. Eng. Chem.*, *Process Des. Develop.*, **13**, (1974), 182-192.

[Conr07] M.S. Conradi, M.P. Mendenhall, T.M. Ivancic, E.A. Carl, C.D. Browning, P.H.L. Notten, W. Kalisvaart, Pieter C.M.M. Magusin, R.C. Bowman Jr., S.-J. Hwang and N.L. Adolphi, "NMR to determine rates of motion and structures in metal-hydrides", *J. Alloy. Compd.*, **446-447**, (2007), 499-503.

[Core08] R.L. Corey, T.M. Ivancic, D.T. Shane, E.A. Carl, R.C. Bowman Jr., J.M.B. von Colbe, M. Dornheim, R. Bormann, J. Huot, R. Zidan, A.C. Stowe, and M.S. Conradi, "Hydrogen Motion in Magnesium Hydride by NMR", *J. Phys. Chem. C*, **112**, (2008), 19784-19790.

[Corn75] D.A. Cornell and E. Seymour, "Nuclear magnetic resonance study of hydrogen diffusion in palladium and palladium-cerium alloys", *J. Less Common Met.*, **39**, (1975), 43-54.

[Cran75] J. Crank, "*The Mathematics of Diffusion*", (1975), Oxford University Press.

[Czer11] F. Czerwinski, "*Magnesium Alloys: Corrosion and Surface Treatments*", (2011), InTech, ISBN: 9789533079721.

[Dam07] B. Dam, R. Gremaud, C. Broedersz, and R. Griessen, "Combinatorial thin film methods for the search of new lightweight metal hydrides", *Script. Mater.*, **42**, (2007), 853-858.

[Dana12] M. Danaie and D. Mitlin, "TEM analysis of the microstructure in TiF$_3$-catalyzed and

pure MgH$_2$ during the hydrogen storage cycling", *Acta Mater.*, **60**, (2012), 6441-6456.

[Davi54] W.D. Davis, "Diffusion of hydrogen through palladium", *USAEC report*, **KAPL-1227**, US Atomic Energy Commission, (1954).

[Davi76] P. Davis, E. Seymour, D. Zamir, W. Williams, and R. Cotts, "Nuclear magnetic resonance study of hydrogen diffusion in palladium-silver alloys", *J. Less Common Met.*, **49**, (1976), 159-168.

[Davi98] J.R. Davis (*ed.*),"*Metals Handbook Desk Edition 2nd Edition*", (1998), CRC Press, ISBN: 9780871706546.

[Demo10] S. Demouchy, "Diffusion of hydrogen in olivine grain boundaries and implications for the survival of water-rich zones in the Earth's mantle", *Earth Planet. Sci. Lett.*, **295**, (2010), 305-313.

[Deng08] Y.H. Deng, W.B. Zhang, B.Y. Tang, X.Q. Zeng, W.J. Ding, "Crystal structure of Mg$_3$Pd from first-principles calculations", *Trans. Nonferr. Met. Soc. China* **18**, (2008), 416-420.

[Deva62] M. Devanathan and Z. Stachurski, "Hydrogen in Palladium: The Adsorption and Diffusion of Electrolytic Hydrogen in Palladium", *Proc. R. Soc. Lond.* A, **270**, (1962), 90-102.

[Deva64] M. Devanathan and Z. Stachurski, "The Mechanism of Hydrogen Evolution on Iron in Acid Solutions by Determination of Permeation Rates", *J. Electroc.*, **111**, (1964), 619-623.

[Dorn02] M. Dornheim, "Spannungen, Dehnungen und Lage der Phasengrenzen in dünnen Nb- und Y-Schichten bei Wasserstoffbe- und entladung", Ph.D thesis, Georg-August-Universität Göttingen, (2002).

[Dorn07] M. Dornheim, S. Doppiu, G. Barkhordarian, U. Boesenberg, T. Klassen, O. Gutfleisch and R. Bormann, *Script. Mat.*, **56**, (2007), 841-846.

[Dorn09] M. Dornheim and T. Klassen, "Fuels – Hydrogen Storage | High Temperature Hydrides", pp. 459-472 in Book: J. Garche (ed.), "*Encyclopedia of Electrochemical Power Sources*", (2009), Elsevier, Amsterdam, ISBN: 9780444527455.

[Dorn10] M. Dornheim, "*Tailoring Reaction Enthalpies of Hydrides*", a chapter at p.187-214 in book ref. [Hirs10].

[Du08] A.J. Du, S.C. Smith, X.D. Yao, C.H. Sun, L. Li, and G.Q. Lu, "The role of V_2O_5 on the dehydrogenation and hydrogenation in magnesium hydride: An ab initio study", *Appl. Phys. Lett.*, **92**, (2008), 163106.

[Dufo07] J. Dufour and J. Huot, "Study of Mg_6Pd alloy synthesized by cold rolling", *J. Alloy. Compd.*, **446-447**, (2007), 147-151.

[Ecke71] P. Eckerlin, H, Kandler, "*Structure Data of Elements and Intermetallic Phases / Strukturdaten der Elemente und intermetallischen Phasen (Landolt-Bornstein: Numerical Data and ... Relationships) (English and German Edition)*", (1971), Springer, ISBN: 9783540055006.

[Earl70] J.G. Early, "Hydrogen diffusion in palladium by galvanostatic charging", *Acta Metallur.*, **26**, (1978), 1215-1223.

[EIA14] U.S. Energy Information Administration (EIA), "*International Energy Outlook 2014*", (2014). (URL: http://www.eia.gov/forecasts/ieo/pdf/0484%282014%29.pdf)

[Ellin44] H.J.T. Ellingham, "Reducibility of Oxides and Sulphides in Metallurgical Processes", *J. Soc. Chem. Ind. Trans.*, **63**, (1944), 125-133.

[Ellin55] F.H. Ellinger, C.E. Holley jr., B.B. McInteer, D. Pavone, R.M. Potter, E. Staritzky, and W.W. Zachariasen, "The Preparation and Some Properties of Magnesium Hydride", *J. Am. Chem. Soc.*, **77**, (1955), 2647.

[Evar10] E. Evard, I. Gabis and V.A. Yartys , "Kinetics of hydrogen evolution from MgH_2: Experimental studies, mechanism and modelling", *Int. J. Hydrogen Energy* , **35**, (2010), 9060-9069.

[Feen83] R. Feenstra, G.J. de Bruin-Hordijk, H.L.M. Bakker, R. Griessen, D.G. de Groot, "Critical point lowering in thin PdH_x films", *J. Phys. F: Met. Phys.*, **13**, (1983), L13-L18.

[Ferr59] R. Ferro, "Research on the alloys of noble metals with the more electropositive elements: II. Micrographic and roentgenographic examination of the magnesium-palladium alloys", *J. Less Common Met.*, **1**, (1959), 424-438.

[Flan91] T.B. Flanagan and W.A. Oates, "The Palladium-Hydrogen System", *Annu. Rev. Mater. Sci.*, **21**, (1991), 269-304.

[Flan91^{+}] T.B. Flanagan, W. Luo and J.D. Clewley, "Calorimetric enthalpies of absorption and desorption of protium and deuterium by palladium", *J. Less Common Met.*, **172-174 Part A**, (1991), 42-55.

[Fried06] O. Friedrichs, F. Aguey-Zinsou, J.A. Fernández, J. Sánchez-López, A. Justo, T. Klassen, R. Bormann, and A. Fernández, "MgH$_2$ with Nb$_2$O$_5$ as additive, for hydrogen storage: Chemical, structural and kinetic behavior with heating", *Acta Mater.*, **54**, (2006), 105-110.

[Fries73] H. Frieske and E. Wicke, "Magnetic Susceptibility and Equilibrium Diagram of PdH$_n$", *Ber. Bunsenges. phys. Chem.*, **77**(1), (1973), 48-52.

[Fukai89] Y. Fukai, "Site occupancy and phase stability of some metal hydrides", *Z. Phys. Chem.*, **164**, (1989), 165-174.

[Fukai05] Y. Fukai, "*The Metal-Hydrogen System*", (2nd ed.), (2005), Springer-Verlag, Berlin Heidelberg New York, ISBN: 9783642046544.

[Freund03] L.B. Freund and S. Suresh, "*Thin Film Materials: Stress, Defect Formation and Surface Evolution*", Cambridge University Press, (2003), pp.186-194.

[Fried88] G.M. Friedlmeier and J.C. Bolcich, "Production and characterization of Mg-10 wt% Ni alloys for hydrogen storage", *Int. J. Hydrogen Energy*, **13**, (1988), 467-474.

[Fried97] G. Friedlmeier and M. Groll, "Experimental analysis and modelling of the hydriding kinetics of Ni-doped and pure Mg", *J. Alloy. Compd.*, **253-254**, (1997), 550-555.

[From76] E. Fromm and E. Gebhardt, "*Gase und Kohlenstoff in Metallen*", Band 26, Springer-Verlag, Berlin Heidelberg, (1976).

[From96] E. Fromm, H. Uchida and B. Chelturi, "*Kinetics of Metal-Gas Interactions at Low Temperatures*", (1998), Springer-Verlag, ISBN: 9780324180237.

[Gaut11] Y.K. Gautam, A.K. Chawla, R. Walia, R. Agrawal and R. Chandra, "Hydrogenation of Pd-capped Mg thin films prepared by DC magnetron sputtering", *Appl. Surf. Sci.*, **257**, (2011), 6291-6295.

[Gaut12] Y.K. Gautam, K.C. Amit, A.K. Saif, R.D. Agrawal and R. Chandra, "Hydrogen

absorption and optical properties of Pd/Mg thin films prepared by DC magnetron sputtering", *Int. J. Hydrogen Energy*, **37**, (2012), 3772-3778.

[Gaut13] Y. K. Gautam, M. Kumar and R. Chandra, "Hydrogen absorption and desorption properties of Pd/Mg/Pd tri-layers prepared by magnetron sputtering", *Surf. Coat. Techn.*, **237**, (2013), 450-455.

[Gemm11] R. Gemma, "Hydrogen in V-Fe thin films and Fe/V-Fe multi-layered thin films (Wasserstoff in V-Fe dünnen Schichten und V-Fe/Fe mehrfachschchten)", PhD thesis, Georg-August-Universität Göttingen, (2011).

[Ghal10] E. Ghali, "*Corrosion Resistance of Aluminum and Magnesium Alloys: Understanding, Performance, and Testing*", (2010), Wiley, ISBN: 9780471715764.

[Gieb04] I.A.M.E. Giebels, J. Isidorsson, and R. Griessen, "Highly absorbing black Mg and rare-earth-Mg switchable mirrors", *Phys. Rev.*, **69**, (2004), 205111.

[Godu12] A. Godula-Jopek, W. Jehle and J. Wellnitz, "*Hydrogen Storage Technologies: New Materials, Transport, and Infrastructure*", (2012), Wiley-VCH, ISBN: 9783527326839.

[Golt75] V. Gol'tsov, N. Timofeev, G. Kagan, M. Aizenbud, and Y. Baichtok, "Hydrogen permeability and hydrogen resistance of some palladium alloys", *Soviet materials science : a transl. of Fiziko-khimicheskaya mekhanika materialov / Academy of Sciences of the Ukrainian SSR* **9**(5), (1975), 534-538.

[Göse82] U. Gösele and K.N. Tu, "Growth kinetics of planar binary diffusion couples: ''Thin-film case'' versus ''bulk cases'' ", *J. Appl. Phys.*, **53**, (1982), 3252-3260.

[Goto05] Y. Goto, H. Kakuta, A. Kamegawa, H. Takamura, and M. Okada, "High-pressure synthesis of novel hydride in Mg-M systems (M = Li, Pd)", *J. Alloy. Compd.*, **404-406**, (2005), 448-452.

[Gray72] D.E. Gray, American Institute of Physics Handbook, Mcgraw-Hill Book Company, New York, (1972).

[Gries88] R. Griessen and T. Riesterer, "*Hydrogen in Intermetallic Compounds I*", *Bd. 63 of Topics in Applied Physics.* , Ed. by L. Schlapbach, Springer-Verlag, Berlin Heidelberg New York, (1988)

[Gries99] R. Griessen, "*The Physics of Hydrogen in Metals*", (1999), Vrije Universiteit, Amsterdam.

[Grün10] E. Grüneisen, "Über die thermische Ausdehnung der Metalle", *Annal. Phys.*, **33**, (1910), p.33.

[Gusa10] A.M. Gusak, T. Zaporozhets, Y.O. Lyashenko, S. Kornienko, M.O. Pasichnyy, and A. Shirinyan, "*Diffusion-controlled Solid State Reactions: in Alloys, Thin-Films, and Nanosystems*", (2010), Wiley-VCH Verlag GmbH & Co. KGaA, ISBN: 9783527408849.

[Gure78] D. Gruen, M. Mendelsohn, and I. Sheft, "Metal hydrides as chemical heat pumps", *Sol. Energy*, **21**, (1978), 153-156.

[Hagi90] H. Hagi, "Boundary Conditions in Electrochemical Measurements of Diffusion Coefficients of Hydrogen in α-Palladium", *Mater. Trans. JIM*, **31**, (1990), 954.

[Hahn96] T. Hahn (*ed.*), "*International Tables for Crystallography, Volume A*", (1996), Springer, ISBN: 9780792342526, Space group 136, pp. 468-469.

[Ham14] B. Ham, A. Junkaew, R. Arróyave, J. Park, H.-C. Zhou, D. Foley, S. Rios, H. Wang, and X. Zhang, "Size and stress dependent hydrogen desorption in metastable Mg hydride films", *Int. J. Hydrogen Energy*, **39**, (2014), 2597-2607.

[Hana05] N. Hanada, T. Ichikawa, H. Fujii, "Catalytic Effect of Nanoparticle 3d-Transition Metals on Hydrogen Storage Properties in Magnesium Hydride MgH_2 Prepared by Mechanical Milling", *J. Phys. Chem.* B, **109**, (2005), 7188-7194.

[Hana06] N. Hanada, T. Ichikawa and H. Fujii, "Catalytic effect of niobium oxide on hydrogen storage properties of mechanically ball milled MgH_2", *Physica B: Condensed Matter*, **383**, (2006), 49-50.

[Hao08] S. Hao and D.S. Sholl, "Hydrogen diffusion in MgH_2 and $NaMgH_3$ via concerted motions of charged defects", *Appl. Phys. Lett.*, **93**, (2008), 251901.

[Harp00] C.A. Harper, "*Modern Plastics Handbook*", McGraw-Hill Professional, (2000), ISBN: 9780070267145.

[Harr91] T.M. Harris and M. Latanision, "Grain boundary diffusion of hydrogen in nickel", *Metallurg. Mater. Trans. A*, **22**, (1991), 351-355.

[Hart57] E. Hart, "On the role of dislocations in bulk diffusion", *Acta Metallur.*, **5**, (1957), 597.

[Hase77] H. Hasegawa and K. Nakajima, "Hydrogen Diffusion and Effect on the Mechanical Properties in Annealed and Cold-worked Palladium (焼なましおよび冷間加工したパラジウムでの水素の拡散およびその機械的性質への影響)", *J. Jpn. Inst. Met.*, **41**, (1977), 813-820.

[Hase79] H. Hasegawa and K. Nakajima, "Effect of hydrogen on the mechanical properties of Pd", *J. Phys. F: Met. Phys.* **9**, (1979), 1035.

[Hawk99] D.L. Hawke, J. Hillis, M. Pekguleryuz, and I. Nakatsugawa, "*Corrosion Behavior*", a chapter in ref.[Aved99], pp.194-210.

[He90] Z.X. He and W. Pong, "X-ray photoelectron spectra of MgH_2", *Phys. Scr.* **41**, (1990), 930.

[Hear79] R.F. Hearmon, (1979), "*The elastic constants of crystals and other anisotropic materials*", In: K.H. Hellwege and A.M. Hellwege (Eds.), "*Landolt-Börnstein Tables*", Group III, Vol. 11, Springer-Verlag, Berlin, pp.1-154.

[Hect07] L.G. Hector, J.F. Herbst, W. Wolf, P. Saxe, and G. Kresse, "Ab Initio thermodynamic and elastic properties of alkaline-earth metals and their hydrides", *Phys. Rev. B*, **76**, (2007), 014121.

[Herz03] C. Herzig, S.V. Divinski, "Grain Boundary Diffusion in Metals: Recent Developments", *Mater. Trans.* **44**, (2003), 14-27.

[Hidn28] P. Hidnert and W.T. Sweeney, "Thermal Expansion of Magnesium and Some of Its Alloys", *J. Resear. Nat. Inst. Stand. Technol.*, **1**, (1928), 771.

[Higu02] K. Higuchi, K. Yamamoto, H. Kajioka, K. Toiyama, M. Honda, S. Orimo, and H. Fujii, "Remarkable hydrogen storage properties in three-layered Pd/Mg/Pd thin films", *J. Alloy. Compd.*, **330-332**, (2002),526-530.

[HinMeI] G. Alefeld *et al.*, "*Hydrogen in Metals I*", (1978), Springer-Verlag, Berlin, Heidelberg, New York, ISBN: 9783540087052.

[HinMeII] G. Alefeld *et al.*, "*Hydrogen in Metals II*", (1978), Springer-Verlag, Berlin, Heidelberg, New York, ISBN: 9780387088839.

[Hirs10] M. Hirscher and K. Hirose (*ed.*), "*Handbook of Hydrogen Storage: New Materials for Future Energy Storage*", (2010), Wiley-VCH Verlag GmbH & Co. KGaA, ISBN: 9783527322732.

[Hjort96] P. Hjort, A. Krozer, and B. Kasemo, "Hydrogen sorption kinetics in partly oxidized Mg films", *J. Alloy. Compd.*, **237**, (1996), 74-80.

[Hoar57] J.P. Hoare and S. Schuldiner, "Effects of Hydrogen Content on the Resistance and the Potential in the Palladium-Hydrogen-Acid System", *J. Phys. Chem.*, **61**, (1957), 399-402.

[Hodg20] C.D. Hodgman, *Phys. Rev.*, **15**, (1920), 218.

[Holl67] G.L. Holleck and E. Wicke, "Diffusion of hydrogen and deuterium in Palladium alloys, part3: Electrochemical methods", *Z. Phys. Chem.*, **56**, (1967), 155-172.

[Holl70] G.L. Holleck, "Diffusion and solubility of hydrogen in palladium and palladium-silver alloys", *J. Phys. Chem.*, **74**, (1970), 503-511.

[Hopc10] M. Hopcroft, W. Nix and T. Kenny, "What is the Young's Modulus of Silicon?", *J. Microelectromech. Sys.*, **19**, (2010), 229.

[Huib96] J. N. Huiberts and R. Griessen and J. H. Rector and R. J. Wijngaarden and J. P. Dekker and D. G. de Groot and N. J. Koeman, "Yttrium and Lanthanum hydride films with switchable optical properties", *Nature*, **380**, (1996), 231.

[Hunt58] H.B. Huntington, "The elastic constants of crystals", *Sol. State Phys.*, **7**, (1958), 213-251.

[Huot01] J. Huot, G. Liang, and R. Schulz, "Mechanically alloyed metal hydride systems", *Appl. Phys.* A., **72**, (2001), 187.

[Ichi10] T. Ichikawa, "*Amides, Imides and Mixtures*", Chapter 6, pp. 159-185 in Book: M. Hirscher and K. Hirose (*ed.*), "*Handbook of Hydrogen Storage: New Materials for Future Energy Storage*", (2010), Wiley-VCH Verlag GmbH & Co. KGaA, ISBN: 9783527322732.

[Isido03] J. Isidorsson, I.A.M.E. Giebels, H. Arwin, and R. Griessen, "Optical properties of MgH_2

measured *in situ* by ellipsometry and spectrophotometry", *Phys. Rev. B*, **68**, (2003), 115112.

[Iwasa03] W. Iwasaki, "A consideration of power density and hydrogen production and utilization technologies", *Int. J. Hydrogen Energy*, **28**, (2003), 1325-1332.

[Izumi05] F. Izumi, "結晶構造と電子状態の三次元可視化システム VENUS", *Rigaku J.*, **36**, (2005), 18-27. (in Japanese)

[Jain88] I. Jain, Y. Vijay, L. Malhotra, and K. Uppadhyay, "Hydrogen storage in thin film metal hydride–a review", *Int. J. Hydrogen Energy*. **13**, (1988), 15-23.

[Janss07] G. Janssen, "*Stress and strain in polycrystalline thin films*", *Thin Solid Films*, **515**, (2007), 6654-6664.

[Jewe65] D.N. Jewett and A.C. Makrides, "Diffusion of hydrogen through palladium and palladium-silver alloys", *Trans. Faraday Soc.,* **61**, (1965), 932-939

[Kael68] E.F. Kaelble, "*Handbook of X-rays: For Diffraction, Emission, Absorption, and Microscopy*", (1968), McGraw-Hill Inc.,US, ISBN: 9780070332003.

[Kame05] A. Kamegawa, T. Funayama, J. Takahashi, H. Takamura, and M. Okada, "Grain refinements of Al-Mg alloy by hydrogen heat-treatments", *Mater. Trans.*, **46**, (2005), 2449-2453.

[Kane08] M. Kanemoto, T. Ozaki, Y. Kawabe, M. Kuzuhara, M. Watada, S. Tanase, and T. Sakai, "Development of Rare Earth-Mg-Ni-based Hydrogen Storage Alloys for Ni-MH Cells", *GS Yuasa Techn. Rep.*, **5**, (2008), p.32-38.

[Kama08] Y. Kamata, R. Kataoka, D. Kyoi, A. Kamegawa, and M. Okada, "High-Pressure Synthesis of MgNi Intermetallic Compound and Its Thermal Stability", *Mater. Trans.* **49**, (2008), 457-460.

[Katl78] V.M. Katlinski, "Some features and parameters of hydrogen diffusion in 10 transition-metals", *Inorg. Mater.*, **14**, (1978), 1299-1304.

[Katz60] O.M. Katz and E.A. Gulbransen, "Permeability and Diffusivity of Hydrogen Through a Palladium Tube", *Rev. Sci. Instrum.*, **31**, (1960), 615-617.

[Kaur95] I. Kaur, Y. Mishin and W. Gust, "*Fundamentals of Grain and Interphase Boundary*

Diffusion", 3rd ed., (1995), Wiley, ISBN 9780471938194.

[Kele07] R. Kelekar, H. Giffard, S.T. Kelly and B.M. Clemens, "Formation and dissociation of MgH$_2$ in epitaxial Mg thin films", *J. Appl. Phys.*, **101**, (2007), 114311.

[Kelly10] S.T. Kelly, B.M. Clemens, "Moving interface hydride formation in multilayered metal thin films", *J. Appl. Phys.*, **108**, (2010), 013521.

[Kelly12] A.A. Kelly and K.M. Knowles, "*Crystallography and Crystal Defects*", (2012), Wiley, ISBN: 9780470750148.

[Kello80] G.L. Kellogg and J.K.G. Panitz, "A direct observation of the trapping of deuterium ions at a grain boundary in tungsten", *Appl. Phys. Lett.*, **37**, (1980), 625-627.

[Kenn60] J.A. Kennelley, J.W. Varwig and H.W. Myers, "Magnesium-Hydrogen relationships1", *J. Phys. Chem.* **64**, (1960), 703-704.

[Kest00] P. Kesten, "Hochaufloesende Untersuchung der lokalen Wasserstoffverteilung in metallischen Multischichten mit Hilfe der tomographischen Atomsonde und der Sekundaerionenmassenspektrometrie", PhD thesis, Georg-August-Universität Goettingen, (2000).

[Klin98] M. Kline, "*Calculus: An Intuitive and Physical Approach (Second Edition) (Dover Books on Mathematics)*", Dover Publications, (1998), p.457.

[Klos95] W. Klose and V. Stuke, "Investigation of the thermodynamic equilibrium in the hydrogen-magnesium-magnesium hydride system", *Int. J. Hydrogen Energy*, **20**, (1995), 309-316.

[Kirch80] R. Kirchheim, "The effect of substitutional impurity atoms on the diffusivity of an interstitial species", *Script. Metall.*, **14**, (1980), 905.

[Kirch80^{+}] R. Kirchheim and R.B. McLellan, "Electrochemical Methods for Measuring Diffusivities of Hydrogen in Palladium and Palladium Alloys", *J. Electrochem. Soc*, **127**, (1980), 2419.

[Kirch86] R. Kirchheim, "Interaction of hydrogen with external stress fields", *Acta Metallur.*, **34**, (1986), 37-42.

[Kirch88] R. Kirchheim, "Hydrogen solubility and diffusivity in defective and amorphous metals",

Prog. Mater. Sci., **32**, (1988), 261-325.

[Kirch88^{+}] R. Kirchheim, T. Muetschele, and W. Kieninger, "Hydrogen in amorphous and nanocrystalline metals", *Mater. Sci. Eng.*, **99**, (1988), 457-462.

[Kirch14] R. Kirchheim and A. Pundt, "*Hydrogen in Metals*", Ch.25 in book: D.E. Laughlin and K. Hono (ed.), "*Physical Metallurgy, Fifth Edition: 3-Volume Set*", (2014), Elsevier, ISBN: 9780444537706.

[Knaa68] J. Knaak and W. Eichenauer, "Die Wanderung von Protonen und Deuteronen in Palladium unter Einfluß eines elektrischen Feldes", *Z. Naturforsch. A*, **23**, (1968), 1783-1789.

[Koen59] J. Koeneman and A.G. Metcalfe, "The solubility of hydrogen in magnesium", *Trans. ASM.*, **51**, (1959), 1072-1082.

[Koff68] S.A. Koffler, J.B. Hudson, G.S. Ansel, "Permeation studies of Hydrogen-Palladium system", *J. Met.*, **20**, (1968), 53.

[Kohl05] H. Kohlmann, G. Renaudin, K. Yvon, C. Wannek, and B. Harbrecht, "Hydrogen-induced atomic rearrangement in $MgPd_3$", *J. Solid State Chem.*, **178**, (2005), 1292-1300.

[Kohn00] T. Kohno, H. Yoshida, F. Kawashima, T. Inaba, I. Sakai, M. Yamamoto, and M. Kanda, "Hydrogen storage properties of new ternary system alloys: La_2MgNi_9, $La_5Mg_2Ni_{23}$, La_3MgNi_{14}", *J. Alloy. Compd.*, **311**, (2000), L5-L7.

[Koji06] Y.Kojima, Y. Kawai and T. Haga, "Magnesium-based nano-composite materials for hydrogen storage", *J. Alloy. Compd.*, **424**, (2006), 294-298.

[Koss11] U. Koss, M. Łukaszewski, K. Hubkowska and A. Czerwiński, "Influence of rhodium additive on hydrogen electrosorption in palladium-rich Pd-Rh alloys", *J. Solid State Electrochem.*, **15**, (2011) , 2477-2487.

[Kras82] G. Krasko, p.367 in book: "*Metal-Hydrogen Systems*", ed. By T.N. Veziroglu, (1982), Pergamon, New York, ISBN: 9780080273167.

[Krau96] W. Kraus and G. Nolze, "POWDER CELL – a program for the representation and manipulation of crystal structures and calculation of the resulting X-ray powder patterns", *J. Appl.*

Crystallogr. **29**, (1996), 301-303.

[Kroz90] A. Krozer and B. Kasemo, "Hydrogen uptake by Pd-coated Mg: absorption-decomposition isotherms and uptake kinetics", *J. Less Common Met.*, **160**, (1990), 323-342.

[Kuer14] J. Kürschner, S. Wagner and A. Pundt, "Delamination-supported growth of hydrides in Pd thin films studied by electrochemical hydrogenography", *J. Alloy. Compd.*, **593**, (2014), 87-92.

[Kunk11] N. Kunkel, J. Sander, N. Louis, Y. Pang, L. Dejon, F. Wagener, Y. Zang, A. Sayede, M. Bauer, M. Springborg and H. Kohlmann, "Theoretical investigation of the hydrogenation induced atomic rearrangements in palladium rich intermetallic compounds MPd_3 (M = Mg, In, Tl)", *Eur. Phys. J. B*, **82**, (2011), 1-6.

[Kyoi04] D. Kyoi, T. Sato, E. Rönnebro, N. Kitamura, A. Ueda, M. Ito, S. Katsuyama, S. Hara, D. Noréus, and T. Sakai, "A new ternary magnesium-titanium hydride Mg_7TiH_x with hydrogen desorption properties better than both binary magnesium and titanium hydrides", *J. Alloy. Compd.*, **372**, (2004), 213-217.

[Ladd03] M.F. Ladd and R.A. Palmer, " *Structure Determination by X-ray Crystallography*", (2003), Springer, ISBN: 9780306474538.

[Lang78] J.I. Langford and A.J.C. Wilson, "Scherrer after sixty years: A survey and some new results in the determination of crystallite size", *J. Appl. Crystallogr.*, **11**, (1978), 102-113.

[Laud98] U. Laudahn, "Spannungen und Dehnungen von mit Wasserstoff beladenen Nb-Einfach- und Pd-Nb-Vielfachschichten", Ph.D thesis, Georg-August-Universität Göttingen, (1998).

[Laud99] U. Laudahn, S. Fähler, H.U. Krebs, A. Pundt, M. Bicker, U.v. Hülsen, U. Geyer and R. Kirchheim, "Determination of elastic constants in thin films using hydrogen loading", *Appl. Phys. Lett.*, **74(5)**, (1999), 647-649.

[Laud99+] U. Laudahn, A. Pundt, M. Bicker, U. von Hülsen, U. Geyer, T. Wagner, and R. Kirchheim, "Hydrogen-induced stress in Nb single layers", *J. Alloy. Compd.*, **293-295**, (1999), 490-494.

[Läss83] R. Lässer and K.-H. Klatt, "Solubility of Hydrogen Isotopes in Palladium" , *Phys. Rev. B*, **28**, (1983), 748-758.

[LeQu14] H. Le-Quoc, A. Lacoste, S. Miraglia, S. Béchu, A. Bès, L. Laversenne, "MgH$_2$ thin films deposited by one-step reactive plasma sputtering", *Int. J. Hydrogen Energy*, **39**, (2014), 17718-17725.

[Leon02] A. Léon, E. Knystautas, J. Huot, and R. Schulz, "Hydrogenation characteristics of air-exposed magnesium films", *J. Alloy. Compd.*, **345**(1-2), (2002), 158-166.

[Li66] J.C.M. Li, R.A. Oriani and L.S. Darken, "The thermodynamics of stressed solids", *Z. phys. Chem*, **49**, (1966), 4.

[Lide04] D.R. Lide (ed.), "*CRC Handbook of Chemistry and Physics 2004-2005: A Ready-Reference Book of Chemical and Physical Data*", (2004), CRC Press, ISBN: 9780849304859.

[Lillo08] M.A. Lillo-Ródenas, K.-F.Aguey-Zinsou, D. Cazorla-Amorós, A. Linares-Solano and Z.X. Guo, "Effects of Carbon-Supported Nickel Catalysts on MgH$_2$ Decomposition", *J. Phys. Chem. C*, **112**, (2008), 5984-5992.

[Lity85] L.M. Lityagina, T.I. Dyulleva, S.S. Kabalkina, T.N. Dimova and V.G. Losev, *Geokhim.*, **1**, (1985), 118. (in Russian)

[Lohs04] W. Lohstroh, R.J. Westerwaal, B. Noheda, S. Enache, I.A.M.E Giebels, B. Dam and R. Griessen, "Self-Organized Layered Hydrogenation in Black Mg$_2$NiH$_x$ Switchable Mirrors", *Phys. Rev. Lett.*, **93**, (2004), 197404.

[Lohs05] W. Lohstroh, R. Westerwaal, A. Lokhorst, J.M. van Mechelen, B. Dam, and R. Griessen, "Double layer formation in Mg–TM switchable mirrors (TM: Ni, Co, Fe)", *J. Alloy. Compd.*, **404-406**, (2005), 490-493.

[Loto14] M. Lototskyy, V. Yartys, B. Pollet, and R.C. Bowman Jr., "Metal hydride hydrogen compressors: A review", *Int. J. Hydrogen Energy*, **39**, (2014), 5818-5851.

[Luo08] Y. Luo, P. Wang, L.P. Ma and H.M. Cheng, "Hydrogen sorption kinetics of MgH$_2$ catalyzed with NbF$_5$", *J. Alloy. Compd.* **453**, (2008), 138-142.

[Luz80] Z. Luz, J. Genossar, and P. Rudman, "Kirkendall marker movement during hydriding of magnesium", *Script. Metall.*, **14**, (1980), 275-277.

[Luz80^{+}] Z. Luz, J. Genossar and P. Rudman, "Identification of the diffusing atom in MgH$_2$", *J. Less Common Met.*, **73**, (1980), 113-118.

[Mako06] J. Makongo, Y. Prots, U. Burkhardt, R. Niewa, C. Kudla, and G. Kreiner, "A case study of complex metallic alloy phases: structure and disorder phenomena of Mg-Pd compounds", *Phil. Mag.*, **86**(3-5), (2006), 427-433.

[Mal78] H.H. van Mal and A.R. Miedema, "Some applications of LaNi$_5$-type hydrides", pp. 251-260 in book: A.F. Andresen and A.J. Maeland (ed.),"*Hydrides for Energy Storage*", (1978), Pergamon Press, ISBN: 9780080227153.

[Manc94] F.D. Manchester, A. San-Martin and J.M. Pitre, "The H-Pd (hydrogen-palladium) System", *J. Phase Equil.*, **15**, (1994), 62-83.

[Mintz78] M.H. Mintz, Z. Gavra and Z. Hadari, "Kinetic study of the reaction between hydrogen and magnesium, catalyzed by addition of indium", *J. Inorg. Nucl. Chem.*, **40**, (1978), 765-768.

[Mooij13] L. Mooij and B. Dam, "Hysteresis and the role of nucleation and growth in the hydrogenation of Mg nanolayers", *Phys. Chem. Chem. Phys.*, **15**, (2013), 2782-2792.

[Mooij14] L. Mooij, T. Perkisas, G. Pálsson, H. Schreuders, M. Wolff, B. Hjörvarsson, S. Bals, and B. Dam, "The effect of microstructure on the hydrogenation of Mg/Fe thin film multilayers", *Int. J. Hydrogen Energy*, **39**, (2014), 17092-17103.

[Mori06] T. Moriwaki, Y. Akahama and H. Kawamura, "Structural Phase Transition of Rutile-Type MgH2 at High Pressures", *J. Phys. Soc. Japan*, **75**, (2006), 074603.

[Muet87] T. Mütschele and R. Kirchheim, "Segregation and diffusion of hydrogen in grain boundaries of palladium", *Script. Metall.*, **21**, (1987), 135-140.

[Muet87^{+}] T. Mütschele and R. Kirchheim, "Hydrogen as a probe for the average thickness of a grain boundary", *Script. Metall.*, **21**, (1987), 1101-1104.

[Must14] N. Mustafa and M. Ismail, "Influence of K$_2$TiF$_6$ additive on the hydrogen sorption properties of MgH$_2$", *Int. J. Hydrogen Energy*, **39**, (2014), 15563-15569.

[Nagen99] D.G. Nagengast, A.T.M van Gogh, E.S. Kooij, B. Dam and R. Griessen, "Contrast

enhancement of rare-earth switchable mirrors through microscopic shutter effect", *Appl. Phys. Lett.*, **75**, (1999), 2050-2052.

[Natt97] H. Natter, B. Wettmann, B. Heisel and R. Hempelmann, "Hydrogen in nanocrystalline Palladium", *J. Alloy. Compd.*, **253-254**, (1997), 84-86.

[Naye85] A. Nayeb-Hashemi and J. Clark, "The Mg-Pd (magnesium-palladium) system", *J. Phase Equilibria*, **6**, (1985), 164-167.

[Neli75] G. Nelin and K. Sköld, "Diffusion of hydrogen in the β-phase of Pd-H studied by small energy transfer neutron scattering", *J. Phys. Chem. Solids*, **36**, (1975), 1175-1182.

[Niki08] E. Nikitin, Controlled delamination of metal films by hydrogen loading, Ph.D thesis, Universität Göttingen, (2008).

[Nish99] C. Nishimura, M. Komaki, M. Amano, "Hydrogen permeation through magnesium", *J. Alloy. Compd.*, **293-295**, (1999), 329.

[Nomu83] K. Nomura, E. Akiba, and S. Ono, "Development of a metal hydride compressor", *J. Less Common Met.*, **89**, (1983), 551-558.

[Nori11] T. Noritake, M. Aoki, M. Matsumoto, K. Miwa, S. Towata, H.-W. Li, and S. Orimo, "Crystal structure change in the dehydrogenation process of the Li-Mg-N-H system", *J. Alloy. Compd.*, **509**, (2011), 7553-7558.

[Nört06] K. Northemann, "*Wasserstoffabsorption in epitaktischen Niobschichten: eine STM-Studie*", Ph.D thesis, Universität Göttingen, (2006).

[Nört08] K. Northemann, A.Pundt, Phys. Rev. B 78 (2008) 014105.

[Nott00] P.H.L. Notten and J.R.G.Van Beek, "Nickel-metal hydride batteries: from concept to characteristics", *Hemijska industrija*, **54**, (2000), 102-115.

[Nott09] P.H.L. Notten and M. Latroche, "Secondary Batteries – Nickel Systems | Nickel–Metal Hydride: Metal Hydrides", pp.502-521 in Book: J. Garche (ed.), "*Encyclopedia of Electrochemical Power Sources*", (2009), Elsevier, Amsterdam, ISBN: 9780444527455.

[Nye85] J.F. Nye, "*Physical Properties of Crystals: Their Representation by Tensors and*

Matrices", (1985), Oxford University Press, USA, ISBN: 9780198511656.

[Oele00] W. Oelerich, T. Klassen, N. Eigen and R. Bormann, "Nanocrystalline Metal Hydrides for Hydrogen Storage", *Euromaterial*, **13**, (2000), 141.

[Oele01] W.Oelerich, T. Klassen, and R. Bormann, "Metal oxides as catalysts for improved hydrogen sorption in nanocrystalline Mg-based materials", *J. Alloy. Compd.*, **315**, (2001), 237-242.

[Özgi10] Ç. Özgit, H. Akyıldız, and T. Öztürk, "Isochronal hydrogenation of textured Mg/Pd thin films", *Thin Solid Films*, **518**, (2010), 4762-4767.

[Ohring91] M. Ohring, "*The Materials Science of Thin Films*", (1991), Academic Press, ISBN: 9780125249904.

[Okam01] H. Okamoto, "H-Mg (Hydrogen-Magnesium)", *J. Phase Equil.*, **22**, (2001), 598-599.

[Okam07] H. Okamoto, "Mg-Si (Magnesium-Silicon)", *J. Phase Equil. Diff.*, **28**(2), (2007), 229-230.

[Orga87] E. Orgaz and P. Dantzer, "Thermodynamics of the hydride chemical heat pump: III considerations for multistage operation", *J. Less Common Met.*, **131**(1-2), (1987), 385-398.

[Oria70] R. Oriani, "The diffusion and trapping of hydrogen in steel", *Acta Metallur.* **18**, (1970), 147-157.

[Orimo07] S. Orimo, Y. Nakamori, J.R. Eliseo, A. Züttel, and C.M. Jensen, "Complex hydrides for hydrogen storage", *Chem. Rev.*, **107**, (2007), 4111-4132.

[Osum99] Osumi *et al* (ed.), "*Hydrogen storage metal*", (1999), (written in Japanese)

[Pana13] "Launch of New 'Ene-Farm' Home Fuel Cell Product, More Affordable and Easier to Install", Press release by Tokyo Gas Co., Ltd. and Panasonic Corporation on 17.Jan.2013, URL: http://panasonic.co.jp/corp/news/official.data/data.dir/2013/01/en130117-5/en130117-5.html.

[Paik10] B. Paik, I. Jones, A. Walton, V. Mann, D. Book, and I. Harris, "$MgH_2 \rightarrow Mg$ phase transformation driven by a high-energy electron beam: An *in situ* transmission electron microscopy study", *Phil. Mag. Lett.*, **90**, (2010), 1-7.

[Paik12] B. Paik, A. Walton, V. Mann, D. Book, I.P. Jones, I.R. Harris, "Electron energy-loss spectroscopy study of MgH_2 in the plasmon energy range", *Appl. Phys. Lett.*, **100**, (2012), 193902.

[Pask10] M. Paskevicius, D.A. Sheppard, and C.E. Buckley, "Thermodynamic Changes in Mechanochemically Synthesized Magnesium Hydride Nanoparticles", *J. Am. Chem. Soc.*, **132**, (2010) , 5077-5083.

[Pasq11] L. Pasquini, F. Boscherini, E. Callini, C. Maurizio, L. Pasquali, M. Montecchi, and E. Bonetti, "Local structure at interfaces between hydride-forming metals: A case study of Mg-Pd nanoparticles by x-ray spectroscopy", *Phys. Rev. B*, **83**, (2011), 184111.

[Peder83] A.S. Pedersen, J. Kjøller, B. Larsen, and B. Vigeholm, "Magnesium for hydrogen storage", *Int. J. Hydrogen Energy*, **8**, (1983), 205-211.

[Pete64] P.G. Peterson, "Isotope Effect in Self-Diffusion in Palladium", *Phys. Rev. A*, **136**, (1964), 568.

[Petr09] O.A. Petrii, "Chemistry, Electrochemictry, and Electrochemical Applications | Hydrogen" , pp.751-761 in Book: J. Garche (ed.), "*Encyclopedia of Electrochemical Power Sources*", (2009), Elsevier, Amsterdam, ISBN: 9780444527455.

[Pivak09] Y. Pivak, R. Gremaud, K. Gross, M. Gonzalez-Silveira, A. Walton, D. Book, H. Schreuders, B. Dam, and R. Griessen, "Effect of the substrate on the thermodynamic properties of PdH_x films studied by hydrogenography", *Script. Mater.*, **60**(5), (2009), 348-351.

[Pivak11] Y. Pivak, H. Schreuders, M. Slaman, R. Griessen, B. Dam, "Thermodynamics, stress release and hysteresis behavior in highly adhesive Pd-H films", *Int. J. Hydrogen Energy*, **36**(6), (2011), 4056-4067.

[Pivak12] Y. Pivak, H. Schreuders, B. Dam, "Thermodynamic Properties, Hysteresis Behavior and Stress-Strain Analysis of MgH_2 Thin Films, Studied over a Wide Temperature Range", *Crystals*, **2**, (2012), 710-729.

[Pivak12^{+}] Y. Pivak, "Validation of Hydrogenography for the search of promising hydrogen storage materials", PhD thesis, Technische Universiteit Delft, Faculty of Applied Sciences, Department of Chemical Engineering, (2012).

[Pist14] C. Pistidda, D. Pottmaier, F. Karimi, S. Garroni, A. Rzeszutek, M. Tolkiehn, M. Fichtner, W. Lohstroh, M. Baricco, T. Klassen, and M. Dornheim, "Effect of NaH/MgB$_2$ ratio on the hydrogen absorption kinetics of the system NaH + MgB$_2$", *Int. J. Hydrogen Energy*, **39**, (2014), 5030-5036.

[Popov68] E.P. Popov, "*Introduction to mechanics of solids*", Prentice-Hall, Inc., Englewood Cliffs, New Jersey, U.S.A. (1968), pp.112 (Japanese ed.)

[Popov75] Z. Popovic and G. Piercy, "Measurement of the solubility of hydrogen in solid magnesium", *Metallurg. Mater. Trans. A*, **6**, (1975), 1915-1917.

[Pour73] M. Pourbaix, "*Lectures on Electrochemical Corrosion*"(Translated by J.A.S. Green, translation ed. by R.W. Staehle), (1973), Plenum Press, New York, ISBN: 9781468418088.

[Proo02] J. Proost and F. Spaepen, "Evolution of the growth stress, stiffness, and microstructure of alumina thin films during vapor deposition", *J. Appl. Phys.*, **91**, (2002), 204-216.

[Puga75] V.A. Pugachev, F.I. Busol, E.N. Nikolaeva and B.P. Nam, "Wasserstoffdurchlässigkeit und Wasserstoffdiffusion in Palladium-Silber-Legierungen", *Zh. Fiz. Khim.*, **49**, (1975), 1781-1785.

[Pundt99] A. Pundt, C. Sachs, M. Winter, M. Reetz, D. Fritsch, and R. Kirchheim, "Hydrogen sorption in elastically soft stabilized Pd-clusters", *J. Alloy. Compd.*, **293-295**, (1999), 480-483.

[Pundt04] A. Pundt, "Hydrogen in Nano-sized Metals", *Adv. Eng. Mater.*, **6**, (2004) , 11-21.

[Pundt06] A. Pundt and R. Kirchheim, "Hydrogen in Metals: Microstructural Aspects", *Annu. Rev. Mater. Res.*, **36**, (2006), 555-608.

[Pred96] B. Predel, "*Phase diagram of Mg-H binary system*", *Landolt-Börnstein - Group IV Physical Chemistry*, (1996).

[Qu10] J. Qu, B. Sun, R. Yang, W. Zhao, Y. Wang, and X. Li, "Hydrogen absorption kinetics of Mg thin films under mild conditions", *Script. Mater.*, **62**, (2010), 317-320.

[Rabi93] A. Rabinkin, "*Selection Criteria for Brazing and Soldering Consumables*", Chapter in: K. Ferjutz and J.R. Davis (*ed.*),"*ASM Handbook Vol. 6: Welding, Brazing, and Soldering*", (1993), ASM International, ISBN: 9780871703828.

[Ravi04] P.S. Ravindran, P. Vajeeston, H. Fjellvåg, and A. Kjekshus, "Chemical-bonding and high-pressure studies on hydrogen-storage materials", *Computat. Mater. Sci.*, **30**, (2004), 349-357.

[Rudm79] P.S. Rudman, "Hydrogen-diffusion-rate-limited hydriding and dehydriding kinetics", *J. Appl. Phys.*, **50**, (1979), 7195-7199.

[Rudm80] P. Rudman, "Comment on hydrogen dissolution in magnesium", *Script. Metallur.*, **14**, (1980), 1365-1366.

[Sabi10] S.Sabitu, G. Gallo and A. Goudy, "Effect of TiH_2 and Mg_2Ni additives on the hydrogen storage properties of magnesium hydride", *J. Alloy. Compd.*, **499**, (2010), 35-38.

[Sing10] R.K. Singh, H. Raghubanshi, S.K. Pandey and O. Srivastava, "Effect of admixing different carbon structural variants on the decomposition and hydrogen sorption kinetics of magnesium hydride", *Int. J. Hydrogen Energy*, **35**, (2010), 4131-4137.

[Sue94] J.A. Sue and G.S. Schajer, "*Stress Determination for Coatings*", Article in Chapter "*Film Thickness Measurements Using Optical Techniques*" in: F.Reidenbach (Ed.) "*ASM Handbook Vol. 5: Surface Engineering*", (1994), ASM International, ISBN: 9780871703842.

[Sule09] M. Suleiman, C. Borchers, N.J.M. Guerdane, D. Fritsch, R. Kirchheim, and A. Pundt, "Size and Structure of Palladium Clusters Determined by XRD and HREM", *Z. Phys. Chem.*, **223**, 169-181.

[Reil67] J.J. Reilly and R.H. Wiswall, "The Reaction of Hydrogen with Alloys of Magnesium and Copper", *Inorg. Chem.*, **6**, (1967), 2220.

[Reil68] J.J. Reilly and R.H. Wiswall, "Reaction of hydrogen with alloys of magnesium and nickel and the formation of Mg_2NiH_4", *Inorg. Chem.*, **7**, (1968), 2254-2256.

[Ren14] C. Ren, Z.Z. Fang, C. Zhou, J. Lu, Y. Ren, and X. Zhang, "Hydrogen Storage Properties of Magnesium Hydride with V-Based Additives", *J. Phys. Chem. C*, **118**, (2014), 21778-21784.

[REN15] Renewable energy policy network for the 21st century (REN21), "*RENEWABLES 2015 GLOBAL STATUS REPORT*", United Nations Environment Programme (UNEP), published on 18. Jun. 2015.

[Renn78] J. Renner and H.J. Grabke, "Bestimmung von Diffusionskoeffizienten bei der Hydrierung von Legierungen", *Z. Metallkd.*, **69**, (1978), 639.

[Riba73] Y. de Ribaupierre and F.D. Manchester, "Isotope dependence for hydrogen diffusion in palladium at low temperatures", *J. Phys. C*, **6**, (1973), L390.

[Rieg93] P. Rieger, "*Electrochemistry - Second Edition*", (1993), Springer Verlag, p.32.

[Ron84] M. Ron, "A hydrogen heat pump as a bus air conditioner", *J. Less Common Met.*, **104**, (1984), 259-278.

[Rönn03] E. Rönnebro, N. Kitamura, and T. Sakai, "The gigapascal pressure thermal technique for synthesising new ternary metal hydrides in the A-Pd-H (A=Li, Na or Mg) system", *J. Alloy. Compd.*, **358**, (2003), 216-222.

[ROS1] Website of Rossendorf Beamline (ROBL), "*ESRF Helmholtz-Zentrum Dresden-Rossendorf, HZDR*", URL: http://www.hzdr.de/db/Cms?pNid=247

[Rous10] S. Rousselot, D, Guay, and L. Rou, "Comparative study on the structure and electrochemical hydriding properties of MgTi; $Mg_{0.5}Ni_{0.5}Ti$ and $MgTi_{0.5}Ni_{0.5}$ alloys prepared by high energy ball milling", *J. Power Sources*, **196**, (2010), 1561-1568.

[Ryde89] J. Rydén, B. Hjörvarsson, T. Ericsson, E. Karlsson, A. Krozer and B. Kasemo, "Unusual kinetics of hydride formation in Mg-Pd sandwiches, studied by hydrogen profiling and quartz crystal microbalance measurements", *J. Less Common Met.*, **152**, (1989), 295-309.

[Saita06] I. Saita, T. Toshima, S. Tanda, T. Akiyama, "Hydriding Chemical Vapor Deposition of Metal Hydride Nano-Fibers", *Mater. Trans.*, **47**, (2006), 931-934.

[Sach01] C. Sachs, A. Pundt, R. Kirchheim, M. Winter, and M.T. Reetz, "Solubility of hydrogen in single-sized palladium clusters", *Phys. Rev. B*, **64**, (2001), 75408.

[Saka81] Y. Sakamoto and N. Tabaru, "Diffusivity and Solubility of Hydrogen in Annealed and Cold Rolled Specimens of Palladium (焼鈍および冷間圧延した Pd 中の水素の拡散および溶解)", *J. Jpn. Inst. Met. Mater.*, **45**, (1981), 1048-1055.

[Saka82] Y. Sakamoto, M. Kawachi, and S. Hirata, "An Investigation on the Hydrogen Permeation Through α/β Phase Palladium by the Electrochemical Method (電気化学的透過法に

よる α / β Pd 相中の水素透過に関する研究)", *J. Jpn. Inst. Met.*, **46**, (1982), 530-537.

[Sams73] G.V. Samsonov, *Dokl. Akad. Nauk SSSR*, **208**, (1973), 621-623.

[Sche18] P. Scherrer, "Bestimmung der Grösse und der inneren Struktur von Kolloidteilchen mittels Röntgenstrahlen", *Nachr. Ges. Wiss. Göttingen*, 26. September, (1918), p.98-100.

[Schob81] T. Schober, "The magnesium-hydrogen system: Transmission electron microscopy", *Metallurg. Trans. A*, **12**, (1981), 951-957.

[Schw06] R.B. Schwarz and A.G. Khachaturyan, "Thermodynamics of open two-phase systems with coherent interfaces: Application to metal-hydrogen systems", *Acta Mat.* **54**, (2006), 313-323.

[Seki75] K. Sekine, "Frequency response method for determination of diffusion coefficient of hydrogen in metal (金属中の水素の拡散係数を測定するための周波数応答法)", *Chem.Lett. Jpn.*, **8**, (1975), 841-846.

[Semenk78] K.N. Semenko, V.N. Verbestkii, Yu. A. Kalashnikov, N.V. Timofeeva, M.I. Ioffe, *Vestn. Mosk. Univ. Khim.*, **19**, (1978), 718.

[Sanma87] A. San-Martin and F. Manchester, "*The H-Mg (Hydrogen-Magnesium) System*", *Bulletin of Alloy Phase Diagrams*, **8**, (1987), 431-437.

[Schim05] H.G. Schimmel, J. Huot, L.C. Chapon, F.D. Tichelaar, and F.M. Mulder, "Hydrogen Cycling of Niobium and Vanadium Catalyzed Nanostructured Magnesium", *J. Am. Chem. Soc.*, **127**, (2005), 14348-14354.

[Schl01] L. Schlapbach and A. Züttel, "Hydrogen-storage materials for mobile applications", *Nature*, **414**, (2001), 353-358.

[Schm98] G. Schmitz, P. Kesten, R. Kirchheim, and Q.M. Yang, "Diffusion of hydrogen through metallic multilayers", *Phys. Rev. B*, **58**, (1998), 7333-7339.

[Schw06] R. Schwarz and A. Khachaturyan, "Thermodynamics of open two-phase systems with coherent interfaces: Application to metal-hydrogen systems", *Acta Mater.* **54**, (2006), 313-323.

[Shao04] H. Shao, Y. Wang, H. Xu and X. Li, "Hydrogen storage properties of magnesium ultrafine particles prepared by hydrogen plasma-metal reaction", *Mater. Sci. Eng. B*, **110**, (2004),

221-226.

[Shap81] V.I. Shapovalov, N.P. Serdyuk and O.P. Semik, *Dop. Akad. Nauk. Ukr. RSR Ser.A, Fiz-Mat. Tekh. Nauki.*, **6**, (1981), 99-101.

[Shep11] D.A. Sheppard, M. Paskevicius, and C.E. Buckley, "Hydrogen Desorption from the NaNH$_2$−MgH$_2$ System", *J. Phys. Chem. C*, **115**, (2011), 8407-8413.

[Shew56] P.G. Shewmon, "Self-diffusion in magnesium single crystals", *Trans. Am. Inst. Min. Metall. Pet. Eng.* (*Trans. Metall. Soc. AIME*), **206**, (1956), 918-922.

[Simo65] J.W. Simons and T.B. Flanagan, "Diffusion of Hydrogen in the α-Phase of the Palladium-Hydrogen System", *J. Phys. Chem.*, **69**, (1965), 3581-3587.

[Siev29] A. Sieverts, "Die Aufnahme von Gasen durch Metalle", *Z. Metall.*, **21**, (1929), 37-46.

[Siev35] A. Sieverts and G. Zapf, "Die Lösichkeit von Deutrium und von Wasserstoff in festem Palladium", *Z. Phys. Chem.*, **174A**, (1935), 359.

[Sime80] C.J. Simensen, " Gas-chromatographic determination of hydrogen in magnesium by means of the capsule method Fresenius", *J. Anal. Chem*., **302**, (1980), 398-401.

[Sköl67] K. Sköld and G. Nelin, "Diffusion of hydrogen in the α-phase of Pd-H studied by small energy transfer neutron scattering", *J. Phys. Chem. Solids*, **28**, (1967), 2369-2380.

[Skri04] V. Skripnyuk, E. Rabkin, Y. Estrin, and R. Lapovok, "The effect of ball milling and equal channel angular pressing on the hydrogen absorption/desorption properties of Mg-4.95 wt% Zn-0.71 wt% Zr (ZK60) alloy", *Acta Mater.*, **52**, (2004), 405-414.

[Slau02] W.S. Slaughter, "*The Linearized Theory of Elasticity*", (2001), Birkhäuser, ISBN: 0817641173.

[Song11] G. Song (ed.), "*Corrosion of Magnesium Alloys (Woodhead Publishing Series in Metals and Surface Engineering)*", (2011), Woodhead Publishing, ISBN:9781845697082.

[Spatz93] P. Spatz, H.A. Aebischera, A. Krozer, and L. Schlapbach, "The Diffusion of H in Mg and the Nucleation and Growth of MgH$_2$ in Thin Films", *Z. Phys. Chem.*, **181**, (1993), 393-397.

[Stac64] M.v. Stackelberg and P. Ludwig, "Zum Diffusionsverhalten des Wasserstoffs im Palladium-Wasserstoff", *Z. Naturforsch. A*, **19,** (1964), 93.

[Stamp60] J.F. Stampfer Jr, C.E. Holley Jr and J.F. Suttle, "The Magnesium-Hydrogen system", *J. Am. Chem. Soc.*, **82**, (1960), 3504-3508.

[Stan77] C.M. Stander, "Kinetics of Formation of Magnesium Hydride from Magnesium and Hydrogen", *Z. Phys. Chem. N. F.*, **104**, (1977), 229.

[Stan78] C.M. Stander and R.A. Pacey, "The Lattice Energy of Magnesium Hydride", *J. Phys. Chem. Solids*, **39**, (1978), 829-832.

[Stei94] J. Steiger, S. Blässer, and A. Weidinger, "Solubility of hydrogen in thin niobium films", *Phys. Rev. B*, **49**, (1994), 5570-5574.

[Stio84] M. Stioui, A. Grayevsky, A. Moran, S. Kreitzman, N. Kaplan and D. Shaltiel, "Proton magnetic resonance study of diffusion-related properties in magnesium-rich compounds", *J. Less Common Met.*, **104**, (1984), 119-124.

[Ston09] G.G. Stoney, "The Tension of Metallic Films Deposited by Electrolysis", *Proc. Roy. Soc. London* **82**, (1909), 172-175.

[Stok48] A.R. Stokes, "A Numerical Fourier-analysis Method for the Correction of Widths and Shapes of Lines on X-ray Powder Photographs", *Proc. Phys. Soc.*, **61**, (1948), 382.

[Taka07] T. Takasaki, D. Kyoi, N. Kitamura, S. Tanase, T. Sakai, "Reversible Hydrogen Storage Property and Structural Analysis for Face-Centered Cubic Hydride $Mg_{0.82}Zr_{0.18}H_2$ Prepared by Gigapascal Hydrogen Pressure Method", *J. Phys. Chem. B*, **111**, (2007), 14102-14106.

[Tal-G10] E. Tal-Gutelmacher, R. Gemma, A. Pundt and R. Kirchheim, "Hydrogen behavior in nanocrystalline titanium thin films", *Acta Mat.*, **58**, (2010) 3042-3049.

[Tan11] Z. Tan, C. Chiu, E.J. Heilweil, and L.A. Bendersky, "Thermodynamics, kinetics and microstructural evolution during hydrogenation of iron-doped magnesium thin films", *Int. J. Hydrogen Energy*, **36**, (2011), 9702-9713.

[Tang12] J.-J. Tang, X.-B. Yang, M. Chen, M. Zhu and Y.-J. Zhao, "First-Principles Study of Biaxial Strain Effect on Hydrogen Adsorbed Mg (0001) Surface", *J. Phys. Chem. C*, **116**, (2012),

14943-14949.

[Tanguy76] B. Tanguy, J.-L. Soubeyroux, M. Pezat, J. Portier, and P. Hagenmuller, "Amelioration des conditions de synthese de l'hydrure de magnesium a l'aide d'adjuvants", *Mater. Resear. Bullet.* , **11**, (1976), 1441-1447.

[Thok95] R. Thokala, J. Chaudhuri, "Calculated elastic constants of wide band gap semiconductor thin films with a hexagonal crystal structure for stress problems", *Thin Solid Films*, **266**, (1995) , 189-191.

[Toep82] J. Töpler, H. Buchner, H. Säufferer, K. Knorr and W. Prandl, "Measurements of the diffusion of hydrogen atoms in magnesium and Mg_2Ni by neutron scattering", *J. Less Common Met.*, **88**, (1982), 397-404.

[Toda58] G. Toda, "Rate of permeation and diffusion coefficient of hydrogen through palladium", *J. Res. Inst. Catalysis HokkaidoUniv.*, **6**, (1958), 13-19.

[Trom11] D. Tromans, "Elastic anisotropy of HCP metal crystals and polycrystals", *IJRRAS* **6**(4), (2011), 462-483.

[Turo02] N.Y. Turova, E.P. Turevskaya, G.K. Vadim, and M.I. Yanovskaya (*ed.*), "*The Chemistry of Metal Alkoxides*", Springer, (2002), ISBN: 9780792375210.

[Uchi04] H. Uchida, "*A Metal Hydride (MH) Refrigerator using Hydrogen Storage Alloys*", *Refrigeration* (*REITOU*)*, **79**, (2004), 837-840. (published by the Japan Society of Refrigerating and Air Conditioning Engineers.)

[Uchi11] H.T. Uchida, R. Kirchheim, and A. Pundt, "Influence of hydrogen loading conditions on the blocking effect of nanocrystalline Mg films", *Script. Mater.*, **64**, (2011), 935-937.

[Uchi15] H.T. Uchida, S. Wagner, M. Hamm, J. Kürschner, R. Kirchheim, B. Hjörvarsson, and A. Pundt, "Absorption kinetics and hydride formation in magnesium films: Effect of driving force revisited", *Acta Mater.*, **85**, (2015), 279-289.

[UNEP14] UNEP (United Nations Environment Programme), "Global trends in renewable energy investment 2014", Frankfurt School of Finance & Management GmbH, (pub. on 7. Apr. 2014), p.30.

[Vaje02] P. Vajeeston, P. Ravindran, A. Kjekshus and H. Fjellvåg, "Pressure-Induced Structural Transitions in MgH$_2$", *Phys. Rev. Lett.*, **89**, (2002), 175506.

[Vaje06] P. Vajeeston, P. Ravindran, B.C. Hauback, H. Fjellvåg, A. Kjekshus, S. Furuseth and M. Hanfland, "Structural stability and pressure-induced phase transitions in MgH$_2$", *Phys. Rev.* B, **73**, (2006), 224102.

[Vaje08] P. Vajeeston, P. Ravindran, and H. Fjellvåg, "Theoretical investigations on low energy surfaces and nanowires of MgH$_2$", *Nanotechnology*, **19**, (2008), 275704.

[Vaje12] P. Vajeeston, S. Sartori, P. Ravindran, K.D. Knudsen, B. Hauback, and H. Fjellvåg, "MgH$_2$ in Carbon Scaffolds: A Combined Experimental and Theoretical Investigation", *J. Phys. Chem. C*, **116**, (2012), 21139-21147.

[Vajo04] J.J. Vajo, F. Mertens, C.C. Ahn, R. Bowman, C. Robert and B. Fultz, "Altering Hydrogen Storage Properties by Hydride Destabilization through Alloy Formation: LiH and MgH$_2$ Destabilized with Si", *J. Phys. Chem. B*, **108**, (2004), 13977-13983.

[Vari06] R. Varin, T. Czujko and Z. Wronski, "Particle size, grain size and γ-MgH$_2$ effects on the desorption properties of nanocrystalline commercial magnesium hydride processed by controlled mechanical milling", *Nanotechnology*, **17**, (2006), 3856.

[Vars70] Y.P. Varshni, "Temperature Dependence of the Elastic Constants", *Phys. Rev. B*, **2**, (1970), 3952-3958.

[Verh75] J.D. Verhoeven, "*Fundamentals of Physical Metallurgy*", Wiley VCH, (1975), ISBN 9780471906162.

[Verm06] P. Vermeulen, R. Niessen, P. Notten, "Hydrogen storage in metastable Mg$_y$Ti$_{(1-y)}$ thin films", *Electrochem. Comm.* **8**, (2006), 27-32.

[Verm06^{+}] P. Vermeulen, E.F.M.J. van Thiel, and P.H.L. Notten, "Ternary MgTiX-Alloys: A Promising Route towards Low-Temperature, High-Capacity, Hydrogen-Storage Materials", *Chemistry - A European Journal*, **13**, (2007), 9892-9898.

[Verm07] P. Vermeulen, E.F.M.J. van Thiel and P.H.L. Notten, "Ternary MgTiX-Alloys: A Promising Route towards Low-Temperature, High-Capacity, Hydrogen-Storage Materials", *Chemistry - A European Journal*, **13**, (2007), 9892-9898.

[Vesb12] P. C. K. Vesborg and T. F. Jaramillo, "Addressing the terawatt challenge: scalability in the supply of chemical elements for renewable energy", *RSC Adv.* **2**, (2012), 7933-7947.

[Vige83] B. Vigeholm, J. Kjoller, B. Larsen, and A.S. Pedersen, "Formation and Decomposition of Magnesium Hydride", *J. Less Common Met.*, **89**, (1983), 135-144.

[Vige84] B. Vigeholm, J. Koller, B. Larsen, and A.S. Pedersen, "On the Hydrogenation Mechanism in Magnesium II", in Book: "*Hydrogen Energy Progress V*", Proc. 5th World Hydrogen Energy Conf., Toronto, Canada, 15.-20. July 1984, T.N. Veziroglu and J.B. Taylor (*Ed.*), Pergamon Press, Vol. 3, 1455-1463 (1984), ISBN: 9780080309538.

[Vige87] B. Vigeholm, K. Jensen, B. Larsen, and A. Pedersen, "Elements of hydride formation mechanisms in nearly spherical magnesium powder particles", *J. Less Common Met.*, **131**, (1987), 133-141.

[Vill98] P. Villars (*ed.*), "*Pearson's handbook desk edition: Crystallographic Data for Intermetallic Phases* ", vol. 2, ASM International, (1998).

[Völk71] J. Völkl, G. Wollenweber, K.H. Klatt and G. Alefeld, "Reversed isotope dependence for Hydrogen diffusion in Palladium.", *Z. Naturforsch.*, **26A**, (1971), 922-923.

[Völk78] J. Völkl and G. Alefeld, p.321 in ref. [HinMeI], Topics in: G. Alefeld and J. Völkl, "Hydrogen in metals I - Basic properties", *Appl. Phys.*, **28**, (1978), 321.

[Vught70] J.H.N. van Vught, F.A. Kuijpers, and H.C.A.M. Bruning, *Philips Res. Reports*, **25**, (1970), 133-140.

[Wage05] R.W.P. Wagemans, J.H. van Lenthe, P.E. de Jongh, A.J. van Dillen, and K.P. de Jong, "Hydrogen storage in magnesium clusters: quantum chemical study.", *J. Am. Chem. Soc.*, **127**, (2005), 16675-16680.

[Wagn84] F.E. Wagner, W. Pröbst, R. Wordel, M. Zelger, and F. Litterst, "^{57}Fe Mössbauer study of hydrogen diffusion in the hydrides and deuterides of vanadium, niobium and palladium", *J. Less Common Metals*, **103**, (1984), 135-144.

[Wagn08] S. Wagner and A. Pundt, "Mechanical stress impact on thin $Pd_{1-x}Fe_x$ film thermodynamic properties", *Appl. Phys. Lett.*, **92**, (2008), 051914-051918.

[Wagn10] S. Wagner and A. Pundt, "Electrical resistivity and hydrogen solubility of PdHc thin films", *Acta Mater.*, **58**, (2010), 1387-1394.

[Wagn11] S. Wagner and A. Pundt, "Combined impact of microstructure and mechanical stress on the electrical resistivity of PdH$_c$ thin films", *Acta Mater.*, **59**, (2011), 1862-1870.

[Wagn11^{+}] S. Wagner, H.Uchida, V. Burlaka, M. Vlach, M. Vlček, F. Lukáč, J. Čížek, C. Baehtz, A. Bell, and A. Pundt, "Achieving coherent phase transition in palladium-hydrogen thin films", *Script. Mater.*, **64**, (2011), 978-981.

[Wagn15] S. Wagner , A. Pundt, "Hydride formation in palladium-hydrogen thin films: Combined impact of elastic and microstructural constraints in structural phase transitions, H-H-interaction and critical temperature", (manuscript submitted in *Int. J. Hydrogen Energy*) (2015).

[Wan13] Q.Wan, P. Li, Z. Li, F. Zhai, X. Qu and A.A.Volinsky, "Improved Hydrogen Storage Performance of MgH$_2$–LiAlH$_4$ Composite by Addition of MnFe$_2$O$_4$", *J. Phys. Chem. C*, **117**, (2013), 26940-26947.

[Wann01] C. Wannek and B. Harbrecht, "Structure and Thermal Stability of the New Intermetallics MgPd$_2$, MgPd$_3$, and Mg$_3$Pd$_5$ and the Kinetics of the Iodine-Catalyzed Formation of MgPd$_2$", *J. Solid State Chem.*, **159**, (2001), 113-120.

[Wata75] T. Watanabe, Y.C. Huang and R. Komatsu, "Solubility of Hydrogen in Magnesium (マグネシウム中の水素溶解度)", *J. Jpn. Inst. Light Met.*, **26**, (1975), 76-81 (in Japanese).

[Wester08] R.J. Westerwaal, C.P. Broedersz, R. Gremaud, M. Slaman, A. Borgschulte, W. Lohstroh, K.G. Tschersich, H.P. Fleischhauer, B. Dam and R. Griessen, "Study of the hydride forming process of *in-situ* grown MgH$_2$ thin films by activated reactive evaporation", *Thin Solid Films*, **516**, (2008), 4351-4359.

[Westl83] D.G. Westlake, "A geometric model for the stoichiometry and interstitial site occupancy in hydrides (deuterides) of LaNi$_5$, LaNi$_4$Al and LaNi$_4$Mn", *J. Less Common Met.*, **91**, (1983). 275-292.

[Westl83b] D.G. Westlake, "Hydrides of intermetallic compounds: A review of stabilities, stoichiometries and preferred hydrogen sites", *J. Less Common Met.*, **91**, (1983). 1-20.

[Wibe52] E. Wiberg and R. Baner, "Der Magnesiumwasserstoff MgH$_2$", *Z. Naturforschung.* B, **6**, (1952), 394-395.

[Wick64] E. Wicke and G.H. Nernst, "Zustandsdiagramm und thermodynamisches Verhalten der Systeme Pd/H$_2$ und Pd/D$_2$ bei normalen Temperaturen; H/D-Trenneffekte (Phase diagram and thermodynamic behavior of the system Pd/H$_2$ and Pd/D$_2$ at normal temperatures; H/D separations effects)", *Ber. Bunsenges. Phys. Chem.* **68**, (1964), 224-235.

[Wick64$^+$] E. Wicke and G. Bohmholdt, "Zur Diffusion von Wasserstoff in Pd-und Pd/Ag-Hydriden hohen Wasserstoff-Gehaltes", *Z. Phys. Chem. N*F., **42**, (1964), 115.

[Wint09] C.-J. Winter, "Hydrogen energy — Abundant, efficient, clean: A debate over the energy-system-of-change", *Int. J. Hydrogen Energy*, **34**, (2009), S1-S52.

[Wrie87] H. Wriedt, "The Mg−O (Magnesium-Oxygen) system", *Bullet. Alloy Phase Diagrams*, **8**, (1987), 227-233.

[Wu09] G. Wu, J. Zhang, Y. Wu, Q. Li, K. Chou, and X. Bao, "Adsorption and dissociation of hydrogen on MgO surface: A first-principles study", *J. Alloy. Compd.*, **480**, (2009), 788-793.

[Wu14] D.H. Wu, H.C. Wang, L.T. Wei, R.K. Pan and B.Y. Tang, "First-principles study of structural stability and elastic properties of MgPd$_3$ and its hydride", *J. Mag. Alloys*, **2**, (2014), 165-174.

[Yama02] K. Yamamoto, K. Higuchi, H. Kajioka, H. Sumida, S. Orimo, and H. Fujii, "Optical transmission of magnesium hydride thin film with characteristic nanostructure", *J. Alloy. Compd.*, **330-332**, (2002), 352-356.

[Yama08] M. Yamauchi, R. Ikeda, H. Kitagawa and M. Takata, "Nanosize Effects on Hydrogen Storage in Palladium", *J. Phys. Chem. C*, **112**, (2008), 3294-3299.

[Yama09] M. Yamauchi, H. Kobayashi, and H. Kitagawa, "Hydrogen Storage Mediated by Pd and Pt Nanoparticles", *ChemPhysChem*, **10**, (2009), 2566-2576.

[Yang91] K. Yang and M. Cao, "Hydrogen trapping in metals under local equilibrium assumption", *Scripta Metallur. Mater.*, **25**, (1991), 2139-2142.

[Yang96] Q. M. Yang, G. Schmitz, S. Fähler, H.U. Krebs, R. Kirchheim, "Hydrogen in Pd/Nb

multilayers", *Phys. Rev. B*., **54**, (1996), 9131-9140.

[Yang11] B. Yang, Y.-P. He, and Y.-P. Zhao, "Hydrogenation of magnesium nanoblades: The effect of concentration dependent hydrogen diffusion", *Appl. Phys. Lett.*, **98**, (2011), 081905.

[Yang11^{+}] B. Yang, Y. He, and Y.Zhao, "Concentration-dependent hydrogen diffusion in hydrogenation and dehydrogenation of vanadium-coated magnesium nanoblades", *Int. J. Hydrogen Energy*, **36**, (2011), 15642-15651.

[Yao08] X. Yao, Z.H. Zhu, H.M. Cheng, G.Q. Lu, "Hydrogen diffusion and effect of grain size on hydrogenation kinetics in magnesium hydrides", *J. Mater. Resear.*, **23**, (2008), 336-340.

[Ye06] S. Ye, L. Ouyang, and M. Zhu, "Hydrogen storage properties of preferentially orientated Mg-Ni multilayer film prepared by magnetron sputtering", *Rare Metals*, **25**, (2006), 295-299.

[Yosh04] K. Yoshimura, Y. Yamada, and M. Okada, "Hydrogenation of Pd capped Mg thin films at room temperature", *Surf. Sci.* , **20**, (2004), 751-754.

[Yu88] R. Yu and P.K. Lam, "Electronic and structural properties of MgH_2", *Phys. Rev. B*, **37**, (1988), 8730-8737.

[Yu09] X.B. Yu, Y.H. Guo, H.Yang, Z. Wu, D.M. Grant and G.S. Walker, "Improved Hydrogen Storage in Magnesium Hydride Catalyzed by Nanosized $Ti_{0.4}Cr_{0.15}Mn_{0.15}V_{0.3}$ Alloy", *J. Phys. Chem. C*, **113**, (2009), 5324-5328.

[Zach63] W.H. Zachariasen, C.E Holley Jr. and J.F. Stamper Jr, "Neutron diffraction study of magnesium deuteride", *Acta Cryst.*, **16**, (1963), 352.

[Zars13] M. Zarshenas, R. Ahmed, M.B. Kanoun, B. ul Haq, A.R.M. Isa, and S. Goumri-Said, "First principle investigations of the physical properties of hydrogen-rich MgH_2", *Phys. Script.*, **88**, (2013), 065704.

[Zeng99] K. Zeng, T. Zeng, W. Oelerich and R. Bormann, "Critical assessment and thermodynamic modeling of the Mg-H system", *Int. J. Hydrogen Energy*, **24**, (1999), 989-1004.

[Zhan99] W. Zhang, S. Luo, and T.B. Flanagan, "Hydrogen solution in homogeneous Pd-Fe alloys", *J. Alloy. Compd.*, **20**, (1999), 1-6.

[Zhan11] J. Zhang, F. Cuevas, W. Zaï di, J.-P. Bonnet, L. Aymard, J.-L. Bobet and M. Latroche, "Highlighting of a Single Reaction Path during Reactive Ball Milling of Mg and TM by Quantitative H_2 Gas Sorption Analysis To Form Ternary Complex Hydrides (TM = Fe, Co, Ni)", *J. Phys. Chem. C*, **115**, (2011), 4971-4979.

[Zhan13] J. Zhang, Y.C. Zhou, Z.S. Ma, L.Q. Sun and P. Peng, "Strain effect on structural and dehydrogenation properties of MgH_2 hydride from first-principles calculations", *Int. J. Hydrogen Energy*, **38**, (2013), 3661-3669.

[Zhda93] V.P. Zhdanov, A. Krozer, B. Kasemo, "Kinetics of first-order phase transitions initiated by diffusion of particles from the surface into the bulk", *Phys. Rev. B*, **47**, (1993), 11044-11048.

[Zhu11] C. Zhu, N. Sakaguchi, S. Hosokai, S. Watanabe, and T. Akiyama, "*In situ* transmission electron microscopy observation of the decomposition of MgH_2 nanofiber", *Int. J. Hydrogen Energy*, **36**, (2011), 3600-3605.

[Zhon14] H. Zhong, H. Wang, and L. Ouyang, "Improving the hydrogen storage properties of MgH_2 by reversibly forming Mg-Al solid solution alloys", *Int. J. Hydrogen Energy*, **39**, (2014), 3320-3326.

[Zhou13] C. Zhou, Z.Z. Fang, J. Lu, and X. Zhang, "Thermodynamic and kinetic destabilization of magnesium hydride using Mg-In solid solution alloys.", *J. Am. Chem. Soc.*, **135**, (2013), 10982-10985.

[Zhou13+] C. Zhou, Z.Z. Fang, C. Ren, J. Li and J. Lu, "Effect of Ti Intermetallic Catalysts on Hydrogen Storage Properties of Magnesium Hydride", *J. Phys. Chem. C*, **117**, (2013), 12973-12980.

[Zhou14] C. Zhou, Z.Z. Fang, J. Lu, X. Luo, C. Ren, P. Fan, Y. Ren, and X. Zhang, "Thermodynamic Destabilization of Magnesium Hydride Using Mg-Based Solid Solution Alloys", *J. Phys. Chem. C*, **118**, (2014), 11526-11535.

[Züch70] H. Züchner, "Untersuchung der Diffusion von Wasserstoff in Pd-und Pd/Ag-Legierungen mit einer Stromstoß-Methode", *Z. Naturforsch.*, **25A**, (1970), 1490.

[Züch84] H. Züchner, H.G. Schöneich, " Improvement of electrochemical methods for studying the diffusion and solubility of hydrogen in metals.", *J. Less Common Met.*, **101**, (1984), 363-372.

[Zütt00] A. Züttel, C. Nützenadel, G. Schmid, C. Emmenegger, P. Sudan, and L. Schlapbach, "Thermodynamic aspects of the interaction of hydrogen with Pd clusters", *Appl. Surf. Sci.* , **162-163**, (2000), 571-575.

[Zütt03] A. Züttel, "Materials for hydrogen storage", *Materials Today* **6**, (2003), 24-33

[Zütt04] A. Züttel, "Hydrogen storage methods", *Naturwiss.*, **91**, (2004), 157-172.

List of publications

[1] H.T. Uchida, R. Kirchheim, and A. Pundt, "Influence of hydrogen loading conditions on the blocking effect of nanocrystalline Mg films", *Script. Mater.*, **64**, (2011), 935-937.

[2] S. Wagner, H. Uchida, V. Burlaka, M. Vlach, M. Vlček, F. Lukáč, J. Čížek, C. Baehtz, A. Bell, and A. Pundt, "Achieving coherent phase transition in palladium-hydrogen thin films", *Script. Mater.*, **64**, (2011), 978-981.

[3] J. Čížek, M. Vlček, F. Lukáč; M. Vlach, I. Procházka, G. Brauer, W. Anwand, A. Mücklich, S. Wagner, H. Uchida, and A. Pundt, A., "Structural studies of nanocrystalline thin Pd films electrochemically doped with hydrogen", Defect and Diffusion Forum, 331, (2012), 137-147.

[4] J. Čížek, F. Lukáč, M. Vlček, M. Vlach, I. Procházka, F. Traeger, D. Rogalla, H.W. Becker, W. Anwand, G. Brauer, S. Wagner, H. Uchida, C. Bähtz, and A. Pundt, "Anisotropy of Hydrogen Diffusivity in ZnO", Defect and Diffusion Forum, 333, (2013), 39-49.

[5] J. Čížek, O. Melikhova, M. Vlček, F. Lukáč, M. Vlach, I. Procházka, W. Anwand, G. Brauer, A. Mücklich, S. Wagner, H. Uchida, A. Pundt, "Hydrogen-induced microstructural changes of Pd films", *Int. J. Hydrogen Energy*, **38**, (2013), 12115-12125.

[6] F. Lukáč, J. Čížek, M. Vlček, I. Procházka, M. Vlach, W. Anwand, G. Brauer, F. Traeger, D. Rogalla, H.W. Becker, S. Wagner, H. Uchida and C. Bähtz, Materials Science Forum, 733, (2013), 228-231.

[7] J. Čížek, O. Melikhova, M. Vlček, F. Lukáč, M. Vlach, P. Dobron, I. Procházka, W. Anwand, G. Brauer, S. Wagner, H. Uchida, R.Gemma, and A. Pundt, "Hydrogen Interaction with Defects in Nanocrystalline, Polycrystalline and Epitaxial Pd Films", *J. Alloy. Compd.*, (2014) (*in Press*).

[8] F. Lukáč, M. Vlček, M. Vlach, S. Wagner, H. Uchida, A. Pundt, A. Bell, and J. Čížek, "Stress release during cyclic loading of 20nm palladium films", *J. Alloy. Compd.*, (2014) (*in Press*).

[9] M. Vlček, F. Lukáč, M. Vlach, S. Wagner, H. Uchida, C. Baehtz, A. Shalimov, A. Pundt, and J. Čížek, "Influence of microstructure and mechanical stress on behavior of hydrogen in 500nm Pd films", *J. Alloy. Compd.*, (2014) (*in Press*).

[10] P. Hruška, J. Čížek, P. Dobroň, W. Anwand, A. Mücklich, R. Gemma, S. Wagner, H. Uchida, and A. Pundt, "Investigation of nanocrystalline Gd films loaded with hydrogen", *J. Alloy. Compd.*,

(2015) (*in Press*).

[11] H.T. Uchida, S. Wagner, M. Hamm, J. Kürschner, R. Kirchheim, B. Hjörvarsson, and A. Pundt, "Absorption kinetics and hydride formation in magnesium films: Effect of driving force revisited", *Acta Mater.*, **85**, (2015), 279-289.

Danksagung

Lebenslauf

Persönliche Daten

Name: Helmut Takahiro Uchida
Geburtsdatum: 19.Sep.1980
Geburtsort: Stuttgart
Familienstand: Verheiratet, 1 Kind
Staatsangehörichkeit: Japan

Ausbildung

Schule	Apr.1986-Mär.1992	Kamikitazawa Grundschule, Setagaya-Ku, Tokio, Japan
	Apr.1992-Mär.1995	Midorigaoka Mittelhochschule, Setagaya-Ku, Tokio, Japan
	Apr.1996-Mär.1999	Shinjuku hochschule, Shibuya-Ku, Tokio, Japan
	Apr.1999-Mär.2000	Paukinsinstitut Sundai-Ocyanomizu, Chiyoda-Ku, Tokio, Japan
Studium	Apr.2000-Mär.2004	Material physics of high-functional materials, Metallurgical- and Material engineering sector, Engineering Department, Tohoku University, Sendai, Miyagi, Japan
	Mär.2004	Bachelor of Engineering.
	Apr.2004-Mär.2006	Graduate school of Tohoku University, Sendai, Miyagi, Japan.
	Mär.2006	Master of Engineering.
	Mär.-Jun.2006	Hilfswissenschaftler in Engeering department, an der Univ. Tohoku, Sendai, Miyagi, Japan.
	seit 2006	Ph.D Student in der Arbeitsgruppe von Prof. Dr. Astrid Pundt im Institut für Materialphysik der Universität Göttingen

Aufbaustudium

Sep.2006-Okt.2007	Wissenschaftlichehilfskraft in der AG Prof. Dr. Astrid Pundt.
Okt.2007-Mär.2011	DAAD Stipendiat für Ph.D Studium
Apr.2011-Mär.2014	Wissenschaftlichehilfskraft in der AG Prof. Dr. Astrid Pundt.